AP-BIOMECH 2023

EXTENDED ABSRACT E-BOOK

12th Asian Pacific Conference on Biomechanics

Kuala Lumpur, Malaysia

15 - 18th November 2023

Editors
Shazlin Shaharudin | Juliana Usman | Nooranida Arifin
Hanie Nadia Shasmin | Muhamad Noor Harun

Organized by:

APAB   MSB
MALAYSIAN SOCIETY OF BIOMECHANICS

Supported by:

Malaysia Convention & Exhibition Bureau   Meet in Malay BE Greater, To   UNIVERSITI MALAYA

Sponsor:

BMEC

AP-BIOMECH2023
Extended Abstract E-Book

12th Asian Pacific Conference on Biomechanics

15th – 18th November 2023
Corus Hotel, Kuala Lumpur, Malaysia

Editors
Shazlin Shaharudin
Juliana Usman
Nooranida Arifin
Hanie Nadia Shasmin
Muhamad Noor Harun

TABLE OF CONTENT

Theme: Soft Tissue Biomechanics

Theme: Hard Tissue Biomechanics

Theme: Human Movement & Robotics

Theme: Sports Biomechanics

Theme: Biomechanics in Injury & Rehabilitation

Theme: Biomechanics in Nature

Theme: BioMEMs & Biomaterials

Theme: Computational Biomechanics

Theme: Tissue & Organ Engineering

Theme: Emerging & Multidisciplinary Biomechanics

PREFACE

The 12th Asian Pacific Conference on Biomechanics held in Kuala Lumpur, from 15th to 18th November 2023, offered a unique platform to facilitate engagement between multiple subfield of biomechanics. This volume includes 154 peer-reviewed abstracts relating to timely issues in Cell & Molecular Biomechanics, Fluid Biomechanics, Soft Tissue Biomechanics, Hard Tissue Biomechanics, Human Movement & Robotics, Sports Biomechanics, Biomechanics in Injury & Rehabilitation, Biomechanics in Nature, BioMEMs & Biomaterials, Computational Biomechanics, Tissue & Organ Engineering, Emerging & Multidisciplinary Biomechanics. The main review criteria include its relevance to the conference, contribution to the body of knowledge, appropriateness of the research method and the clarity of the results. This biannual conference will not have been possible without the dedication of the conference committee, University of Malaya, sponsors, reviewers, speakers, presenters and delegates. We would like to thank all of them and hope that this book of abstracts may offer a record of the topics discussed at AP-Biomech 2023 and a source of inspiration for new ideas and collaboration.

Organizing Committee

Chairperson	Dr Juliana Usman (UM)
Secretary	Dr Nooranida Arifin (UM)
Bursary	Pn Hanie Nadia Shasmin (UM)
Program Scientific & Technical	Dr Muhamad Noor Harun (UTM)
	Dr Aizreena Azaman (UTM)
	En Chok Chuen Leang (ISN)
Secretariat	Dr Rizal Mohd Razman (UM)
	Pn Siti Nur Khairunnisa Mad Arifin (ISN)
	Desdemona Mollon (ISN)
	Yeap Ming Wei (ISN)
Publication	Dr Shazlin Shaharudin (USM)
	Yallini Selva (ISN)
Website	Dr Krishnamurithy A/L Genasan (UM)
	En Mohd Shukri Hadafi Md Nor (PTM-UM)
	Siti Rabiatul Madia binti Malek Razuan (UM)
Public & Industry Relation	Dr Nasrul Anuar Abd Razak (UM)
	En Yuvaraj A/L Ramasamy (ISN

MECHANICAL ADAPTATION OF ACTOMYOSIN FIBERS: EXPERIMENT AND SIMULATION

Shihang Ding[1,2], Daiki Matsunaga[1], Taeyoon Kim[2] and Shinji Deguchi[1]

[1] Graduate School of Engineering Science, Osaka University, Osaka, Japan.
[2] Weldon School of Biomedical Engineering, Purdue University, West Lafayette, USA.
Email: kimty@purdue.edu; deguchi.shinji.es@osaka-u.ac.jp

INTRODUCTION

Mechanical forces play an essential role in non-striated muscle cell (NSMC) processes including morphogenesis, migration, and cytokinesis. Among them, how cells adapt to external force is intimately associated with biological functions, but still requires elucidation. Actomyosin fibers (AFs), which are the major origin of intracellular force in NSMCs, exhibit environment-dependent dynamics that dominate their mechanical adaptation profoundly. Distinct from the highly specific structures in striated muscles, AFs proteins in such adaptive cells are disorganized and are known to change adaptively according to the surrounding mechanical environment, which further alters the cell configuration. However, the molecular basis for AFs adaptation and their inherent force-dependent dynamics lacks a comprehensive understanding. In this study, we propose an effective method that can analyze AFs adaptation quantitatively by combining the single-fiber experiments and the agent-based simulations.

METHODS

For the single-fiber experiments, AFs were isolated from A7r5 cells by applying the hypotonic shock technique [1]. It can remove the apical cell membrane, cytosol, and nucleus by exposing cells to the jet flow of the buffer from a Pasteur pipette. Subsequently, AFs that still attach to the substrate can be remained by treating the de-roofed cells with detergent. A dynamic load can be exerted by a functionalized glass needle with the silane-coupled glutaraldehyde (Figure 1a). In this single-fiber experiment, the contractility of isolated AFs can be retained with the presence of a physiological level of magnesium-ATP buffer that can reactive myosin ATPase.

In our agent-based model, AFs components including the filamentous actins (F-actins), motors, and α-actinin, a type of actin cross-linking proteins (ACPs), are simplified cylindrical segments connected by elastic hinges, which recapitulates their realistic structures and dynamics [2]. Briefly, F-actin is coarse-grained by several segments with length and diameter equal to 140 nm and 7 nm, respectively, which are connected in tandem and have polarities defined by their barbed and pointed ends. A motor consists of a backbone with several arms attached, which mimics the architecture of non-muscle myosin thick filaments. The backbone is composed of a symmetric structure with a central segment and side segments of 42 nm. Each arm represents 8 myosin heads. In addition, each ACP is described as two arms of 23.5 nm connected by an elastic hinge.

RESULTS AND DISCUSSION

In our *in-vitro* experiments, the isolated AFs exhibited diverse responses depending on their external loads. Stretch-compression cycles were conducted with different strain values. In these cycles, we observed distinct buckling scales of AFs followed by a gradual deformation into a straight shape. By recording the change in their contour length over time, we found the SFs compressed with a larger strain or higher strain rate showed more significant buckling and required a longer time for reforming the linear appearance. To analyze it quantitatively, parameters in our model were set by reasonable values. According to the polarity, 50 F-actins are symmetrically distributed in the computational domain, which can reproduce the stretch-compression experiment well (Figure 1b). Based on this simulation, we found that larger deformation brings a longer distance for myosin to walk, which consequently consumes longer recovery time. In addition, we found that the buckling can be affected by the fiber persistence length as well. With the increase of persistence length, the curvature of the compressed fiber becomes larger. However, its contour length and recovery time are not altered significantly. Based on these findings, it reveals that the contour length and recovery time mainly depend on the magnitude of AFs deformation and the myosin walking rate instead of its persistence length.

CONCLUSION

The inherent adaptation of the *in-vitro* AFs was extrapolated, and it predominantly depends on the magnitude of the extracellular forces and the protein interactions instead of their initial mechanical properties.

REFERENCES

[1] Matsui, T. S. et al. *Biorheology* **46**: 401-415, 2009.
[2] Kim T. *Biomech. Model. Mechanobiol.* **14**: 345-355, 2015.
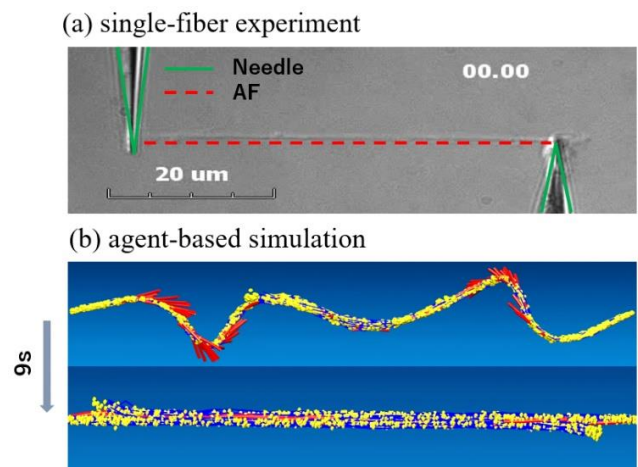
Figure 1 Mechanical adaptation of AFs.

METASTATIC COMPETENCY OF BREAST CANCER CELLS AFTER CONFINED MIGRATION

Xiao Song[1], Kuan Jiang[2], Lanfeng Liang[2] and Chwee Teck Lim [1,2]
[1] Biomedical Engineering Department, National University of Singapore, Singapore.
[2] Mechanobiology institute, National University of Singapore, Singapore.
Email: ctlim@nus.edu.sg

INTRODUCTION

Previous studies have shown that highly metastatic competent cancer cells that have successfully completed the process of metastasis are correlated to their wrinkled nuclei [1]. In fact, wrinkled nucleus has been associated with increased malignancy of metastasizing cancer cells as well as poor prognosis [2]. However, the mechanisms underlying the formation of nuclear envelope invagination and the connection between nuclear wrinkling and enhanced malignancy remain poorly understood.

METHODOLOGY

The protocol of the experiment is shown in Figure 1. MDA-MB-231 cells were seeded onto the top of the filter membrane of transwells with a density of 300,000 cells/cm^2 and left to migrate under normal culture conditions. After three days, cells after confined migration through transwells were collected at the bottom of the well plates. The wrinkling index (surface to volume) of nuclei is quantified in this confined migration sorted cells. Cells were forced to flow through our previously developed high throughput microfluidics chip with capillary-sized constrictions[3]. The cells that exited the microfluidics were collected and subjected to a live and dead assay to assess their viability.
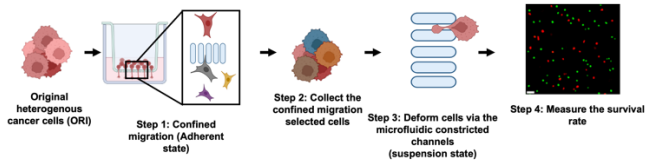
Figure 1 Experiment protocol.

RESULTS AND DISCUSSION

By forcing confined migration sorted cancer cells to flow through capillary-sized constriction, these cells were found to have more wrinkled nucleus and exhibited high resilience to mechanically squeezed-related death (Figure 2a). Additionally, higher heterochromatin expression was found in the confined migration group as well as survival cells after mechanical deformation (Figure 2b and c). By flowing Lamin A/C transfected cells through capillary-sized mechanical deformation, it was demonstrated that the invagination sites of their nucleus declined. Cells with smoother nuclear envelopes were associated with the observation of broken nuclear envelopes and DNA leakage, providing further evidence of the importance of a wrinkled nucleus. Using drugs to manipulate heterochromatin expression, we showed that an upregulated heterochromatin level may lead to the formation of a more wrinkled nucleus and consequently, resulted in increased cell viability following exposure to capillary-sized constriction (Figure 2d).
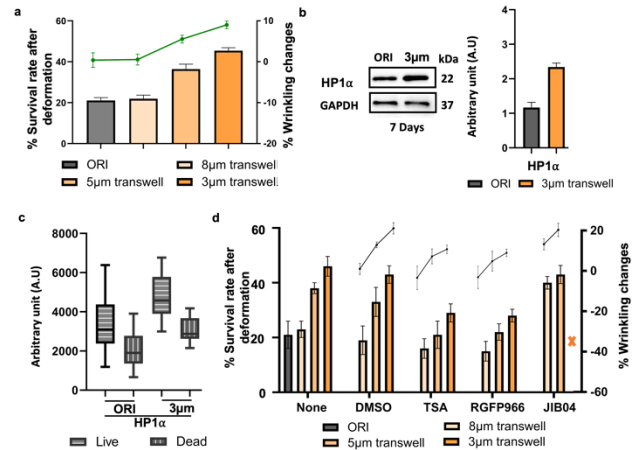
Figure 2 a) Quantification of survival rate after deformation and wrinkling index in cells after confined migration. b) Comparison of confined migration sorted cell HP1α expression. C) Quantification of HP1α intensity in live and dead cells. d) Quantification of survival rate after deformation and wrinkling index in cells after confined migration after heterochromatin expression manipulation.

CONCLUSION

We demonstrated that confined migration may induce the formation of a wrinkled nucleus by upregulating heterochromatin expression. In turn, this wrinkled nuclear envelope may serve as a protective mechanism, enabling cancer cells to withstand passive capillary-sized mechanical deformation by unfolding and releasing the pressure accumulated. Additionally, our findings emphasize the possible connection between physical confinement within the microenvironment and the increased aggressiveness of metastatic cancer cells. This connection could potentially be harnessed to develop innovative therapeutic approaches aimed at inhibiting the distal spread of cancer cells.

ACKNOWLEDGEMENT

REFERENCES

[1] Cosgrove B. D. et al. *Biomaterials*, **270,** 2021.
[2] Elston C. W. & Ellis I.O. *Histopathology,* **19**(5): 403-410, 1991.
[3] Jiang K. et al. *Adv. Sci.*, 2023.

EFFECT OF GOLD NANOPARTICLES ON ABLATION AREA OF CELL-CONTAING TISSUE PHANTOM IN IRREVERSIBLE ELECTROPORATION

Kentaro Funada[1] and Kosaku Kurata[2]

[1] Graduate School of Engineering, Kyushu University, Fukuoka, Japan.
[2] Department of Mechanical Engineering, Kyushu University, Fukuoka, Japan.
Email: kurata@mech.kyushu-u.ac.jp

INTRODUCTION

Irreversible electroporation (IRE) is a technique that necrotizes a volume of targeted tissue by using intense electric pulses at a few kV/cm. It has been studied as a promising method of minimally invasive tumor ablation. However, under the limitation of the applied voltage of a few kilovolts, a requirement arises to make the ablation area as large as possible, *i.e.*, to reduce the critical electric field strength of the tissue. Previous studies showed that modification of the extracellular fluid by the addition of surfactants led to a reduction of the critical electric field [1, 2]. In this study, we investigated the effect of gold nanoparticles added to alter the electrical properties of the extracellular matrix on the ablation area of cell-containing tissue phantom.

METHODS

Cardiomyocyte cell line P19CL6 cells purchased from RIKEN Bioresource Center (Tsukuba, Japan) were mixed with 20, 40, 60, or 80 nm dia. gold nanoparticles (Cytodiagnostics, Inc., Canada) at the concentration of 10^5, 10^7, or 10^9 particles/ml in 2.5 % agarose sol (SeaPlaque Agarose, Lonza Rockland, Inc., USA). Cell density in the sol was adjusted to 10^7 cells/ml. Then, 0.5 ml of the sol was poured on a 35 mm dia. glass bottom dish and allowed to gel at 4°C for 20 min. A homemade pin-and-ring electrode (a pin with 1 mm outer dia. and a ring with 10 mm inner dia., Figure 1(a)) was put on the gel, *i.e.*, cell-containing tissue phantom, and used to apply 10-μs long electric pulses at 500 V. The pulse number and interval were 120 times and 100 ms, respectively. The electroporated gels were further incubated in a culture medium at 37°C for 30 min, and stained with propidium iodide (PI) and calcein-AM to distinguish between living and dead cells using a confocal laser microscope. The diameter of PI-positive dead cell area was determined in fluorescent microscopic images.

RESULTS AND DISCUSSION

Figure 1(b) shows a fluorescent micrograph of the cell-containing tissue phantom after applying electric pulses. PI-positive red cells were observed around the central pin electrode. Figure 1(c) shows the effects of the concentration and diameter of gold nanoparticles on the ablation area occupied by the PI-positive dead cells. The ablation area of the tissue phantom with 80 nm dia. nanoparticles was comparable to that of the control without particles irrespective of concentration. The ablation area decreased as the diameter of the nanoparticles decreased, and the effect was more significant at higher particle concentrations.

We initially hypothesized that the introduction of nanoparticles into tissue phantom would enhance the disruption of the cell membrane by effectively localizing the electric field. However, our experimental findings diverged from this expectation. Gold nanoparticles of at least 20~80 nm diameter had only a negative effect on the ablation area by IRE. Further experimental studies and numerical analysis of the electric field are needed to understand the mechanism.
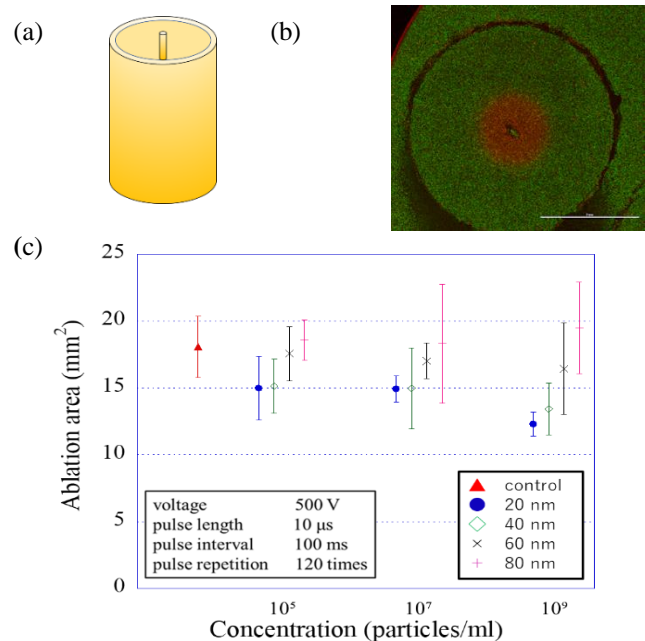
Figure 1 (a) Homemade pin-and-ring electrode, (b) fluorescent micrograph of tissue phantom after applying electric pulses (bar: 5 mm), and (c) effects of concentration and diameter of gold nanoparticles on ablation area.

CONCLUSION

Gold nanoparticles ranging 20~80 nm in diameter reduced the ablation area resulting from the application of electric pulses. This negative effect was more significant at higher particle concentrations.

ACKNOWLEDGEMENT

REFERENCES

[1] Kurata K et al. *IEEE Trans Biomed Eng* **67**: 420-427, 2020.
[2] Jiang C et al. *Ann Biomed Eng* **42**: 192-204, 2014.

CHANGE IN CELL MEMBRANE PERMEABILITY DURING APPLICATION OF ELECTRIC PULSES

Taishin Kinoshita[1] and Kosaku Kurata[2]

[1] Graduate School of Engineering, Kyushu University, Fukuoka, Japan.
[2] Department of Mechanical Engineering, Kyushu University, Fukuoka, Japan.
Email: kurata@mech.kyushu-u.ac.jp

INTRODUCTION

Electroporation is a technique that temporarily forms nanoscale pores in the cell membrane by repeatedly applying electric pulses to cells in a short period of time, thereby increasing the permeability of the cell membrane. Despite its potential as a minimally invasive cancer therapy, the underlying mechanism behind membrane permeabilization and repair process remains unclear. Therefore, our study aimed to investigate the alteration in cell membrane permeability during electroporation by analysing cell swelling upon the application of intense electric field pulses.

METHODS

A fibroblast cell line NIH3T3 and a cardiomyocyte cell line P19CL6 were cultured glass bottom dishes, respectively. By using a pair of 0.3 mm dia. tungsten wires attached to an electric manipulator, electric pulses of 100-μs long were applied to the cells 90 times at 1-s interval. Applying voltages of 50~200 V across 1 mm electrode separation resulted in electric fields ranging from 0.5 to 2 kV/cm. Microscopic images of the cells were recorded every five seconds during the application of electric pulses. Then, the cell volume was calculated with the assumption of cells as hemispheres.

When there is an osmotic pressure difference $\pi - \pi'$ [Pa] across a semipermeable membrane with an area of A [m²], the water inflow volume V [m³] in a minute time t [s] is expressed by

$$\frac{dV}{dt} = L_p A(\pi - \pi') \qquad (1)$$

using the water permeability L_p [m/(Pa・s)][1]. Osmotic pressure $\pi(t)$ [Pa] at a time t is calculated by

$$\pi(t) = \frac{n}{V(t)} RT \qquad (2)$$

according to Van't Hoff's law, where n [mol] is the amount of colloidal solute, R [Pa・m³/(K・mol)] is the gas constant, and T [K] is the temperature. Furthermore, n is expressed by

$$n = C_0 V_0 \qquad (3)$$

where C_0 [mol/m³] is molarity of colloidal solute before voltage application and V_0 [m³] is cell volume before voltage application. Assuming that the osmotic pressures of the intra- and extra-cellular fluids become equal when the cell swelling ceases at the volume of V_∞, the following equation is derived from Eqs. 1, 2, and 3:

$$L_p(t) = \frac{dV(t)}{dt} \frac{V_\infty V(t)}{A(t) C_0 V_0 RT\{V_\infty - V(t)\}} \qquad (4)$$

The change in L_p as a function time was finally calculated by using $V(t)$ measured.

RESULTS AND DISCUSSION

The lower limit of the electric field causing cell swelling was 0.58 kV/cm for NIH3T3 cells and 0.65 kV/cm for P19CL6 cells, respectively. Blebbing, in which a part of the cell membrane was extruded, was observed when electric fields above 0.75 kV/cm were applied to NIH3T3 cells and 0.85 kV/cm to P19CL6 cells.

Figure 1 shows the periodic change in water permeability obtained for NIH3T3 cells. The water permeability across the cell membrane increased with time. The higher the electric field strength, the greater the rate of increase in the water permeability. This is because larger electric fields induce greater Maxwell stresses, *i.e.*, damage, to the cell membrane, resulting in a larger total area of nanopores.

NIH3T3 cells showed higher water permeability than P19CL6 cells. This would be attributed to 1.12 times larger cell diameter and 1.26 times larger surface area of NIH3T3 cells then P19CL6 cells. Cells with a larger diameter will suffer more damage because they are exposed to a larger potential difference across the cell in the electric field.
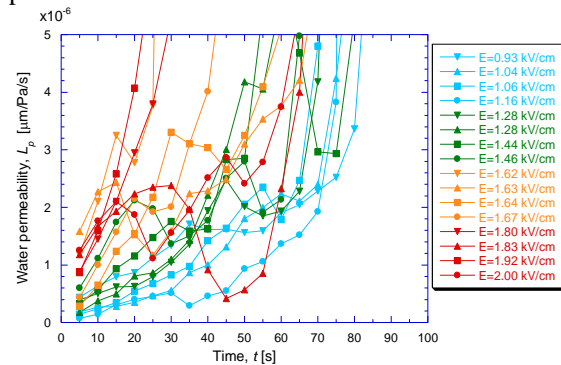
Figure 1 Change in water permeability L_p across the cell membrane of NIH3T3 fibroblasts

CONCLUSION

The electric field strengths at which cell swelling and blebbing occur were respectively obtained for NIH3T3 and P19CL6 cells. Water permeability across the cell membrane increased not only with electric field strength applied but also with cell diameter.

ACKNOWLEDGEMENT

REFERENCES

[1] McGrath JJ. *Heat Transfer in Medicine and Biology* **2**: 185-238, 1985.

DEVELOPMENT OF PLANAR LIPID MEMBRANES FOR ANALYSIS OF AN INNER-EAR MOTOR PROTEIN PRESTIN

Hayato Niioka[1], Michio Murakoshi[2]

[1] Division of Frontier Engineering, Graduate School of Natural Science and Technology, Kanazawa University, Kanazawa, Japan.
[2] Faculty of Frontier Engineering, Institute of Science and Engineering, Kanazawa University, Kanazawa, Japan.
Email: niioka054@stu.kanazawa-u.ac.jp

INTRODUCTION

Sound vibrates the tympanic membrane, and the vibration is transmitted to the basilar membrane inside the cochlea via the ossicles. There is a sensory organ, called the organ of Corti, on the basilar membrane. Outer hair cell (OHC) located in such organ amplify sound by expanding and contracting their cell length. This movement is thought to be caused by conformational changes of the motor protein "prestin", which exists in the plasma membrane of OHC. However, its structure and function have not yet been clarified. Although previous studies have attempted to analyze the structure of prestin by using mammalian cells [1-3] and a planar lipid membrane [4], the function remains unclear since there are many steps in the process of preparing planar lipid membranes. In the present study, therefore, we attempted functional analysis of prestin by using a simpler method of creating a planar lipid membrane.

METHODS

Two types of phospholipids, DOPC (D4250, Tokyo Chemical Industry, Tokyo) and DPPC (850355P-200mg, Avanti, USA), were used. Liposomes were prepared by the electroformation method [5]. A lipid solution was applied and dried on a glass slide. The lipid was hydrated and swollen in a sugar solution to obtain liposomes (Vesicle Prep Pro, Nanion, Germany). The liposomes were observed by the inverted microscope (BZ-X800, Keyence, Osaka). The DOPC liposomes were then distributed on a glass substrate with a micro hole of 1 μm diameter, and negative pressure of -2 kPa was applied from the lower part of the hole to cleave a liposome and the planar lipid membrane was prepared. The formation of the planar lipid membrane was confirmed by measuring membrane resistance before and after the cleavage (Port-a-patch, Nanion).

RESULTS AND DISCUSSION

Figure 1 shows the DOPC and DPPC liposomes. The densities of DOPC and DPPC liposomes with diameter of 10 - 60 μm were estimated to be 2,614 pieces/mm² and 7.6 pieces/mm², respectively. Diameter analysis revealed that the DOPC liposomes with a diameter of 8.0 ± 0.4 μm were prepared. A reason for the low number of DPPC liposomes may be due to insufficient formation of the dried lipid membrane. Figure 2 shows the results of resistance measurement. Before the liposome cleavage, the resistance showed 3.6 MΩ. After the liposome cleavage, the resistance increased to be 20.5 GΩ, suggesting that the planar lipid membrane was formed.
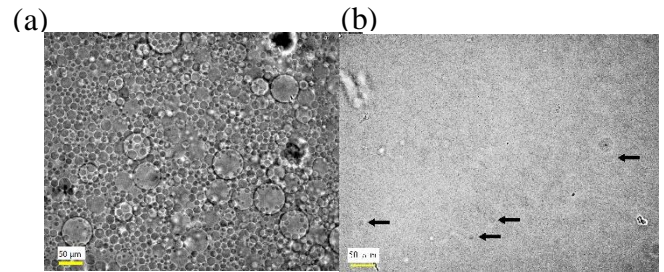
Figure 1 Liposomes prepared by the electroformation method. (a) DOPC. (b) DPPC. Scale bars show 50 μm.
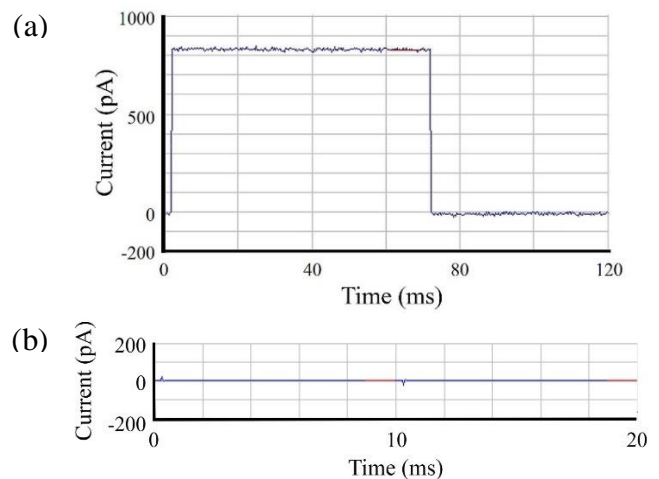
Figure 2 Resistance measurement of a planar lipid membrane. (a) Before the liposome cleavage. (b) After the liposome cleavage.

CONCLUSION

Liposomes were prepared with DOPC and DPPC by the electroformation method. The planar lipid membrane was possibly developed by cleaving these liposomes.

ACKNOWLEDGEMENT

REFERENCES

[1] Murakoshi M et al. *J Assoc Res Otolaryngol* **7**: 267-278, 2006.

[2] Murakoshi M et al. *Pflugers Arch* **457**: 885-898, 2009.

[3] Murakoshi M & Wada H. *J Biomech Sci Eng* **16**: 21-25, 2021.

[4] Kumano S et al. *FEBS Lett* **584**: 2872-2876, 2010.

[5] Angelova M & Dimitrov DS. *Prog Colloid Polym Sci* **76**: 59-67, 1988.

LIVING CELLS SIDE-VIEW IMAGING METHOD FOR CELL ADHESION EVALUATION

Mao Otake[1, 2], Takaaki Abe[3], Yoshiaki Ukita[4] and Hiromi Miyoshi[1]

[1] Department of Mechanical Systems Engineering, Tokyo Metropolitan University, Hachioji-shi, Japan.
[2] Research Fellow, Japan Society for the Promotion of Science, Chiyoda-ku, Japan.
[3] Department of Advanced Materials and Implementations, Osaka University, Suita-shi, Japan.
[4] Graduate Faculty of Interdisciplinary Research Faculty of Engineering, University of Yamanashi, Kofu-shi, Japan.
Email: mao-otake@tmu.ac.jp

INTRODUCTION

Adherent cells seeded in a culture medium sink to the bottom and attach onto the substrate through non-specific interactions. Then, in the initial phase of cell spreading, the cells adhere to the substrate by the integrins binding to ligand molecules deposited on the substrate and flatten slightly from its spherical morphology. Then, in the later phase, the cell spreads by the local clustering of integrin, and the development of stress fibers, which assumes a larger and more expanded morphology [1]. At this stage, protein dynamics and subcellular deformation are mutually affected. The cell membrane is deformed by changes in protein dynamics inside the cell, and vice versa, the deformation of the cell membrane affects the accumulation of integrins [2]. However, the behavior of adhering cells, specifically in the initial adhesion process, has not fully elucidated. Conventional observation of cells including adhesion dynamics have been performed by irradiating light vertical to the culture surface. The images obtained with such the method are projected on the substrate, which unable to detect the membrane deformation near the interface with the surface, specifically in cells during spreading. To cope with the problem, we developed a side-view imaging method.

METHODS
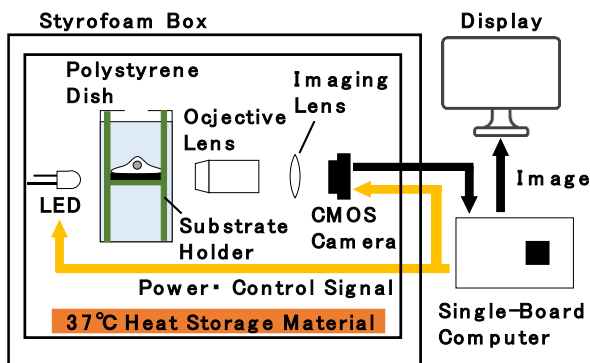
Figure 1 Overview of the living cells side-view imaging system.

A mouse fibroblast cell line (3T3-Swiss albino) was used as a normal cell model, and a human fibrosarcoma cell line (HT1080) was used as a cancer cell model. The cells were suspended in Leibovitz medium L-15 supplemented with 10% fetal bovine serum and penicillin-streptomycin and seeded on a glass substrate at 20,000 cells/dish for 3T3 Swiss albino and 40,000 cells/dish for HT1080. Figure 1 shows the developed side-view imaging system. A small microscope optical system including a φ35 mm polystyrene dish with a substrate holder for horizontally holding a substrate to which cells adhere was placed in a styrofoam case insulated from the surroundings. The temperature inside the case was maintained at 37°C by installing a heat storage material in a styrofoam box. Imaging was started immediately before cell seeding, and the adhesion behavior of cells was recorded at 1 fps for 12 hours.

RESULTS AND DISCUSSION

The side-view imaging system enabled the evaluation of the subcellular deformation of the cells near the interface. By comparing immediately after cell seeding to the late adhesion processes of 3T3-Swiss albino and HT1080, we identified the difference in adhesion behavior of the cells. The 3T3-Swiss albino attached to the substrate immediately after the cells contacted the substrate. In addition, HT1080 showed cells moving in a direction after contact with the substrate. Since this movement direction matches the flow direction of the medium, the cells are assumed to move on the substrate surface due to the flow of the medium. Another difference was that 3T3 Swiss albino showed large deformation of the cell membrane in transition to the late adhesion stage, whereas HT1080 showed less deformation. These differences in moving and membrane deformation are possibly related to the metastatic ability of cancer cells.

CONCLUSION

We developed a side-view imaging method for living cells and evaluated the behavior in the initial adhesion process between normal and cancer cell models. The normal cell model is attached to the substrate immediately after contacting the substrate. Then, the cells sowed dynamical deformation. The magnitude of deformation gradually increased, and the deformation came to an abrupt stop, followed transition to a late adhesion process. In contrast, the cancer cell model migrated in the direction of the medium flow still after contacting the substrate surface. Further analysis of these differences in the adhesion behavior is expected to provide new knowledge about cancer metastasis mechanisms.

ACKNOWLEDGEMENT

REFERENCES

[1] Amelia AK & Mohd RA, *Int. J. Mol. Sci.*, **16**: 18149-18184, 2015.
[2] Jonathan F, et al., *PNAS*, **111**: 313075-13080, 2014.

INTERNAL FLOW OF *C. ELEGANS* BODY PROMOTED BY LOCOMOTION

Yasuhiro Asoshina[1], Kenji Kikuchi[1,2], and Takuji Ishikawa[1,2]
[1]Department of Finemechanics, Tohoku University, Sendai, Japan
[2]Department of Biomedical Engineering, Tohoku University, Sendai, Japan
Email: yasuhiro.asoshina.p8@dc.tohoku.ac.jp

INTRODUCTION

The nematode *C. elegans* is a slender organism with about 1 mm in length, which has a transparent body and organs in common with humans. For this reason, a nematode is an ideal model organism for observing internal flow. In addition, the body wall of nematodes contains four pairs of muscles called body wall muscles, and they perform undulating body movements by entraining contractions of these muscles.

In humans, nutrient transport is carried out by the digestion and vascular systems. Nematodes, however, do not have an obvious vascular system. The detailed mechanism of nutrient transport in nematodes has not been clarified. In addition, few studies have investigated how locomotion affects nutrient transport in the nematode body. In a previous study, they successfully observed the transport of lipoprotein-modified fluorescent particles injected into the intestine of *C. elegans* [1] and nutrient uptake promoted by a defecation motor program of the reciprocating intestinal flows [2]. In this study, we investigated the effects of body motion on the flow in nematodes by visualization of the flow in the nematode body and analysis of particle transports from a hydrodynamic point of view.

METHODS

Nematodes were cultured on an agarose gel medium, which was seeded *E. coli* OP50-1 on the top surface of the gel as a food source in a Petri dish of 60 mm in diameter in an incubator at 20°C for 3 days. Only adult nematodes were used in the experiment.

For microinjection into nematodes, 2% agarose pads were prepared on a coverslip. Place a drop of halocarbon oil (series 700, Sigma-Aldrich, USA) on the pads, and nematodes were transferred in the oil drop and allowed to touch the pads to immobilize the nematodes [3]. After immobilization, the coverslip was transferred to the microscope stage (IX71, OLYMPUS, Japan), and inserted injection needle into the nematodes. The fluorescent particles were injected into the pseudo-coelom. Injection needles were made by pulling a glass capillary (GD-1, NARISHIGE, Japan) with a puller (PC-100, NARISHIGE, Japan) to a sharp shape.

After injection, we collected the nematode by adding a drop of Ringer's solution and observed the behavior of fluorescent particles in the nematode body. Since the nematodes repeat periods of active swimming and quiescent state [4], the behaviors of particles during swimming and quiescence were captured by a digital camera.

After imaging, particle velocity in nematode body was calculated by particle tracking method using image analysis software (ImageJ, NIH, USA) The particle trackings were performed using a TrackMate plug-in of ImageJ for the nematodes in quiescence and a manual tracking for the swimming nematode, respectively.

RESULTS AND DISCUSSION

Compared to the average particle velocity in quiescence nematodes body, the average particle velocity in swimming nematodes body was significantly greater as shown in Fig.1. This result suggests that the locomotion by body wall muscle promotes the flow in the pseudo-coelomic cavity. On the other hand, compared to the average particle velocity in the M9 buffer, the average particle velocity in swimming nematodes was smaller. The fact that the particle behavior in the cavity was slower than that in the M9 buffer and water may suggest that the liquid filling the pseudo-coelomic cavity might be more viscous than water or M9 buffer.
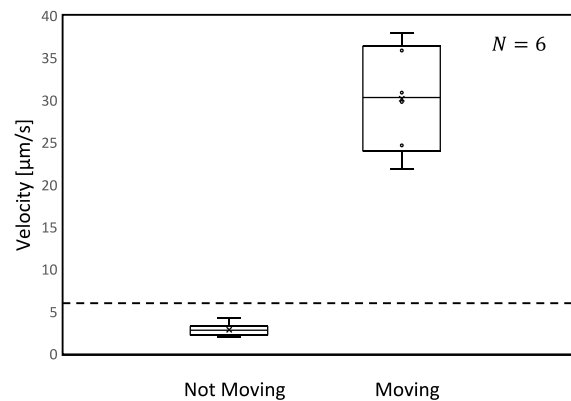
Figure 1 Average particle velocities of swimming nematodes and quiescence nematodes. The broken line shows the average particle velocity measured in M9 buffer.

CONCLUSION

In this study, the effects of locomotion were investigated by visualizing the flow within the nematode body by injecting fluorescent particles. In the experiment, we found that flow occurs in pseudo-coelomic cavity by nematodes swimming. These results suggest that nematode body motion contributes to nutrient diffusion.

REFERENCES

[1] Kuo Y., et al. *Biomaterials* **34**: 8352-8360, 2013.
[2] Suzuki Y., et al. *Sci. Rep.*, **12**:15310, 2022
[3] Mello C. C., et al. *EMBO Journal* **10**: 3959-3970, 1991
[4] Ghosh R., et al. *Journal of Experimental Biology* **211** 3703-3711, 2

ANALYSIS OF THE TEMPERATURE FIELD IN A CELL SEPARATION DEVICE USING DIELECTROPHORESIS

Yoshinori Seki[1], Aoi Nagasaka, Shigeru Tada

[1] Department of Applied Physics, National Defense Academy, Yokosuka, Kanagawa, Japan.

Email: ed22004@nda.ac.jp

INTRODUCTION

Cell separation technology using dielectrophoresis has attracted much interest as an effective method for non-invasive separation of cells [1]. However, cell separation devices based on dielectrophoresis have a problem that cells inside the device are exposed to a high temperature environment due to Joule heating. In this study, we measured the temperature rise of the electrode surface in the device using the LIF method. At the same time, by analysing the cell cycle, we discussed the effect of the temperature rise on the physiological functions of the cells.

METHODS

The temperature field analysis was performed using the cell separation device we proposed in the past [2]. The cell separation device has a parallel-plate micro flow channel structure in which a planar electrode is on the top and a counter interdigitated electrode (electrode width and interval were 50 μm) was installed on the bottom surface of the micro channel. As shown in Fig.1, the experimental setup mainly consists of the cell separation device, a confocal laser scanning microscope, a waveform generator, and a syringe pump. A syringe pump was used to introduce 20 μM Rhodamine B solution into the device, and the microscope was used to acquire time-lapse fluorescence images of the bottom surface of the micro flow channel in the cell separation device where the interdigitated electrodes were placed. Experimental conditions were as follows: the applied voltage $V = 20$ V$_{pp}$, AC frequency $f = 57.6$ kHz, flow rate of the cell sample solution $Q = 5.0$ mL/h, and the solution conductivity $\sigma_f = 40$ mS/m. The acquired fluorescence images were analyzed by imaging analysis using ImageJ to obtain the average temperature rise at the bottom of the micro channel, ΔT_{av}. For cell cycle analysis, human mammary epithelial normal cells (MCF10A) and tumor cells (MDA-MB231) were suspended in 300 mM mannitol solution, respectively. Cell samples were passed through the device under the above-mentioned operating conditions, collected after cell separation, and were subjected to cell cycle analysis by flow cytometry. In this study, the G1 and S and G2 phases of the four main stages before cell division were used as indicators for analysis.
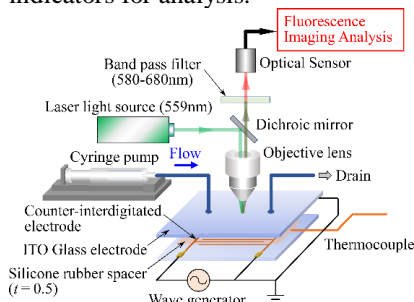
Figure 1 Schematic of the experimental setup

RESULTS AND DISCUSSION

Figure 2 (a) shows the transient of ΔT_{av}. As shown in Fig.2 (a), ΔT_{av} monotonically increased before it reached an equilibrium state at $t\sim720$ s. The maximum of ΔT_{av} was found to be around 20 °C. The ambient temperature was ~20 °C. Therefore, the maximum temperature in the flow channel could be higher than 40 °C. An example of the results of cell cycle analysis is shown in Fig.2 (b). No clear difference was observed between control (no high temperature exposure) cells and cells collected after separation. For control and collected cells, the G1 period was 61.1 ± 5.0 % and 71.3 ± 7.4 %, respectively, the S period was 13.5 ± 2.5 % and 10.8 ± 3.4 %, and the G2 period was 25.4 ± 6.3 % and 17.8 ± 4.8 %. In all cycles, the statistics were below the 5% (P = 0.05) level and were not significantly different. This may be because the ΔT_{av} identified in the present experiment was not a value that produced significant changes for the cell functions. And the other reason was time period for the exposure of high temperature environment. It was approximately only a few minutes.
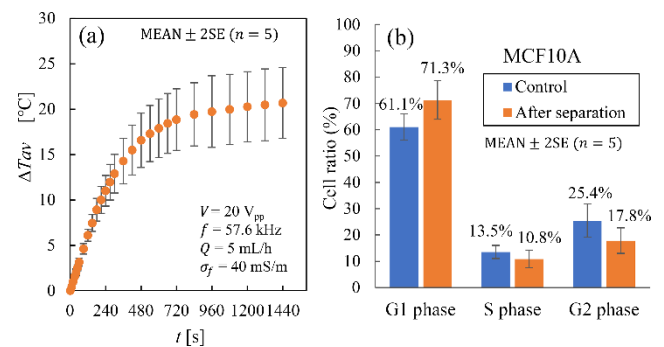
Figure 2 (a) ΔT_{av} variation with time (b) Cell cycle analysis

CONCLUSION

The temperature rise in the cell separation device was measured by the LIF method, and the average temperature rise was found to be approximately 20 °C. Analysis of the cell cycle of the cells after cell separation showed no distinctive effect of the temperature rise on cell viabilities.

REFERENCES

[1] Rahman N. A., et al. *Sensors*, **17**: 449-475, 2017.

[2] Seki Y., et al. *Proc. of the 11th Asian-Pacific Conference on Biomechanics*, PP1-83, 2021.

BIOMECHANICAL ANALYSIS IN SPHEROID CULTURE:
INDUCTION OF HYPERTROPHIC CHONDROCYTE DIFFERENTIATION

Jeonghyun Kim[1], Kosei Tomida[1], Eijiro Maeda[1], Taiji Adachi[2] and Takeo Matsumoto [1]

[1] Department of Mechanical Systems Engineering, Nagoya University, Nagoya, Japan.

[2] Department of Biosystems Science, Institute for Life and Medical Sciences, Kyoto University, Kyoto, Japan.

Email: jkim@nagoya-u.jp

INTRODUCTION

3D culture of cells provides structures and functions similar to those of living tissue and has been widely used as a useful *in vitro* tool to reproduce the formation process of the living tissue. In previous study [1], we represented that the 3D scaffold-free culture of mesenchymal stem cells highly up-regulated the gene expression levels of hypertrophic chondrocyte differentiation within 7 days in the absence of chemical differentiation supplements, compared to a conventional 2D monolayer model. Recently, we also fabricated the cartilage spheroid model reconstructed by pre-chondrocyte cells to examine the effect of spheroid culture in the chondrocyte differentiation [2]. In this study, we conducted biomechanical analysis in the cartilage spheroid culture with regard to hypertrophic chondrocyte differentiation.

METHODS

In this study, we subcultured 2,500 cells of mouse chondrocyte precursor ATDC5 cells in each well of U-bottom ultra-low culture plate (ThermoFisher, USA) to fabricate the cartilage spheroids based on the previous study [2]. The spheroids were incubated for 2, 7, or 14 days with DMEM/F12 medium (Gibco, USA) without chondrogenesis differentiation supplements. We then collected for real-time PCR and cryosectioning to stain with anti-collagen X antibody (Abcam, USA), Hoechst 33342 (Invitrogen, USA), and Alexa Fluor 546 Phalloidin (Invitrogen, USA). The staining images with Hoechst 33342 were also observed using a confocal microscope (ZEISS LSM880, Germany) and further analyzed with Imaris (Bitplane, Australia) for 3D image analysis to quantify the nuclear morphology.

RESULTS AND DISCUSSION

Corresponding to the previous study [2], the long term-culture up to Day 14 provoked the increase in the size of the spheroid. As a result of real-time PCR, the 14-day spheroid culture up-regulated the gene expression levels of the hypertrophic chondrocyte differentiation markers compared to the 2-day spheroid culture. In Fig. 1(A), COL10 expression was locally expressed around the surface of the 2-day-old spheroid, whereas the COL10 expression was entirely detected in the 14-day-old spheroid. We then conducted the 3D image analysis using Imaris for segmentation of the nuclei in the spheroid to quantify the nuclear morphology in the spheroid. As represented in Fig. 1(B), each of the nuclei in the 14-day spheroid were hypertrophied than 2-day spheroids. We also found that there was a correlation in the nuclear volume in 2-day and 7-day spheroids, whereas there was almost no correlation on the 14-day spheroids. In other words, the cells in the
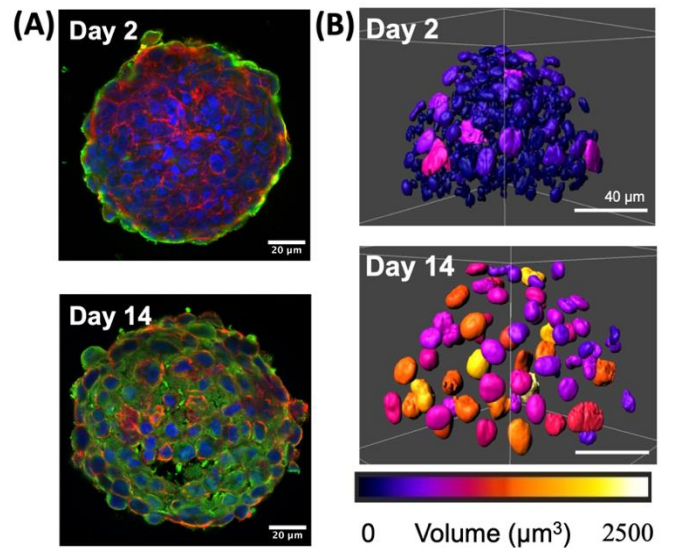
spheroid after 14-day incubation were entirely hypertrophied.

Figure 1 (A) Immunostaining images of COL10 (green), nuclei (blue), and F-actin (red) in 2-day and 14-day spheroids reconstructed by mouse pre-chondrocyte ATDC5 cells. (B) 3D image analysis using Imaris for 2-day and 14-day spheroids.

CONCLUSION

In this study, we conducted the biomechanical analysis focusing on temporospatial change in gene and protein expressions as well as morphological and functional changes for the cartilage spheroid. As a result, we confirmed the induction of hypertrophic chondrocyte differentiation was achieved by spheroid culture even without the chemical differentiation medium, which is an initial stage of the endochondral ossification. We believe our biomechanical analysis will be applicable for other 3D culture model such as organoids.

ACKNOWLEDGEMENT

REFERENCES

[1] Kim *et al*. *Sci Rep* **11**, 13204, 2021.

[2] Kim *et al*. *Biotechnol Bioeng* **119(11)**, 3311-3318, 2022

TRANSGENIC MICE EXPRESSING FRET-BASED ACTININ TENSION SENSOR FOR THE MEASUREMENT OF INTRACELLULAR TENSION IN TISSUES WITH CONVENTIONAL CLSMS

Takeo Matsumoto[1], Junfeng Wang[1], Eijiro Maeda[1], Yuki Tsujimura[2], Hideo Yokota[2], Tetsuya Kitaguchi[3]

[1] Department of Mechanical Systems Engineering, Nagoya University, Nagoya, Japan.
[2] RIKEN Center for Advanced Photonics, RIKEN, Wako, Japan.
[3] Institute of Innovative Research, Tokyo Institute of Technology, Yokohama, Japan.
Email: takeo@nagoya-u.jp

INTRODUCTION

Tension sensors using Förster resonance energy transfer (FRET) have been developed to visualize intracellular forces [1-2]. However, it is extremely difficult to introduce these sensors into tissues using conventional methods such as electrophoresis. Recently, Tao *et al*. [3] developed transgenic mice expressing a tension sensor to visualize forces at the tissue level. Their results were obtained with a high-cost FLIM (Fluorescence Lifetime Imaging Microscopy) but not with a widely used CLSM (confocal laser scanning microscope), possibly because the fluorescent intensity of their system is not so high. Furthermore, the fluorophores used in their sensor cannot be observed with the widely used 488-nm laser system. In a previous study, we developed a tension sensor by inserting a FRET cassette made of two fluorophores, EGFP and mCherry, connected with spider silk protein into actinin [4]. This sensor was bright enough and the tension can be evaluated with a FRET ratio that is the ratio of the acceptor (mCherry) to the donor (EGFP) fluorescence using a conventional 488 nm CLSM system. In this study, we introduced the gene of this sensor into C57BL/6N mice to obtain mice expressing the tension sensor [5].

METHODS

We introduced our tension sensor gene engineered with the Cre/loxP system into the ROSA26 locus of C57BL/6N mice and crossbred them with Cre mice to obtain animals expressing the tension sensor. We excised various tissues including the aorta, tail tendon, heart, and skin, and isolated cells from the tissues with enzymes. The isolated tissues and cells were stretched with a tensile tester (STB 150W NK, Strex, Japan) under a conventional CLSM (LSM880, Carl Zeiss, Germany) with a 63× oil immersion objective at room temperature in phosphate-buffered saline (PBS). The fluorescence signals of EGFP and mCherry were obtained under excitation with a 488 nm wavelength laser at each stretch step to calculate the FRET ratio.

RESULTS AND DISCUSSION

The expression of the sensor can be observed in all excised tissues (Fig.1). The fluorescence intensity was high enough to observe the change in the FRET ratio with the confocal microscope. We conducted tensile tests of the aortic tissues and tail tendons and smooth muscle cells (SMCs) isolated from the aortic tissue and confirmed that the FRET ratio decreased in response to stretch, as expected. The FRET ratio decreased linearly in aortic tissues and SMCs. For tendons, it did not change until collagen fibers became straight and began to decrease beyond this point. The sensitivity of the FRET sensor was dependent on tissue types and cells. It was -0.63, -1.39, and -2.78 (%FRET/%strain) for aortic tissues, SMCs, and tendons, respectively.
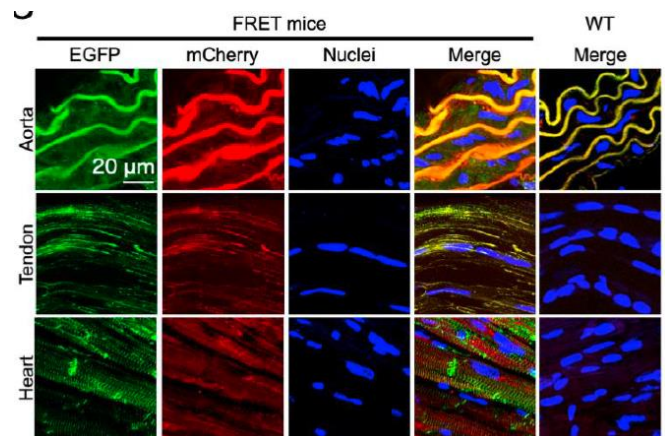
Figure 1 Examples of FRET sensors expressed in various tissues.

It has been reported that strain in actin stress fibers in SMCs in the direction of the fiber axis was half of the strain in the smooth muscle layers in the circumferential direction of the aorta [6]. The relatively low FRET ratio change in aortic tissues compared with SMCs observed in this study may support this observation.

CONCLUSION

We have established transgenic mouse lines expressing an actinin tension sensor. The present mice may become a powerful tool in mechanobiology.

ACKNOWLEDGEMENT

REFERENCES

[1] Grashoff C et al. *Nature* **466**: 263-266, 2010.
[2] Meng F & Sachs F. *J Cell Sci* **124**: 261-269, 2011.
[3] Tao H et al. *Nat Commun* **10**: 1703, 2019.
[4] Wang J et al. *J Biomech Sci Eng* **11**: 16-00504, 2016.
[5] Wang J et al. under review (Preprint at: https://doi.org/10.21203/rs.3.rs-2994461/v1)
[6] Sugita S et al. *Biomech Model Mechanobiol* **20**: 1003-11, 2021.

ANALYTICAL AND SIMULATION STUDY ON BROWNIAN COLLISION FOR DENSE CHROMATIN DYNAMICS

Yukitaka Ishimoto [1] and Yuki Takahashi [1]

[1] Department of Mechanical Engineering, Akita Prefectural University, Yurihonjo, Akita, Japan.

Email: ishimoto@akita-pu.ac.jp

INTRODUCTION

For medical applications, it has been anticipated to elucidate physical details of chromatin condensation or decondensation in a dense chromatin situation such as in human cells. However, Brownian dynamics method for long time simulation assumes relatively constant force at each time step and collisions violate it and prevented a naive application of the method. Here, we propose two ways of collision algorithms to overcome this difficulty. The constructed functions offer faithful representation of the chromatin dynamics for a time step longer than 1 ns.

METHODS

Nucleosomes are coarse-grained as beads which are linearly connected by spring elements as linker-DNAs. We invoke the worm like chain model (WLC) for the spring elements of linker-DNA with a finite length. For BD simulation, we set the time step $\Delta t = 1$ ns unless otherwise stated. The diffusion constant of nucleosome and the spring constant of liker-DNA were estimated from that of EGFP in a nucleus [1] and the elastic nature of double-stranded DNA. We also implement the interaction between histone octamers estimated from experiment by the Lennard-Jones potential based on the DNA origami experiment [2] as its depth. The basic dynamics of a bead is given by the Langevin equation in the overdamped limit, and its integral solution by the Euler-Maruyama method in the absence of collision.

When a two-body collision happens during a time step, the corresponding Langevin equations are to be modified subject to a pair of colliding force dW_c, so the integral solution of each bead may not be accurate. In conventional BD, we set $\Delta t \sim 1$ ps to avoid such collisions. Here, we rearrange the equations as below:

$$\begin{cases} \xi \frac{dr_G}{dt} = -\frac{dU(r_G)}{dr} + f_G(t) \\ \xi \frac{d(\Delta r)}{dt} = -\frac{dU(\Delta r)}{d(\Delta r)} + f_\Delta(t) \end{cases}' \qquad (1)$$

where ξ is the friction coefficient of the bead and r_G is the centre-of-gravity (COG) position. U is the potential function of the positions. $f_G(t)$ and $f_\Delta(t)$ are the random forces, the former of which is purely of thermal fluctuation with the diffusion coefficient multiplied by the square root of two, while the latter consists of the same diffusion and dW_c.

We propose two ways of collision algorithms to integrate $f_\Delta(t)$: one is to construct a probability function of two-body collision by Fourier-Bessel series from in-silico experiments at a smaller time scale, while the other is to do so by an analytical solution with a similar fitting to the in-silico experiment. In the latter, we find an approximate form of an analytic solution for the diffusion equation with a pair of spherical boundaries and fit it to the in-silico experiment.

RESULTS AND DISCUSSION

We performed the in-silico experiments of the collision for $1\mu s$ and extracted the relative displacements of a pair of nucleosomes. The initial distance between the nucleosomes were set to be $L_d = 12.1$ nm, and the relative displacement Δr_i for the bond vector $r_{i,i+1}$ was extracted and plotted from the final result in the l-y plane (Fig. 1), l being the radial direction of the cylinder and y along the axis. We fit the Fourier-Bessel series expansion to the data, and fit the asymptotic form of the solution to the data which was plotted by Mathematica.
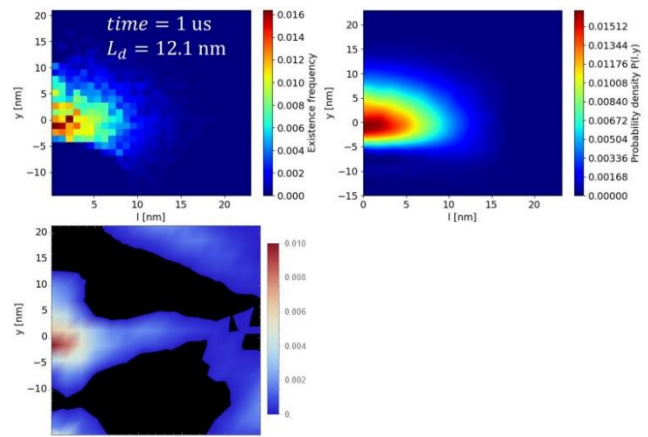
Figure 1 Histogram of the in-silico experimental result (top-left), and the constructed probability density functions (top-right) Fourier-Bessel, (bottom) fitted by the asymptotic analytic solution.

CONCLUSION

We proposed two ways of implementing the two-body collision to BD by fitting the in-silico data. The distorted forms from the normal distribution suggest that the effect may contribute to the suppression of nucleosome mobility as sub-diffusion observed in experiments. Further implementation will be done in the near future.

ACKNOWLEDGEMENT

REFERENCES

[1] Nozaki T et al. *Nucleus* **4**(5): 349-356, 2013.
[2] Funke JJ et al. *Sci. Adv*. **2**: e1600974, 2016.

SIMULATION OF THROMBUS FORMATION IN
A CEREBRAL ANEURYSM WITH FLOW DIVERTER STENTING

Kenji Komiya[1], Shuta Imada[1], Kaito Kurata[1], Yoshihiro Ujihara[1], Shukei Sugita[1] and Masanori Nakamura[1]
[1] Department of Electrical and Mechanical Engineering, Nagoya Institute of Technology, Nagoya Japan
Email: masanorin@nitech.ac.jp

INTRODUCTION

Flow diverter (FD) stenting has attracted attention as a treatment of cerebral aneurysms. This treatment aims to promote thrombosis within the aneurysm by stagnating blood flow in the aneurysm, thereby occluding it with a thrombus. However, complete occlusion of large aneurysms is difficult to achieve; the complete occlusion rate was 77.9% after 3 years of long-term follow-up [1]. It would be helpful for the optimal design of treatment strategies in aneurysms if thrombus formation after the FD treatment is predicted preoperatively. In this study, we developed a mathematical model of the thrombogenic process, and applied it to an aneurysm model to examine whether it is possible to express a general trend of the thrombus formation depending on the presence or absence of FD.

METHODS

A mathematical model of thrombus formation was developed based on the following idea. To begin, endothelial cells in low wall shear stress area are activated, and adhesion factors are expressed on the cell membrane. Platelets adhere to the activated endothelial cells and become activated. Activated platelets activate surrounding platelets by releasing active substances. Since the concentration of the active substances would be high in stagnation, platelet activation is further promoted there. Activated platelets bind to each other and form a thrombus. A series of these phenomena were mathematically modelled in reference to Menichini et al. [2]. Transport of resting platelets activated platelets, and bound platelets (thrombus) was expressed by the advection-diffusion equation. Hemodynamics was expressed with the equations of the Navier-Stokes and continuity. Physical effects of thrombus on flow were expressed by the external force and the blood viscosity which were determined as a function of the concentration of bounded platelets. The blood flow passing through FD was expressed using Darcy's law and the Cozeny-Kalman equation. Simulations were conducted for a geometry model of a cerebral artery with an aneurysm (Fig. 1(a)). A FD model was deployed to cover the neck of the aneurysm. The dimensions and porosity of FD were determined in reference to [3]. Blood flow and transports of resting, active and bound platelets were solved interactively using scFLOW ver2022 (Hexagon). The simulations were commenced assuming that a small portion of resting platelets are initially activated.

RESULTS AND DISCUSSION

Thrombus was formed only for the case with FD placement. Figure 1 (a) presents the progress of thrombus formation for the case with FD. As seen, the thrombus was initially formed at the upstream side of the apex of the aneurysm and grew towards the neck. Complete occlusion of the aneurysm was observed by the end of the simulation. Figure 1 (b) plots changes in a volume fraction of thrombus that occupied the aneurysm and a flowrate entering the aneurysm. In looking at Fig. 1 (b), we found that no thrombus was formed until the end of the simulation when FD was not placed, whereas the aneurysm was gradually embolized with thrombus when FD was placed. The flow into the aneurysm was diminished with the growth of thrombus.
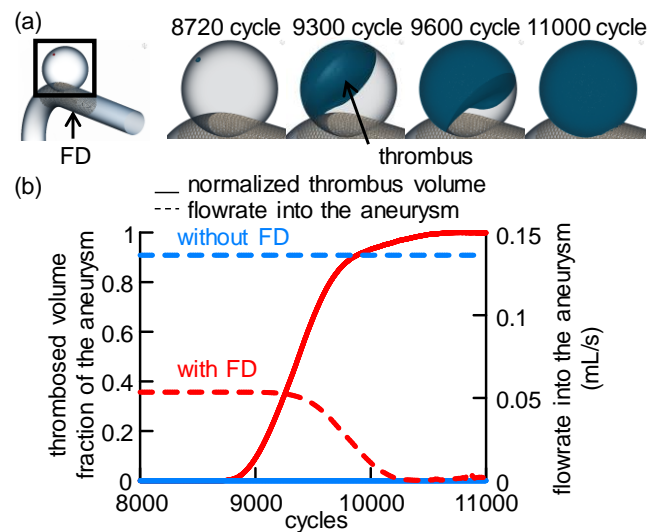
Figure 1 (a) Geometry model of blood vessel with an aneurysm. The region enclosed by a black box is magnified to show development of thrombus in the aneurysm. (b) Time variations of a thrombosed volume fraction of the aneurysm and the flowrate into the aneurysm.

CONCLUSION

Thrombus formation in cerebral aneurysm with/without FD was simulated. We succeeded in reproducing general trends of the thrombus formation after FD treatment; thrombosis did not occur without FD, and the aneurysm was completely occluded with a thrombus when FD was placed. Further ameliorations of the model along with parameter tuning and comparison with clinical data are necessary will lead to the establishment of thrombus prediction technology.

REFERENCES

[1] Fujii T et al. *Neurol Med Chir* (Tokyo), **62**: 19-27, 2022
[2] Menichini C et al. *J Math Biol*, **73**: 1205-1226, 2016
[3] PIPELINE[TM] FLEX with Shield Technology[TM] Flow diverter system, Catalog, Medtro

FLOW DATA ASSIMILATION OF MAGNETIC RESONANCE IMAGES CONSIDERING PARTIAL VOLUME EFFECT

Kakeru Ueda[1], Kazuma Imata[1], Tomohiro Otani[1] and Shigeo Wada[1]
[1] Graduate school of engineering science, Osaka University Toyonaka-shi, Osaka, Japan.
Email: k.ueda@biomech.me.es.osaka-u.ac.jp

INTRODUCTION

The phase-contrast resonance imaging (PC-MRI) can measure *in vivo* flow velocity map invasively, while the outputted velocity map has spatiotemporal resolution limitations and does not satisfy the flow conservation law. To overcome this issue, several flow data assimilation approaches have been proposed by minimizing the error between MRI and computed flow maps (e.g., [1]). Here, the intravoxel flow fields in MRI images were averaged in each voxel (partial volume effect), and thu s appropriate consideration of this effects would be desired especially for the data assimilation of low-resolution images. Therefore, this study proposes a reasonable flow data assimilation of the MRI images with respect to inlet velocity profiles taking into account the partial volume effect based on [1].

METHODS

We assume that the MRI velocity $\mathbf{v}_m^i$ $(i = 0, \dots, N)$ is discretely assigned in each voxel, where N is the number of voxels. Once the flow velocity in computational simulation is dented as $\bar{\mathbf{v}}$ with inlet velocity $\mathbf{V}$ on Γ_I, cost function between the MRI and computed velocities is given by

$$\mathcal{O}(\mathbf{v}, \mathbf{V}) = \frac{\alpha}{2}\sum_{i=1}^{N}\left\|\bar{\mathbf{v}} - \mathbf{v}_m^i\right\|^2 + \frac{\beta}{2}\int_{\Gamma_I}\|\partial_s\mathbf{V}\|\,d\Gamma, \quad (1)$$

Where ∂_s is spatial derivative of Γ_I and α, β are the constants. Here, we define $\bar{\mathbf{v}}$ as the voxel-averaged velocity of the computed flow map $\mathbf{v}$, shown as

$$\bar{\mathbf{v}} = \frac{1}{A^i}\int_{\Omega^i}\mathbf{v}\,d\Omega, \quad (2)$$

where Ω^i is the voxel domain and A^i is the area/volume of Ω^i. In computation, we treated the flow map in the Cartesian grid which coincides the MRI images. The flow is assumed as steady incompressible Newtonian properties, described by the equation of continuity and steady Navier-Stokes equation, given by

$$\nabla \cdot \mathbf{v} = 0 \quad (3)$$

$$\rho(\mathbf{v}\cdot\nabla)\mathbf{v} = -\nabla p + \mu\nabla^2\mathbf{v} - \mathbf{K}\mathbf{v}, \quad (4)$$

where p is pressure, p is density, μ is viscosity, and $\mathbf{K}$ is the flow resistances to express the wall boundary in the Cartesian grid [1]. Here, we consider the minimization of the following Lagrange function $\mathcal{L}$ with respect to $\mathbf{V}$, given by

$$\min \mathcal{L}(\mathbf{v}, \mathbf{w}, p, q, \boldsymbol{\lambda}, \boldsymbol{\eta}, \mathbf{V})$$
$$:= \mathcal{O}(\mathbf{v}, \mathbf{V}) - \mathcal{L}_s(\mathbf{v}, \mathbf{w}, p, q, \boldsymbol{\lambda}, \boldsymbol{\eta}, \mathbf{V}), \quad (5)$$

where q, $\boldsymbol{\lambda}$, $\boldsymbol{\eta}$ are Lagrange multipliers and $\mathcal{L}_s$ is the weak form of eqs. (3) and (4). Stationary conditions of eq. (5) were treated by Galerkin least-square method and V was iteratively updated by steepest descent method.

As a numerical example, flow in a two-dimensional 90-degree elbow pipe (Reynolds number = 200) was considered and only the downstream domain after elbow was selected for the data assimilation domain (Fig. 1 (left)) which flows from bottom top. This flow map was downsampled to 2x4 pixels to model the MRI velocity map (Fig. 1 (right)).

RESULTS AND DISCUSSION

Fig. 2 (left) shows the iteration history of the cost function. The cost function of the proposed method has two-order lower than that of method [1]. Fig. 2 (right) shows the streamline of the assimilated flow map of the propsed and previous methods. The flow map in the proposed method successfully expresses the backflow near the inlet region observed in the original flow map. These results exhibited the valuabilities of the proposed method taking into account the partial volume effect.
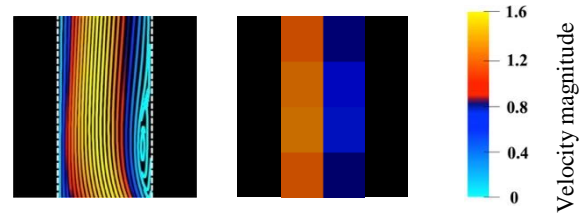
Figure 1 Original (left) and target (right) velocity map after bent section.
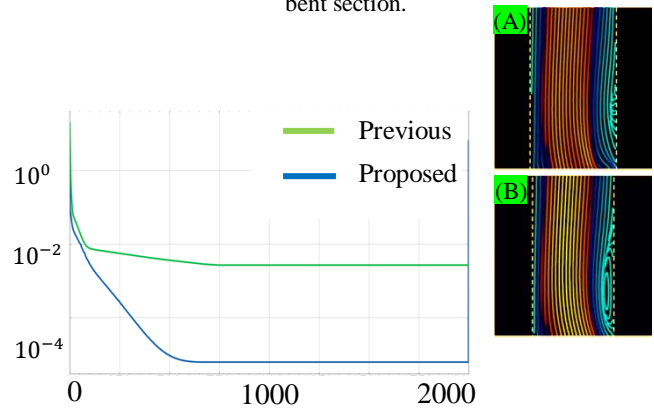
Figure 2 Iteration history of cost function (left) and estimated velocity map by method [1] (A) and proposed method (B) (right).

CONCLUSION

This study proposed a flow data assimilation that takes partial volume effect into account and demonstrates its usefulness. This approach is potentially valuable for the flow analyses using low-resolution MRI images.

REFERENCES

[1] Otani, T., et al., *J Biomech Sci Eng*, **17**(3), 22-50, 2022.
[2] Borrvall, T., and Petersson, J. *Int J Numer Methods Fluids*, **41**(1), 77–107, 2003.

TRANSDERMAL TRANSPORT THROUGH INTERCELLULAR GAPS OF LIPOSOMES IN SUSPENSIONS

Jiawei Huang[1], Kenji Kikuchi[1,2], Keiko Numayama-Tsuruta[2] and Takuji Ishikawa[2,1]

[1] Department of Finemechanics, Tohoku University, Sendai, Japan.
[2] Department of Biomedical Engineering, Tohoku University, Sendai, Japan.
Email:huang.jiawei.t2@dc.tohoku.ac.jp

INTRODUCTION

Liposomes (LIPs) are small vesicles composed of a phospholipid bilayer, making it easier to penetrate the skin for non-invasive drug delivery. LIP penetration exhibits a pronounced size dependence, although they are dorsally generally believed to be deformable and penetrate the body through gaps with smaller sizes [1]. However, the mechanism of how LIPs permeate through cellular interstitial spaces is unclear due to the difficulty of measuring various LIP properties at the nanoscale. This study measured the distribution of liposomes in depth as they penetrated the skin and compared LIP with Rhodamine B solution (RhB) and fluorescent nanoparticles (FNPs) to elucidate the properties of LIP in suspensions while penetrating the skin.

METHODS

LIP prepared by ethanol injection [2]: injected the ethanol solution containing 1,2-Dioleoyl-sn-glycero-3-phosphocholine (DOPC, Wako), CM-DiI (C7000, Invitrogen) Dimethyldioctadecylammonium Bromide (DDAB, TCI) into Milli-Q water at the rate of 500 μL/min, stirring at 300rpm, the composition of the organic solution is shown in Table 1.

The resulting LIP suspension was mixed with Milli-Q water, RhB (Wako, 250 μM) solution or FNPs (FluoSpheresTM Carboxylate-Modified, F8787, 1011 particles/L) suspension in a one-to-one ratio, and 10 μL was dropped on the surface of pigskin for administration. The liposome suspension mixed with RhB and FNPs was prepared without CM-DiI to avoid fluorescence interference.

In this study, suspension of 30 nm fluorescent LIP was used to administrate pigskin for one and two hours, then measured the distribution of fluorescence along depth in the pigskin; Measuring the total fluorescent intensity of fluorescent LIP of four sizes, RhB solution and FNPs suspension in pigskin after one hour of administration; Measuring the total intensity of fluorescence in pigskin administrated with the mixture of non-fluorescent LIP suspension and RhB or FNPs for one hour.

Table 1: Protocol of organic solution used in ethanol injection for LIP preparation.

DOPC (mM)	DDAB (mM)	CM-DiI (g/L)	Measured Size (nm)
1	1	1	30
2	1	1	75
3	1	1	112
4	1	1	129

RESULTS AND DISCUSSION

As shown in Figure 1A, permeation rate of LIP along the depth reached to a limited flux and Figure 1B demonstrates the size dependence of the permeability of LIP.

Figure 1C exhibits the amount of permeation when RhB and FNPs were permeated alone, while mixing with LIPs of different sizes, permeation was facilitated and showed size dependence, as shown in Figure 1D. The permeability of LIP decays inversely with size, whereas the facilitation of the permeation of RhB and FNPs decays close to linearly. When RhB and FNPs indicate the permeability of the suspension, it means that the LIP is relying on its own properties to permeate further even when the suspension is no longer permeating further.
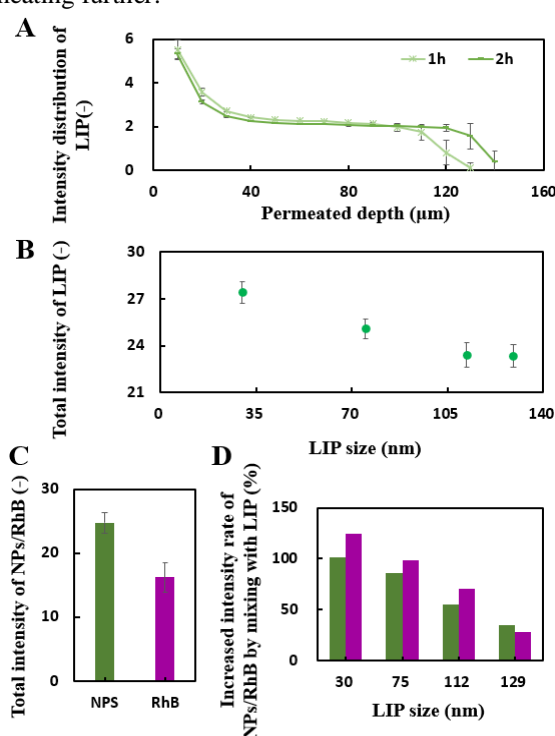
Figure 1 Results of penetration of liposomes or two other fluorescent tracers in pigskin administration.

CONCLUSION

LIP maintains a relatively constant rate of penetration in the deeper layers of the skin, penetrating deeper and deeper with time, and penetrating in an inverse proportion to size. LIP also facilitates the permeation of other substances in the suspension, but by its own nature brings more permeability than other substances.

ACKNOWLEDGEMENT

REFERENCES

[1] Liu J et al. *Pharm Res* **38**: 1429-1437, 2021.
[2] Carugo D et al. *Sci Rep* **6**: 25976, 2016.

STAGNATION PHENOMENON OF MOTILE *E. COLI* IN A FOLDING WALL

Toma Isaka[1], Kenji Kikuchi[2,1], Keiko Numayama-Tsuruta[1] and Takuji Ishikawa [1,2]

[1] Graduate School of Biomedical Engineering, Tohoku University, Sendai, Japan.

[2] Graduate School of Engineering, Tohoku University, Sendai, Japan.

Email: isaka.touma.s6@dc.tohoku.ac.jp

INTRODUCTION

Intestinal bacteria are deeply involved in digestion, absorption and immunity. However, digestion and excretion in the body occur faster than the swimming speed of bacteria. In such an environment, it is not well understood how the intestinal bacteria stay in the intestine. Previous studies have investigated the behavior of *E. coli* in a non-flow environment, but it is necessary to understand the behavior of bacteria in a flow environment in order to elucidate their behavior *in vivo* [1]. In this study, we flowed *E. coli* or particles into the microchannels with folding structures, which are similar shapes with the zebrafish intestine, and investigated their staying ability in the folding.

METHODS

E. coli suspension and fluorescent particles were flowed into the PDMS microchannel at 0.01 µL/min by a syringe pump and were observed by microscope with a 40× objective lens. The fold structure of the microchannel was fabricated based on the previously measured dimensions of the zebrafish intestinal folding with a maximum width of 131 µm, a fold depth of 47 µm and a height >100 µm. AcGFP1-expressing *E. coli* was used, which was transfected with pAcGFP1 into MG1655. Successfully transfected individuals were selected by adding ampicillin (50 µg/mL final concentration) to *E. coli* suspension during incubation and incubated for 8 hours. Fluorescent particles (2% solids) with a diameter of 1 µm were used, diluted 100-fold with TB. After observation, *E. coli* and fluorescent particles were tracked using TrackMate in ImageJ and the mean square displacements (MSD) were calculated.

RESULTS AND DISCUSSION

E. coli was flowed and recorded at 0.01 µL/min and the trajectories of the *E. coli* were displayed and tracked in ImageJ. The most of cells were carried downstream, some cells, however, were moved across the streamline and swam towards the folds.

The fluorescent particles were moved more along the streamlines than the *E. coli*. Some particles were also observed to leave from the streamlines near the folds and entered the folds.

Similar behavior was observed with both *E. coli* and particles. Figure 1 shows the results of the probability density distribution with the intensity normalized to the channel center as 1. The position from the channel center to the folds was normalized by r / R. Here, r is the distance from the channel center and R is the distance from the channel to the bottom of the fold. For the *E. coli* in Fig. 1(a), although there was little change from the channel center to around $r / R = 0.8$. The intensities increased rapidly from around $r / R = 0.8$

to the bottom of the fold. In contrast, the results of particles in Fig. 1(b) show that the intensities did not change much from the center of the channel to the bottom of the fold. These

results indicated that *E. coli* might tend to stay deep in the fold, whereas the particles did not. This might be due to *E. coli* is able to move further into the flowless region due to its swimming ability, whereas the particles are unable to move as far as *E. coli* due to the lack of flow.

The MSD of *E. coli* and particles near the folds and the center of the channel were calculated to indicate their behaviors. The diffusion phenomenon was enhanced near the folds compared to the center of the channel for both *E. coli* and particles. This is thought to be the effect of random walk and Brownian motion for *E. coli* and particles, respectively.
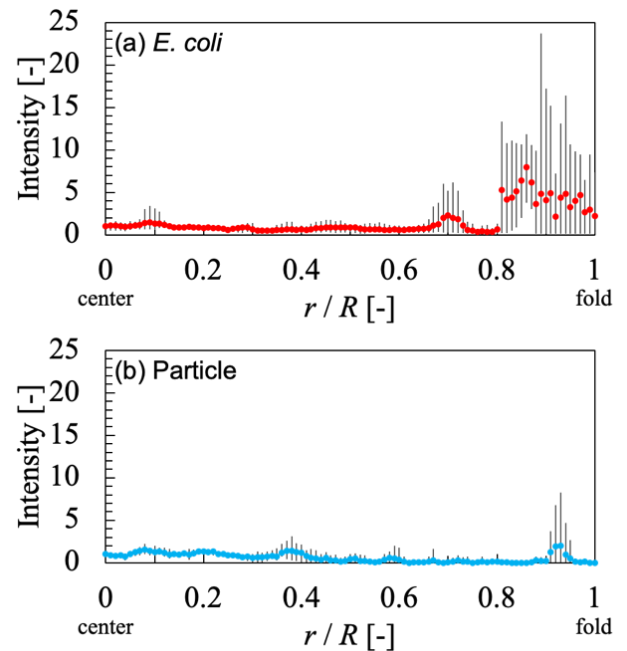
From these results, it is considered that *E. coli* move faster and random walk near the folds, which makes them more likely to move deeper into the fold.

Figure 1 Probability density distributions in folds. Channel center is set to 1. (a) *E. coli*. (b) Particle. n=5

CONCLUSION

Observation of the stagnation of *E. coli* and particles in microchannels with folds showed that bacteria had the ability to accumulate in the folds owing to the motility.

REFERENCES

[1] Mok R et al. *Phy. Rev. E* **99**: 052607, 2019.

NUMERICAL ANALYSIS OF LATERAL MIGRATION OF THE RIGID SPHERE IN BIO-INSPIRED PUMP

Tomoki Takada[1], Taimei Miyagawa[1], Takahiro Okabe[1] and Minori Shirota [1]

[1] Graduate School of Science and Technology, Hirosaki University / 3 Bunkyo-cho, Hirosaki, Aomori, Japan.

Email: miyagawa@hirosaki-u.ac.jp

INTRODUCTION

In the small intestine, the high-viscosity fluid and solid-liquid mixtures containing solid food components are transported by cyclic wall motility patterns of muscle called peristalsis, segmentation contractions, and pendular motions. Recently, the transport properties of the small intestine have been applied to the development of the pump using artificial rubber muscle [1]. However, the flow in the pump has yet to be discussed and remains unclear. Therefore, it is necessary to clarify these phenomena by using numerical simulation.

Connington et al. [2] numerically clarified that the rigid sphere initially placed off the centreline laterally migrates toward the centreline, oscillating in both the lateral (vertical) and longitudinal (horizontal) directions due to the peristaltic contractions.

In this study, we mainly focus on segmentation contractions and numerically evaluate the lateral migration of the rigid sphere due to segmentation contractions.

METHODS

This study considers the two-dimensional flow of incompressible viscous fluids driven by segmentation contractions in the bio-inspired pump of the half-width of channel a and wavelength λ. The shape of the channel at position x and time t is expressed as follows:

$$h(x,t) = \pm a \pm b \sin\left(\frac{2\pi x}{\lambda}\right) \sin\left(\frac{2\pi t}{T}\right), \qquad (1)$$

where, b is the amplitude of the wave and T is the period of the wave. The Navier-Stokes and continuity equations of the governing equations were discretised using the ALE finite element method based on the fractional step method. These equations are solved with no-slip boundary conditions at the wall, zero pressure gradient and periodic boundary conditions at both ends of the channel. The motion of the rigid sphere was traced in a Lagrangian manner proposed by Kajishima et al. [3].

RESULTS AND DISCUSSION

Trajectories of rigid particles with different initial positions were compared to evaluate the lateral (vertical) migration in biomimetic pumps. Figures 1(a) and 1(b) show the time history of the centre of gravity of the rigid sphere initially placed off the centreline. The rigid sphere laterally migrated toward the centreline, oscillating in both the lateral and longitudinal directions. This result is consistent with the previous study of peristalsis [2]. Furthermore, the rigid sphere migrated to the antinode of the wall displacement. Initially placed at $X_0/\lambda = 0.1$, the rigid sphere reached its position in about 10 cycles and oscillated laterally until about 20 cycles. Finally, it stopped due to the symmetrical flow field centred on the rigid sphere. The speed of migration was different from the initial position.

We consider that the driving force of lateral migration is the wall effects, such as the Saffman lift force caused by the

velocity gradient of the fluid and the Magnus lift force caused by the rotation of the rigid sphere.

(a)

(b)
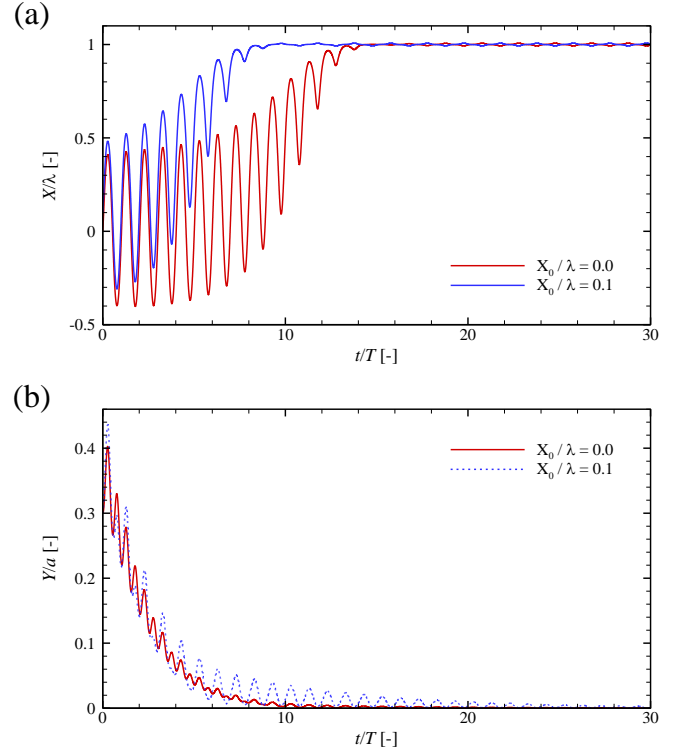
Figure 1 The trajectories of the centre of gravity of the rigid sphere initially placed on $Y_0 / a = 0.3$. (a) X-coordinate; (b) Y-coordinate.

CONCLUSION

We numerically evaluated the lateral migration of the rigid sphere due to segmentation contraction. We clarified that the rigid sphere laterally migrates toward the centreline, oscillating in lateral and longitudinal directions like the previous study of peristalsis. This is caused by the wall effect, such as the Saffman lift force and the Magnus lift force.

REFERENCES

[1] Nakamura, T. and Suzuki, K., *Advanced Robotics*, **25**(3): 371-385, 2011.
[2] Connington, K. et al., *Phys. Fluids,* **21**(5): 053301, 2009.
[3] Kajishima, T. et al., *JSME Int. J. Ser. B,* **44**(4): 526-535, 2001.

NUMERICAL SIMULATION OF FLOW BEHAVIOR IN BASILAR BIFURCATION COMPUTED TOMOGRAPHY ANGIOGRAPHY

Ryo Shimodoumae[1], Gaku Tanaka[1], Ryuhei Yamaguchi[2], Makoto Ohta[2]

[1] Graduate School of Science and Engineering, Chiba University, 1-33 Yayoi-cho, Inage-ku, Chiba, Japan
[2] Institute of Fluid Science, Tohoku University, 2-1-1 Katahira, Aoba-ku, Sendai, Miyagi, Japan

INTRODUCTION

A cerebral aneurysm is a bump-like bulge that forms at an arterial bifurcation in the brain. The development, growth, and rupture of cerebral aneurysms are thought to be caused by hemodynamic factors. Hemodynamic factors include wall shear stress (WSS), and numerical simulations have been used to study hemodynamics in order to predict the growth and rupture of cerebral aneurysms. Until now, CFD simulations that assume wall stiffness without considering wall motion have been widely accepted in computational fluid dynamics. Recently, FSI simulations have been applied to models of elastic cerebral aneurysms to reproduce wall motion [1]. In this study, hemodynamics of basilar artery aneurysms (BAA) was numerically simulated in a realistic moving boundary deformation model obtained from high temporal resolution 4D computed tomography (4D-CTA) data. Four hemodynamic factors, WSS, WSSD, OSI, and RRT, were evaluated by numerical simulation using the moving boundary method, and the effect of the moving boundary wall was clarified by comparison with the rigid model.

METHODS

Analysis Model The construction of the basilar artery aneurysm morphology model was based on 4D-CTA data, and the deformation behavior of BAA was captured 30 times per beat CTA data was measured using a 16-detector multi-slice acquisition CT scanner. The aneurysm shape was constructed based on a patient- specific model, as shown in Figure 1 for each phase (t/T). Amira was used as the morphogenesis application. In this study, 30 real geometry models were used to create the walls of the moving boundary model. Ten intermediate shapes were created to satisfy the time steps, interpolated between the real shape models. The moving boundary deformation model was then created by giving the real and intermediate shape models as wall boundary conditions. STAR-CCM was used to create the intermediate shapes. To interpolate between the real geometry with 10 intermediate geometries, n/11 (n is an integer) was multiplied by the displacement $\Delta x_i = (\Delta x_i, \Delta y_i, \Delta z_i)$. i is a cell.

Analysis Conditions STAR-CCM + Ver. 14.06 was used for the simulations. The analysis conditions were three-dimensional, unsteady, laminar flow, and for the wall surface, the non-slip condition, the moving boundary condition created from the real geometry model, and the rigid wall condition were applied. The fluid properties were assumed to be Newtonian, with density $\rho = 1057$ kg/m³ and viscosity $\mu = 3.7 \times 10^{-3}$ Pa-s. The discrete time step (phase) was $\Delta t = 1/330$ s. The inlet boundary (inlet) was the pulsating waveform of a human cerebral aneurysm. The governing equations are the continuity equation and the Navier-Stokes equation that takes into account the mesh movement speed.
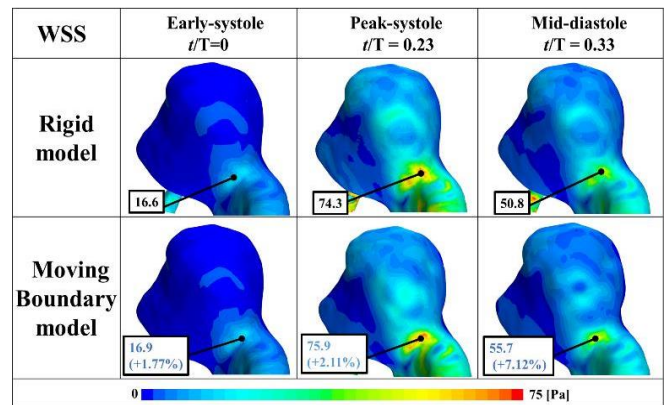
Figure 1 Comparison of 3-phase WSS in rigid and moving boundary models. Values are maximum values.

RESULTS AND DISCUSSION

Figure 1 shows WSS for three representative phases (early, peak systolic, and mid-systolic) for the rigid model (top) and the moving boundary model (bottom). The maximum value of WSS in each phase (indicated by the numbers) is large at the right neck where the inlet flow impinges, reaching 75.9 Pa at peak systole in the moving boundary model. On the other hand, WSS is generally smaller on the walls other than the right neck of the aneurysm. WSS in the moving boundary model is slightly larger than that of the rigid model.

CONCLUSION

In this study, rigid body and moving boundary wall conditions were given in a 4D angiography-based model for comparative evaluation. Four hemodynamic factors resulting from the rupture of cerebral aneurysms were shown to affect hemodynamic factors, particularly wall shear stress.

REFERENCES

[1] Torii, R., et al. *Computers & Fluids.* 2005; **36**: 160-168, 2005.

HEMODYNAMICS WITHIN ELASTIC ANEURYSM IN MCA

Shuhei Sato[1], Ryuhei Yamaguchi[2], Gaku Tanaka[1], Albadawi Muhamed[3], Khalid Saqr[4], Toshiyuki Nakata[1], Makoto Ohta[2]

[1] Graduate School of Engineering, Chiba University, Japan. [2] Institute of Fluid Science, Tohoku University, Japan
[3]Faculty of Engineering, Alexandria University, Egypt.
[4]Arab Academy for Science, Technology and Maritime Transport, 1029 Abou Keer, Egypt.
Email: ryuhei.yamaguchi.e8@tohoku.ac.jp

INTRODUCTION

In the present study, flow characteristics such as wall shear stress (WSS) and gradient of WSS (WSSG) along the aneurysm wall are examined in pulsatile flow using semi 3D-PIV in vitro. The aneurysm was located at the apex of the middle cerebral artery (MCA) bifurcation, and an elastic, image-based, life- size, patient-specific middle cerebral aneurysm phantom was used. The phantom was carefully fabricated with silicone elastomer using a specialized technique. The wall elasticity affects the behaviour ofWSS and WSSG greatly in the elastic modelcompared with the rigid model [1,2].

METHODS

The phantom was reproduced from an image-based, full-scale, patient-specific middle cerebral aneurysm. The current phantom was fabricated with silicone elastomer (Sylgard 184) using a specialized technique via a mold made from water-soluble plaster. The velocity pattern was measured by semi 3D-PIV using UV Laser (i.e., CW ultraviolet Laser of wave length 375 nm with 0.8W). The working fluid is aqueous glycerol potassium solution. WSS was estimated from the tangential velocity along the aneurysm wall.

The flow waveform was approximated in a simple sinusoidal pulsatile wave at average velocity with average Reynolds number of 350, and average flow rate of 182 mL/min at typical phases at the xy plane. In addition, the inlet vessel diameter was 2.8 mm.

RESULTS AND DISCUSSION

First, the velocity contour at the xy plane in the elastic model are shown in Figure 1 [at early and mid-, peak-systole (t/T= 0.31) and mid-diastole]. In each image, the inlet vessel flows from the top, through the middle region of the aneurism, and the flow bifurcates into two outlet vessels at the xy (median) plane (i.e., the left and right sides). The two velocity contours (at median plane [xy] and perpendicular to median plane [not shown] were separately measured. In other words, we express semi-3D velocity contours. The inlet flow enters the aneurysm and circulates clockwise within the aneurysm. The interval between captured images was set to 250 μs. The interrogation window size was 12 × 12 pixels [0.24 × 0.24 mm (0.0202 mm/pixel)], with an overlap of 50%. The WSS was estimated from the tangential velocity 0.25 mm from the aneurysm wall, excluding the interrogation window size at the aneurysm wall. Thus, 10 velocity vector images at the same phase were taken and overlapped, and one velocity vector image was estimated as an ensemble average during

10 cardiac cycles. At all phases, the magnitude of WSS in the elastic model is slightly smaller than that in rigidmodel (Figure 2). The gradient of WSS (i.e., WSSG) is also shown in Figure 2. Except at early-systole, WSSG in the elastic model is smaller than in the rigidmodel. The smaller WSSG in the former indicates weaker stretching or compression force on lumen vessels of the endothelial cells.
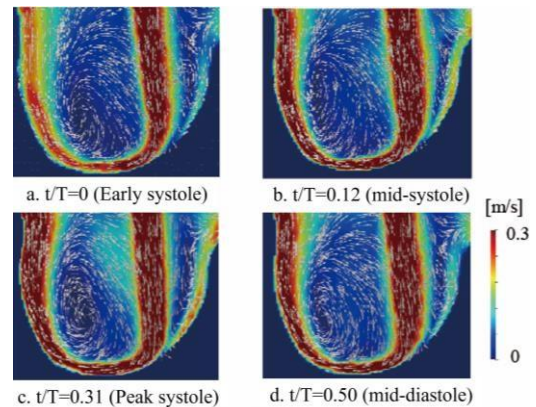
Figure 1 Velocity contour in elastic model at xy plane
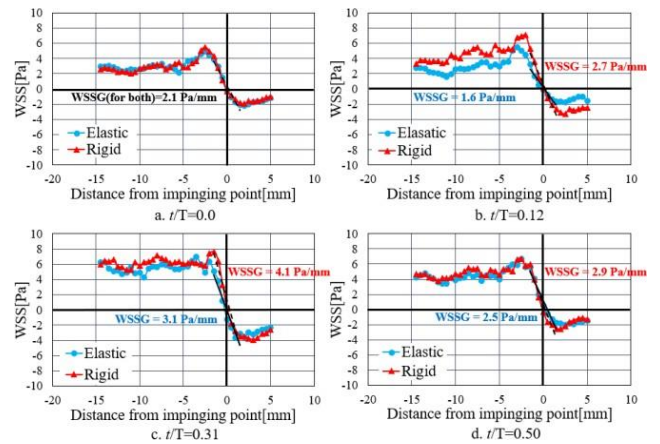
Figure 2 Comparison of elastic with rigid models at xy plane

CONCLUSION

The elastic wall suppresses the magnitude of WSS and WSSG. In particular, small WSSG retards the progress of vascular disease.

ACKNOWLEDGEMENT

REFERENCES

[1] Meng H, et al, American *J. Neuroradiology*, **35**, 2014.
[2] Ryuhei Y, et al, *J Applied Phys*, **105**, 2023.

UPPER AIRWAY SIMULATION OF OBSTRUCTIVE SLEEP APNEA SYNDROME

Yuka Funaki[1], Atsuro Tanabe[1], Hiroyuki Tada[2] and Gaku Tanaka[1]
[1] Graduate School of Engineering, Chiba University, Chiba, Japan.
[2]Makuhari ENT Clinic, Chiba, Chiba, Japan.
Email: ryuhei.yamaguchi.e8@tohoku.ac.jp

INTRODUCTION

Sleep apnea syndrome (SAS) is a disorder in which apnea and hypopnea occur five or more times per hour during sleep [1]. Obstructive sleep apnea syndrome (OSAS) is caused by narrowing of the pharyngeal region (soft palate and root of the tongue). In this study, we investigate the correlations between the severity of OSAS, as measured by the apnea hypopnea index (AHI) and pressure drops in the nasal cavity and throat and between the AHI and minimum cross-sectional area of the throat, CFD simulations of human snoring during sleep were performed.

METHODS

The polygon models were reconstructed from CT images (resolution 0.243×0.243 mm, image intervals 0.243 mm, NAOMI-CT, RF) using a commercially available image segmentation software (Amira Ver. 5.2.2, Visage Imaging). CT imaging for OSAS including four mild and six severe cases was performed in the open-mouth state. Table 1 lists the participants' information. In the open-mouth state, the mouth is open, but the flow from the mouth is blocked by the tongue; therefore, only nasal breathing occurs. In this study, CFD analysis of the upper airway was performed using FFV-C (Frontflow/violet Cartesian ver.2.1.5, RIKEN), which is a three-dimensional unsteady incompressible thermal flow simulator integrated with a Cartesian grid generator [2].

The pressure drops in the nasal cavity, P_n, and throat area, P_{th}, downstream of the nasal cavity were used as indicators for evaluating the internal pressure of the upper airway. The correlations between AHI and these variables were evaluated using the Spearman's correlation coefficient.

Table 1 Information on CT images subjects

Case	AHI	BMI [kg/m²]
No. 1	5.1	23.7
No. 2	10.1	22.6
No. 3	16.5	22.0
No. 4	18.1	27.3
No. 5	45.7	26.8
No. 6	47.2	25.2
No. 7	49.2	28.8
No. 8	69.2	35.5
No. 9	73.2	26.7
No. 10	75.3	39.2

RESULTS AND DISCUSSION

Figure 1 shows the pressure drop in the nasal cavity in each case. The average pressure drop was 32.41 ± 47.21 Pa. Statistics analysis showed that the correlation between the AHI and pressure drop in the nasal cavity was 0.745, indicating a significant correlation (p = 0.013). The average pressure drop was 5.52 ± 1.75 Pa in the mild case and 50.34 ± 53.94 Pa in the severe case, indicating a significant difference between the two groups.

Statistical analysis showed a tendency for weak correlations between the AHI and throat pressure drop; however, this was not significant (r = 0.430, p = 0.214).

Some cases have been reported in which nasal obstruction is experienced and a shift from nasal breathing to mouth breathing is observed; this results in an open-mouth state, which eventually leads to apnea and hypopnea [3]. Considering these, it can be estimated that severe cases are more likely to shift to an open-mouth state and snore than mild cases.
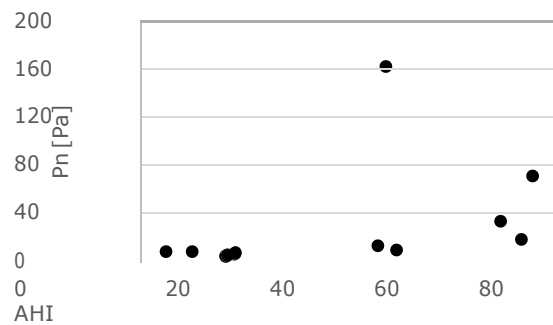
Figure 1 Pressure drop in the nasal cavity for each case

CONCLUSION

These results suggest that the pressure drop in the nasal cavity affects the severity of OSAS.

ACKNOWLEDGEMENT

REFERENCES

[1] Berry RB et al. *J Clin Sleep Med* **8**(5): 597-619, 2012.
[2] Kimura S et al. *Comput Methods Biomech Biomed Eng* **24**(4), 459-466, 2020.
[3] McLean HA et al. *Eur Respir J* **25**(3), 521–527, 2005.

ANTERIOR OBLIQUE LIGAMENT STIFFNESS MEASUREMENT AT VARIOUS ELBOW FLEXION ANGLES USING STRAIN ULTRASOUND ELASTOGRAPHY

Yuto Takanezawa[1], Makoto Sakamoto[2], Takuya Sugawara[1], Kei Itoh[1], Koichi Kobayashi[2], Kazuhiko Hiramoto[1]
and Tomohiro Sasaki[1]

[1] Graduate School of Science and Technology, Niigata University / Niigata, Japan.

[2] Department of Health Sciences, Niigata University School of Medicine / Niigata, Japan.

Email: sakamoto@clg.niigata-u.ac.jp

INTRODUCTION

The ulnar collateral ligament (UCL) of the elbow joint is a complex consisting of the anterior oblique ligament (AOL), transverse ligament (TL), and posterior oblique ligament (POL). It connects the humerus and ulna bones. The superior support capacity of the AOL against valgus force has been elucidated by several *in vitro* studies [1]. However, few studies have investigated the mechanical properties of the AOL *in vivo*. Therefore, in this study, we used a non-invasive diagnostic technique called strain ultrasound elastography (SE) to evaluate the stiffness of the AOL *in vivo* in healthy subjects. The evaluation of AOL stiffness was performed by assessing changes in stiffness at different angles of elbow flexion.

METHODS

The subjects of this study were 10 healthy adult males (mean age: 22.8 years) and 10 females (mean age: 21.3 years). The target tissue of interest was the AOL of the right elbow joint. SE measurements were performed in the supine position with the shoulder abducted to 90°. Measurements were taken at elbow flexion angles of 0°, 30°, 60°, 90°, and 120°. SE is a semi-quantitative method of measuring tissue stiffness using longitudinal ultrasound waves. The examiner applies compressive forces at a frequency of several Hz to the skin surface over a target tissue using an ultrasound probe. The strain of the tissue is obtained from the displacement of the tissue in the depth direction of the skin. In general, SE determines the relative stiffness of the target tissue by comparing the strain ratio between the region of interest (ROI) of the target tissue and the ROI of the reference tissue. However, depending on the location of the target tissue, it may be difficult to identify a suitable reference ROI, and there may be variations in stiffness within the reference ROI among different subjects. Therefore, in this study, a plastic acoustic coupler with a known Young's modulus (22.6 ± 2.2 kPa) was attached to the probe and substituted for the reference tissue [2]. In this study, we used a medical ultrasound diagnostic device and equipped it with an ultrasonic linear probe. The strain ratio of the AOL was measured using SE, in which a periodic compressive force was manually applied to the probe at a frequency of approximately 2 Hz. The strain ratio (*SR*) parameter is defined as the ratio of the strain (ε_B) of the AOL within the ROI to the strain (ε_A) of the coupler within the ROI, as follows:

$$SR = \varepsilon_B / \varepsilon_A \qquad (1)$$

A lower *SR* value indicates a higher stiffness of the target tissue.

RESULTS AND DISCUSSION

It is well known that the measurement technique in SE can influence the results. Therefore, to investigate the measurement reliability of SE, the intraclass correlation coefficient (ICC), which is an indicator of intra- and inter-rater reliability, was calculated for the measurement of AOL at 0° elbow flexion angle. This measurement was performed by two examiners on 20 subjects, with each subject undergoing three measurements. As a result, the ICC (2, 3) values were found to be above 0.8, indicating that the *SR* values obtained with this measurement technique are considered sufficiently reliable. The relative stiffness of the AOL remained relatively constant between elbow flexion angles of 0° and 60°. However, a significant increase in AOL stiffness was observed at flexion angles greater than 60°. It was also found that the stiffness of the AOL was lower in females compared to males at all elbow flexion angles (Figure 1).
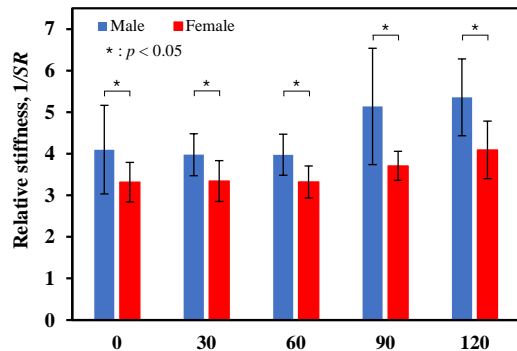
Figure 1 Relative stiffness (1/*SR*) of the AOL as a function of elbow flexion angle.

CONCLUSION

We measured the stiffness of the AOL at the elbow joint *in vivo* using SE at different elbow flexion angles. The results showed that AOL stiffness remained relatively constant between elbow flexion angles of 0° and 60° and increased between 60° and 120°. Furthermore, our results showed that the AOL stiffness of males was consistently higher than that of females at all elbow flexion angles.

REFERENCES

[1] Matsuura Y et al. *J Shoulder Elbow Surg* **30**: 359-364, 2021.

[2] Wadugodapitiya S et al. *Biomed Mater Eng* **33**: 337-349, 2022.

THE RELATIONSHIP BETWEEN VISCOELASTIC PARAMETERS OF THE ARTERIAL WALL AND ATHEROSCLEROSIS RISK STATUS IN PATIENTS

Duc-Manh Dinh, Juho Kim, and Kyehan Rhee
Department of Mechanical Engineering, Myongji University, Yongin-si, South Korea.
Email: khanrhee@mju.ac.kr

INTRODUCTION

Atherosclerosis, characterized by plaque formation in the arterial walls, is a major contributor to cardiovascular diseases. Previous studies have evaluated arterial wall stiffness using pulse wave velocity and elastography, while a few studies have been performed on wall viscosity which is affected by the contents of vascular smooth muscle cells (VSMCs) and contractility. Also, the effect of wall thickness and the viscoelastic properties on radial wall motion remains unclear. This study aims to investigate the effects of wall thickness and viscoelastic parameters on radial wall motion and to explore the relationship between these factors and the risk status of atherosclerotic diseases.

METHODS

The carotid artery is modelled as a thin-wall tube, and the standard linear model (SLM) is employed to estimate the viscoelastic parameters. Carotid pressure is estimated from a brachial pressure waveform, while the diameter waveform is measured from B-mode ultrasound images [1]. In order to assess the influence of intima-media thickness (IMT) on arterial wall motion, the commercially available software ANSYS (Ansys Workbench, Canonsburg, PA) is utilized. The arterial wall structure is simplified to a single layer representing IMT. The dimensions of the wall, including its length, diastolic radius, and various thicknesses, are defined as 100 mm, 3 mm, and ranging from 0.5 to 1.5 mm, respectively. The arterial wall is assumed to be isotropic elastic with a Poisson ratio of 0.49. The outer wall of the cylindrical tube corresponds to the surrounding tissue and is modelled using perivascular pressure. Both ends of a cylindrical tube are fixed in all directions. To replicate the measured diameter waveform of a patient, a standard model with viscoelastic parameters (E_0=400kPa, α=0.5 and =0.03s) [2] is used. The viscoelastic parameters are determined from the diameter and pressure waveforms by solving an inverse problem. The optimization process involves minimizing the mean square errors through the adjustment of parameters (E0 and η). For clinical application, the patients are categorized into three groups based on the Framingham risk score (FRS) [3]. This categorization allows for the evaluation of the risk status of 105 patients with atherosclerotic cardiovascular diseases.

RESULTS AND DISCUSSION

The amplitude of the radius waveforms decreases as the intima-media thickness increases, while the phase lags between the pressure and radius waveforms remain mostly unchanged. To assess the viscosity of the arterial wall, the energy dissipation ratio (EDR) is calculated. The EDR decreased from 3.4% to 3.1 % as the IMT increased from 0.5 mm to 1.5 mm.
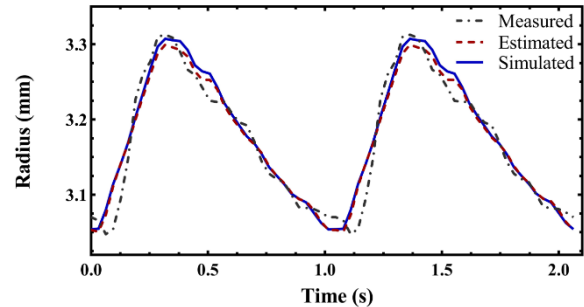
Figure 1 Validation of viscoelastic parameters

A two-parameter optimization is performed on the simulated radius waveform to validate the iterative optimization algorithm. The estimated viscoelastic parameters (E_0=430kPa and η=10kPa·s) closely matched the estimated values obtained from the measured radius waveform and the relative errors between the reference and afresh estimated parameter (E_0) are very small less than 6%. Patients are categorized into three groups: low-risk (FRS≤10%, LR), intermediate-risk (FRS=10~20%, IR), and high-risk (FRS>20%, HR). There is no significant difference in the viscous parameters (EDR and η) between IR and HR groups, while these parameters are significantly higher in the IR group compared to the LR group.

CONCLUSION

This study investigated the effects of wall thickness and viscoelastic parameters on radial walls. Findings revealed that a thicker wall decreased radius amplitude while it did not influence the viscous response of radial wall motion. The clinical study showed that arterial stiffness should be an index for the high-risk group while viscosity would be an index for the intermediate-risk group. Further research is needed for clinical applications.

ACKNOWLEDGEMENT

REFERENCES

[1] Shin J et al. *Med Eng Phy* **108**:103886, 2022.
[2] Daniela VJ et al. *Ann Biomed Eng* **39**:1438-1456, 2011.
[3] Perez HA et al. *Arch Med Sci* **12(3)**:513-520, 2016.

INFERENCE OF AREA EXPANSION RATE DISTRIBUTION IN 3D SHEET MORPHOGENESIS

Kentaro Morikawa[1], Shinichi Morita[2,3], Kazuki Sakura[2,4], Akiteru Maeno[5], Hiroki Gotoh[6], Teruyuki Niimi[2,3] and Yasuhiro Inoue[1]

[1] Department of Micro Engineering, Graduate School of Engineering, Kyoto University, Kyoto, Japan.
[2] Division of Evolutionary Developmental Biology, National Institute for Basic Biology, Okazaki, Japan.
[3] Basic Biology Program, Graduate Institute for Advanced Studies, The Graduate University for Advanced Studies, SOKENDAI, Okazaki, Japan.
[4] Japan Society for The Promotion of Science Research Fellowship.
[5] National Institute of Genetics, Shizuoka, Japan.
[6] Department of Biological Science, Faculty of Science, Shizuoka University, Shizuoka, Japan.
Email: morikawa.kentaro.68a@kyoto-u.jp

INTRODUCTION

The formation of complex three-dimensional (3D) organ shapes in many organisms is driven by differential growth, a process where growth rates vary across different regions. Despite our understanding of its qualitative impact on morphogenesis, our quantitative knowledge of its mechanical contribution remains limited. In this study, we present a method to quantitatively infer the distribution of area expansion rates that govern the 3D curved surface growth.

METHODS

From a geometric point of view, differential growth is a deformation characterized by a conformal expansion of the area at each point on the surface, with expansion rates that vary spatially. Our method calculates the distribution of area expansion rate distribution by constructing a conformal map between pre- and post-growth shapes. We achieve this by parameterizing both shapes onto a common planar region (unit disk) using the conformal parameterization technique [1]. By composing the map from the post-growth shape to the planar domain and the inverse map from the pre-growth shape to the planar domain, we compute the conformal map from the post-growth shape to the pre-growth shape. We successfully applied our method to CT data of the horn primordium formation process in a Japanese rhinoceros beetle, as shown in Fig. 1a and b. In applying our method, it is necessary to establish correspondences between regions in the pre- and post-growth shape. To address the challenge of uncertain region correspondences between pre- and post-growth shapes, we considered 2×2 pairwise combinations of regions.

RESULTS AND DISCUSSION

Our inference of area expansion rate distribution during the horn primordium formation, shown in Fig. 1c, revealed a locally concentrated expansion region with particularly large expansion rates at its left and right edges within that expansion region. Remarkably, our results align with experimental observations of cell division frequency distribution [2].
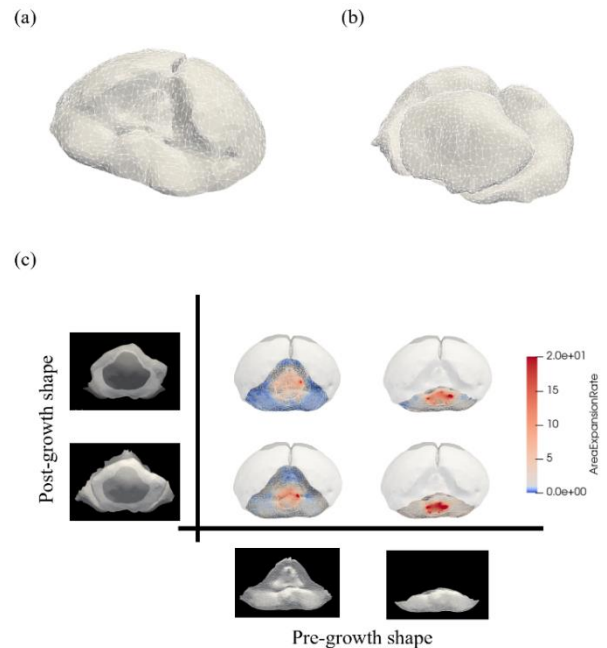
Figure 1 Application of our method to the beetle horn primordium formation process. (a) The pre-growth shapes. (b) The post-growth shapes. (c) The inference result of area expansion rate distribution.

CONCLUSION

Our developed method of inference of the area expansion rate distribution has been validated by its remarkable consistency with experimental observations of cell division frequency. This confirms the power of our approach in analysing complex 3D sheet morphogenesis.

ACKNOWLEDGEMENT

REFERENCES

[1] Eck M et al. *SIGGRAPH'95*: 173-182, 1995.
[2] Adachi H et al. *Sci. Rep.* **10**: 18687, 2020.

RELATION BETWEEN INTERSTITIAL FLOW AND MMP2 EXPRESSION

Shukei Sugita[1,2], Hiroomi Kaida[1], Yoshihiro Ujihara[1] and Masanori Nakamura [1,2,3]

[1] Department of Electrical and Mechanical Engineering, Nagoya Institute of Technology, Nagoya, Japan.
[2] Center of Biomedical Physics and Information Technology, Nagoya Institute of Technology, Nagoya, Japan.
[3] Department of Nanopharmaceutical Sciences, Nagoya Institute of Technology, Nagoya, Japan.
Email: sugita.shukei@nitech.ac.jp

INTRODUCTION

Aortic dissection (AD) is a serious disease with a 50% mortality rate within 24 h of AD development [1]. Although hypertension is involved with AD [2], the cause of AD remains unknown. We previously established a method to measure the interstitial flow in the aorta, which is the flow from the lumen to the adventitial side in the radial direction, and confirmed that interstitial flow was faster under higher intraluminal pressure [3]. Furthermore, the interstitial flow measured at the AD-expected sites of the mouse AD model sometimes showed faster interstitial flow [4]. From these results, we hypothesized that the faster interstitial flow due to hypertension caused AD development. However, we did not deny the probability that a small failure in the aortas to result in AD was first developed, and this failure increased the interstitial flow.

In this study, we applied the interstitial flow to the healthy aorta *in vitro* and investigated the changes in matrix metallo protease 2 (MMP2) expression [5], which was reported to be seen in AD, to evaluate the hypothesis.

METHODS

All animal experiments were approved by the Institutional Review Board of Animal Care at Nagoya Institute of Technology (Approved #2022003). After mice (C57BL/6, 15–29 g, Japan SLC) purchased were euthanized, the thoracic aorta was excised according to previous studies [3,4].

The following four groups were prepared. The thoracic aorta was under 160 mmHg of intraluminal pressurization to cause faster interstitial flow (Group A). However, this intraluminal pressurization causes higher hydrostatic pressure at the intraluminal side and circumferential stretch. To consider the effects of those mechanical stress on the MMP2 expression, we also prepared the thoracic aorta under 160 mmHg of hydrostatic pressure (group B) and circumferentially stretched aorta (Group C). A control specimen, which was under no mechanical stress, was also prepared (Group D). These thoracic aortas were incubated in an incubation medium for three days under 37°C and a 5% CO_2 environment.

Incubated specimens were collected and homogenized. Total RNA was isolated as reported elsewhere. RNA samples were reverse transcribed with Primer Script[TM] RT Master Mix (RR036A, Takara Bio) and TaqMan[TM] gene expression assays for MMP2 (Mm00439498_m1, Life Technologies). Each mRNA was quantified with Glyceraldehyde-3-phosphate dehydrogenase (GAPDH) as reference genes using the $\Delta\Delta C_t$ method.

RESULTS AND DISCUSSION

Figure 1 shows the C_t of GAPDH and MMP2. Although GAPDH expression was confirmed in all the groups, the MMP2 expression was only detected in Group A. Since the MMP2 expression was not detected under hydrostatic pressure (Group B) and circumferential stretch (Group C) groups, interstitial flow caused MMP2 expression. Since this study used healthy thoracic aorta without small failure at an early stage of AD, faster interstitial flow caused the MMP2 expression and appears to result in AD development.

In our preliminary study, 100 mmHg of intraluminal pressurization did not increase the MMP2 expression. These results indicate that faster interstitial flow due to hypertension causes AD.
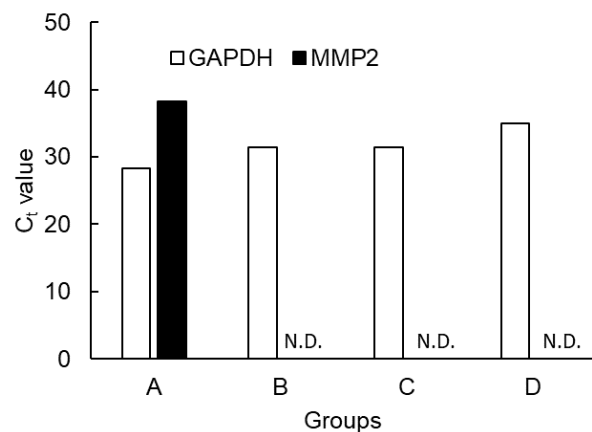
Figure 1 C_t value of GAPDH and MMP2. Group A, circumferential stretch + hydrostatic pressure + interstitial flow; Group B, hydrostatic pressure; Group C, circumferential stretch; Group D, control. N.D., not detected.

CONCLUSION

Not higher hydrostatic pressure nor circumferential stretch, but faster interstitial flow, increased MMP2 expression level. Thus, the faster interstitial flow is probably a trigger of AD development.

ACKNOWLEDGEMENT

REFERENCES
[1] Mészáros I et al. *Chest* **117**: 1271-8, 2000.
[2] Nienaber CA et al. *Circulation* **109**: 3014-21, 2004.
[3] Fukui W et al. *Sci Rep* **12**: 5381, 2022.
[4] Kaida H et al. *AP Biomech 2021*, 2021

EXPERIMENTAL STUDY ON THE DEFORMATION BEHAVIOR OF ADJACENT VERTEBRAE WITH KISSING SPINE

Sotaro Baba[1], Takaya Kato[2], Motoyoshi Fujiwara[3], Tetsutaro Mizuno[4] and Tadashi Inaba[1]

[1] Department of Mechanical Engineering, Graduate School of Engineering, Mie University, Tsu, Mie, Japan.

[2] Department of Mechanical Engineering, Graduate School of Regional Innovation Studies, Mie University, Tsu, Mie, Japan.

Mie Prefecture Industrial Research Institute, Tsu, Mie, Japan.

[4] Department of orthopedics, Seirei Hamamatsu General Hospital, Hamamatsu, Sizuoka, Japan.

Email: baba@mach.mie-u.ac.jp

INTRODUCTION

The enlargement of spinous processes with aging (Kissing Spine, KS), which has been associated with lumbar degeneration and back pain [1]. Although clinical reports on Kissing Spine are available, there is a few studies examining its biomechanics.

It is suggested that intervertebral segments with Kissing Spine experience reduced rotational angle at the extension due to spinous process contact, resulting in increased angle on the adjacent segments. In this study, investigated the effect of Kissing Spine on the deformation behavior of adjacent segments through mechanical testing using animal spines as test specimens.

METHODS

Three segment of deer cadaver spines (L3-L6) obtained were used in this study (N=5). The deer spines were prepared by removing soft tissues such as muscles and fat. Three experimental models were created: an *intact model* without any damage, a *Non-KS model* with excision of the supraspinous and interspinous ligaments at the L4/L5, and a *KS model* simulating Kissing Spine by attaching dental resin between the spinous processes based on CT images of Kissing Spine.

Reflective markers were placed at locations on each vertebral body and basement jig. The deformation behavior of each intervertebral segment was measured by tracking the markers on digital video recordings using motion analysis software.

A six-axis material testing machine, specifically developed in our group, was used for the testing [2]. Each specimen model was bent in the flexion and extension directions up to a target angle. Target angles were set to the angle at 2 Nm bending for each *intact model*.

To evaluate the deformation behavior of each intervertebral segment, the Range of Motion (ROM) were calculated based on the torque-angle curves obtained from the experiment and the deformation behavior of each intervertebral segment obtained from the motion analysis.

RESULTS AND DISCUSSION

The ROM at the responsible segment (L4/L5) of the *KS model* in extension was significantly decreased compared to other models (Figure 1a). And the ROM between adjacent segment (L3/L4 and L5/L6) of the *KS model* in extension was increased compared to other models (Figure 1b). During extension, contact between the spinous processes, which have extremely high stiffness compared to the intervertebral discs, caused a decrease in ROM. Therefore, it is suggested

that when extending to the same angle as the *Non-KS model*, the *KS model* requires a higher torque, causing an excessive load on spinal structures such as the intervertebral discs.
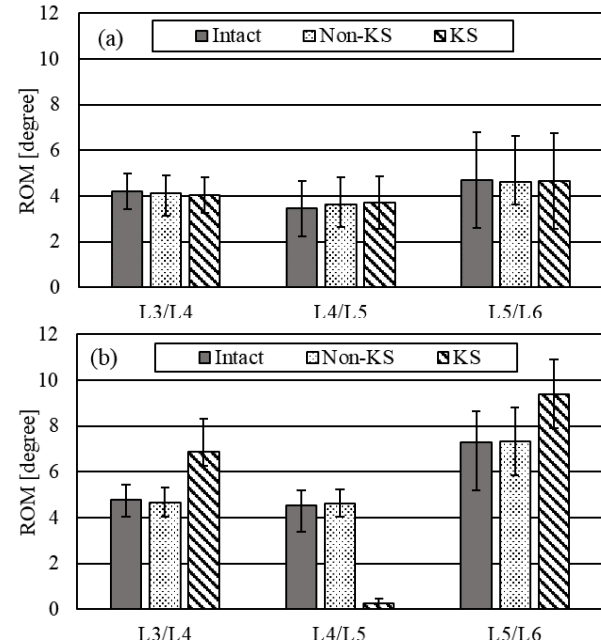
Figure 1 ROM of each segment (mean±S.D.). (a): flexion, (b): extension.

CONCLUSION

To investigate the effect of kissing spines on the deformation behavior of adjacent segments, mechanical tests were carried out on deer cadaver vertebrae the following findings were obtained. In extension, contact between the spinous processes of the kissing spine increased the stiffness of the responsible segment, resulting in a reduced ROM. The reduced range of motion is taken over by the movement of the adjacent vertebrae, suggesting that a large torque is applied to the adjacent segment.

ACKNOWLEDGEMENT

REFERENCES

[1] Baastrup I, *Acta radiol*: 52-55, 1933.
[2] Fujiwara M et al. *Robo and Mech* 18: 160-166, 2006.

ON THE MECHANISMS OF DISTAL STENT GRAFT-INDUCED NEW ENTRY (D-SINE)

Shinri Morodomi[1], Homare Okamura[2], Yoshihiro Ujihara[1], Shukei Sugita[1], and Masanori Nakamura[1]

[1]Department of Electrical and Mechanical Engineering, Nagoya Institute of Technology, Japan.
[2] Department of Cardiovascular Surgery, Jichi Medical University Saitama Medical Center, Japan.
Email: s.morodomi.553@stn.nitech.ac.jp

INTRODUCTION

The frozen elephant trunk (FET) procedure is widely used for acute aortic dissection to restore true lumen patency and occlude descending aortic intimal tears. However, sometimes FET placement postoperatively leads to creating a new intimal tear at the distal edge of the FET, so called distal stent graft-induced new entry (d-SINE). Reportedly, there are two preferential sites of d-SINE: the distal edge of FET and its downstream [1]. While the former is often explained with stress concentration due to elastic restoration of FET, the mechanism of the latter remains unclear. The present study thus aims at understanding the mechanical environment of the aorta after the elastic restoration of FET to propose the underlying mechanisms of d-SINE.

METHODS

The stress field in the aortic wall after the placement and restoration of FET was calculated with ANSYS (2019 R3). The geometry model of the aorta and FET are shown in Fig. 1 (a). We constructed the geometry model of the aorta under the assumption of geometrical symmetricity about the sagittal plane. The FET procedure was virtually applied to the aorta model; the arch part of the aorta was replaced with a rigid covered stent part of an FET model, while an elastic conventional tube part of the FET model that is straight in nature was bent and forcedly inserted into the rest of the aorta (Fig. 1 (b)). Deformation of the aorta and FET models after the elastic restoration of the FET under the intraluminal pressurization of 100 mmHg was solved with taking account of mechanical interactions between the aorta and FET models.

Blood flow in the intraluminal space of the aorta and FET models after the restoration of FET was simulated. using scFLOW ver2022 (Hexagon).

The simulations were conducted with various oversizing rate defined as a ratio of the diameter of FET to that of the aorta.

RESULTS AND DISCUSSION

The results of the oversizing rate of 0.13 are representatively shown in Fig. 1 (c) and (d). Regardless of the oversizing rate, the elastic restoration of FET caused its distal edge to push the posterior side of the aorta and induced concentration of the circumferential stress there (arrowed in Fig. (c)). The elastic restoration also created a discontinuous notch of the aortic wall at the distal edge of FET and caused flow separation. Consequently, wall share stress (WSS) was locally high at the downstream of the distal edge of FET (arrowed in Fig. 1 (d)).

Figure 1 (e) demonstrates how the oversizing rate affects the maximum circumferential stress at the distal edge of FET and the maximum WSS at the downstream of the FET edge. Looking at Fig. 1 (e) and taking account of a report that undersized FET to the true lumen was associated with d-SINE [2], we speculate that d-SINE occurs at the distal edge

of FET due to the circumferential stress when FET is oversized, and that does at its downstream due to WSS when undersized.
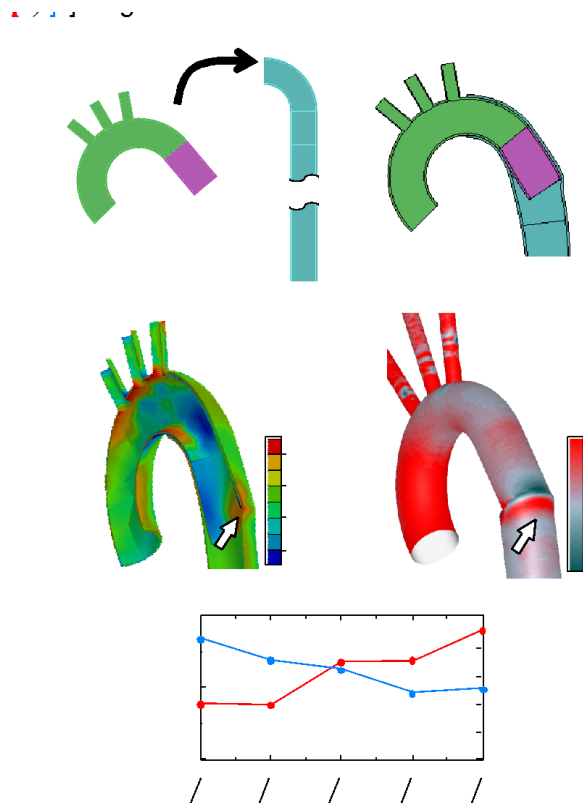
Figure 1 (a) Virtual FET procedure. (b) Deformation of the aorta and FET models after the elastic restoration of FET. Contour plots of (c) the circumferential stress (σ_θ) and (d) WSS. (e) Change in the maximum σ_θ and WSS against the oversizing rate.

CONCLUSION

The present study explored the mechanisms of d-SINE after FET procedure. The results suggested that stress concentration due to oversized FET and high WSS due to undersized FET would be a cause of d-SINE at the distal edge of FET and its downstream, respectively.

REFERENCES

[1] Tan et al. *J. Thorac. Cardiovasc. Surg.* **158 (2)**, 343-350, 2019.
[2] Hiraoka et al. *Eur. J. Cardiothorac. Surg.* **62 (1)**, ezac325, 2022.

GROWTH-INDUCED FOLD FORMATION OF A SHEET-LIKE TISSUE IN A VISCOUS FLUID: AN ISOGEOMETRIC BOUNDARY ELEMENT ANALYSIS

Togo Hayashi [1], Hironori Takeda [1], Shunichi Ishida[1] and Yohsuke Imai [1]
[1] Graduate School of Engineering, Kobe University, Kobe, Japan.
Email: 237t349t@stu.kobe-u.ac.jp

INTRODUCTION

Various biological tissues have the folds whose pattern affects the physiological function of tissues. For example, the folds of the cerebral neocortex are suggested to relate to intellectual abilities by increasing the surface area [1,2]. In tissue morphogenesis, the fold formation is driven by the growth of the sheet-like tissue. The growth-induced deformation is possibly subjected to viscous resistance due to the surrounding cells and tissues [3]. Thus, we aim to clarify the influence of the viscous resistance on the fold formation by the numerical analysis of the growth of the sheet in a viscous fluid.

METHODS

In this study, the deformation of the sheet was formulated by Kirchhoff—Love shell theory [4]. Growth-induced deformation was formulated by continuum mechanics for biological growth [5]. The material property of the sheet was modeled as the incompressible neo-Hookean model. The governing equation was formulated in a weak form using the principle of virtual work. Viscous fluid flow was formulated by the boundary integral method. We used the isogeometric boundary elemental method to couple the fluid and sheet.

In this study, we assumed the in-plane isotropic growth of the sheet. The growth rate was constant. The initial shape of the sheet was a rectangle sheet. The length of the long side was L, the short side was 0.1L, and the thickness was H. We introduced a non-dimensional number $\alpha = (GH)/(\mu\dot{\theta}L)$ where μ was viscosity, and G was shear elastic modulus. α represents a ratio of the viscous force and elastic force.

RESULTS AND DISCUSSION

To clarify the influence of the viscous resistance on the fold formation, we simulated the growth-induced deformation by changing α from 10^{-1} to 10^3. Figure 1 (a) shows the change in the sheet shape with α. When the sheet grew in the viscous fluid, the sheet formed folds. The compression of the sheet decreased with α. When $\alpha = 10^{-1}$, the sheet formed minute folds. When $\alpha = 10^0 \sim 10^3$, the folds became simple and few with α. To evaluate the shape of the folds, we measured the length of the long side of the sheet l/L, the wave number per unit length u/L, and the maximum height d/L of the folds in the area enclosed by a dashed line in Fig.1 (b). Figure 1 (c), (d), and (e) shows that l/L increased with α. u/L and d/L increased, and then decreased with α. These changes in l/L, u/L, and d/L were caused by the balance of the stiffness and the viscous-induced compression. When α was low, the thickness of the sheet increased due to the incompressibility of the sheet under in-plane compression. Thus, the apparent bending rigidity of the sheet

increased. This may be because, u/L was suppressed when α was low.
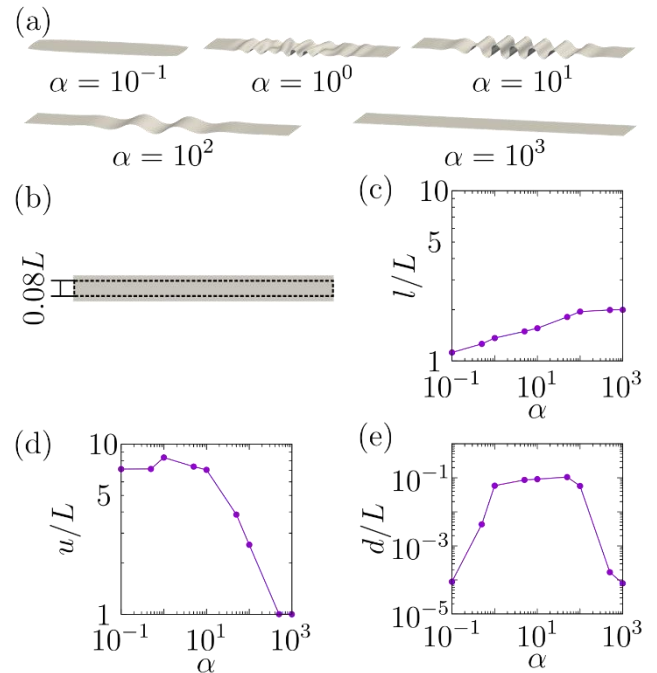
Figure 1 The change in (a) the sheet shape with α . (b) indicates the measurement area. The changes in (c) the length of the long side l/L, (d) wave number per unit length u/L, and (e) maximum height of the folds d/L with α.

CONCLUSION

In this study, we clarified the influence of the viscous resistance on the fold formation by the numerical analysis of the growth of the sheet in the viscous fluid. The balance of the stiffness and the viscous-induced compression of the sheet determined the shape of the folds.

REFERENCES

[1] Lui JH et al. *Cell* **146**(1): 18-36, 2011
[2] Nelson CM et al. *J Biomech Eng* **138**(2): 021005, 2016
[3] Okuda S et al. *Biomech Model Mechanobiol* **14**: 413-425, 2015
[4] Takizawa K et al. *Comp Mech* **63**: 681-700. 2019
[5] Rodriguez EK et al. *J Biomech* **27**(4): 455-467, 1994

COMPUTATIONAL STUDY ON MECHANISMS OF TONGUE FORWARD PROTRUSION

Kyoichi Inoue[1], Tomohiro Otani[1], Kazunori Nozaki[2], Tsukasa Yoshinaga[1] and Shigeo Wada[1]

[1]Graduate School of Engineering Science, Osaka University Toyonaka-shi, Osaka, Japan.

[2]Dental Hospital, Osaka University Suita-shi, Osaka, Japan.

Email: k.inoue@biomech.me.es.osaka-u.ac.jp

INTRODUCTION

Tongue forward protrusion is one of the basic motor functions of the tongue and is used to assess neurological disorders. The tongue protrusion has been believed to be driven by the contraction of the genioglossus (GG), which connects the tongue body to the mandible [1]. However, recent computational studies reported that only the GG contraction provided insufficient tongue protrusion compared to that observed in daily life [2]. To overcome this limitation, we hypothesized that the rigid-like tongue motion with hyoid bone (HB), which connects to the tongue root, is a non-negligible factor in tongue protrusion. Therefore, this study investigated the mechanism of the tongue forward protrusion considering the HB displacements by the ultrasound measurement-based computational simulation.

METHODS

2-1 ULTRASOUND MEASUREMENTS

Ultrasound measurements of the HB displacement during tongue protrusions were performed for three healthy subjects using EPIQ7 (PHILIPS & Co., Netherlands). Subjects were instructed to sit upright, with their backs against the wall and heads fixed. A probe was placed under the chin, and the subjects protruded their tongues within 3 seconds with the lowered chin (Fig. 1a). The HB displacement was extracted by tracking a point on the HB in ultrasound images using the optical flow algorithm (Fig. 1b).

2-2 COMPUTATIONAL MODELING

A computational tongue model was developed based on our previous study [3] using a CT-based tongue model at rest (Fig. 2a). The GG orientation from the mandible to the tongue body was determined based on [4] (Fig. 2a). The tongue was modelled as a nearly incompressible Mooney Rivlin material, and the mechanical equilibrium state considering GG contraction and HB displacement were computed by Galerkin finite element method. Here, the GG contraction stress $\boldsymbol{\sigma}_f$ is given by

$$\boldsymbol{\sigma}_f = a_f^p(\mathbf{e}^p \otimes \mathbf{e}^p), \quad (1)$$

where ep represents the unit vector indicating the muscle fibre orientation, and afp represents the stress value of 1.5 kPa [3]. Fixed boundary condition was set on the attachment plane of the mandible and prescribed displacement was applied to the tongue-HB connection based on the measured HB displacement.

RESULTS AND DISCUSSION

Figure 2 (b) shows the HB trajectory of a representative subject during the tongue protrusion. Anterior and superior HB displacements were approximately 5.9 mm and 6.6 mm, respectively. Figure 2 (c) shows the displacement distribution on the midsagittal plane of the tongue considering GG contraction and HB displacement. Anterior

tongue displacement was mainly caused by the GG contraction. Furthermore, HB displacement enhanced further tongue displacement, and displacement magnitude was approximately 1.3 times larger than that in GG contraction only. These results suggest that the rigid-like tongue motion with HB displacement works to support the tongue forward protrusion.
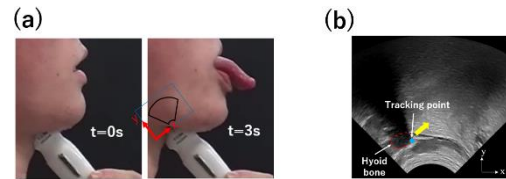
Figure 1 Ultrasound measurements of the hyoid bone (HB) displacement during tongue protrusion, lateral view (a) and an ultrasound image (b).
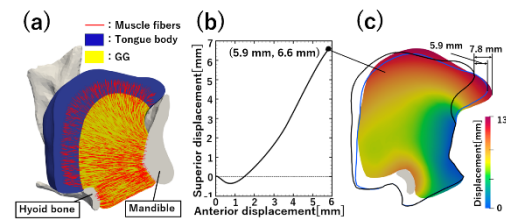
Figure 2 Tongue shape model with muscle fibres (a), HB displacement (b), and displacement distribution in the tongue during protrusion (c), in which blue and black lines show the outlines of the equilibrium by the GG contraction only and the initial shape, respectively.

CONCLUSIONS

This study considered a reasonable mechanism of the tongue forward protrusion considering rigid-like tongue motion with HB displacements. Computational modelling of the tongue protrusion based on ultrasound measurements demonstrated the larger anterior displacement of the tongue by the GG contraction and the HB displacements. These findings suggest that the rigid-like tongue motion is a non-negligible factor to cause the tongue forward protrusion.

ACKNOWLEDGEMENTS

REFERENCES

[1] Pittman et al., *J. Neurophysiol.*, 2009

[2] Stavness et al., *J Biomech*, 2012

[3] Koike et al., *J Biomech*, 2017

[4] Gomez et al., *Biomech Model Mechanobiol*, 2018

EVALUATION OF THE EFFECT OF A CELL CYCLE CHECKPOINT ON MULTICELLULAR TISSUE GROWTH

Yuka Yokoyama[1], Yoshitaka Kameo[2] and Taiji Adachi [1,3]

[1] Department of Micro Engineering, Graduate School of Engineering, Kyoto University, Japan.
[2] Department of Engineering Science and Mechanics, College of Engineering, Shibaura Institute of Technology, Japan.
[3] Institute for Life and Medical Sciences, Kyoto University, Japan.

Email: yokoyama.yuka.75e@st.kyoto-u.ac.jp

INTRODUCTION

Characteristic tissue shapes in the biological body are determined by spatially heterogeneous cell activities, such as proliferation. Cell proliferation is known to be regulated by a mechanism called cell cycle checkpoints [1]. To evaluate the effect of the checkpoint on tissue growth, we aimed to evaluate the tissue mechanical behaviors depending on a cell size checkpoint using a novel computational model of cell proliferation.

METHODS

To simulate the mechanical behaviors of the tissue caused by multicellular activities, we extended the material point method (MPM) [2], in which material points are used for discretization. We developed a mathematical model of cell proliferation expressed as unidirectional growth and division of a material point, regarded as a cell [3]. The effect of a cell size checkpoint in the cell cycle was incorporated into the model by assuming that if the cell volume ratio J^e is smaller than a threshold J^e_{th}, the cell cannot enter the proliferative state and stay quiescent.

RESULTS AND DISCUSSION

Based on the developed model, we simulated the growth of spherical tissue with the surface of the lower half fixed (Fig. 1). The composing cells proliferated with random planes of division at random timings. In the tissue without the checkpoint, uniform proliferation and sporadical strain accumulation were observed over the tissue (Fig. 1a). Conversely, because of the checkpoint, the proliferation in the constraint lower half was suppressed, leading to lower strain energy density (Fig. 1b). Consequently, when compared with the tissues composed of the same number of cells, as the effect of the checkpoint became larger, the total volume and average strain energy density became larger (Fig. 1c) and smaller (Fig. 1d), respectively. Therefore, the volume checkpoint is suggested to suppress cellular strain energy and regulate tissue shapes.

CONCLUSION

We evaluated the mechanical behaviors of growing multicellular tissues depending on the cell cycle checkpoint. The strain accumulation depending on the checkpoint can promote the large deformation of the tissue at a later stage of morphogenesis. Therefore, this study will contribute to understanding the mechanism underlying tissue development.
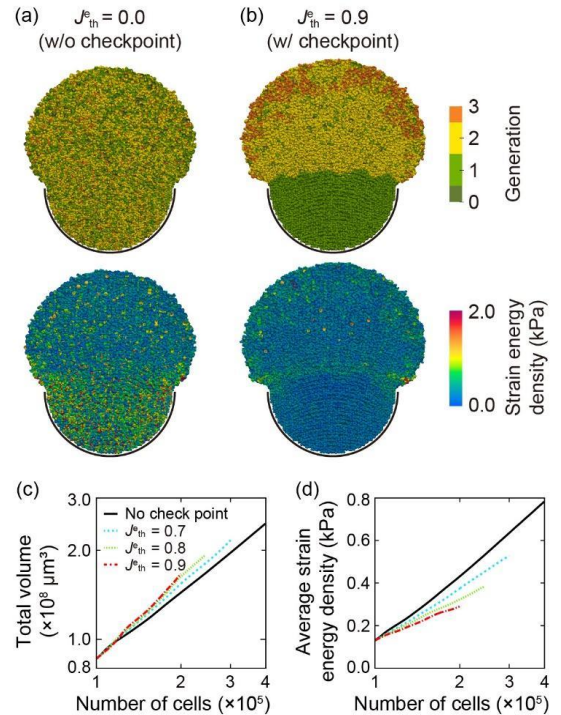
Figure 1 Cell generation and strain energy density in the tissue as a result of cell proliferation without a checkpoint (a) and with a checkpoint (b) when the total number of cells $\sim 2.2 \times 10^5$. Total volume (c) and average strain energy density (d) of the tissue against the number of cells in the tissue, for 5 days, depending on the cell cycle checkpoint [3].

ACKNOWLEDGEMENT

REFERENCES

[1] Xie S & Skotheim JM, *Curr Biol*, **30**:916-924, 2020.
[2] Bardenhagen SG & Kober EM, *CMES*, **5**:477-495, 2004.
[3] Yokoyama Y et al, *J Mech Behav Biomed Mater*, **142**, 2023.

COMPARISON OF THORACIC SKIN DEFORMATIONS ASSOCIATED WITH SHOULDER JOINT ABDUCTION AND FLEXION

Kazuma Kajiyama[1], Takayuki Aimi[1,2], Yasuo Nakamura[3]

[1] Graduate School of Health and Sports Science, Doshisha University, Kyoto, Japan
[2] Research Fellow DC1 of Japan Society for the Promotion of Science, Tokyo, Japan
[4] Faculty of Health and Sports Science, Doshisha University, Kyoto, Japan
Email: yanakamu@mail.doshisha.ac.jp

INTRODUCTION

Understanding the behavior of human skin during joint motion is essential in designing artificial skin, orthotics, and garments. From a mechanical point of view, human skin shows a variety of deformation patterns due to its anisotropic and elastic properties. Because of the anisotropic behavior, Iberall theorized that skin contains lines of nonextension (LoNE), or contours of the skin that rotate during joint motion but do not extend [1]. Many previous studies have measured skin strain and LoNE in the knee and elbow joints during flexion and extension. When a joint with a high degree of freedom moves, such as the shoulder joint, different motions of the joint may cause different skin deformations. Therefore, in this study, a motion capture system was used to measure and compare skin strain and LoNE associated with shoulder joint abduction and flexion.

METHODS

A motion capture system (Mac3D, Motion Analysis) was used to measure skin deformations in four adult males (age: 24.3±0.4 years, height: 170.5±1.3cm, body weight: 67.1±8.9kg) using 16 cameras. Reflective markers were attached to the chest in a grid (7x7 matrix) approximately 2-3 cm apart. Participants performed shoulder abduction from 0° to 120° and shoulder flexion from 0° to 120°, with each motion lasting approximately 3 seconds. Principal strains and LoNE at 30°, 60°, 90°, and 120° of abduction and flexion were compared. MATLAB R2023a (MathWorks) was used for the analysis. A refined mesh was created from the position data of the grid of reflective markers (Figure 1). The principal strain and LoNE were calculated from this mesh data. The calculation methods of principal strain and LoNE were described in the previous study [2].

RESULTS AND DISCUSSION

Reflective marker position data for the four participants were averaged. The principal strains and LoNE at 60° of abduction and flexion are shown in Figure 1. The distribution of the principal strain is indicated by a color map, with the direction indicated by a black line. The red and blue lines indicate the first and second directions of non-extension [1]. The skin strain was generally consistent, but the direction of deformation changed between abduction and flexion. The maximum principal strain during abduction extended obliquely toward the shoulder joint, whereas during flexion it extended vertically. The first direction of LoNE was consistent between abduction and flexion, but the second direction (LoNE 2) changed obliquely during flexion. The

difference in principal strain and LoNE between motions is thought to be largely due to the position of the shoulder joint during the motion. During abduction, the shoulder joint is positioned more laterally, and the skin is stretched horizontally. During flexion, the greater pectoral muscle relaxes when the shoulder joint is positioned more medially. This might have caused the greater pectoral muscle to become more prominent and contribute to the vertical deformation.

The LoNE system was validated to be essentially the same for a series of motions such as elbow flexion and extension [3]. The data in this study suggest that this is not valid for complex joints such as the shoulder joint.
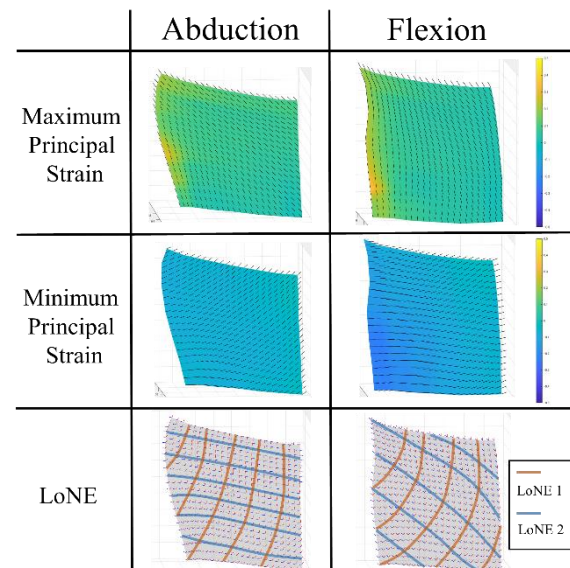
Figure 1 The principal strains and LoNE at 60°of abduction and flexion

CONCLUSION

A motion capture system was used to measure the skin deformations of the thoracic region associated with abduction and flexion of the shoulder joint. The direction of the principal strain tended to differ during abduction and flexion of the shoulder joint. Similarly, the direction of LoNE tended to differ between motions. The data in this study suggest that skin strain and LoNE may vary from motion to motion in complex joints such as the shoulder joint.

REFERENCES

[1] Iberall A.S. *J Basic Eng* **92**: 251-364, 1970.
[2] Wessendorf et al. *IEEE* **59**: 3432-3438, 2012.
[3] Obropta E. et al. *IEEE:* March 2015.

NUMERICAL ANALYSIS OF THE MIDGUT ELONGATION UNDER THE EFFECT OF THE MESENTERY

Michina Saiki[1], Hironori Takeda[1], Shunichi Ishida[1] and Yohsuke Imai [1]

[1] Department of Mechanical Engineering, Kobe University, Kobe, Japan.

Email: 225t325t@stu.kobe-u.ac.jp

INTRODUCTION

The gastrointestinal tract develops from the primordial gut. The midgut is the middle part of the primordial gut and forms the part of the gut from the duodenum to the colon. The midgut loop is connected to a mesentery in an embryo, the midgut elongates and forms a U-shaped loop. Then, the loop extends into the umbilical cord. In the umbilical cord, the loop rotates 90° counterclockwise and forms coiled loops. The midgut rotates a further 180° and the midgut loop returns to the abdominal cavity. These are well-known explanations of midgut morphogenesis.

Malrotation, such as insufficient and reversed rotation, causes irregular gut arrangement, which results in severe symptoms including intestinal obstruction. The mechanism of midgut morphogenesis has not been elucidated in detail. Therefore, it remains unknown whether malrotation is a cause of the abnormal intestinal arrangement. In this study, we investigate the mechanism of midgut morphogenesis from a mechanical viewpoint.

METHODS

We performed finite element analysis of midgut morphogenesis. The elongation deformation of the midgut is formulated based on continuum mechanics. The material property of the midgut is expressed using the neo-Hookean model. The stress-free shape of the midgut model is set to a Gauss-shaped circular tube (Figure 1(a)). The ends of the tube are fixed.

The midgut is pulled by the mesentery because the mesentery is stiffer and grows slower than the midgut [1]. Accordingly, we hypothesize the mesentery is necessary for the midgut morphogenesis. Therefore, we performed simulations by changing the ratio of Young's modulus $G = \frac{G_{\text{mes}}}{G_{\text{mid}}}$ and the elongation rate $v = \frac{\theta_{\text{mes}}}{\theta_{\text{mid}}}$.

RESULTS AND DISCUSSION

Figure 1 shows two typical simulation results. When $v = 0$ and $G = 10$, the midgut rotated counterclockwise and returned to the abdominal cavity (Figure 1(b)). When $v = 0.5$ and $G = 5$, the midgut rotated clockwise and returned to the abdominal cavity (Figure 1(c)).

To investigate what condition generates the rotation and return, we change the parameters v from 0 to 1 and G from 1 to 10. Figure 1(d) is the phase diagram of the rotation which shows the kind of rotation with the timing of the return to the abdominal cavity. The midgut rotated counterclockwise when v was relatively small and G was large. When G was small, the midgut rotate clockwise. On the other hand, when v was large, the midgut did not rotate or return. These results suggest that the degree of the difference in the elongation rate and stiffness between the

midgut and the mesentery determines whether the midgut enters the umbilical cord, rotates or returns to the abdominal cavity.
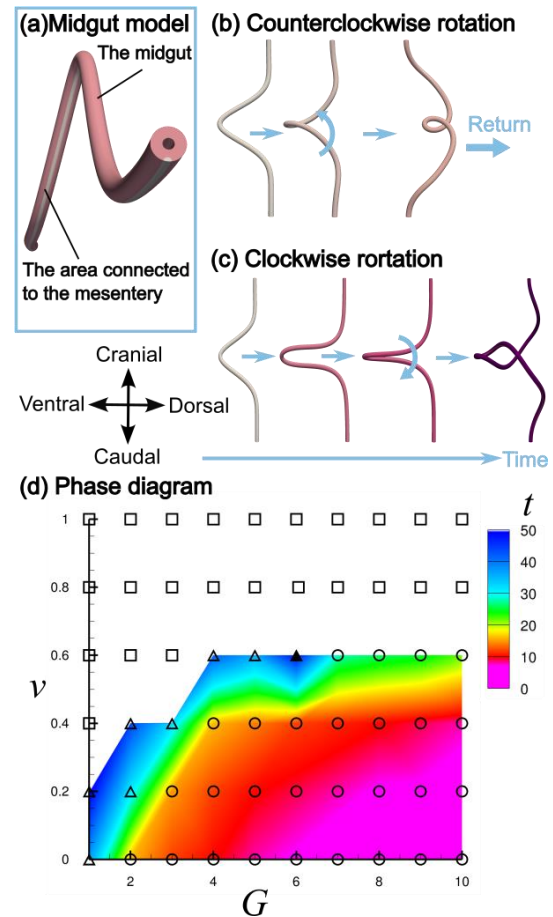
Figure 1 Simulation results. (a)Midgut model. (b)Counterclockwise rotation. (c)Clockwise rotation. (d)Phase diagram. The circle shows the midgut counterclockwise rotation. The open triangle shows the midgut clockwise rotation. The square shows that the midgut doesn't rotate or return. The closed triangle shows an exceptional result. The color shows the time t of returning to the abdominal cavity.

CONCLUSION

Our results suggest that the differences in the growth rate and Young's modulus between the midgut and the mesentery cause not only "coiled loops formation", but also "entering to the umbilical cord", "rotation", and "return to the abdominal cavity".

REFERENCES

[1] Savin T et al. *Nature* **476**: 57-63, 2011

TELEMEDICINE FOR REMOTE MONITOR AND MECHANICAL ANALYSIS OF WOUND HEALING USING NEGATIVE PRESSURE WOUND TREATMENT SYSTEM

Chia-Ching (Josh) Wu[1], Chen-Han Ho[1], Dinh-Toi Chu[2], Thamil Selvee Ramasamy[3]
[1]National Cheng Kung University, Tainan, Taiwan
[2]Vietnam National University, Hanoi, Vietnam
[3]University of Malaya, Malaysia
Email: joshccwu@mail.ncku.edu.tw

Abstract

The remote wound monitoring and caring system will be developed and applied to medical centers as well as the countryside of the city. It can provide telemedicine and personalized medicine for wound healing, thereby reducing the inequality of medical resources. The negative pressure wound treatment (NPWT) system can promote wound healing by applying negative pressure to the wound bed, removing potential infection/inflammation factors, and especially benefiting chronic or infectious wounds. In this study, we have developed a real-time monitoring and feedback control NPWT system (SmartNPWT) to record and investigate the pressure during the application of NPWT. From large animal experiments, we observed superior wound closure dynamics using the SmartNPWT platform during a 7-day study of full-thickness skin wound injuries in pigs. The SmartNPWT resulted in a better-regenerated skin structure, indicated by an increased ratio of low-tension collagen fibers in histological staining. Cytokine analysis from the collected wound fluid revealed increased levels of regenerative cytokines, such as VEGF and PDGF, during the early phase of SmartNPWT application. To further understand the progress of wound healing, we analyzed wound bed morphology using deep learning image analysis. The observed biomechanical and tissue morphological responses hold valuable potential in developing a remote wound care system and telemedicine for patients with wound injuries. By providing real- time monitoring and feedback, the SmartNPWT system can revolutionize wound care and bridge the gap in medical resource distribution.

BIOMECHANICAL STUDY TO DETERMINE SURGICAL SITES DURING ANTERIOR CRUCIATE LIGAMENT RECONSTRUCTION SURGERY

Bo Won Jung[1] and Tae Soo Bae[2]

[1]Dept. of Convergence Engineering, Jungwon University, Chungbuk, South Korea [1]Dept. of AI Biomedical Engineering, Jungwon University, Chungbuk, South Korea

Email: bmebae@jwu.ac.kr

INTRODUCTION

To increase the success rate of anterior cruciate ligament reconstruction, it is important to select the location of the femoral tunnel before surgery. Static experiments at specific angles related to the location of the femoral tunnel have been conducted, but biomechanical studies considering the continuous movement of the knee are lacking. Therefore, the aim of this study was that a biomechanical experiment using a continuous knee motion simulator was conducted to validate the results of the previous computational analyses through a biomechanical experiment.

METHODS

Customized equipment capable of finely adjusting the insertion position and angle was designed to compare the change in maximum tensile force and length according to the femoral graft insertion position. The simulator used in this study can repeatedly simulate the flexion/extension motion of the knee at an angle set between 0° and 90° and can measure and record the tensile force received by the inserted graft in real time using a load cell.
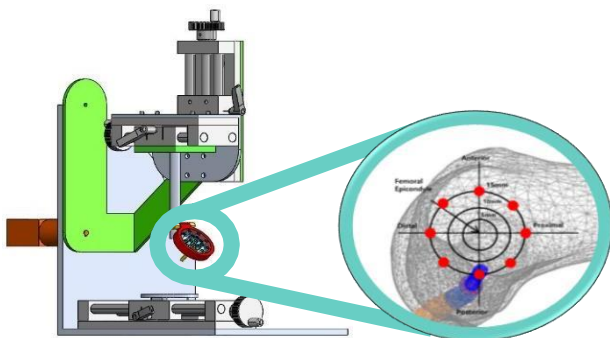
Figure 1 System diagram and surgical site with a jig capable of setting the attachment location of the graft

Based on the computational analysis of previous studies, the experiment was conducted by setting the location of the graft in 8 directions with a radius of 15 mm for 3 femoral aspect ratios [104.42%, 93.89%, 83.66%]. The vertical simulator (0°) was set as the initial state, and the internal angle between the starting point of the femur and the femoral and tibial footprints was expressed as the bending angle of the implanted tendon. A specimen was fabricated using bovine tendon with reference to existing papers, and an initial tensile force of 10 N was

applied to realign the specimen tissue. To simulate the knee motion of repetitive motion, the reciprocating motion of the simulator was set to 30 times per minute in the same way as previous computational analysis, and a total of 1000 repeated experiments were conducted for each graft. The results of the computational analysis were validated based on the maximum tensile force of the tendon in continuous knee motion and the change in the length of the tendon before and after the experiment.

RESULTS AND DISCUSSION

As the femoral aspect ratio increased, the maximum tensile force received by the graft (104.42%: 46.55N, 93.89%: 44.35N, 83.66%: 42.35N) and the displacement of the graft before and after the experiment (104.42%: 2.05mm, 93.89%: 1.99mm, 83.66%) :1.85mm) appeared high. As a result of confirming the location where the maximum and minimum von-Mises stress appeared (distal anterior and proximal posterior, respectively) of the preceding computational analysis through experiments, the maximum tensile force received by the graft tendon was 79.13N and 19.86N, respectively, and the displacement of the graft tendon before and after the experiment were 3.92 mm and 0.48 mm, respectively. When comparing the research results through experiments and the results of previous studies through computational analysis, it was confirmed that the trends appeared similar.

CONCLUSION

Although there are differences in the numerical absolute values of the maximum tensile force and length change, the computational analysis and experimental results show similar tendencies, so it is thought that the future prediction of surgical results through computational analysis will be applicable to clinical practice.

ACKNOWLEDGEMENT

REFERENCES

[1] Bae TS et al. *IJPEM* **21(3)**: 519-524, 2020.
[2] Bae TS et al. *IJPEM* **23**: 205-211, 2022.

EFFECT OF A NEWLY DEVELOPED TITANIUM IMPLANT PLATE FIXATION ON NEW BONE FORMATION DURING EARLY STAGE OF HEALING

Norain Binti Abdullah[1,2], Daisuke Miyazaki[2], Ei Yamamoto[3], Kosuke Ueki[2], Masaaki Nakai[2], and Tamio Ida[1]

[1] Bio-Coke Research Institute, Kindai University, Higashiosaka, Japan.
[2] Department of Mechanical Engineering, Kindai University, Higashiosaka, Japan.
[3] Department of Biomedical Engineering, Kindai University, Kinokawa, Japan.
Email: norainabdullah95@gmail.com

INTRODUCTION

In recent years, many researchers have been developing a biomaterial with low elastic modulus to be used for bone repair. This is because a material with low elastic modulus is expected to prevent stress shielding phenomenon after a long-term implantation. Although Ti-6Al-4V ELI (Ti-64) with elastic modulus of 110 GPa has been used generally as metallic biomaterials, vanadium element in this alloy is gaining concerns as it is said to be a toxic element. Due to that, Ti-29Nb-13Ta-4.6Zr (TNTZ) is developed from toxic-free element with lower elastic modulus of 60 GPa. This show that elastic modulus of TNTZ alloy is much lower than Ti-64 alloy and nearer to that of bone; 30 GPa. As that being said, TNTZ alloy is expected to be used safely for long-term implantation. In contrast, it is also important to study the early stage of healing, especially the callus formation stage. By doing this, the properties that are needed for implant plate to aid in successful healing can be described. Hence, the effect of fixation using titanium implant plates with different alloy-type and thickness on bone formation during early stage of healing was investigated [1].

METHODS

Titanium alloys such as Ti-64 and TNTZ are being used to prepare implant plate with size of 25.0 mm x 5.0 mm, and thickness of 1.5 mm and 0.5 mm. These plates were then undergoing hole drilling on both ends of the plates and polished as the final step. The stiffness of each implant plates was calculated and the order from low stiffness to high stiffness is as follows: TNTZ with thickness of 0.5 mm (TNTZ 0.5), Ti-64 with thickness of 0.5 mm (Ti-64 0.5), TNTZ with thickness of 1.5 mm (TNTZ 1.5), Ti-64 with thickness of 1.5 mm (Ti-64 1.5). The animal experiments were carried out on rabbit femur. Bone defect (anterior region) with half-cylindrical shape was made on femur bone, and fix with implant plate on the top by using two screws on both ends. After three weeks of healing period, femur bone was extracted and evaluated. Scanning electron microscopy (SEM). The image analysis was carried out and bone formation pattern was described.

RESULTS AND DISCUSSION

After 3 weeks of healing, the new bone formation under each fixation state can be said to be similar. This new bone seems to have porous structure (Refer as callus) (Figure 1). However, when looking at the region other than defect (posterior, medial, lateral), callus is formed in larger area especially on the opposite side of defect region (posterior region) under high stiffness of Ti-64 1.5 fixation. By using SEM micrograph, the image analysis was carried out to calculate the area of callus on bone cross-sections which then plotted in the graph (Figure 2). The observation results and calculations results are comparable. A fixation with high stiffness can obtained a rigid system, thus refrained the interfragmentary movement of bone (IFM) on anterior, resulted in asymmetric callus formation. On the other hand, low stiffness failed to obtain a stable fixation system, thus resulted in excessive callus formation.
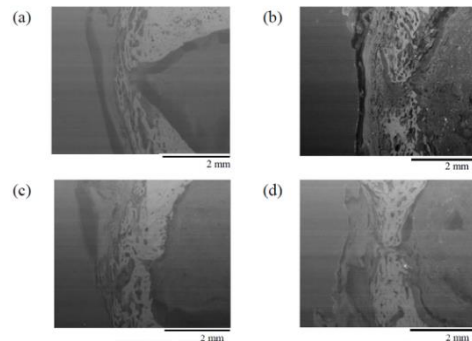
Figure 1 SEM micrograph of defect region (anterior) under fixation of (a) TNTZ 0.5, (b) Ti-64 0.5, (c) TNTZ 1.5, and (d) Ti-64 1.5.
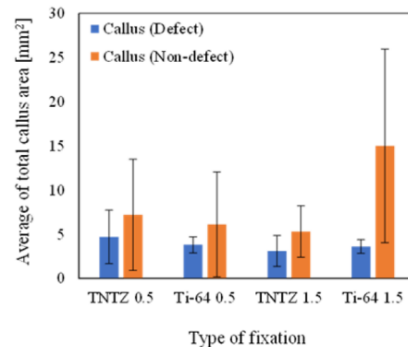
Figure 2 SEM micrograph of defect region (anterior) under fixation of (a) TNTZ 0.5, (b) Ti-64 0.5, (c) TNTZ 1.5, and (d) Ti-64 1.5 [1].

CONCLUSION

This study suggests that suitable stiffness of implant plate is required so that a balance IFM can be transferred throughout the bone, thus ensure a regular callus formation during early stage of healing.

REFERENCES

[1] Norain BA et al. *Mech Eng J* **9**: 22-00282, 2022.

ENHANCING POSTOPERATIVE STABILITY IN HEMIFACIAL MACROSOMIA: A CUSTOMIZED BSSO RECONSTRUCTION PLATE DESIGN APPROACH

Yu-Tzu Wang[1,*], Che-Kai Hsu[1], Po-Fang Wang[2,3]

[1] Department of Mechanical and Electro-Mechanical Engineering, TamKang University, New Taipei City, Taiwan.
[2] Department of Biomedical Engineering, National Yang Ming Chiao Tung University, Hsinchu, Taiwan.
[3] Craniofacial Center, Department of Plastic and Reconstruction Surgery, Chang Gung Memorial Hospital, Taoyuan, Taiwan.
Email: YTLWH@mail.tku.edu.tw

INTRODUCTION

Hemifacial Microsomia (HFM) is a common congenital craniofacial defect that results in asymmetric appearance and malocclusion, and it is usually treated with the bilateral sagittal split osteotomy (BSSO). However, the frequent relapse after BSSO leads to restoring the mandibular segment to the preoperative position. This study aimed to develop a customized asymmetric fixed plate (CAF plate) with resistance to relapse due to occlusal forces and muscular traction on both sides of the mandible.

METHODS

The reconstructed mandibular segmental bone model was established from an actual HFM[1] and fixed with a rectangular CAF plate (the original CAF plate)(Fig.1(a)) according to BSSO in the finite element analysis software. By topology optimization, the CAF plate was optimized for the HFM asymmetrical muscle traction and occlusal force to maximize structural strength and minimizing weight. The optimized CAF plate was compared to the miniplate for the von-Mises stress and displacement of the mandibular segment to evaluate which had superior relapse resistance in the biomechanical simulation[2,3]. In order to verify the resistance of the CAF plate to relapse, an HFM mandibular model fixed with the metal 3D printed (selective laser melting, SLM) CAF plate was tested with a fatigue force of 250,000 cycles and constant muscle traction in the in-vitro biomechanical test[4](Fig.1(b)).
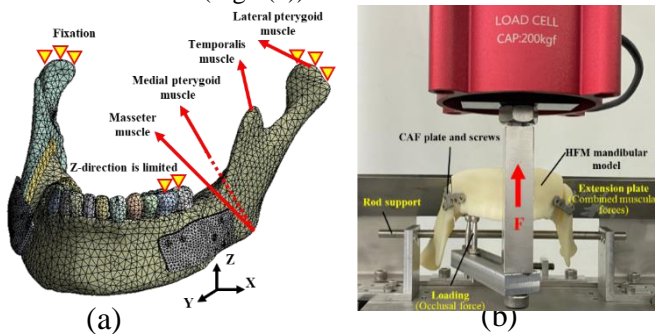
Figure 1 The HFM model in the simulation. (a) Display the mesh model and analysis conditions of Topology Optimization Analysis. (b) Biomechanical test that simulate fixed plate resistance to occlusal forces and relapse.

RESULTS AND DISCUSSION

The topology optimization showed that the CAF plate got better structural strength and lighter weight at 30% volume retention. In the biomechanical analysis, the maximum von Mises stress of the mini-plate was 2.71 times higher than that of the CAF plate, and the amount of mandibular relapse with the mini-plate was 1.62 times higher than that with the CAF plate (Table 1).

By the biomechanical testing, the resistance of the CAF plate to relapse had been verified and only 0.29mm of relapse was found on the mandibular segment. These results suggested that CAF plates possessed significantly better structural strength and resistance to relapse rather than mini-plates (Table 1).

Table1: Biomechanical test results of CAF plate and Mini-plate individual relapse displacement

	CAF plate		Mini-plate	
	Relapse of the mandibular segment (mm)			
sample 1	0.23	pass	1.38	pass
sample 2	0.36	pass	1.29	pass
sample 3	0.28	pass	1.49	pass
avg. ± sd.	0.29 ± 0.07		1.39 ± 0.10	
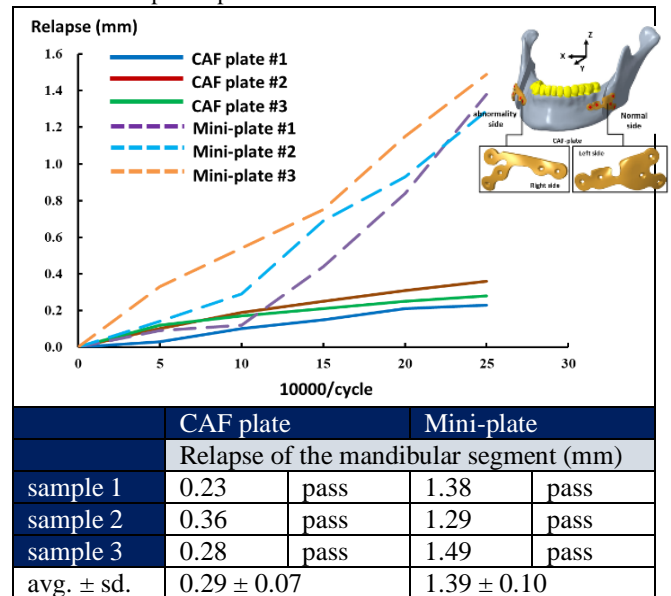
CONCLUSION

In this study, to reduce mandibular relapse and improve fixation stability, a customized asymmetric fixation plate for hemifacial microsomia was developed through topology optimization and metal 3D printing and tested in vitro for its biomechanical performance.

ACKNOWLEDGEMENT

REFERENCES

[1] Barink M. et al. *Biomaterials* **24**: 1427-1435.
[2] Schwartz-Dabney C.L. et al. *Am J Phys Anthropol* **120**: 252-277.
[3] Reina-Romo E. et al. *Med Eng Phys* **32**: 860-866.
[4] Lin C.L. et al. *Int J Bioprint* **8**: 437.

MOTION RESISTANCE OF SACROILIAC JOINT CAUSED BY ARTICULAR SURFACE MORPHOLOGY

Ryota Toyohara[1,2], Niels Hammer[3,4,5] and Toshiro Ohashi[1]

[1] Faculty of Engineering, Hokkaido University, Sapporo, Japan.
[2] Creative Research Institution, Hokkaido University, Sapporo, Japan.
[3] Division of Clinical and Macroscopic Anatomy, Medical University of Graz, Graz, Austria.
[4] Department of Orthopedic and Trauma Surgery, University of Leipzig, Leipzig, Germany.
[5] Division of Biomechatronics, Fraunhofer Institute for Machine Tools and Forming Technology (Iwu), Dresden, Germany.
Email: toyohara.rt@eng.hokudai.ac.jp

INTRODUCTION

Sacroiliac joints (SIJs) are located between sacra and ilia in pelves and composed of synovial joints and tough ligamentous area (Fig. 1) [1]. Due to the strong ligaments, SIJs have comparably low mobility [2]. The SIJs can serve as a damper, thereby transmitting effectively during bipedal walking [3]. Since the joint line is parallel to the gravity line, SIJs are exposed to compress and shear stress environment. Unexpected or repeated impacts are believed to cause joint misalignment and bring pain to SIJs [4]. Fixing the SIJs and preventing excessive motion is considered effective in relieving the pain. In the synovial joint area, the articular surface has fine irregularities, potentially restricting the motion of the joints. This study aims to clarify how the SIJ surface affects resistance of the joint motion.
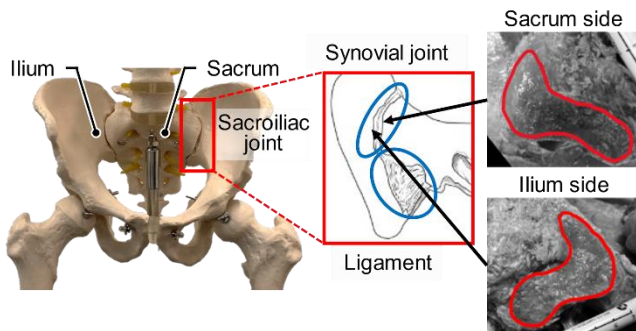
Figure 1 The position of sacroiliac joints.
The edges of synovial joint area are shown in red lines.

METHODS

SIJ surface models were fabricated with a 3D printer based on an X-ray CT data of three patients. Shear resistance and repositionability of SIJs were measured in the four directions and on three different combined positions using an experimental setup by applying and unloading a shear force, respectively (Fig. 2).
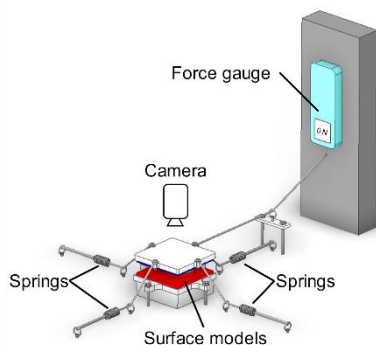
Figure 2 Schematic of in-house experimental setup.
Springs can apply compression.

RESULTS AND DISCUSSION

The shear resistance of SIJs was the highest in the inferior directions and the lowest in the superior directions on in vivo condition (Fig. 3(a)). It is reasonable for bipedal walking that the friction coefficients were high during downward motion and consistently low during upward motion.

The surface models returned to their original positions after unloading in the anterior and inferior directions on in vivo condition (Fig. 3(b)). On nutation and counter-nutation position, the models could not return, indicating these positions increase the risk of subluxation.
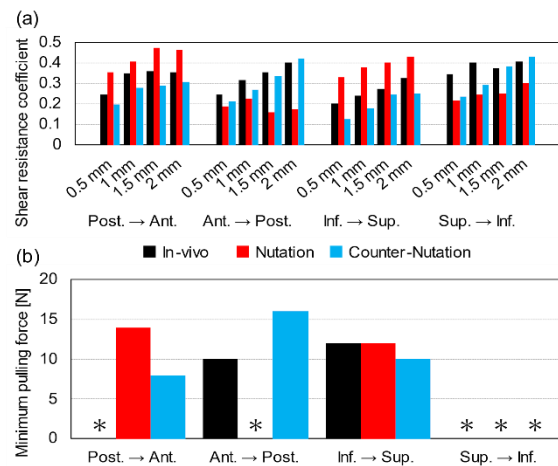
Figure 3 (a) Shear coefficients at four displacement points from initial positions. (b) Minimum pulling forces for more than 2 mm displacements. Asterisks indicates conditions did not exceed a displacement of 2 mm until 20 N pulling force.

CONCLUSION

The SIJ surface morphology may be designed to accommodate an upright bipedal walking and joint misalignment could increase the risk of subluxation.

REFERENCES

[1] Cohen et al, *Anesth Analg*, **101**:1440-53, 2005.
[2] Poilliot et al, *Pain Phys*, **22**:E247-74, 2019.
[3] Toyohara et al, *Sci Rep*, **10**:13683, 2020.
[4] Murakami et al, *Clin Neurol Neurosurg*, **165**:43-6, 2018.

COMPUTER SIMULATION OF BONE ADAPTATION AND MICRODAMAGE REPAIR BY REMODELING IN SINGLE TRABECULA

Tsuyoshi Muto[1], Yoshitaka Kameo[2, 3], Young Kwan Kim[3, 4], and *Taiji Adachi[1, 3]

[1] Department of Micro Engineering, Kyoto University, Kyoto, Japan.
[2] Department of Engineering Science and Mechanics, Shibaura Institute of Technology, Tokyo, Japan.
[3] Department of Biosystems Science, Institute for Life and Medical Sciences, Kyoto University, Kyoto, Japan.
[4] Department of Orthopaedic Surgery, The University of Tokyo, Tokyo, Japan.
Email: adachi@infront.kyoto-u.ac.jp

INTRODUCTION

The maintenance of bone strength, achieved by bone adaptation and microdamage repair through remodeling [1], is important to prevent fractures [2]. Whereas the effective prevention of fractures is demanded, the quantitative prediction of the remodeling behavior remains challenging owing to the complex mechano–biochemical couplings involved in remodeling. The objective of this study is to simulate bone adaptation and microdamage repair through remodeling in a single trabecula to facilitate the quantitative prediction of the remodeling behavior.

METHODS

We constructed a mathematical model by incorporating the accumulation and repair of microdamage into a previously proposed mathematical model that considers complex mechano–biochemical coupling [3]. In this model, signaling molecules that regulate bone resorption and formation are generated in response to stress and damage.

We performed a remodeling simulation to reproduce bone adaptation and microdamage repair in silico. As a simple case, we simulated remodeling in a cylindrical Y-shaped trabecula subjected to constant compressive loading along the z-axis. The initial damage distribution was assumed to be random. To confirm that bone adaptation and repair were reproduced, we analyzed cellular dynamics (osteoclastic bone resorption and osteoblastic bone formation) and bone morphological changes caused by remodeling.

RESULTS AND DISCUSSION

As shown in Figure 1 (a), the Y-shaped trabecula was aligned with the loading direction due to remodeling. Specifically, the inclined segment of the trabecula is transformed into a vertical segment. This indicates that the trabeculae acquired a morphology suitable for loading. Additionally, as shown in Figure 1 (b), the amount of damaged bone decreased along with the process of adaptation. This indicates that the undamaged new bone replaced the damaged old bone concurrently with adaptation.

These results confirm that bone adaptation and microdamage repair were reproduced in silico. In the future, we plan to simulate bone adaptation and repair in cancellous bones with multiple trabeculae using the constructed mathematical model. Our model will allow us to explore clinically applicable strategies for fracture prevention.
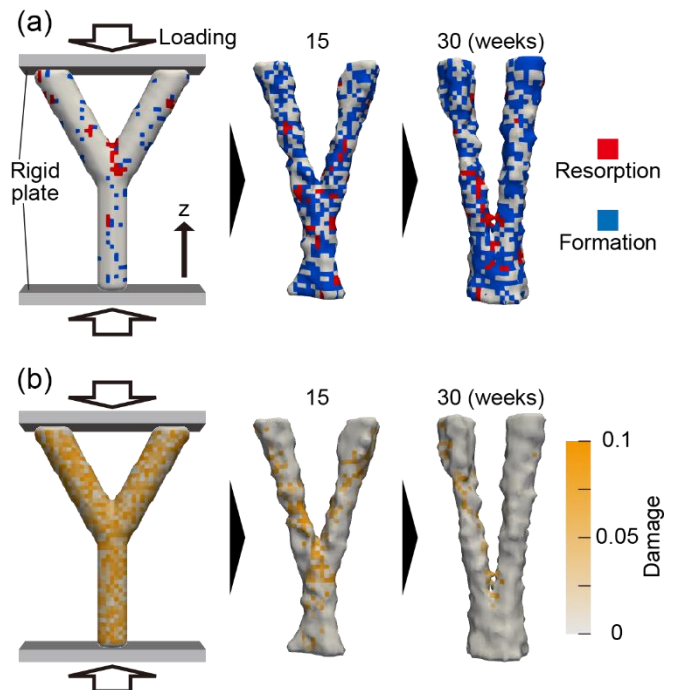
Figure 1 Computer simulation results of bone adaptation and microdamage repair in Y-shaped trabecula. (a) Bone resorption and formation. (b) Change in damage distribution.

CONCLUSION

Bone adaptation and microdamage repair through remodeling in a single trabecula were reproduced in silico via a remodeling simulation based on a mathematical model that considers mechano–biochemical couplings.

ACKNOWLEDGEMENT

REFERENCES

[1] Bolamperti S et al. *Bone Res* **10**: 48, 2022.
[2] Hoenig T et al. *Nat Rev Dis Primers* **8**: 26, 2022.
[3] Kameo Y et al. *Sci Adv* **6**: eaax0938, 2020.

EXTENDED ABSTRACTS│ Human Movement & Robotics

Paper ID58

A COMPARISON OF MECHANICAL ENERGY FLOW PATTERN BETWEEN YOUNG AND OLD ADULTS DURING THE SIT-TO-STAND TASK

Nai-Wen Hsu[1], Yun-Lin Tsai[1], Ling-Wei Yen[1], and Chih-Hsiu Cheng[1]

[1] School of Physical Therapy and Graduate Institute of Rehabilitation Science, Chang Gung University, Taoyuan, Taiwan

Email: chcheng@mail.cgu.edu.tw

INTRODUCTION

Maintaining independence and quality of life becomes increasingly crucial as the population ages. The sit-to-stand is an essential task of daily life as it enables individuals to transition between different positions and locations. During the seat-off phase, the lower limb extensors generate force at unfavorable points on the length-tension curve, which, combined with muscle weakness, makes the STS task a maximum effort for older adults [1]. Mechanical energy flow analysis is used to examine energy distribution and flow patterns across joints and limb segments during movements. Therefore, this study aimed to explore the influence of age on energy transfer during the chair-off phase of a sit-to-stand task.

METHODS

This cross-sectional study recruited 20 young females (age: 22.0 ± 1.9 years) and 20 elderly females (age: 69.9 ± 2.9 years). The kinematics and kinetics data were collected using two force plates and an 11-camera motion capture system. The sit-to-stand task was performed with a symmetric foot placement in bilateral knee flexion at 90 degrees. The study measured the kinematics and kinetics data to calculate mechanical energy flow patterns during the task.

RESULTS AND DISCUSSION

Regarding the trend of mechanical energy flow during the chair-off phase, there was a higher energy transfer from the knee joint to the thigh segment in young subjects (thigh distal flow at right side: 0.20±0.27 J/kg; at left side: 0.19±0.26 J/kg) compared to older subjects (thigh distal flow at right side: 0.11±0.20 J/kg; at left side: 0.07±0.18 J/kg).

Young subjects absorbed part of the energy at their hip joint and transmitted the rest upwards to the pelvis and trunk, while older subjects transferred energy downwards from their trunk through the lumbosacral and hip joints to the thighs. According to previous studies, older adults may exhibit greater trunk flexion than young adults when rising from a seated position, potentially due to reduced knee and hip strength [2].

CONCLUSION

Age-related differences in mechanical energy flow were observed during the chair-off phase from sitting to standing. This study found that the elderly tend to transmit energy from the trunk to the thighs, while the energy of young adults is mainly derived from their lower extremities. This finding suggests that older adults may need to rely on compensatory trunk movements to overcome insufficient lower extremity energy.

ACKNOWLEDGEMENT

REFERENCES

[1] Greve, C. et al. *Eur J Appl Physiol* **119**, 419–428, 2019
[2] Eline van der K. et al. *J Biomech* **122**: 110411, 2021

INVESTIGATING IN-VEHICLE DISTRACTIONS: A DRIVING SIMULATOR AND FNIRS STUDY

Chih-Hao Liu[1], Sheng-Yuan Chen[1], Bing-Shiang Yang[1,2]

[1] Department of Mechanical Engineering, National Yang Ming Chiao Tung University, Taiwan
[2] Mechanical and Mechatronics Systems Research Labs, Industrial Technology Research Institute, Taiwan
Email: bsyang@nycu.edu.tw

INTRODUCTION

Driving distractions are responsible for 20% of road accidents, with two-thirds originating within the vehicle. Although technological advancements like Adaptive Cruise Control (ACC) and Level 2 automation exist, these systems have limitations under certain conditions. A significant gap in current research lies in the comparative evaluation of different distractions; most studies contrast a single distraction to control [1], which hampers our comprehension of distraction severity. Our research addresses this by employing functional Near-Infrared Spectroscopy (fNIRS) and the NASA-TLX questionnaire to assess multiple distractions, thereby aiming to provide both subjective and objective perspectives of the severity ranking.

METHODS

We utilized a driving simulator, furnished with a large display screen, functional steering wheel, and pedals (G923, Logitech, USA), in addition to functional Near-Infrared Spectroscopy (NIRSport2, NIRx Medical Technologies, USA) to gauge driver behaviour and the change of oxygenated haemoglobin in the prefrontal cortex (PFC), which can be indicated as the mental workload level. The study involved four male participants aged 24.5 ± 1.3 years with 2.5 ± 1.3 years of driving experience and no history of driving accidents. The participants were exposed to four conditions: No distraction (control), chatting, listening to the radio, and drinking water, in a randomly assigned order. Each participant drove on the same predetermined route under each condition. We collected data from the steering wheel (steering angle), pedals (throttle and brake), and fNIRS, with participants instructed to adhere to driving rules and maintain a comfortable speed in a traffic-free environment. Mental Workload was also subjectively evaluated after finishing each condition using the NASA-TLX questionnaire [2].

RESULTS AND DISCUSSION

Our analysis combined fNIRS data and NASA-TLX scores to assess mental workload in different driving conditions. Beta values represented brain activation levels, with higher values indicating stronger activation. The mean beta value averaged activation across channels with significant differences. Results revealed a clear hierarchy of mental workload: chatting > drinking > radio. These rankings aligned with NASA-TLX evaluations for mental demand, effort, and frustration, confirming our fNIRS findings. Figure 1 visually reinforced these results, displaying significant cerebral activation compared to the control condition. Our study enhances understanding of cognitive demands during in-vehicle distractions.

Mean beta value results of former condition subtracted by the latter (Positive values indicate that the former condition is more mental demanding than the latter)	
Mean beta value comparison	Results
Chatting vs. Radio	1.602 e-07
Chatting vs. Control	1.8254 e-07
Control vs. Radio	1.6844 e-07
Drinking vs. Control	3.6639 e-08
Chatting vs. Drinking	7.1254 e-08
Drinking vs. Radio	1.0733 e-07

Table 1 Mean beta value comparison
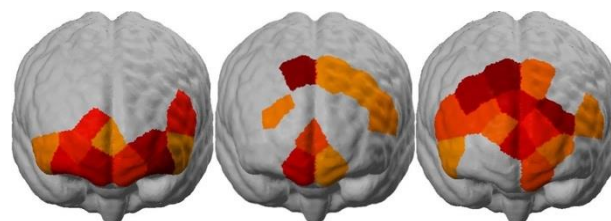
Figure 1. The areas of significant activation using fNIRS, in comparison to the 'control' condition, are arranged from left to right as follows: chatting, radio, and drinking.

CONCLUSION

In conclusion, our initial findings shed light on the distinct impacts of in-vehicle distractions on driving cognitive load. Utilizing both fNIRS data and NASA-TLX scores, we have established a hierarchy of cognitive demands associated with various tasks, with chatting ranking as the most demanding, followed by drinking, and finally, radio listening. Notwithstanding these insights, our current small sample size highlights the need for further data collection to enhance the generalizability and robustness of these results.

ACKNOWLEDGEMENT

REFERENCES

[1] Balters, S., et al., *Frontiers Hum Neurosci,* **15**, 2021.
[2] Tsunashima, H. & Yanagisawa, K., *Comp Intel Neurosci,* **2009**: 164958, 2009.

FALL-FROM-HEIGHT DETECTION USING AN IMU SENSOR IN A WEARABLE AIRBAG

Seunghee Lee[1], Sumin Yang[1], Bummo Koo[1], Dongkwan Kim[1] and Youngho Kim[1]

[1]Department of Biomedical Engineering, Yonsei University, Korea.

Email: younghokim@yonsei.ac.kr

INTRODUCTION

Fall-from-height (FFH) accidents account for a significant proportion of accidents at construction sites and have a relatively high mortality rate [1]. Therefore, the development of FFH detection algorithms is crucial to ensure the safety of workers at construction sites. Protective devices such as wearable airbag are needed to reduce works risk. In this study, a threshold based FFH detection algorithm was developed using an IMU sensor in a wearable airbag.

METHODS

Dataset 1 consisted of twenty healthy male subjects (aged 23.6 ± 1.9 years, height 174.4 ± 5.1 cm, weight 73.4 ± 8.5 kg) recruited from Yonsei University (IRB: 1041849-202004-BM-042-02). Each subject performed 15 non-fall-from-height (non-FFH) movements and 1 fall-from-height (FFH) movement. The IMU sensor used in this dataset was MPU950 (InvenSens, USA), which was attached to the T7 position of each subject [2]. Data from 16 out of 20 subjects were used to determine the thresholds. Dataset 2 consisted of nine healthy male subjects (aged 22.8 ± 1.5 years, height 173.1 ± 5.6 cm, weight 73.7 ± 6.0 kg). These subjects were measured using a prototype wearable airbag sensor (ICM-20948, InvenSens, USA) to test the thresholds. Each subject in Dataset 2 performed 15 non-FFH movements and 2 FFH movements. A 5 Hz low-pass filter was applied both datasets to reduce noise. Acceleration SVM, angular velocity SVM, vertical angle, and vertical velocity were extracted for the algorithm. The vertical velocity was calculated by integrating the vertical acceleration, considering the jerk value. To minimize integration errors, a lag filter was applied to reduce phase delay. Additionally, the norm velocity was obtained by applying the signum function to reduce the gravitational component. Threshold 1 was determined using data from 16 subjects in Dataset 1 to select the optimal thresholds for the vertical angle, vertical velocity, and norm velocity. Threshold 2 was determined using data from six out of nine subjects in Dataset 2. Both datasets were evaluated for accuracy, sensitivity, specificity, and lead-time.
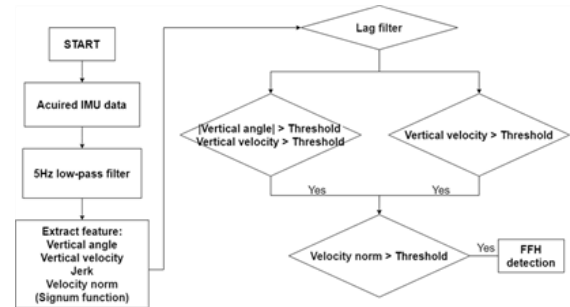
Figure 1 The block diagram of algorithm.

RESULTS AND DISCUSSION

In Table 1, dataset 1 with threshold 1 showed better performance than dataset 2 with threshold 1. Threshold 2, which optimized for Dataset 2, had a lower value than threshold 1, because the prototype sensor showed less resolution and required less computing calculation. As a result, the algorithm in the prototype sensor was optimized by its dataset. Dataset 2 with threshold 2 showed a 97% accuracy and a lead-time of 306.20 ± 122.73 ms, which is sufficient time to deploy the airbag.

CONCLUSION

A threshold based FFH detection algorithm was developed using IMU sensor. Dataset 1 outperformed Dataset 2. The optimization of Dataset 2 using threshold 2, with a prototype sensor with lower resolution yielded satisfactory results.

ACKNOWLEDGEMENT

REFERENCES

[1] Choi et al. *Int J Industr Ergon* **71**: 64-74, 2019.
[2] Koo et al. *Int J Precision Eng Manufac*, **21**: 1985-1995, 2020.

Table 1: Performance of the algorithms

	Accuracy	Sensitivity	Specificity	Lead-time (ms)
Dataset 1 with threshold 1	0.94	0.96	0.94	538.22 ± 197.17
Dataset 2 with threshold 1	0.89	0.00	0.99	0
Dataset 2 with threshold 2	0.97	0.94	0.97	306.20 ± 122.73

DEVELOPMENT AND EVALUATION OF ROBUST FALL DETECTION ALGORITHM USING ELDERLY PUBLIC DATASETS

Bummo Koo[1], Seunghee Lee[1], Sumin Yang[1] and Youngho Kim[1]

[1]Department of Biomedical Engineering and Institute of Medical Engineering, Yonsei University, Wonju, Korea

Email: younghokim@yonsei.ac.kr

INTRODUCTION

Falls are a major cause of injury and death in the elderly [1] Detection of a fall before impact is necessary for fall prevention. In general, simulated fall data from young adults are used for algorithm development for safety reasons. However, the evaluation using elderly data is necessary for the development of a robust fall detection algorithm. In this study, fall detection algorithm was developed and evaluated using elderly public dataset.

METHODS

Simulated fall data of young adult from the KFall [2] dataset was used to develop the ResNet-based fall detection algorithm. The model was developed for binary classification of falls and activities of daily living (ADLs) using 3-axis accelerations and 3-axis angular velocities as inputs. The dataset was measured at a sampling frequency of 100 Hz with an IMU sensor attached to the low back of 32 young adults (age: 24.9 ± 3.7 years, height: 174.0 ± 6.3 cm, weight: 69.3 ± 9.5 kg), including 21 ADLs and 15 falls. The model was trained with data from 26 subjects and evaluated with the remaining 6 subjects. Additionally, two public elderly datasets were applied to evaluate the model. The KFall enhanced dataset [3] was measured from 10 community dwelling elderly subjects (age: 80.8 ± 2.2 years, height: 166.6 ± 11.9 cm, weight: 65.1 ± 7.2 kg). Only 18 ADLs were performed excluding 4 potentially dangerous ones to avoid the risk. Some participants could not perform some ADLs due to physical limitations. Another one is the FARSEEING dataset [4] which collected real fall movements of the elderly. Considering sensor location and sampling frequency, 15 of total 22 files were used for evaluation, acquired from 8 elderly subjects (age: 66.9 ± 6.5 years, height: 162.2 ± 9.3 cm, weight: 74.2 ± 10.3 kg). As most of the FARSEEING data does not provide angular velocity, the model was retrained using only 3-axis accelerations from the KFall dataset. The sensitivity was calculated from the FARSEEING dataset and specificity was calculated from the KFall enhanced dataset. Shifting window was applied with 0.5s window length and 0.1s steps. Falls were considered to detect well if any window before impact was classified as a fall, and ADLs were considered to detect well if no window was classified as a fall.

RESULTS AND DISCUSSION

The developed algorithm was evaluated against the young participants, showing a sensitivity of 99.32%, a specificity of 96.84%, and a lead time of 539.00 ± 278.07 ms. However, the performance was represented that a sensitivity of 80%, a specificity of 87.81%, and a lead time of 500.0 ± 0.0 ms when tested with the elderly dataset. The sensitivity was assumed to decrease because only acceleration data was used to train the model. The specificity of the algorithm was good for all static movements, however, most frequent false detections occurred during movements with significant changes in the center of gravity and movements from elderly individuals with limited physical abilities. It indicates that the rate of false detection might be higher in the elderly due to their diminished sense of balance. The algorithm was optimized for the elderly. The step of the window was changed to 0.01s for more frequent determination. The algorithm was finally recognized the fall if three consecutive windows were classified as fall. As a result, the performance of the algorithm was enhanced showing a sensitivity of 86.67, a specificity of 97.97% and a lead time of 477.7 ± 5.8 ms.

CONCLUSION

In this study, a robust fall detection algorithm was successfully developed by evaluating and optimizing the algorithm based on a public fall dataset for the elderly. In the future, it is expected to contribute to protecting the elderly from injuries and improving their quality of life through wearable airbag system.

ACKNOWLEDGEMENT

REFERENCES

[1] Kenny R A et al. *Age & Aging* **31.4**: 272-275, 2002.
[2] Yu X et al. *Front. Aging Neurosci.* **13**: 692865, 2021.
[3] Yu X et al. *Measurement* .**201**: 111785, 2022.
[4] Klenk J et al. *Eur. Rev. Aging Phys. Act.* **13**: 1-7, 2016.

Table 1: The performance of the proposed fall detection algorithm based on ResNet

Algorithm	Evaluated Dataset	Sensitivity (%)	Specificity (%)	Lead time (ms)
Developed algorithm	KFall (young subject=6)	99.32	96.84	539.00±278.07
Developed algorithm	KFall (old subject=10) & FARSEEING (old subject=8)	80.00	87.81	500.00±0.00
Optimized algorithm	KFall (old subject=10) & FARSEEING (old subject=8)	86.67	97.97	477.7±5.8

EFFECTS OF A NOVEL DRONE GUIDANCE SYSTEM ON MOVEMENT PERFORMANCE DURING BADUANJIN EXERCISES FOR OLDER ADULTS: A COMPARATIVE STUDY WITH TRADITIONAL AUDIO AND VIDEO GUIDANCE

Kanjana Chaitika[1], Chien-Ju Lin[2], Hsiao-Feng Chieh[2] and Fong-Chin Su [1,2]

[1]Department of Biomedical Engineering, National Cheng Kung University, Tainan, Taiwan.
[2]Medical Device Innovation Center, National Cheng Kung University, Tainan, Taiwan.
Email: fcsu@ncku.edu.tw

INTRODUCTION

In an aging society, promoting healthy aging is of utmost importance. Regular exercise is highly recommended for older individuals, but many face challenges in performing exercises. To address this, providing suitable tools for support and guidance is advantageous. Our previous study examined the effectiveness of two traditional exercise guidance materials: Baduanjin practicing audio and video [1]. The results showed that participants had better arm movement control when following the video guidance. Additionally, Baduanjin, a Chinese martial art exercise, has been proven safe and effective for older adults, particularly in improving balance control. Building upon this research, the current study investigates the effects of a newly developed exercise guidance system that utilizes a small drone to guide older adults in performing Baduanjin exercises [2]. Furthermore, the outcomes of this innovative tool are compared with the traditional audio and video methods from the previous study, contributing to our understanding of effective exercise guidance tools for older adults.

METHODS

This study recruited fifteen healthy older individuals (12 females and 3 males) with an average age of 67.40 ± 5.85 years, who had no prior experience in performing Baduanjin and did not have chronic musculoskeletal diseases. The experiment utilized a motion capture system with eight cameras (Motion Analysis) and two force plates (Kistler). Approval was obtained from the NCKU Institutional Review Board. Two specific Baduanjin movements, namely "draw a bow" and "arm-up," were selected for analysis.

An intrasubject experiment was conducted to assess the impact of traditional and newly developed exercise guidance tools on movement performance during Baduanjin exercise. Various parameters related to balance control were analyzed, including the path length of the center of pressure (COP), resultant COP mean velocity, COP mean velocity in the medio-lateral and antero-posterior directions, root mean square (RMS) amplitude, and RMS velocity of COP. Additionally, the smoothness of arm movements was evaluated through the calculation of the number of movement units (NMU) and the normalized jerk score (NJs) for both the left and right hands. Data were recorded in five trials for each condition and were divided into seven phases based on the movement patterns (Figure 1). Statistical analysis involved repeated measures ANOVA, and post-hoc analysis was performed using the Wilcoxon signed-rank test.
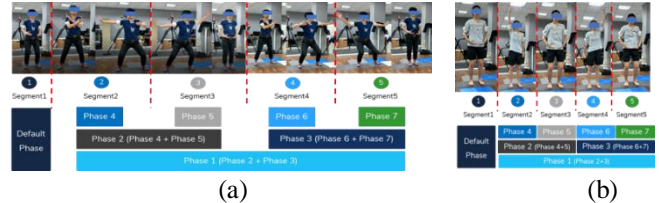
Figure 1 Phase segmentation of (a) draw a bow movement and (b) arm-up movement.

RESULTS AND DISCUSSION

The analysis of the COP in both the draw a bow movement and arm-up movement revealed significant differences between the drone, audio, and video conditions. In the draw a bow movement, the RMS amplitude of the COP was significantly greater in the drone condition during phases 2 and phase 5 compared to the audio condition. Additionally, in the arm-up movement, the path length of the COP in the drone condition during phase 3 was significantly greater than in the video condition. The smoothness analysis showed that both the NJs and NMU parameters had significantly higher values in the drone condition across multiple phases of both movements. For instance, in the draw a bow movement, the NJs value in phase 3 of the drone condition was significantly higher than in both the audio and video conditions. These findings suggest that participants put more effort and focus into following the drone, resulting in a wider distribution of the COP and decreased smoothness. However, it is important to consider the potential influence of the limited sample size in this study on the results.

CONCLUSION

By utilizing the novel drone guidance system, the participants could better follow and focus on the guidance of the drone compared to the traditional audio and video guidance tools during specific phases of the movement. This manifested as a broader distribution in the COP on the force platforms, facilitating the maintenance of body balance throughout the entire movement. Additionally, the smoothness parameters of their arm movements showed lower values compared to the other guidance methods, indicating a stronger effort to follow the drone.

ACKNOWLEDGEMENT

REFERENCES

[1] Chaitika et al. *TSBME annual conference.* 2021.
[2] Kanjana, C. *Unpublished master's thesis.* National Cheng Kung University, Taiwan. 2021.

SENSOR-EMBEDDED NOVEL HOLDING DEVICE FOR UPPER EXTREMITY ASSESSMENTS AND REHABILITATION

Charlie C. Ma[1], Chien-Ju Lin [1], Hsiao-Feng Chieh [1] and Fong-Chin Su[1,2]

[1]Medical Device Innovation Center, [2]Department of Biomedical Engineering, National Cheng Kung University, Tainan, Taiwan.

Email: fcsu@ncku.edu.tw

INTRODUCTION

Effective evaluation and monitoring of upper extremity (UE) rehabilitation are vital due to various causes of weakness, such as stroke, trauma, and aging. However, conventional assessment tools often require clinician assistance and are limited to specific clinical settings. Although some wearable devices have been used for innovative assessments, they still rely on clinicians or caregivers for further tests. To overcome these limitations and enhance the assessment process, this study introduces the sensor-embedded holding device (SEHD). Specifically designed to evaluate UE function, considering the prevalence of cylindrical grasp and grip movements in daily activities, the SEHD not only aims to improve the assessment process but also has the potential for utilization in UE rehabilitation.

METHODS

A 6-axis IMU (MPU-6050 sensor) was integrated into the SEHD to monitor acceleration and angular velocity, commonly utilized in motion control studies [1]. The IMU, Bluetooth wireless transmitter, and battery were positioned at the center of the device (Figure 1 (A)). For the study, 12 healthy individuals (3 males, average age 44.495) were recruited to perform two upper extremity (UE) tasks: forearm pronation/supination and wrist flexion/extension (Figure 1 (C, D)). Each subject completed five trials per task using a standardized procedure. Movement smoothness and angular changes were evaluated, with movement smoothness measured using the log dimensionless jerk (LDLJ) formula [2]. Data processing was conducted using MATLAB, and statistical analysis employed Spearman's correlation in SPSS. Apart from its assessment functionalities, we created a rehabilitation game that replicates everyday activities. The game incorporates basic addition tasks resembling calculations made while grocery shopping. The SEHD's shaking motion (pronation-supination) controls the tens digit of the answer, while twisting the SEHD (flexion-extension) controls the units digit (Figure 1 (B)).

RESULTS AND DISCUSSION

The findings revealed a positive correlation between pronation angular changes and performance on the Purdue Pegboard Test in dominant, both-hands, and assembly tasks. This aligns with the observation that pronation movement is

crucial for performing the Purdue Pegboard test. Additionally, the results demonstrated a negative correlation between movement smoothness during extension and the Purdue Pegboard Test in the both-hands task. A smaller LDLJ value indicates smoother movement during the task, suggesting that smoother extension movements could lead to better outcomes on the Purdue Pegboard Test (Table 1).

To gauge user experience, visual analog scales (VAS) were used to collect participant feedback. The average VAS score was 9.67 out of 10, indicating that all users found the system easy to understand and operate.
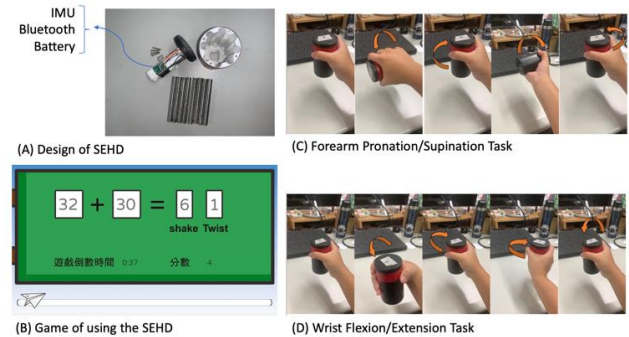
Figure 1 (A) is the design of the SEHD, (C) and (D) are the tasks of using SEHD, and (B) is the designed game using SEHD for rehabilitation.

CONCLUSION

The SEHD with simple movement tasks could provide digitized data correlated to the PPT and might be able to represent one's UE abilities. The users accepted the gamified system using SEHD for rehabilitation and might be able to be applied in clinical use.

ACKNOWLEDGEMENT

REFERENCES

[1] Ma, CC. et al. *Frontiers Bioeng Biotech* **10**. 2022.
[2] Balasubramanian, S. et al. *J Neuroeng Rehabil* **12**(1), 1-11, 2015.

Table 1: The correlation between the Purdue Pegboard Test and the movement parameters using SEHD.

		PPT (Dominant)	PPT (Both)	PPT (Assembly)
Angular Changes of Pronation	Correlation Coefficient	.615*	.583*	.609*
LDLJ of Extension	Correlation Coefficient	-.559	-.752**	-.571

**. Correlation is significant at the 0.01 level (2-tailed). *. Correlation is significant at the 0.05 level (2-tailed).

EFFECT OF ACCELERATION AND DECELERATION ON GAIT ROBUSTNESS

F. Ferryanto[1], Daffa Faisal Afif[2] and Andi Isra Mahyuddin[1]

[1] Mechanical Design Research Group, Faculty of Mechanical & Aerospace Engineering, Institut Teknologi Bandung, Indonesia
[2] Mechanical Engineering Study Program, Faculty of Mechanical & Aerospace Engineering, Institut Teknologi Bandung, Indonesia.

Email: f.ferryanto@itb.ac.id

INTRODUCTION

Gait could be seen as a chaotic signal that has recurrence propertie. However, it was observed that every gait cycle was inconsistent due to an unlimited amount of environmental perturbances. Changes in walking speed are common in human walking movement; thus, it is proposed to be the perturbation during this research. Rosenstein's Lyapunov Exponent (*LE*) will measure the degree of instability between walking speeds, and the *RQA* method will be used to quantify the predictability using determinism (*DET*) scores of gaits. To the author's knowledge, knee angle in the sagittal plane is a good parameter with a high Range of Motion (*ROM*). This parameter will be analyzed through the *LE* and *RQA* methods. The measurement of λ_L and *DET* could estimate the robustness of gait, as stated in a previous study describing how much perturbance could be handled during gait movements [1].

METHODS

The data acquisition utilizes motion capture with stereo pairs of action cameras, capturing a clear sagittal view during walking movements. 29 gait data were acquired from eleven participants. The participants were obliged to walk on the treadmill and find their Preferred Walking Speed (*PWS*). It is acquired that the *PWS* factors of all participants were similar compared to a prior study (*p=0.145*) [2]. Furthermore, they were not allowed to know when the acceleration (*Acc*) and deceleration (*Dec*) were applied to naturalize the perturbances effect. During observation, the participants experienced slow (70% *PWS*), fast (130% *PWS*), and rapid (150% *PWS*) walking speeds. Before LE and RQA were performed, the phase space reconstruction was applied using 7 embedding dimensions and 70 samples of time delay using the giotto-tda python library [3]. The *DET* values from the *RQA* method [4] described the predictability behavior of the gait movements while λ_L described the signal state of the gait movements.

RESULTS AND DISCUSSION

The *LE* quantifiers showed a remarkable score difference between alternating and constant walking speeds. During constant walking speed, the gait achieved around zero scores implying a limit cycle state is more likely achieved, in which the right foot gave similar action (*p=0.933*), as shown in Figure 1. Deceleration was observed to affect the participants' lower predictability at the slower walking speed than its previous walking speed. Observed in *DET* scores, the participants' gait could perform more predictable gait and reached the most predictable gait at a rapid speed. Comparing both feet during the same walking modes, it was found that both feet achieved similar scores (*p>0.05*).
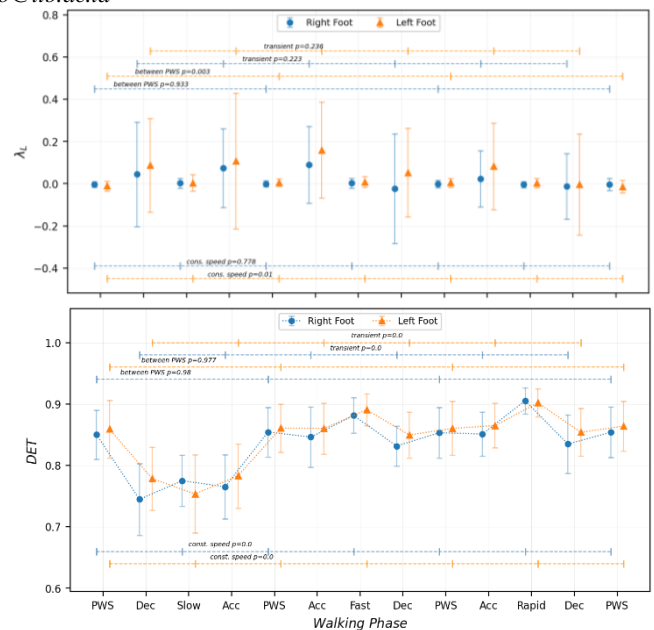
Figure 1 The *LE* and *DET* scores between walking orders.

CONCLUSION

The set of walking modes applied in this research affects the behavior of human gait as examined using *LE* and *RQA* methods. During constant speed, the participants could handle their gait in a stable operating range (*limit cycle attracted*) with near-zero values of λ_L, while deceleration perturbance allows the participants to manage their gait to become more predictable, as shown in the *DET* graph. Furthermore, the participants achieved the most predictable gait with the highest DET scores at fast and rapid walking speeds. The behavior between both feet showed similar action during the same walking mode as the scores were statistically indifferent.

ACKNOWLEDGEMENT

REFERENCES

[1] Bruijn S. M. et al. *J R Soc Interface* **10**:83, 2013.
[2] Wodarski P. et al *Acta Bioeng Biomech* **22**:1, 2020.
[3] Tauzin G. et al. *J Mach Learn Res* **38**:170-174, 2021.
[4] Rawald T. et al. *Comput Geosci* **104**:101-108, 2016.

SOFT ROBOTIC GLOVE SYSTEM WITH HALF BELLOWS-SHAPED SOFT ACTUATOR FOR REPETITIVE EXERCISE OF HAND THERAPY

Ayu G. Risangtuni[1,2] and Yul Y. Nazaruddin[2]

[1] Engineering Physics Doctoral Program, Institut Teknologi Bandung, Indonesia.

[3] Instrumentation and Control Research Group, Institut Teknologi Bandung, Indonesia.

Email: ayugareta@itb.ac.id

INTRODUCTION

Hand therapy for patients with hand severe muscle weakness mostly done with helps from therapists. The number of available clinics and therapists might be a problem for low- and middle-income country [1]. Thus, the development and utilization of assistive device such as orthosis or robotic gloves have shown a positive impact in the patients' healing process [2], [3]. However, robotic orthosis usually has a massive size. They utilize motor and linkage bar as the main driver of the system [4]–[6]. Thus, many have turn to soft robotics for implementation for robotic orthosis. Soft robotics give a better performance in terms of degree of freedom (DoF), motion conformity, and size. The motion driver that shows a promising performance is the Pneumatic Network (PneuNet) soft actuator [7], [8]. In this work, we propose an active soft robotic system with half bellows-shaped soft actuator as the main motion driver for hand therapy and exercises.

METHODS

In this research, we develop a complete soft robotic glove system for hand flexion therapy. Two components are included in the proposed system: 1) time scheduling pneumatic control system, 2) soft actuator. The time scheduling control was applied to ensure that the soft robot can accommodate different needs from the users. A manipulated PWM signal is used since the main pneumatic actuator was an ON/OFF solenoid valve. From the dynamic PWM evaluation of the pneumatic control system on a constant frequency and pressure of 2 Hz and 200 kPa, a three modes time-scheduling scheme is determined by the system duty cycle percentage and settling time. It includes slow, medium, and fast mode which duration is set as follows respectively: 6, 4, and 2 seconds. Then the maximum flexion angle for each mode will be the evaluated parameter by the RMSE (Root Mean Squared Error) value.

RESULTS AND DISCUSSION

From the evaluated system, we can see that the proposed system shows that it is capable of performing a repetitive motion in three modes: slow, medium, and fast (see Figure 1).

The setpoint for flexion angle is set at 60° for each mode and the system response is as shown in Table 1.
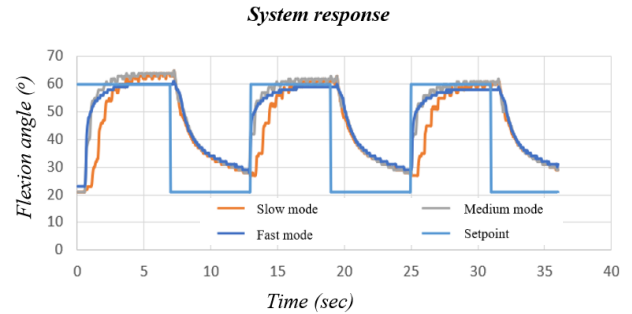
Figure 1 System response in slow, medium, and fast mode
The shifting speed of flexion angle and air pressure was determined by the system mode, and it can be utilized as needed by the user condition.

CONCLUSION

A soft robotic glove system for with half-bellows PneuNet soft actuator was developed for a repetitive exercise of hand therapy. The system includes several main components, which are the soft actuator and time scheduling control system with pneumatic control signal.

REFERENCES

[1] Silveira, A.T., et al., *Research on Biomedical Engineering*, **34**(4), 2018.

[2] Portnova, A.A., et al., *PLoS One*, 1-18, 2018.

[3] McPherson, A. I. W., et al., *Proceedings of the Annual International Conference of the IEEE Engineering in Medicine and Biology Society, EMBS*, 2020.

[4] Alici, G., *MRS Adv*, **3**(28), 1557-15682018.

[5] Yue, Z., et al., *Behavioural Neurology*, 2017.

[6] Pundik S. et al., *Front Neurol*, **13**, 2022.

[7] Wang Z. & Hirai, S. "Analytical Modeling of a Soft Pneu-net Actuator Based on Finite Strain Beam Theory," 1-7, 2021.

[8] Gu, G. et al., *Soft Robot*, 8(4), 2021.

Table 1 The system performance based on the RMSE of flexion mode, flexion angle shift speed, and air pressure shift speed

Mode	RMSE of Flexion Mode			Flexion Angle Shift Speed (°/s)			Air Pressure Shift Speed (°/s)		
	1st cycle	2nd cycle	3rd cycle	1st cycle	2nd cycle	3rd cycle	1st cycle	2nd cycle	3rd cycle
Slow	19.09	13.79	15.72	9.57	7.14	6.71	66.82	62.36	59.48
Medium	11.27	14.42	15.27	10.50	9.00	10.00	62.88	79.28	80.50
Fast	12.06	17.53	12.01	16.00	15.00	18.50	127.92	129.90	159.04

SIMULATIONAL ANALYSIS OF THE ENERGY EFFICIENCY OF WALKING WITH A BACKPACK

Makoto Yoshida[1], Justyna Zasada[2] and Kazunori Hase[1]

[1] Department of Mechanical Systems Engineering, Tokyo Metropolitan University, Tokyo, Japan.

[2] International Faculty of Engineering, Faculty of Mechanical Engineering, Lodz University of Technology, Lodz, Poland.

Email: yoshida-makoto@tmu.ac.jp

INTRODUCTION

In a crowded situation such as that in a commuter train in big cities in Japan, many people carry their backpack in the front, instead of on the back, to reduce the personal space occupied per individual. Since feet protrude anteriorly with respect to the ankles, and flexion is preferred over extension in shoulder joints, the frontal area is usually occupied by an individual anyway, while the rear area is occupied only when the individual is carrying a backpack on the back. Probably because wearing back the backpack that was once worn in the front on the back again is somewhat troublesome, some people continue to carry their backpack in the front, even after getting off a crowded train.

Because whether one actually conducts this somewhat troublesome action or not is a personal decision, experimental approaches to estimate the energy efficiency of walking with carrying a backpack in different modes may be significantly influenced by personal preferences. Since simulational approaches are promising because they are not influenced by subjectivity, the current study aims to evaluate the energy efficiency of walking with a backpack carried on the back or in the front, using a three-dimensional whole body human gait simulation system [1], which may contribute in improving the design of backpacks.

METHODS

A model that reproduces the whole body of a human is constructed. Each joint was modelled as a single or a combination of rotational degrees of freedom. The body weight of the model is 60 kg. A 4 kg of mass representing a backpack is attached to the thorax segment (Figure 1).

This model is controlled by a network of neuron models constructed according to that of Taga [2]. This neuromimetic controller, which serves as a rhythmic pattern generator, consists of paired neuron models. Each pair of neuron models acts as a neural oscillator, due to mutual inhibition of the neuron models in the pair. Each pair of neuron models is assigned to a rotational degree of freedom of a joint, where the state of a neuron model in a pair represents either the positive or the negative torque acting on the rotational degree of freedom, thus driving the model periodically.

The states of the neuron models are modulated by proportional-derivative feedback systems employing some of the somatic senses. The parameters of the neuromimetic controller are optimized based on the energy efficiency of the movement. The sum of work positively acting on each joint was employed to calculate the energy efficiency.

The simulation system used in this study [1] is based on SCONE [3], a platform for predictive simulations, which supports OpenSim file formats [4]. The algorithm used in this system was originally implemented by Hase and Yamazaki [5].

RESULTS AND DISCUSSION

Preliminary results demonstrated that carrying a backpack in the front required more than 10% additional work per unit distance of travel, compared to carrying on the back. The causal relationship between the mode of carrying a backpack and the energy efficiency will be discussed.
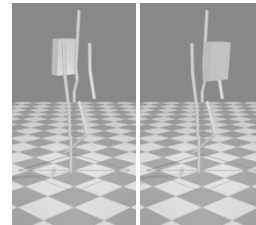
Figure 1 The three-dimensional whole body human models. The models simulate individuals carrying a backpack either on the back (left model) or in the front (right model).

CONCLUSION

The energy efficiency of gait while carrying a backpack was simulationally evaluated. Preliminary results demonstrated that carrying a backpack in the front is less efficient than carrying it on the back. Elucidating this mechanism should aid designing a new type of backpacks that is more suitable for urban lives with inevitable crowded commuter trains.

REFERENCES

[1] Yoshida M & Hase K, *9th World Congress of Biomechanics*, Taipei, P-1216, 2022.
[2] Taga G, *Biol Cybern* **73**: 97-111, 1995.
[3] Geijtenbeek T, *J Open Source Softw* **4**: 1421, 2019.
[4] Delp SL et al. *IEEE Trans Biomed Eng* **54**: 1940-1950, 2007.
[5] Hase K & Yamazaki N *JSME Int J Ser C* **45**: 1040-1050, 2002.

ANALYSIS OF DELAYED OUTPUT FEEDBACK CONTROL PARAMETERS USING FORWARD DYNAMICS SKELETAL SIMULATION

Seungwoo Yoon[1] and Seungbum Koo[1]

[1] Department of Mechanical Engineering, Korea Advanced Institute of Science and Technology, Daejeon, Republic of Korea

Email: skoo@kaist.ac.kr

INTRODUCTION

A delayed output feedback control (DOFC) algorithm has been proposed that applies assistive torque to the hip joint without identifying the gait phase [1,2]. The selection of control parameters is important because these algorithms interact with the human body to generate torque [3]. In a previous study [1], a simplified model was used to select parameters, and the parameters were evaluated by measuring the metabolic energy of the human through subject experiments. In this study, we investigated DOFC parameters for hip torque assist and change in total body power using a forward dynamics simulation of human model. The objective of the study was to find optimal DOFC parameters that minimize the mechanical work of human model during walking.

METHODS

This study was approved by the Institutional Review Board (IRB) of KAIST. We obtained full-body motion capture data during normal walking from a healthy subject (23 years old, weighing 65.4 kg). We prepared the reference gait kinematics using the motion data. The skeletal model used had 25 joints, each driven by a torque. Each joint torque was controlled by a neural network controller, which was trained using deep reinforcement learning methods to imitate actual human gait kinematics. To maintain walking even when an assistive torque was applied to the hip joint, the neural network was trained to follow reference movements that include a 10% change in walking speed and cadence. In addition, a reward function that minimizes the sum of the absolute values of mechanical power was added.

The DOFC algorithm was implemented based on the formula presented in Figure 1. (a). The DOFC algorithm provides assistive torque (τ) proportional to the difference in hip joint angles q_r, q_l of both legs. The hip joint angle was smoothed according to a low pass filter gain of 0.5. The assistive torque profile was determined by two parameters: torque gain (k) and delay time (Δt). The magnitude of assistive torque was determined by the torque gain, and the timing of providing assistive torque changes according to the delay time. The torque gain and delay time were arbitrarily set, and the model was made to walk for 10 seconds. Then, the mechanical power was calculated according to the gait cycle. The mechanical power was calculated as $\sum_{n=1}^{joints} \int^{cycle} |\tau \cdot w| \, dt$, where τ is the torque and w is the angular velocity of each joint.

RESULTS AND DISCUSSION

Torque gain varied from 0 to 15 Nm, and delay time from 0 to 1.0 seconds. The mechanical power generated by the human body was depicted in Figure 1. (b). When the torque gain was set to 0, same as, no assistive torque was provided, the skeletal model reproduced the gait pattern with 411 W of mechanical power. The optimal case was when the torque gain was set to 10 Nm and the delay time was 0.37 seconds. In this case, the human body's mechanical power was 391 W, a decrease of 20 W compared to when no assistive torque was applied.
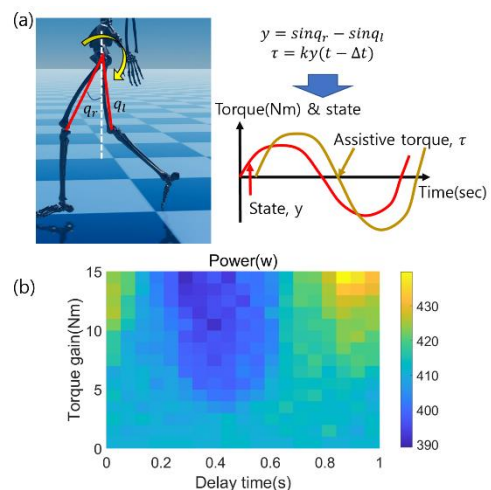
Figure 1. (a) DOFC algorithm (b) Heat map of human mechanical power for different torque and delay time

CONCLUSION

The study results indicated that when the torque gain was set to 10 Nm and delay time was 0.37 s, the human's mechanical power the human mechanical power was reduced by 20 W. The heatmap graph shows that as the coefficient of delay time changes from 0 to 1.0, the assistive and resistive areas change. This suggests that we can intuitively observe the controller's performance over a broader range than explored in [1]. Further, if detailed validation is conducted for the skeletal model, it is believed that it could be helpful in quantitatively assessing the algorithm's performance using the skeletal gait model, instead of human experiments which are difficult to quantify.

ACKNOWLEDGEMENT

REFERENCES

[1] Lim B et al. *IEEE Trans Robot* **35(4)**: 1055-1062, 2019.
[2] Lim B et al. *IEEE Robot Autom Lett*, 2023.
[3] Baud R et al., Neuroeng Rehabil, 18(1), 1-34, 2021.

ROBOTIC ANKLE PROSTHESES: DESIGNING AND FABRICATING A COMPACT MOTOR DRIVER CIRCUIT BOARD FOR ENHANCED MOTOR CONTROL

Zaina Al-Hashimi[1], Nooranida Arifin[1], Hamam Mokayed[3] and Noor Azuan Abu Osman[1,2]
[1]Biomedical Engineering / Universiti Malaya, Kuala Lumpur, Malaysia.
[2] The Chancellery, Universiti Tenaga Nasional, 43000, Kajang, Malaysia.
[3]Department of Computer Science, Electrical and Space Egnieering, Luleå University of Technology, Luleå, Sweden
Email: azuan@um.edu.my

INTRODUCTION

In recent years, the field of prosthetics has witnessed remarkable advancements, enabling individuals with limb loss to regain their mobility and improve their quality of life. Among these advancements, robotic ankle prostheses have shown tremendous potential in replicating the natural gait patterns and providing enhanced functionality [1]. Central to the success of these robotic ankle systems is the development of efficient and precise motor control mechanisms [2]. This project aims to address the critical need for accurate motor control in robotic ankle prostheses by designing and fabricating a compact motor driver circuit board.

METHODS

The project focuses on designing a compact motor driver circuit board for a robotic ankle prosthesis, with the goal of achieving accurate motor control. The methods employed include schematic design using OrCAD and PCB board design using Cadence Allegro. IC devices from Microchip and Infineon are chosen for integration into the circuit board. The schematic design phase involves creating the circuit diagram using OrCAD, selecting IC devices based on their compatibility with motor control requirements. Cadence Allegro is then used for PCB layout design, ensuring the placement of components, routing of traces, and incorporation of power and ground planes. Special attention is given to the compactness of the board design to facilitate integration within the prosthesis. IC devices from Microchip and Infineon are integrated into the PCB layout, leveraging their advanced features and control capabilities. Validation and testing procedures are conducted to verify the circuit's performance through simulations, signal integrity analysis, and electrical testing. Upon successful validation, the fabrication process begins, adhering to high-quality manufacturing standards. Factors such as material selection, soldering techniques, and quality control measures are considered. The methods ensure accurate motor control and integration within the robotic ankle prosthesis, contributing to enhanced functionality and control for the users.

RESULTS AND DISCUSSION

The design and implementation of the compact motor driver circuit board for the robotic ankle prosthesis project have been successfully completed. The preliminary results demonstrate exceptional accuracy, as indicated by a Root Mean Square Error (RMSE) value of 0.02. Figure 1 shows the results of the preliminary results of the board test at 3 different duty-cycles of 25%, 50% and 75%.
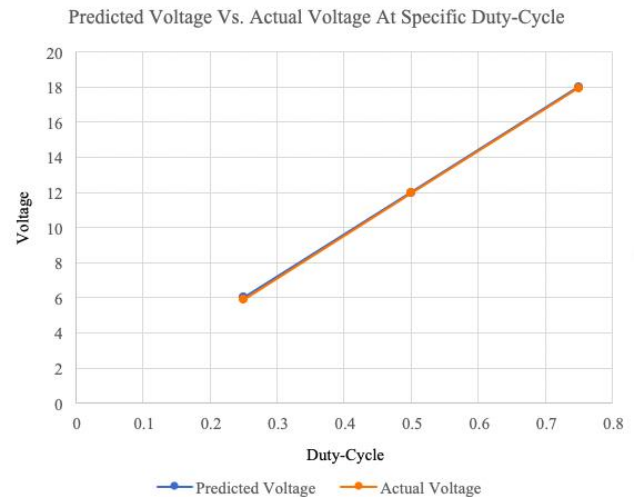
Figure 1 Predicted Voltage Vs. Actual Voltage at Specific Duty-Cycle.

CONCLUSION

In conclusion, the successful design and implementation of the compact motor driver circuit board for the robotic ankle prosthesis project have yielded excellent results. The achieved accuracy with an RMSE of 0.02 showcases the effectiveness of the motor control system and its potential to provide users with a natural and seamless walking experience. These results lay a solid foundation for advancing the field of prosthetics and improving the quality of life for individuals with limb loss.

ACKNOWLEDGEMENT

REFERENCESP

[1] Al Kouzbary et al. *Int J Fuzzy Sys* **22**: 1299-1313, 2020.
[2] Anderson et al. *TechRxiv.* 2022.

ASSOCIATIONS BETWEEN TRUNK MOVEMENTS IN THE SAGITTAL PLANE AND GAIT DEVIATIONS IN ADULTS WITH UNILATERAL DEVELOPMENTAL DYSPLASIA OF THE HIP DURING WALKING

Ching-Ru Chen[1], Kuan-Wen Wu[2,3], Ting-Ming Wang[2,3] and Tung-Wu Lu[1,3]

1 Department of Biomedical Engineering, National Taiwan University, Taipei, Taiwan
2 Department of Orthopaedic Surgery, National Taiwan University Hospital, Taipei, Taiwan
3 Department of Orthopaedic Surgery, School of Medicine, National Taiwan University, Taipei, Taiwan
Email: twlu@ntu.edu.tw

INTRODUCTION

Developmental dysplasia of the hip (DDH) is a condition characterized by abnormal development of the hip joint. Previous studies on untreated DDH gait have primarily focused on specific gait variables such as temporal and distance measures, lower limb joint kinematics and kinetics, and ground reaction forces [1]. However, there is a lack of understanding regarding how these patients' gait deviations compensate for the resulting instability, particularly in relation to trunk and lower extremity kinematics and kinetics in the sagittal plane. Therefore, the objective of this study is to investigate these relationships, aiming to gain insights into the balance control strategy during walking in individuals with DDH. Our study aims to assess trunk movement patterns, as well as lower extremity kinematics and kinetics in the sagittal plane during level walking in adults with DDH. We hypothesize that individuals with DDH will exhibit distinct trunk movement patterns compared to healthy controls.

METHODS

Twelve adult patients were included in the study, along with control subjects matched in terms of age, sex, and body type. They walked at their preferred pace on an 8-meter walkway while wearing 39 light-reflecting markers. The locomotor system was represented by a 7-link model, consisting of the pelvis, thighs, shanks, and feet as fixed links, each with its own orthogonal coordinate system. To minimize the impact of soft tissue artifacts on the pelvis-leg apparatus, a global optimization method was applied [2]. Inverse dynamics analysis was utilized to determine internal joint moments, which were then normalized to body mass and limb length. Gait variables were calculated for each limb in the control group and averaged across limbs for each trial. Statistical analysis involved examining peak values of joint angles and moments, pelvic and trunk angles at specific points during the gait cycle. The independent t-test was used to compare the two groups, while the Wilcoxon signed-ranks test was employed to compare the affected and unaffected sides within the DDH group. A significance level of 0.05 was set.

RESULTS AND DISCUSSION

Compared to the control group, the DDH group showed a reduced hip extension angle of the affected side at the contralateral heel strike in the sagittal plane. On the other hand, bilateral excessive trunk extension angle was found at the contralateral heel strike (Figure 1).
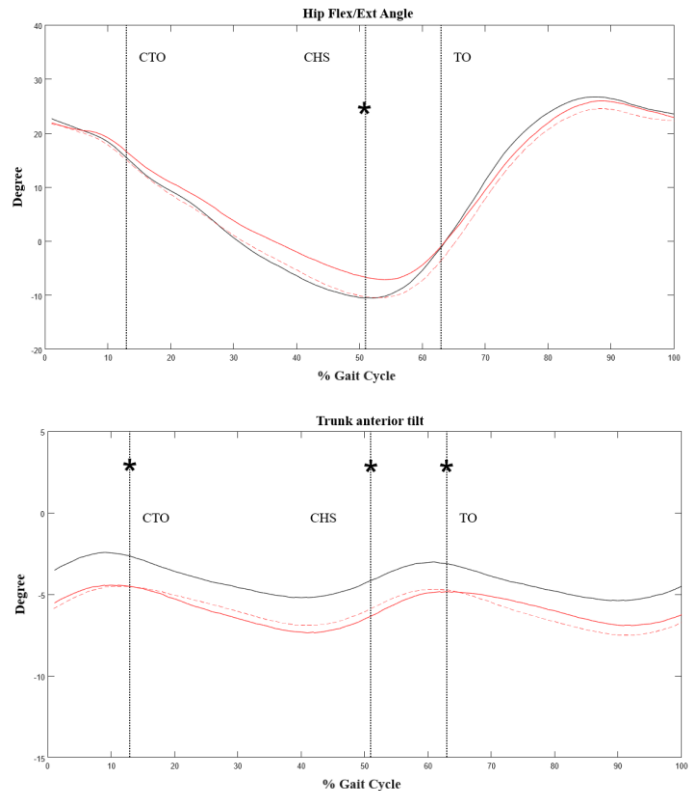
Figure 1 Ensemble-averaged three-dimensional joint angles at the hip joint and trunk during level waking in the affected limb (red, solid line) and unaffected limb (red, dotted line) of the DDH group and in that of the normal group (black, solid line).(* : significant differences between the affected limb and controls)

CONCLUSION

The study findings indicate the presence of asymmetrical kinematic patterns, particularly in the trunk and hip joints during contralateral heel strike. Specifically, there was a reduced hip extension angle observed on the affected side, potentially aimed at reducing hip pain by decreasing anterior hip force. However, this asymmetry may have a negative impact on gait stability and result in compensatory movements in other joints. It appears that trunk over-extension during contralateral heel strike serves as a compensatory strategy to enhance hip joint stability.

REFERENCES

[1] Romano, C., et al. *JBJS*, **78**(10): 1468-1479, 1996.
[2] Lu, T.-W. & O'connor J., *J Biomechanics*, **32**(2): 129-134, 1999.

DEVELOPMENT OF ROBOTIC KNEE JOINT INCORPORATING CYCLOIDAL GEAR DRIVES AND SERIES ELASTIC ELEMENT

Quazi Isha Nafisa[1], Mouaz Al Kouzbary[1], Noor Azuan Abu Osman[1] and Nasrul Anuar Abd Razak[1]

[1] Department of Biomedical Engineering, Universiti Malaya, Kuala Lumpur, Malaysia.

Email: quaziisha@gmail.com

INTRODUCTION

The development of prosthetic devices for people with amputations is an important area of research. This study aims to investigate the effect of tooth geometry on designing a robotic knee joint with a cycloidal gear system and series elastic element. The study is conducted in three stages: statistical analysis of the effect of tooth geometry on cycloidal gear efficiency, optimization for the coupling between cycloidal-based actuator and end effector, and a case study on the effect of using a robotic knee-joint based on a cycloidal actuator for people with above knee amputation.

METHODS

1. Mechatronics system design: The prosthesis design can be divided into two categories: mechanical system design, which focuses on selecting the cycloid reduction ratio and motor specifications based on knee functional analysis, and control system design, which considers impedance or hierarchical systems. Mechanical system design involves selecting cycloidal drive with specific tooth geometry, optimizing the elastic element to reduce motor power consumption and store energy for the system's swing phase. Cylindrical (flat) waterproof motors are suitable for passive mode, and power and motor size are restricted to allow the system to function on passive mode. Control system design involves implementing impedance or impedance-like hierarchical systems, and adding a control barrier function could improve smother motion.

2. System Evaluation: System evaluation involves assembling and testing three AC-actuators with cycloidal gears on a joints' emulator station, analyzing cycloid drives efficiency, driver ability for dive back, power consumption at maximum load, and temperature analysis for the electronical driver.

3. Biomechanical Analysis: Biomechanical analysis evaluates the functionality of the control system and mechanical design compared to normal tibia orientation, using a load simulator and random perturbations to evaluate the series elastic element. Clinical evaluation is conducted to study socket perturbations and gait abnormalities, and subjects' ambulation is compared with passive knee-joint prostheses.

RESULTS AND DISCUSSION

The study will aim to investigate the effect of tooth geometry on designing a robotic knee joint with a cycloidal gear system and series elastic element. The research will be conducted in three stages: statistical analysis of the effect of

tooth geometry on cycloidal gear efficiency, optimization for the coupling between cycloidal-based actuator and end effector, and a case study on the effect of using a robotic knee-joint based on a cycloidal actuator for people with above knee amputation.

The statistical analysis aims to reveal that tooth geometry will have a significant effect on cycloidal gear efficiency, particularly in terms of life cycle and actual transmission ratio. The optimization stage will result in a coupling design that will improve the efficiency of force transmission and absorb mechanical shocks on joint motors during active mode. Finally, the case study will show that the use of a robotic knee-joint based on a cycloidal actuator will improve the gait of people with above knee amputation.

Figure 2 shows a schematic diagram of the overall proposed transfemoral prothesis design.
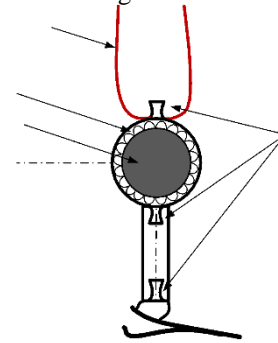
Figure 1 Active knee joint with cycloid reducer, and 0 to 90° range of movement configuration

CONCLUSION

In conclusion, the study aims to demonstrate that tooth geometry plays a crucial role in designing a robotic knee joint with a cycloidal gear system and series elastic element. The optimization of the coupling design will improve the efficiency of force transmission and absorb mechanical shocks on joint motors during active mode. The case study plans to show that the use of a robotic knee-joint based on a cycloidal actuator improves the gait of people with above knee amputation. These findings will have significant implications for the development of more efficient and effective robotic knee joints for people with amputations. Further research will be needed to explore the potential of this technology in other areas of prosthetics and robotics.

ACKNOWLEDGEMENT

DEVELOPMENT OF A PASSIVE EXOSKELETON FOR CARE WORKERS TO ASSIST THE LOWER BACK AND THE LOWER LIMBS

Bian Yoshimura[1], Naoto Haragchi[1], Makoto Yoshida[1] and Kazunori Hase[1]

[1]Department of Mechanical Systems Engineering, Tokyo Metropolitan University / Tokyo, Japan.

Email: yoshimura-bian@ed.tmu.ac.jp

INTRODUCTION

Caregiving including patient lifting and transferring is physically demanding, and many care workers suffer from musculoskeletal disorders such as low back pain. In recent years, various devices have been developed to avoid their burdensome postures and movements. While a certain number of workers in the nursing care field suffer from lower limb pain [1], most of the devices actually used in the field are designed to reduce the burden on the lower back only [2]. This study aims to develop a device to assist the lower back and the lower limbs for care workers and evaluate its effectiveness.

METHODS

The prototype exoskeleton consists of pads that support the chest, posterior parts of the thighs and the knees, shoes that hold the feet, and aluminum frames connected with rotational joints with springs installed (Figure 1). When the user puts his/her weight on each pad from an upright posture, the springs at each joint extend and exert torques to return the user to an upright posture. The torques generated at the joints support extensions of the hip and knee joints and plantar flexion of the ankle joints in place of the muscles. This mechanism provides support in movements such as lifting and static support in postures such as bent posture, thereby reducing the burden on the lower back and the lower limbs.

Eleven healthy adult males performed the tasks with and without the exoskeleton, and the sensory evaluation was conducted afterward. Four of the participants also recorded electromyograms (EMG) during the tasks. The sensory evaluation was based on the results of a questionnaire using a Likert scale, and five items were scored: load on the lower back, load on the lower limbs, comfortability, operability and stability. The EMG sensors (S&ME, DL-142) were placed at six muscle sites on the dominant hand side: erector spinae, rectus abdominis, biceps femoris, vastus medialis, medial head of gastrocnemius, and tibialis anterior. Participants were given five tasks that simulated a nursing-care situation: lifting and lowering a weight, moving a weight laterally while keeping a bent posture, standing posture, and walking. In addition, ease of wearing, portability and storability were evaluated based on wearing time, weight, size and questionnaire.

RESULTS AND DISCUSSION

When lifting and moving laterally a weight, the sensory evaluation showed significantly higher scores for the items of load on the lower body and stability when the exoskeleton was worn, while no significant differences were observed for the items of comfort and mobility scores. This could be interpreted as that the exoskeleton was able to assist trunk extension without encumbering the rotation. In standing posture and walking, the exoskeleton did not show an assistive effect, and mobility scores were significantly lower than no exoskeleton in walking. Possible causes include that the measurement time was too short in the standing position and that the directions in which the exoskeleton assisted the knee joint and hip joint torque were also in directions that encumbered walking motion. EMG data results showed that the exoskeleton significantly reduced the muscle activity of the biceps femoris in the lifting, and the assist effect was about 22% of that without the exoskeleton.

Four participants put on and took off the exoskeleton by themselves for the first time, it took 110 ± 24 seconds and 24 ± 8 seconds, respectively. Improvements in the fixing bands and the shoes are expected to reduce the time greatly. While the weight is about 5.25 kg, the heaviness is not experienced by the users since the frame is in contact with the ground when worn. The storage size was about 75 cm × 25 cm × 20 cm by folding each frame to overlap each other. In a questionnaire for eleven participants, more than 60% responded positively to the ease of wearing, and more than 80% responded positively to portability and storability.

Figure 1 The prototype exoskeleton. It supports part of the body weight as indicated by the arrows and assists bent posture and extensions of the lower back and the lower limbs.

CONCLUSION

A passive exoskeleton for care workers was developed and its performance was evaluated. Sensory evaluation and EMG data demonstrated that the exoskeleton prototype reduced the burden on the lower back and the lower limbs in lifting and forward-leaning tasks. On the other hand, in standing posture and walking, the prototype was not effective and encumbered some of the walking movements. The practicality was shown to some extent by the evaluations of the ease of wearing, portability and storability.

REFERENCES

[1] Davis KG et al. *Hum Factors* **57**: 754-792, 2015

[2] Hwang J et al. *Appl Ergon* **93**: 103373, 2021

PRELIMINARY INVESTIGATION: IMPACT OF CONTROL STRUCTURE IN BATTERY CHARGER ON PROSTHETIC BATTERY PACK

Nor Akmal Farhan Kamsani Tuah[1], Nooranida Arifin[1] and Noor Azuan Abu Osman[1,2]

[1] Centre for Applied Biomechanics, Department of Biomedical Engineering, Faculty of Engineering, Universiti Malaya, 50603 Kuala Lumpur, Malaysia.

[2] The Chancellery, Universiti Tenaga Nasional, 43000 Kajang, Malaysia.

Email: azuan@um.edu.my

INTRODUCTION

The field of wearable robotics has made great strides in recent years, inspiring the creation of cutting-edge applications that improve quality of life and expand human potential [1]. The power source that enables wearable robots to operate continuously is a crucial component [2]. Due to its high energy density, small weight, and extended lifespan, lithium batteries have become a popular option [3]. However, it can be difficult to charge these lithium batteries effectively and consistently [4].

For accurate regulation of both constant current and constant voltage charging modes for battery-operated light electric vehicles, the converter makes use of a simplified control algorithm [5]. This feature provides effective charge management, reducing battery stress, and optimising operations by incorporating a fuzzy logic controller into a voltage-oriented control scheme [6]. To address prolonged charging times, a circuit design divides the battery into two sections and employs dual chargers to simultaneously charge each part, effectively halving the overall charging time [7].

The capability of a single CPU and a digital signal processor (DSP) to track and control voltages, current, and battery temperature [8]. The effective battery temperature was significantly lowered because of this novel strategy [9]. The gains were calculated using the particle swarm optimization (PSO) technique, and [10] proposed an integrating fuzzy logic control (FLC) and a conventional proportional integral (PI) controller that performed better than a traditional PI. It was clear from simulations that the suggested controller considerably improved system performance. These results demonstrate how sophisticated control approaches have the potential to revolutionize battery management systems [11]. By replicating the impacts of the control system, this study investigates the influence of battery charging time on prosthesis functioning. A model of a battery charger control system that was specifically created was used to replicate real-world situations using a variety of control algorithms. Various charging techniques, such as the optimized feedback controller, were evaluated. According to preliminary findings, improved control algorithms can improve prosthesis functioning by speeding up charging. Validating the results with actual charging board is an ongoing research project. Future research intends to improve control algorithms, test outcomes with actual hardware, and look at underlying processes for enhanced functionality.

METHODS

The main phases in the research process for creating battery chargers are described in this technique. With this method, a charger that is dependable, secure, and designed for battery charging will be created. In this study, Simulink in MATLAB is utilized to model various battery charging control topologies, employing a feedback controller due to the system's nonlinearity.

First, the parameters for the buck converter will be computed using the appropriate formulae to assure accuracy. The performance and functionality of the buck converter circuit will then be evaluated through simulation. The charger's efficiency and dependability are enhanced in the following stage by careful selection of electronic components, such as MOSFET. A thorough PCB design will be created, taking into consideration the unique needs and limits, to make the actual implementation of the charger easier. Following industry best practices and standards, PCB manufacture will begin as soon as the design is complete. The charger will next undergo an open-loop test to assess its initial performance and make any required corrections. Figure 1 shows the summary of the research process.
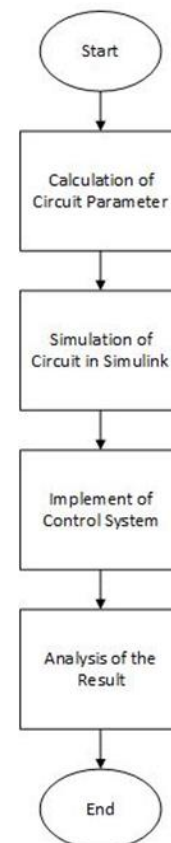
Figure 1 The process flow of a research project.

An effective power conversion system consists of a synchronous buck converter and a fuzzy logic controller in Figure 2. By varying the duty cycle of the switching transistor, the converter uses a pulse-width modulation

(PWM) approach to control the output voltage. Based on language variables and rules, the fuzzy logic controller intelligently changes the duty cycle in accordance with input voltage and load circumstances. This integrated system is appropriate for a variety of applications, including renewable energy systems, portable electronics, and automotive electronics, thanks to modelling that assures efficient power transmission, resilience against parameter fluctuations, and quick transient response.
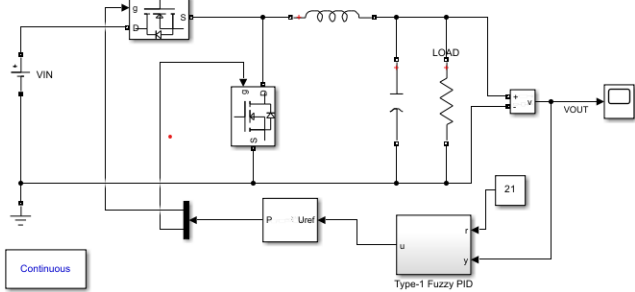
Figure 2 The Fuzzy controller in a circuit.

RESULTS AND DISCUSSION

The graphic displays the outcome of the simulation of the buck converter with the use of a fuzzy logic controller. The output voltage with time is shown on the graph. The output voltage is shown by the green line, which rises progressively from left to right. The output ascends approximately 21V, almost touching the reference. The behaviour of the output voltage in the buck converter system is represented visually in this graphic, illustrating how well the fuzzy logic controller controls the voltage output in Figure 3 and 4.
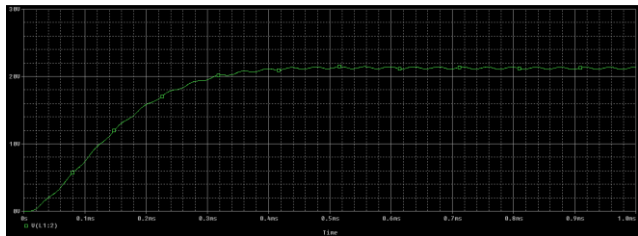
Figure 3 The output voltage for circuit.
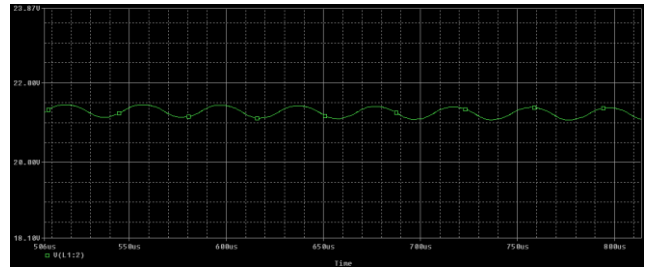
Figure 4 Zoom in for output voltage.

CONCLUSION

To sum up, buck converter integration with fuzzy logic control is a potential strategy for boosting power conversion effectiveness and dynamic response in a variety of applications. The system provides ideal voltage control while minimising the impacts of load disturbances by utilising the flexibility and resilience of fuzzy logic.

Future studies should aim to refine the proposed approach by incorporating analog-to-digital converters, current and voltage sensors, an advanced management system, and conducting experiments on a real PCB board for improved parameter measurement, control, and practical implementation validation, in order to fully explore the potential of the buck converter with fuzzy logic.

REFERENCES

[1] Alvarez-Perez MG et al. *Disability and Rehabilitation: Assistive Technology* **15**: 394-408, 2020.
[2] Sekretaryova A. *Elsevier* 89-132, 2020.
[3] Schmuch R et al. *Nature Energy* **3**: 267-278, 2018.
[4] Albertus P et al. *Nature Energy* **3**: 16-21, 2018.
[5] Blinov A et al. *Energies* **13**: 774, 2020.
[6] De Luca F et al. *Electronics* **9**: 946, 2020.
[7] Kharade JM et al. *IEEE* 157-161, 2021.
[8] Huang CH et al. *IEEE* 1412-1417, 2009.
[9] Yarn KF et al. *Tech Publications Ltd* **219**: 941-944, 2011.
[10] Kim JY et al. *Energies* **4**: 1443-1460, 2011.
[11] Zhao H et al. *Journal of Modern Power Systems and Clean Energy* **3**: 422-428, 2015.

COMPARISON OF RECURRENT NEURAL NETWORK ALGORITHMS FOR ESTIMATING THE BODY'S CENTRE OF MASS MOTION RELATIVE TO THE CENTRE OF PRESSURE DURING GAIT USING A SINGLE WAIST-WORN IMU

Cheng-Hao Yu[1], Chih-Ching Yeh[1], Yi-Fu Lu[2], Frank Yeong-Sung Lin[2] and Tung-Wu Lu[1]

[1] Department of Biomedical Engineering, National Taiwan University, Taipei, Taiwan
[2] Department of Information Management, National Taiwan University, Taipei, Taiwan

Email: twlu@ntu.edu.tw

INTRODUCTION

Monitoring dynamic balance during walking is crucial for fall prevention in older people. In standard gait laboratories, the stability of dynamic balance during gait is well-established by describing the inclination angles (IAs) of the body's centre of mass (COM) relative to the centre of pressure (COP) and their rates of change (RCIAs) [1]. Inertial measurement units (IMUs) have become popular for gait monitoring in outdoor environments due to their reduced size and costs. However, capturing IAs and RCIAs requires multiple IMUs to measure different body segments, making it impractical for daily monitoring. Recurrent neural networks (RNN) have shown the potential to reduce the number of sensors [2]. Nevertheless, it remains unclear whether the predicted data from RNN can maintain sufficient test validity, namely the statistical between-group effects similar to the gold standard. Therefore, the current study aimed to develop a new approach based on RNN techniques, namely Long Short-Term Memory (LSTM) and Gated Recurrent Unit (GRU) models, for extracting IA and RCIA variables from a single waist worn IMU and to compare the test validity among the models by evaluating the statistical differences between a young and an old groups of healthy subjects during walking.

METHODS

Thirteen healthy young and thirteen older adults wore an IMU on the waist and walked on a 10-meter walkway while the body's COM and COP position were obtained using the forceplates and a motion capture system. These data were used to calculate gold standard IAs and RCIAs [1], together with the low-pass filtered IMU data, were used to train four proposed models, namely the uni-directional LSTM (UniLSTM), bi-directional LSTM (BiLSTM), uni-directional GRU (UniGRU) and bi-directional GRU (BiGRU) models. Data from 680 gait cycles were used to train the models, and 10% of trials were used to test the model. The model predictions were compared to the gold standard, giving percentage relative root-mean-squared errors (rRMSEs). For both model-predicted data and experimental ground truth, the key values of the IA and RCIA in the sagittal plane and frontal plane were obtained [1], while independent t-tests were used to identify the between-group effects in all calculated variables. Sensitivity, specificity and Pearson's r for effect sizes between model-predicted data and experimental ground truth were used to quantify the test validity of each proposed model.

RESULTS AND DISCUSSION

All proposed models gave mean rRMSEs below 5.62%, 6.75%, 9.64%, and 6.84%, respectively (Table 1). Among the models, the Bi-GRU model performed the lowest prediction error in all predicted balance variables. Compared to experimental ground truth, similar between-group effects were also obtained using the Bi-GRU model-predicted data (Table 1). The LSTM models showed decreased sensitivity, while the uni-directional model showed decreased specificity. For the between-group effect sizes, the Bi-GRU model also performed a strong correlation with the experimental ground truth as compared to other models (Table 1).

CONCLUSION

This study was the first in the literature to investigate the test validity of RNN models for predicting whole-body balance variables during gait based on a single waist worn IMU. The results showed that the proposed BiGRU model was shown to have high accuracy with reasonable test validity, leading to an excellent potential for real-life monitoring of dynamic balance in older people with fall risks.

REFERENCES

[1] Hong, S.W., et al. *Gait Posture* **42(4)**: 523-528, 2015.
[2] Choi, A., et al. *Sensors* **19(13)**: 2974, 2019.

Table 1: Means (standard deviations) of rRMSEs of the inclination angles (IAs) and rate of change of IAs (RCIAs) in the sagittal and frontal planes and sensitivity, specificity and Pearson's r for effect sizes for the four RNN models in the statistical comparisons between the older and young groups when compared with the statistical results of the experimentally measured data.

Variables	UniLSTM	BiLSTM	UniGRU	BiGRU
		rRMSEs		
Sagittal IA (%)	5.38 (1.47)	5.62 (1.90)	5.34 (1.16)	4.84 (1.49)
Frontal IA (%)	6.75 (3.47)	6.57 (3.17)	6.53 (3.33)	5.15 (1.86)
Sagittal RCIA (%)	9.23 (2.56)	9.64 (2.81)	9.43 (2.24)	8.90 (2.91)
Frontal RCIA (%)	6.57 (2.27)	6.84 (2.67)	6.46 (1.88)	6.05 (2.25)
		Test Validity		
Sensitivity (%)	0.00	33.33	100.00	100.00
Specificity (%)	91.11	100.00	82.22	100.00
Pearson's r for Effect Sizes	0.28	0.48	0.47	0.65

ANTICIPATORY WHOLE-BODY BALANCE CONTROL IN THE ELDERLY FOR CROSSING OBSTACLES OF DIFFERENT HEIGHTS

Ju Yang Tiong[1], Yi-Chen Wu[1], Cheng-Hao Yu[1], Yi-Ling Lu[1,2], Kuan-Wen Wu[3,4], Ting-Ming Wang[3,4] and Tung-Wu Lu[1,4]

[1] Department of Biomedical Engineering, National Taiwan University, Taiwan
[2] Department of Ophthalmology, Cheng Hsin General Hospital, Taiwan
[3] Department of Orthopaedic Surgery, National Taiwan University Hospital, Taiwan
[4] Department of Orthopaedic Surgery, School of Medicine, National Taiwan University, Taiwan
Email: twlu@ntu.edu.tw

INTRODUCTION

Obstacle-crossing impairs balance and increases the riskof falls in the elderly. Inadequate control of the locomotor system may lead to body imbalance, which could cause tripping over obstacles. Previous studies have shown that older people used smaller medial COM–COP motions with increased toe-obstacle clearance to cross the obstacle, suggesting that older people adopted a conservative approach for prioritising whole-body stability during obstacle negotiation [1]. For a successful obstacle-crossing, necessary anticipatory postural adjustments (APA) are required for the maintenance of the body's balance before stepping over an obstacle. However, it remains unclear what role APA adopted by the elderly play in obstacle avoidance. Understanding the mechanisms ofthe increased incidence of trip-related falls in older people may be contributed by identifying the effects of APA on whole-body dynamic stability for obstacle-crossing. Therefore, the purpose of the current study was to identify the anticipatory whole-body balance control for obstacle-crossing in older people, in terms ofCOM-COP inclination angles (IAs) and their rates of change (RCIAs) [2].

METHODS

Seventeen healthy older adults walked at their preferred pace under four test conditions, namely on an unobstructed walkway (level walking, LW) and an obstructed walkway (obstacle-crossing, OC) with obstacles of three heights (i.e., 10%, 20%, and 30% of the subject's leg length). For the OC conditions, the transferring cycle (TC) was defined as the gait cycle last before the leading toe-off during obstacle-crossing. Data for two complete gait cycles in each test conditionwere obtained for each subject. The body's COMposition was calculated as the weighted sum of the positions of the COM's of all the body segments using the marker data and segmental inertial properties. The COP position was calculated using forces and momentsmeasured from the forceplates. The whole-body balance control was quantified by inclination angles (IAs) of the line joining the body's COM and COP, andtheir rates of change of IA (RCIAs) [2]. For all calculated variables, paired t-tests were used for comparisons between the LW condition and each OC condition at a significance level of $\alpha=0.05$.

RESULTS AND DISCUSSION

The Older group showed a different COM-COP control strategy during OC conditions as compared to LW condition walking (Fig 1). Compared with the LW condition, significant statistical differences were found even during the initiation phase of the transferring cycle in the sagittal plane during OC conditions. A recent study has shown that young adults perform differentCOM-COP control strategies during OC conditions only during tDLS. The current results suggested that the order adults altered their anticipatory whole-body balance control for more room to control the swing foot with sufficient foot clearance for obstacle crossing.
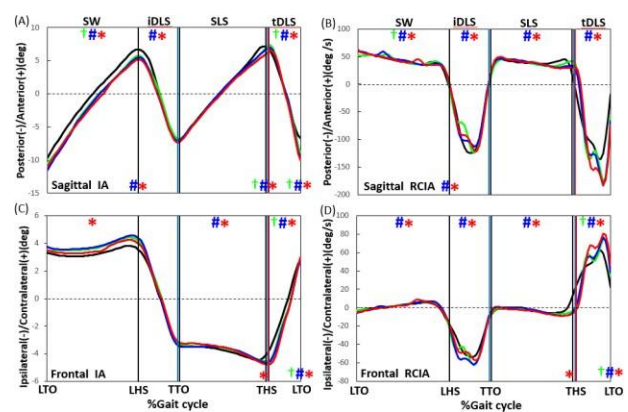
Figure 1 Ensemble-averaged curves of COM-COP inclination angles (IAs) and their rates of change (RCIAs) in the sagittal and frontal planes during the transferring cycle for level walking condition (Black line) and obstacle-crossing condition with obstacles of 10%LL(Green line), 20%LL (Blue line) and 30%LL (Red line). LTO: leading toe-off; LHS: leading heel-strike; TTO: trailing toe-off; THS:trailing heel-strike; SLS: single limb support; iDLS: initial double limb support; SW: swing; tDLS: terminal double limb support. (†: 10%LL significantly different from LW; #: 20%LL significantly different from LW; *: 30%LL significantly different from LW.)

CONCLUSIONS

The current study was the first in the literature to identify the effects of APA on whole-body balancecontrol for obstacle-crossing in the elderly. The results suggested that the elderly altered COM-COP control strategies for crossing obstacles of differentheights - even during the initiation phase of the transferring cycle – that may be considered an anticipatory preparation for maintaining whole-bodybalance during obstacle-crossing.

REFERENCES

[1] Chen, H. L., & Lu, T. W. *Gait Posture* **23(1)**: 69-77, 2006.
[2] Lee, H. J., & Chou, L. S. *Arch. Phys. M.* **87(4)**: 569-575, 2005.

PATTERNS AND STABILITY OF INTER-JOINT COORDINATION FOR PATIENTS WITH AMNESTIC MILD COGNITIVE IMPAIRMENT DURING OBSTACLE CROSSING

Shiuan-Huei Lu [1], Yi-Chun Kuan [1,2], Yu-Lin Tsai [1] and Tung-Wu Lu [1]

[1] Department of Biomedical Engineering, National Taiwan University, Taipei, Taiwan, ROC.
[2] Department of Neurology, Taipei Medical University Shuang-Ho Hospital, New Taipei City, Taiwan, ROC.
Email: twlu@ntu.edu.tw

INTRODUCTION

Mild cognitive impairment (MCI) is a transitional stage between the expected cognitive decline of normal ageing and the more serious cognitive decline of dementia. Obstacle-crossing is a complex motor task, requiring precise end-point control while maintaining body balance via highly coordinated joint movements. Previous clinical studies on MCI have found altered temporal-spatial parameters [1] and joint kinematics during obstacle negotiation [2]. However, no studies investigated the inter-joint coordination to provide insights into the essential timing and sequencing of neuromuscular system control, and the variability of coordination for patients with MCI. The purpose of this study was to identify the patterns and stability of the inter-joint coordination of the lower extremities in the patient with MCI during obstacle-crossing.

METHODS

Twelve patients with aMCI and twelve healthy adults were recruited in the current study. Each subject walked and crossed a height-adjustable obstacle at a self-selected pace. Phase plots of normalized angular velocities (x') against normalized angular displacements (x) in the sagittal plane for the hip, knee, and ankle were measured and calculate the phase angles. The continuous relative phases (CRP) of the hip-knee and knee-ankle coordination of the leading limb were calculated by subtracting the phase angle of the distal joint from that of the proximal. Coefficients of multiple correlations (CMC) and root-mean-squared differences (RMSD) were used to quantify the similarities and differences in the magnitude and changes in the patterns of relative phases between the MCI and control groups. Deviation phase (DP) was also calculated for the standard deviation of each point on the ensemble curve over each crossing phases to identify the variability of the inter-joint coordination. A two-way mixed-design analysis of variance (ANOVA) was performed to analyse the effect of between-subjects and within-subjects (obstacle height) on all calculated variables.

RESULTS AND DISCUSSION

For the leading limb, MCI group altered the patterns and magnitudes of the hip-knee coordination over iDLS and knee-ankle coordination over swing and SLS phases, as indicated by the relatively low CMC values and high RMSD values (Fig. 1). The CMC values of the hip-knee CRP curves between the MCI and Control groups over whole crossing cycle, tDLS, swing and SLS phases were all greater than 0.907 for all obstacle-height conditions, but those over the iDLS were less than 0.858. The between-group RMSD values of the hip-knee CRP curves ranged from 1.8 to 3.9

over Swing and SLS, while the knee-ankle RMSD values greater than 15.0 were found during almost the whole crossing cycle. However, the MCI group showed decreased variability of the inter-joint coordination of the lower extremity during leading limb crossing, especially over weight-transfer.
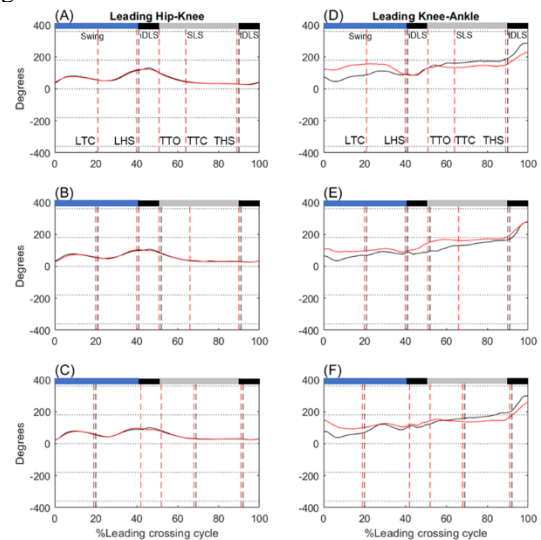
Figure 1 Ensemble-averaged relative phase angles of the leading hip-knee coordination when crossing obstacles of (A) 10%, (B) 20%, and (C) 30% of leg length for the MCI (red lines) and Control (black lines) groups. Corresponding plots for the leading knee-ankle coordination are given in (D), (E), and (F). (Black horizontal bar: initial or terminal double-limb support; Gray horizontal bar: single-limb support; Blue horizontal bar: swing phase; LTC: leading toe-crossing; LHS: leading heel-strike; TTO: trailing toe-off; TTC: trailing toe-crossing; THS: trailing heel-strike.)

CONCLUSION

In the current study, the MCI group changed their patterns of inter-joint coordination, but showed the reduced variability of the swing hip-knee coordination during trailing-crossing, a major difference from the healthy controls. The results of the current study indicate that MCI with limited ability of attention, memory and executive functions to have the stability strategy regarding the movement control of the lower extremities when executing the repeated movement, for the leading swing-limb over weight-transfer during obstacle-crossing.

ACKNOWLEDGEMENT

REFERENCES
[1] Robinovitch SN et al. *The Lancet* **381**: 47-54, 2013.
[2] Lu SH et al. *Front Aging Neurosci* **14**: 56-62, 2022

COORDINATION STABILITY ON THE BODY'S CENTRE OF MASS MOTION RELATIVE TO THE CENTRE OF PRESSURE DURING WALKING: FROM TODDLERHOOD TO ADULTHOOD

Chia-Tung Chung[1], Cheng-Hao Yu[1], Shiuan-Huei Lu[1] and Tung-Wu Lu[1]

[1] Department of Biomedical Engineering, National Taiwan University, Taipei, Taiwan.

Email: twlu@ntu.edu.tw

INTRODUCTION

Independent walking is a complex functional activity requiring adequate coordination skills to maintain balance. For typically developing children, the ability of balance control is improved with age, leading to decreased postural sway with more stable motions between the body's centre of mass (COM) relative to the centre of pressure (COP) [1]. Previous studies have shown that toddlers adopt a wide base of support with decreased step length during gait for preventing stumbling and maintaining dynamic stability [2]. As they mature, their ability to balance is increased to maintain their body weight over the supporting limb [2]. However, it remains unclear how the coordination ability of whole-body balance control while walking develops with age. Therefore, the current study aimed to quantify the age effects on the COM-COP inter-plane coordination from toddlerhood to adulthood during double limb support (DLS) and single limb support (SLS).

METHODS

Twelve toddlers, twelve children, twelve adolescents and twelve youth adults participated in the current study. Each subject wearing 50 skin markers walked on a 10-meter walkway while the ground reaction forces were measured with four forceplates and marker data by a motion capture system. The body's COM position was calculated as the weighted sum of the positions of the COM's of all the body segments using the marker data and segmental inertial properties. The COP position was calculated using forces and moments measured from the forceplates. These data were used to calculate the COM-COP inclination angles (IA) and their rates of change (RCIAs) in both sagittal and frontal planes [3]. Phase plots of normalised IA and RCIA for frontal and sagittal planes were generated to give the phase angles (Fig. 1A). Continuous relative phase (CRP) was obtained by subtracting the frontal phase angles from the sagittal angles. The deviation phase (DP) of the CRP curves described the variability of the coordination. A lower DP value indicates a smaller variability. For the DP values during both single-limb support (SLS) and double-limb support (DLS), a one-way analysis of variance (ANOVA) was used to study the between-group (age) effect. A post hoc analysis was further applied when a significant age effect was found, using an independent t-test for the comparison between each group. A p-value of ≤ 0.05 was considered statistically significant for all tests.

RESULTS AND DISCUSSION

During DLS, the toddler group showed significantly greater coordination variability as compared to the children, adolescent and adult groups (Fig 1B). During DLS, coordination variability showed statistically significant differences among all four groups, with DP values decreasing with age (Fig 1C). The results showed that the development of COM-COP inter-plane coordination during gait might be ongoing throughout toddlerhood to adulthood, while changes in coordination variability during DLS can be considered a staged milestone in gait maturation.
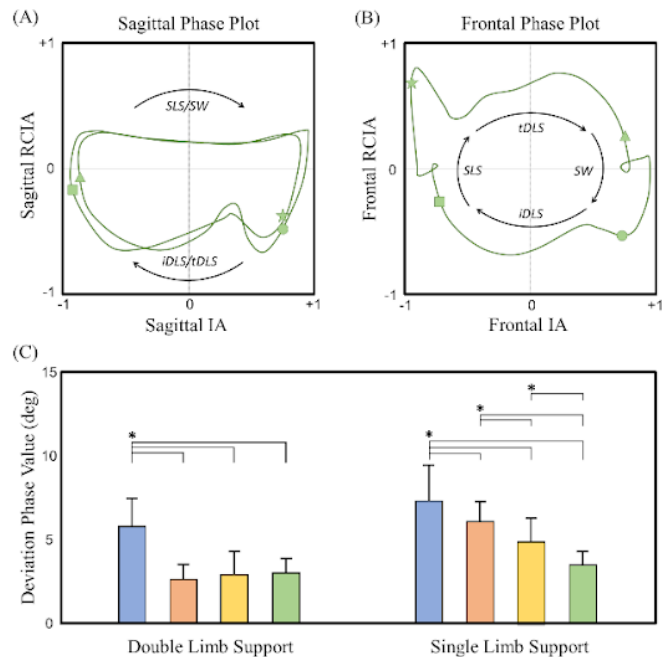
Fig. 1: The ensemble average of the normalised IA and RCIA in the phase plots for both (A) sagittal and (B) frontal planes in the adult group were shown, while (C) means (standard deviations) of the DP values in the toddler (blue bar), children (orange bar), adolescent (yellow bar) and adult (green bar) groups during gait were also reported. SLS: single limb support; iDLS: initial double limb support; SW: swing; tDLS: terminal double limb support. *: P < 0.05.

CONCLUSION

The current study was the first in the literature to identify the development of the coordination ability on whole-body balance control during gait. The results suggested that the development of COM-COP inter-plane coordination during gait may continue from early childhood to adulthood.

REFERENCES

[1] Ivanenko, Y. P., et al. *Exerc. Sport Sci. Rev.* **35**(2), 67-73, 2007.

[2] Sutherland, D. H., et al. *J. Bone Joint Surg. Am.* **62**(3), 336-353, 1980.

[3] Hong, S.W., et al. *Gait Posture* **42**(4): 523-528, 2015.

PREDICTION OF HUMAN COM TRAJECTORY WITH A SLIP MODEL BASED COMPLIANT LEG BIPED DURING WALKING AND JOGGING AT LOW SPEEDS

Paper ID281

Saptarshi Jana[1], Abhishek Gupta[1]

[1] Mechanical Engineering Department, Indian Institute of Technology Bombay, Mumbai, India.

Email: saptarshi.jana@iitb.ac.in

INTRODUCTION

The fundamental template of human walking and running is the spring-loaded inverted pendulum (SLIP) model [1]. The existing models make a trade-off between the lesser complexity of the model and the accuracy of results. This study explores the dynamics of a 2D SLIP model biped robot with two degrees of freedom to predict the center of mass (CoM) trajectory of periodic walking and jogging gaits. The study considers the vertical ground reaction force (vGRF) patterns as the distinguishing factor between these gaits. We introduce the initial leg compression as a model parameter and employ numerical optimization to obtain different gaits by adjusting parameters such as initial leg compression, spring stiffness, and touchdown angle, while gait speed serves as the output parameter.

METHODS

We consider walking/jogging gaits comprising two phases: a single stance during which one of the legs is in contact with the ground and an instantaneous double support phase. The swinging leg impacts the ground at a predefined angle. The equations of motion (EoM) have been determined using the Euler-Lagrange method, followed by a heel strike event. The transition from stance to swing and swing to stance occurs instantaneously during the heel strike. The initial compression of the leg, measured in terms of displacement from the static equilibrium position, is considered positive when measured above the equilibrium position (jogging) and negative when measured below (walking). In order to find a periodic gait, the error between two initial states of consecutive steps is minimized using the MATLAB optimization function *'fmincon'*. A feasible periodic gait is considered when the step cycle repeats at least 25 steps.

RESULTS AND DISCUSSION

For this study, we considered the body mass and touchdown length of the leg spring as constant. We found several stable periodic gaits at various speeds corresponding to double-peak vGRF (walking) and single-peak vGRF (jogging). During walking, solutions have been found for. The resultant locomotion speed varies between 0.38–0.75 m/s. The dynamics of jogging and walking are combined in this model. The CoM trajectory during movement oscillates sinusoidally, approximately around its landing height. The amplitude (maximum-minimum) found in the vertical CoM trajectory varies between 0.05–0.08 m during walking and between 0.08–0.10 m during jogging for the specified model parameters. In the literature, experimental data at low-speed ranges are not reported. However, these results show a qualitative match with those presented literature at higher speeds [2]. Note that in our case, the range of can be varied through variation of, whereas in reported SLIP models, this is a function of chosen spring stiffness.
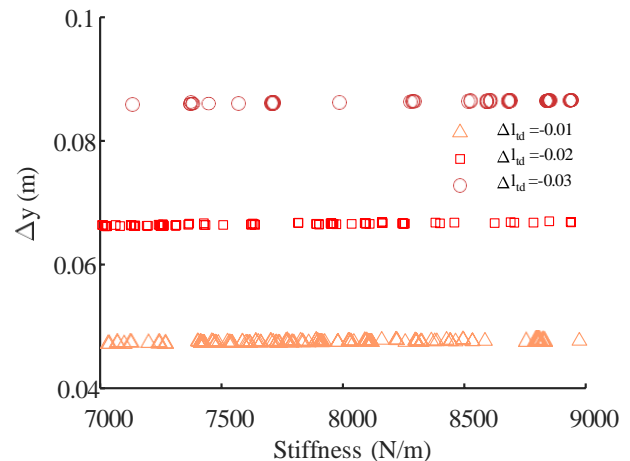
Figure 1 Walk: Impact of three different initial compression lengths () along with increasing stiffness () on maximum fluctuation in the oscillation of CoM in the sagittal plane during walking. Where Values related to different gait speeds for three different

CONCLUSION

The results highlight the significance of initial leg compression in predicting the CoM trajectory of walking and jogging gaits of human. This approach accurately captures the CoM trajectories for both walking and jogging, allowing additional control over CoM oscillation amplitude. In contrast to existing models, which incorporate an asymmetric single support phase and an aerial phase for jogging, the proposed approach achieves both slow walking and jogging gaits without significant changes in resulting gait speeds, presenting a unified framework for analyzing these locomotion patterns.

REFERENCES

[1] Geyer H et al. *Proc. R. Soc. B.* **273**, 2861–2867, 2006.

[2] Jung C et al. *J Biomech* **47:** 223–229, 2014.

GAIT EVENT DETECTION USING A SINGLE IMU IN ELECTROMECHANICAL KAFO: HEALTHY ADULT VS HEMIPLEGIC PATIENT

Sumin Yang, Seunghee Lee, Bummo Koo and ˙Youngho Kim
Department of Biomedical Engineering and Institute of Medical Engineering, Yonsei University, Wonju, Korea.
Email: younghokim@yonsei.ac.kr

INTRODUCTION

Gait analysis is important in assessing motor impairments and monitoring rehabilitation progress in individuals with lower limb pathologies. Patients with gait disorders use knee-ankle-foot orthoses (KAFOs) to improve their gait and be stable during gait. Gait analysis using a motion capture system in the laboratory while wearing KAFO has temporal and spatial difficulties. [1,2] Recently, a wearable device like an inertial measurement unit (IMU) was applied to gait analysis for convenience. In this study, a gait event detection algorithm using a single IMU placed on the thigh is developed and applied to healthy adults with and the hemiplegic patient wearing KAFO. Four gait events (initial contact(IC), opposite initial contact(OIC), toe off(TO), and opposite toe off(OTO)) were determined. The temporal gait parameters were calculated using detected events, and compared to the reference.

METHODS

One healthy adult and one hemiplegic patient were recruited for the study. (IRB: RERI-IRB-221208) Four force plates (AMTI, USA; 120Hz) were used to detect the reference gait events. Subjects walk 20 times wearing electro-mechanical KAFO and step every force plate during each trial. In the KAFO, an IMU sensor (EBIMU-9DOFV5; 100Hz) was embedded on the lateral surface of the thigh component.

The RMS of 3-axis angular velocities (gyroRMS) were calculated. Pitch angular velocity (gyroY) was low pass filtered by 3Hz (gyroY3). All signals were used to detect gait events. IC was determined by the median point of peak vertical acceleration and anterior-posterior acceleration. OTO was determined by the local peak of gyroY after IC. OIC was determined when gyroY3 is zero-crossed to negative. After gyroRMS was above the threshold, the peak point of gyroRMS was determined as TO. (Figure 1)

The difference (ms) between the reference and the detected event was calculated as an error. The error % was defined as follows:

$$Error\%(Gait\ Cycle\%) = \frac{Detected - True}{1\ Stride\ time} \times 100 \quad (1)$$

RESULTS AND DISCUSSION

The error % of healthy adult was $-0.12\% \pm 0.48\%$, $0.58\% \pm 0.73\%$, $1.50\% \pm 1.01\%$, and $-1.43\% \pm 4.09\%$ for IC, TO, OIC, and OTO, respectively. The error % of hemiplegic patient was $0.27\% \pm 0.37\%$, $-1.00\% \pm 1.10\%$, $1.09\% \pm 1.01\%$, and $-2.73\% \pm 1.57\%$, for IC, TO, OIC, and OTO, respectively. (Table 1).

The detection of OTO showed the largest error rate for hemiplegic patient. Our results, obtained by attaching an IMU to the tibia, align with previous studies that detected IC (Initial Contact) and TO (Toe-Off) and reported an average error rate of 2-3% for both healthy individuals and amputees. [3]
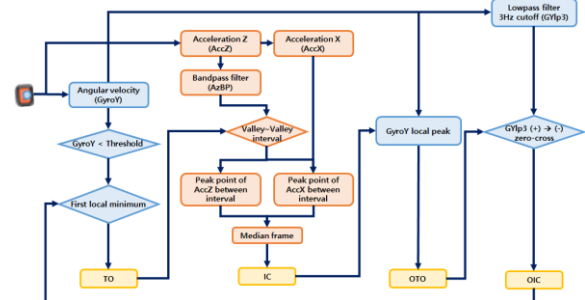
Figure 1 The flow chart of the gait event detection algorithm

CONCLUSION

The gait event detection algorithm was developed to monitor the temporal gait parameters of the subjects wearing electromechanical KAFO with a single IMU. It was applied to a healthy adult and one hemiplegic patient. The result showed that the error in detecting main gait events was relatively small, which suggested our algorithm was satisfied to monitor gait parameters. The error was larger for the hemiplegic patients than for the normal subjects, especially in OIC. Further studies will be made with additional experiments of more patients.

ACKNOWLEDGEMENT

REFERENCES

[1] Zhao H et al. *ICSAI. IEEE* **105**: 622-626, 2017.
[2] Manz S et al. *Clin Biomech* 105988, 2023.
[3] Ledoux ED. et al. *IEEE. Trans. Biomed. Eng.* **65.12**: 2704- 2712, 2018.

Table 1 Error rate of healthy adults and the hemiplegic patient.

Error rate (%)	IC	TO	OIC	OTO
Healthy adult	-0.12 ± 0.48	0.58 ± 0.73	1.50 ± 1.01	-1.43 ± 4.09
Hemiplegic patient	0.27 ± 0.37	-1.00 ± 1.10	1.09 ± 1.01	-2.73 ± 1.57

WI-FI-BASED HUMAN ACTIVITY RECOGNITION AND QUANTIFICATION FOR CONTINUOUS MONITORING OF MOTOR FUNCTIONS IN PARKINSON'S DISEASE

Chi-Lun Lin[1], Shih-Yuan Chen[1]

[1] Department of Mechanical Engineering, National Cheng Kung University, Tainan, Taiwan.

Email: linc@ncku.edu.tw

INTRODUCTION

Parkinson's disease (PD) is a neurodegenerative disorder that worsens over time, with significant fluctuations throughout the day, making accurate drug treatment difficult. This study proposes a human activity recognition (HAR) method for patients with PD using commodity Wi-Fi devices and deep learning techniques. The aim is to continuously detect PD-related movements and provide quantitative information on motor fluctuations and drug efficacy for physicians to prescribe more precisely.

METHODS

The proposed system gathers Wi-Fi channel state information from two antennas of a receiver and calculates the phase of the CSI ratio. The results are transformed into grayscale CSI images with enhanced contrast. We conducted experiments to obtain CSI images of different daily activities and activities related to PD and trained a convolutional neural network based on the VGG19 network. We created a computer algorithm that processes an input CSI image of recorded Wi-Fi signals over a long period and identifies specific activities. Our previously published methods [1,2] are used to quantify the data segment of the target activities for this study, which are walking and tremor.

For this study, we collected CSI data using a DELL P40G i8 laptop PC (Rx) with an Intel 5300 wireless NIC, three antennas, and Linux 802.11n CSI Tool. The Rx was connected to a D-Link DIR-853 router, which acted as the transmitter (Tx). We used a 2.4 GHz band and ping packets with a 200 Hz ping rate and 250 Hz packet sampling rate for data communication.

To collect training data for CNN, we designed four main activity categories. These included walking (1-2 steps per minute), simulated hand rest tremors, body movements (such as head nodding, handshaking, scratching, and leg kicking), and static postures (including sitting and standing). All experiments were conducted in a 6.2x4.2 square meter discussion room where we recorded CSI and video simultaneously. We had three healthy participants, aged 22-25 years, with heights ranging from 169-181 cm and weights ranging from 52-90 kg.

RESULTS AND DISCUSSION

Our system's recognition performance was tested using 50-second CSI sequences. During each experiment, participants completed five 10-second activities in a specific order: walking randomly, sitting in the nearest chair, performing tremors, sitting quietly in the same chair, and performing a random body movement.

After comparing the recorded footage with the labeled data, we found that errors ranged from 1 to 6 s in the ten experiments, resulting in an average accuracy of 93.82%. Walking had the most significant proportion of errors, followed by static postures, tremors, and body movements.

In additional ten experiments conducted in another room, the proposed system achieved an average accuracy of 95.19% when recognizing and segmenting activities performed. The two rooms had no significant difference ($p=0.457$), indicating that the proposed system could adapt to environmental changes.

To evaluate person generalization, we conducted ten experiments of 50 s each with five new participants, leading to an average accuracy of 91.92%. We also conducted experiments using two new Wi-Fi arrangements, resulting in average accuracies of 94.25% and 94.12%, respectively. The differences between the three Wi-Fi arrangements (four-corner, linear, single-point) were within 0.5%.

For a long-term test, we designed a 30-minute action script containing a sequence of activities (15 sessions of 2 minutes each) and instructions on where and what activities should be performed. The results showed an average accuracy of 94.74%, similar to the outcome obtained in the 50-second experiments conducted earlier in this study.

The processing time on a computer with an Intel i7-4790 CPU and an NVIDIA Quadro RTX4000 GPU was 155.43 seconds for converting CSI of 1,844 s to images and 1205.64 s for recognizing the types of produced images and dividing them into segments of individual activities. In other words, the total time to recognize an activity per second was 0.65 seconds. Therefore, the proposed system could continuously perform real-time activity recognition. Please see Table 1 for a summary.

Table 1 Performance summary of the proposed system

Test	Average Accuracy (%)
Basic	93.82
New Environment	95.19 ($p=0.457$)
New Persons	91.92
New Wi-Fi Arrangements	94.12–94.25 ($p=0.757$–0.871)
Long-term Test	94.74

CONCLUSION

The study proved that the proposed system could precisely identify PD-related activities using Wi-Fi CSI. It can also adjust to new usage conditions and has the potential for real-time health monitoring applications.

REFERENCES

[1] Hsu H-H et al. *Bioengineering* **10(2)**: 228, 2023.
[2] Chang W-J et al. *IEEE IOT* **9(11)**: 8935-8942, 2022.

EXPLORING THE FEASIBILITY OF USING REINFORCEMENT LEARNING FOR SHOULDER JOINT MOMENT ESTIMATION

Muhammad Fairuz Abdul Jalal [1,2], Hazreen Haizi Harith [2,3*]

[1] Department of Mechanical Engineering, College of Engineering, Universiti Tenaga Nasional, Kajang, Malaysia.
[2] Department of Biological and Agricultural Engineering, Faculty of Engineering, Universiti Putra Malaysia, Serdang, Malaysia.
[3] Malaysian Research Institute on Ageing (MyAgeing), Universiti Putra Malaysia, Serdang, Malaysia
Email: hazreen@upm.edu.my

INTRODUCTION

Musculoskeletal modelling tools are often used to estimate joint moment [1]. Joint moment is estimated as it cannot be measured directly during motion. It could serve as a controlling input to human-machine interface systems, such as exoskeletons and prosthetics designed for rehabilitation [2–4]. It is proposed that machine learning approaches can enable near real-time joint moment estimation, important for quick feedback required in rehabilitation and assistive robotics applications [5]. Recently, reinforcement learning has been proposed to estimate joint moments for 2- dimensional joints [3]. This study aims to explore the feasibility of reinforcement learning (RL) for estimating joint moments in a 3-dimensional joint, i.e. the shoulder. In this study, initial results indicating the feasibility of using an RL agent to estimate torque during shoulder abduction-adduction is presented.

METHODS

The Reinforcement Learning (RL) Framework. *Modelling Environment.* The RL framework was developed using the Reinforcement Learning Toolbox in MATLAB, comprising (i) an RL agent that is trained to estimate shoulder torque that produces the same motion as the input data, (ii) measured joint kinematics as the input data, (iii) a reward function to guide the agent's torque estimation, (iv) a set of observation data to partly determine the agent's next step, and (v) an upper limb kinetic model developed in Simulink that moves based on the estimated torque (Figure 1). The observation data for the agent consists of subject- specific anthropometry, simulated shoulder girdle kinematics (previous timestep), joint moment (previous timestep), simulated and measured joint kinematics (7 previous timesteps). The kinetic model can be customised for each participant based on anthropometric data: body mass, stature height, shoulder width and segmental length (upper arm, forearm and hand). *Model training.* A 90:10 training- testing split is adopted for model training and testing. The RL agent is trained to estimate joint moment using Trust Region Policy Optimization using 10s kinematics data. In this study, the agent was trained to estimate joint torque using during shoulder abduction-adduction. The root mean square error between measured and simulated data is used to indicate the ability of the model to reproduce measured shoulder kinematic.

Training and Testing Dataset. Healthy female elderly participants from Klang Valley were recruited with the approval of the Ethics Committee for Research Involving Human Subjects of Universiti Putra Malaysia. The upper limb anthropometry and joint kinematics were collected at the Malaysian Research Institute on Ageing, Universiti Putra Malaysia. Three shoulder movements were recorded, involving the motion of the right arm while the elbow was kept flexed at 90° at a (i) self-selected speed abduction-adduction, (ii) self-selected speed horizontal abduction-adduction, and (iii) self-selected movement at varied speed ranges. Each participant

performed five trials for 30 seconds and rested between trials. Joint kinematics data were collected using Wave Track inertial motion unit sensors system (Cometa Systems, Italy) at a sampling rate of 2000 Hz. The datasets were used for training, and two datasets were used for testing.

RESULTS AND DISCUSSION
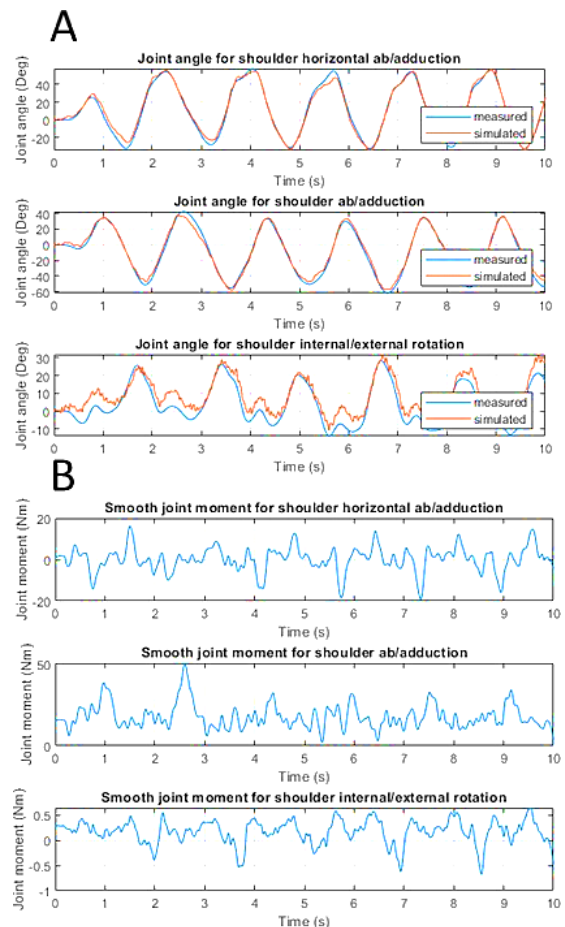
Figure 1 (A) A comparison between measured and simulated shoulder motion by an RL agent trained using shoulder abduction-adduction data. The overall difference between measured and simulation motion is more obvious during internal-external rotaiton compared to during abduction-adduction and horizontal abduction- dduction. (B) The corresponding joint moment for each shoulder's range of motion.

For this study, the RL agent was trained to estimate shoulder torque during shoulder abduction and adduction. Figure 1 (A) shows the measured and estimated shoulder kinematics for an RL agent that was trained using shoulder abduction-adduction kinematic data. The average RMSE during the 10s simulation was 3.47° for horizontal abduction-adduction, 4.10° for abduction-adduction and 6.0° for internal-external rotation.

CONCLUSION

Based on the relatively low RMSE values, reinforcement learning may be feasible for estimating joint moment in near real-time. However, the agent's performance can only be assessed when the agent is trained and tested for the complete shoulder's range of motion**.**

ACKNOWLEDGEMENT

REFERENCES

[1] Ajay S et al. *PLoS Comput Biol* **14**: e1006223, 2018
[2] Dustin LC et al. *J Biomech* **49**: 3901-3907, 2016.
[3] Wen W et al. *J Biomech Eng* **143**: 1-9, 2021.
[4] Gian MG et al. *IEEE Trans Neural Syst Rehabil* **27**: 751-759, 2019.
[5] Jonathan C et al. *J Biomech* 134: 111020, 2022.

EXTENDED ABSTRACTS│ Sports Biomechanics

EXPLORING THE INFLUENCE OF FLEXIBILITY ON CARDIAC LOAD DURING EXERCISE IN OLDER ADULTS: A K-MEANS CLUSTERING ANALYSIS APPROACH

Chih-Chun Lin[1], Ting Hsuan Cho[2], Yu-Sheng Lin[3], Jenn-Jier James Lien[4], Li-Chieh Kuo[5], and Fong-Chin Su[2]

[1] Medical Device Innovation Center, National Cheng Kung University, Tainan, Taiwan.
[2] Department of Biomedical Engineering, National Cheng Kung University, Tainan, Taiwan
[3] Department of Mechanical Engineering, Southern Taiwan University of Science and Technology, Tainan, Taiwan
[4] Department of Computer Science and Information Engineering, National Cheng Kung University, Tainan, Taiwan.
[5] Department of Occupational Therapy, National Cheng Kung University, Tainan, Taiwan
Email: z9902026@email.ncku.edu.tw

INTRODUCTION

Considering the vulnerabilities associated with the musculoskeletal system in older adults, it is imperative to tailor their exercise programs through comprehensive fitness evaluations. Traditionally, physical training instructors have provided exercise prescriptions based on assessments of muscle strength and aerobic endurance. This study aims to investigate the impact of flexibility on cardiac load during exercise.

METHODS

Twenty females (age: 63.6±5.8 years) underwent physical fitness tests, including assessments of muscle strength (hand grip, sit-to-stand), aerobic endurance (2-minute step, 4-meter walk), and flexibility (back-stretch, sit reach), and then exercised using an exergame-integrated IoT-based ergometer system (EIoT-ergo) [1], with 1 upper arm and 1 lower arm training session per week for 11 weeks. EIoT-ergo, gradually increasing the workload, collected personal heart rate at 1 Hz. The personal cardiac load was defined as the percentage of maximum heart rate (%HRmax) [2]. K-means clustering was employed to analyze heterogeneity in physical fitness. Average cardiac loads in each session for each cluster were calculated and plotted to elucidate the effects of physical fitness on exercise-induced cardiac load.

RESULTS AND DISCUSSION

Cluster plot showed the inhomogeneous distribution of flexibility (Figure 1). Three cluster centroids in flexibility were all distributed on the (back stretch, sit reach) space: ([high] back stretch, [low] sit reach) for cluster1, ([low] back stretch, [middle] sit reach) for cluster 2 and ([high] back stretch, [high] sit reach) for cluster 3. In Figures 2 and 3, the data showed that individuals with higher flexibility (cluster 3) exhibited higher cardiac loads during both upper and lower arm exercise. Interestingly, no clear trend in cardiac loads was observed among individuals with different levels of muscle strength or aerobic endurance (data not shown).

CONCLUSION

This study highlights the significance of flexibility as a crucial parameter influencing cardiac loads during exercise, in addition to muscle strength and aerobic endurance. Understanding the role of flexibility in exercise-induced cardiac load can provide valuable insights for optimizing exercise prescriptions in older adults.
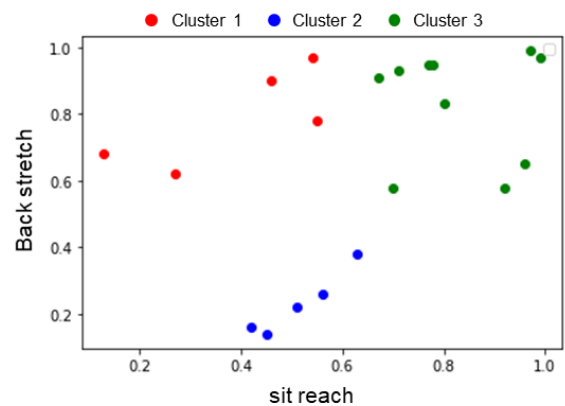
Figure 1 The distribution of three cluster centers in flexibility
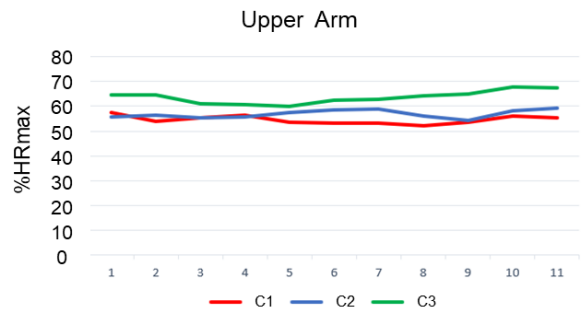
Figure 2 Cardiac loads of each cluster in upper arm exercise.
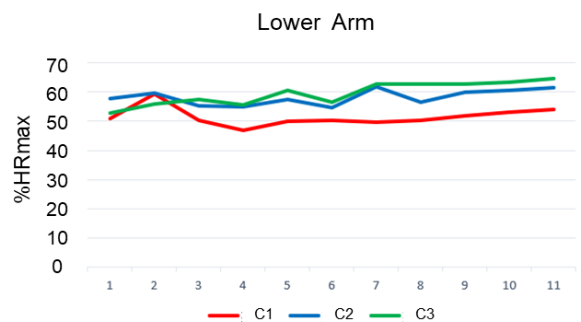
Figure 3 Cardiac loads of each cluster in lower arm exercise.

REFERENCES

[1] Lin CC et al. *Gerontology*. **6**: 1-15, 2023.
[2] Tanaka H et al. *J Am Coll Cardiol.* **37**(1):153-156, 2001

VISUALIZATION OF CONTACT STRESS ACTING ON PALM DURING BAT SWING

Daisuke Shimizu[1], Kazuhiko Sasagawa[1], Kazuhiro Fujisaki[1], and Kotaro Miura[1]

[1]Graduate School of Science and Technology, Hirosaki University, Hirosaki-shi,Japan
Email: h23ms521@hirasaki-u.ac.jp

INTRODUCTION

Recently, a thin and flexible sensor that can simultaneously measure contact pressure and shear stress acting on the contact interface has been developed [1]. In this study, a thin flexible sensor was attached directly on the palm, to measure the contact stress between palm and bat during a bat swing. This method allows us to obtain and visualize the change in the contact stress.

METHODS

The sensor consists of a stress-sensitive layer sandwiched between upper and lower electrodes. The thickness of the stress-sensitive layer changes with contact pressure, and the overlap area between the upper and lower electrodes changes with shear stress, resulting in a change in electrical resistance between them. Triaxial stress can be detected even though the sensor is a thin film. Copper-clad polyimide film was used for the upper and lower electrodes. Copper surface was covered with photoresist by spin coating method, and pattern mask was overlaid, and the photoresist was developed after exposure. Next, a thin copper film electrode pattern was formed by wet etching. each electrode was covered with a conductive carbon ink as a stress-sensitive layer using a screen-printing method. The upper and lower electrodes were then overlapped and covered with a polyurethane film. The measurement area was 2.56 mm × 2.56 mm. The thickness was 270 μm.

The contact pressures and shear stresses at eight positions on the palm as shown in Figure1 were measured at a sampling frequency of 100 Hz. The measured stresses were visualized by the software that displays the change in vector of stress. Eight sensors were attached on the palm of a 23-year-old male, who is a right-handed baseball player. The subject attempted hitting an imitated ball on the outside and inside corner. The direction of stress applied on the sensors is shown in Figure 1. In addition, video was taken along with the stress measurements to synchronize the contact stress measurements with the swing motion.

RESULTS AND DISCUSSION

Figure 1 shows an example of the change in measured stresses. The contact pressure and shear stress changes at measurement points 4 and 7 during the outside corner swing. The time points ①, ②, and ③ indicate the start, impact and end of the swing, respectively.

As shown in Figure 1, the contact pressure increased from the start of the swing to the impact. During the outside corner swing, the left hand pulled the bat. In this term, the shear stress in the positive direction of the X-axis was

detected on both hands. On the other hand, during the inside corner swing, the right hand pulled the bat and shear stress in the negative direction of the X-axis was detected on both hands. The absolute deviation values of shear stress on both hands in the case of the outside corner swing, was greater than that in case of the inside corner swing. In the outside corner swing, the bat grip part was tensioned by both hands, and in the inside corner swing, the grip was compressed.
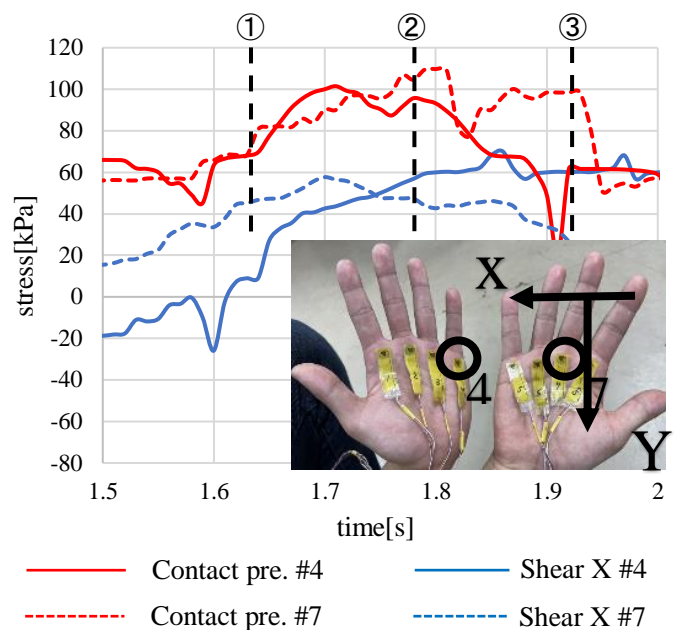
Figure 1 Stress change during bat swing in outside corner.

CONCLUSION

A thin flexible sensor capable of simultaneously measuring contact pressure and shear stress was fabricated and used to measure contact stress on the palm during a bat swing. The difference in stress change between the inside corner and outside corner swings was found, and the changes of stress in the palm were successfully visualized based on the measured stress data.

REFERENCES
[1] Kudo Y et al. *Mech Eng Letters*, **9**, 22-00309, 2023.

IMPACT OF ALTERED TORSIONAL STIFFNESS OF AIR PRESSURE SHOES ON ANKLE JOINT DURING TURNING IN LEVEL WALKING: A BIOMECHANICAL STUDY

Md Samsul Arefin[1,4], Hsiao-Feng Chieh[1,2], Chien-Ju Lin[1,2], Cheng-Feng Lin[3] and Fong-Chin Su[1]

[1] Department of Biomedical Engineering, [2] Medical Device Innovation Centre, [3] Department of Physical Therapy, National Cheng Kung University, Tainan, Taiwan.

[4] Department of Leather Engineering, Khulna University of Engineering & Technology, Khulna, Bangladesh.

Email: fcsu@ncku.edu.tw

INTRODUCTION

Turning in walking is essential to daily living, and turning steps comprise about 20–50% of steps in daily activities [1,2]. Side-step cutting generates rotational or twisting motion that exerts on the foot or shoe during shoe–ground contact [3,4]. Shoe torsional stiffness is an important design criterion for shoe design, which quantifies the resistance of twisting of a shoe about its long axis between the heel part and the toe part [5]. However, prior findings are not conclusive for a variety of shoe structures and directional changes in gait. The aim of this study was to investigate the effect of altered shoe torsional stiffness particularly on the ankle joint biomechanics during turning in level walking.

METHODS

Seventeen healthy (mean±SD; age 22.76 ± 2.63 years; height 173.06 ± 3.73 cm; body weight 64.69 ± 4.55 kg, BMI 21.61 ± 1.55 kg/m²) male recreation athletes took part in this study. Ethics board approved the protocol (NCKU HREC-E-110-456-2). Participants performed turning during level walking at self-selected speed with an angle of 45° with two shoe conditions. Kinematic and kinetic data were acquired synchronously using a 3D motion capture system (8 cameras, 100 Hz, Motion Analysis Corp), one force plate (Kistler, 1000 Hz). 19 reflective markers were attached to participants' lower extremity based on modified Helen-Hayes marker system. Torsional stiffness was measured in a materials testing system using the custom-made fixtures to hold the hind and forepart of the shoe. Biomechanical parameters were calculated by Orthotrack®6.6. gait analysis software. Custom-written codes (MATLAB, R2022a) used for further data analysis. Shoe conditions evaluated are unadjusted shoe (UAS) that is a specially designed shoe consist of air pressure chambers in sole construction, and adjusted shoe (AS) that is adjusted the sole by adding elastomeric spacers into the cavities formed by the air pressure chambers. Two shoe conditions were compared using paired t-tests for normal data and Wilcoxon signed rank tests performed for non-normal data with a significance level $\alpha=0.05$.

RESULTS

No significant differences were observed during turning in walking between UAS and AS shoe conditions for the peak force and impulse of ground reaction force (GRF) in the vertical, anterior-posterior & medio-lateral (ML) directions and for the twisting moment. But AS showed a trend of lower GRF impulse in ML direction compared to UAS. At ankle joint, there was no difference between shoe conditions for peak joint angles and moments, although a tendency of higher peak internal rotation angle, reduced inversion angle, increased peak external rotation moment and decreased peak eversion moment observed for AS compared to UAS. Some variables are presented in Table 1.

DISCUSSION AND CONCLUSION

GRF impulse governs athletes' velocity change [6]. Impact loading has been linked to lower limb injury risk [7] and hence a tendency of reduction in GRF impulse in ML direction in this study might decrease the injury risk due to sole modification and changed torsional stiffness. A tendency toward changed ankle joint moments might be an indicator of altered joint loading. However, although no significant differences observed in twisting moment, sole modification in shoes may be righteous in reducing the risk of injuries with increasing stability during turning in walking movements and more study needed to get additional insights.

REFERENCES

[1] Sedgman R et al. *ConfProc LaTrobeUni,* 1994.
[2] Glaister BC et al. *Gait Posture* **2**: 289-294, 2007.
[3] Andrews JR et al. *Am J Sports Med* **5**: 111-121, 1977.
[4] Cong Y et al. *J Biomech* **47**: 3799-3806, 2014
[5] Zifchock R et al. *Footwear Sci* **9**: 121-126, 2017.
[6] Hunter JP et al. *J Appl Biomech* **21**: 31-43, 2005
[7] Samaan CD et al. *J Sport&HealSci*.**3**:143-151, 2014.

Table 1: Mean ± standard deviation of peaks of ground reaction forces, twisting moments, and ankle joint angle and moments variables.

	UAS	AS	*p-value*
Impulse ML-GRF (BWs)	0.057 ± 0.018	0.055 ± 0.017	$p = 0.068$
Ankle Peak Internal Rotation Angle (°)	4.247 ± 7.957	4.730 ± 8.010	$p = 0.069$
Ankle Peak Inversion Angle (°)	$-2.907 \pm 2.689)$	-2.577 ± 2.576	$p = 0.086$
Ankle Peak External Rotation Moments (Nm/kg)	0.085 ± 0.060	0.094 ± 0.069	$p = 0.078$
Ankle Peak Eversion Moments (Nm/kg)	0.452 ± 0.177	0.430 ± 0.191	$p= 0.080$

Note: Angles: Internal rotation (+) ve/external rotation (-) ve, Moments: Internal rotation (-) ve/external rotation (+) ve, Inversion (-) ve/eversion (+) ve. Abbreviations: BWs, body weight second; Nm/kg, newton meter per kilogram.

INFLUENCE OF SUBJECTIVE EFFORT LEVEL ON BADMINTON SHOT ACCURACY AND MOVEMENT

Shimizu M.[1,2], Ozawa Y.[2], and Yamada H.[3]
[1]Graduate School of Physical Education, Tokai University, Hiratsuka, Japan
[2]Sport Medical Science Research Institute, Tokai University, Hiratsuka, Japan
[3]School of Physical Education, Tokai University, Hiratsuka, Japan
Email: bad.shmz@outlook.jp

INTRODUCTION
In sports, athletes adjust their performance according to the situation, and there are different strategies for them to adjust their movements according to their skill level [1,2]. The purpose of this study was to compare the accuracy and upper-limb movements of badminton backhand drives performed at different subjective effort levels and to identify the mechanisms of performance coordination.

METHODS
Seven male badminton players (height: 173.0 ± 4.3 cm, age: 19.6 ± 1.0 years old, experience: 10.6 ± 1.5 years) participated as the skilled group and 7 males (height: 172.8 ± 5.2 cm, age: 21.4 ± 0.7 years old) participated as the unskilled group. The unskilled group had no competitive training experience in badminton. The participants aimed at a 1.0 m square target placed at 3.0 m in front of them with backhand drive. The target was a 0.5 m square in the center. All the participants shot backhand drives with 60%, 70%, 80%, 90%, and 100% subjective effort. Ten trials were conducted for each subjective effort level. To reduce the influence of lower-limb and trunk movements, the subjects performed the backhand drive in a seated position. All the trials were recorded using 3D motion capture.
The elbow joint and forearm rotation angular velocities were calculated using musculoskeletal model analysis software (nMotion musculous ver. 1.58, nac Image Technology).
Shot accuracy was scored visually using the recorded video as follows: 0, missed shot; 1, did not hit the target; 2, hit the 1.0 m square; 3, hit 0.5 m square.

RESULTS AND DISCUSSION
There was no consistent tendency between the accuracy scores and subjective effort in either group, although the accuracy scores were higher in the skilled group than in the unskilled group (Table 1). In the skilled group, the elbow angular velocity increased with increasing subjective effort (Figure 1). In contrast, in the unskilled group, the angular velocity did not change with increasing subjective effort. In both groups, the angular velocity of the forearm rotation increased with increasing subjective effort.
There was no difference in the accuracy scores with increasing subjective effort. The backhand drives are shot in situations requiring high accuracy in the actual game; therefore, the accuracy was maintained at 60% or greater. The accuracy scores of the unskilled group were significantly lower than those of the skilled group because most unskilled participants did not have a control strategy for the backhand drive. Thus, the unskilled participants could not hit the target despite changing their subjective efforts. However, the unskilled group did not have greater elbow angular velocities than the skilled group because they reduced their elbow movement while trying to hit the target.
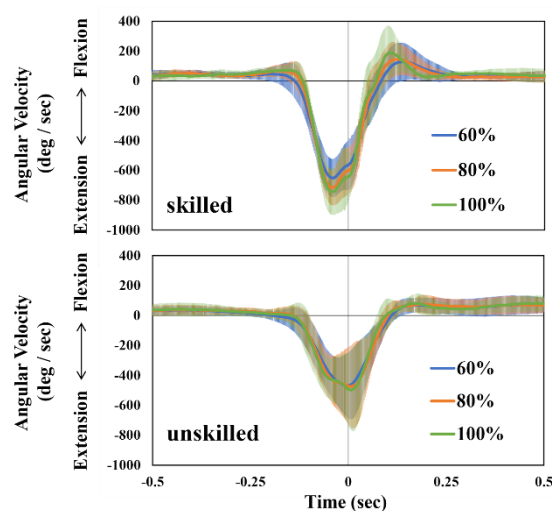
Figure 1. Angular velocity of elbow joint at 0.5 s before and after impact at 60%, 80%, and 100% subjective efforts.

CONCLUSION
In the present study, the participants performed badminton backhand drives at different subjective effort levels. The skilled group controlled backhand drives using elbow and forearm movements when they changed the shot of the subjective effort. In contrast, the unskilled group only performed forearm rotation. These results suggested that the skilled group achieved greater accuracy with multiple-joint coordination.

REFERENCES
[1] Ozawa Y et al. *Sports Biomech* **7**:1-18, 2022.
[2] Sakurai S et al. *J sports Sci* **18**:901-914, 2000.

Table 1: Accuracy scores for each subjective effort level.

	60%	70%	80%	90%	100%
Skilled	2.36 ± 0.37	2.29 ± 0.25	2.50 ± 0.19	2.51 ± 0.35	2.44 ± 0.10
Unskilled	1.40 ± 0.44	1.37 ± 0.41	1.37 ± 0.50	1.34 ± 0.43	1.43 ± 0.36

CHANGES IN MUSCLE ACTIVITY WHEN MANIPULATING THE DIFFICULTY OF THE SERVE

Furuya R.[1], Ozawa Y.[1], and Yamada H.[2]

[1] Sport Medical Science Research Institute, Tokai University, Hiratsuka, Japan

[2] School of Physical Education, Tokai University, Hiratsuka, Japan

Email: fr904644@tsc.u-tokai.ac.jp

INTRODUCTION

The serve is an important shot for winning the tennis game [1]. The skilled tennis player can shoot the serve with high velocity and smooth motion. However, unskilled tennis players cannot hit the ball with a smooth motion. In unfamiliar motion, human increase the co-contraction level of their antagonist muscle to fix the joints for reducing the flexibility as the difficulty of task execution increases [2]. It is thought the same phenomenon occur in the tennis serve in unskilled player, but there are no studies to clarify that. Therefore, the purpose of this experiment was to clarify the differences in muscle activity between unskilled and skilled tennis players when they shoot the serve at different levels of difficulty.

METHODS

The subjects were asked to shoot the 2 types of tennis serve, 1) normal serve; shoot the normal serve toward to target and 2) easy serve; hit the stationary ball which was hanging from the ceiling as the serve. The experiment was conducted in the laboratory. To acquire the electromyogram (EMG), the telemeter devices (Trigno wireless EMG system, Delsys, USA) were attached to the wrist flexor, extensor, Biceps brachii (BB), triceps brachii (TB), Anterior and posterior deltoid (AD and PD) . Each trial was repeated 2 times and randomized. The EMG data for each muscle were standardized as % EMG using the mean MVC value. The EMG was collected 200ms before and after impact that was detected based on racket acceleration which was captured high speed cameras. The moving root mean square (RMS) value was calculated 50ms interval in the 200 ms before and after impact duration for each shot. Each interval was denoted 1 to 8.

RESULTS AND DISCUSSION

The skilled player showed greater activity of the wrist flexor muscle activity before impact and greater activity of the extensor muscle after impact in both trials. In particular, the wrist flexor muscle activity before impact was greater in the normal serve. In the skilled players, the timing of peak activity in the TB was later than that of BB in the easy serve, but these peak appeared almost the same timing in the normal serve. For the shoulder muscles, PD activity was greater than AD activity in both trials and amounts of muscle activity are similar in the skilled players.

In unskilled players, wrist flexor activity was greater than the extensor muscles before impact in easy serve. But the

muscle activity difference was smaller than skilled players. There is a unskilled player who had the greater muscle activity in extensor than flexor. For the elbow muscles, in the unskilled players, TB activity was greater than BB activity during the analysis interval in the easy serve. Although similar muscle activity was observed in the normal serve, the amount of TB activity was less than that of the easy serve.

For the wrist muscles, the switch from flexor to extensor muscles was not clear in the unskilled players than skilled player. It is suggested that unskilled players trying to stable their racket angles by antagonist co-contraction in the wrist. In contrast, unskilled players showed greater elbow extensor muscle activity than flexor muscle activity. For that reason, unskilled players try to hit the ball with stable surface of racket face by extending their elbow whereas skilled player hit the serve using their wrist and elbow to increase the racket speed. Also, in the normal serve, subjects have to hit the ball thrown up by themselves with the racket and adjusting the position where they hit is more difficult than easy serve. Therefore, the lower TB activity was needed because the normal serve requires a more precise reaching motion to the hitting position (Fig.1).
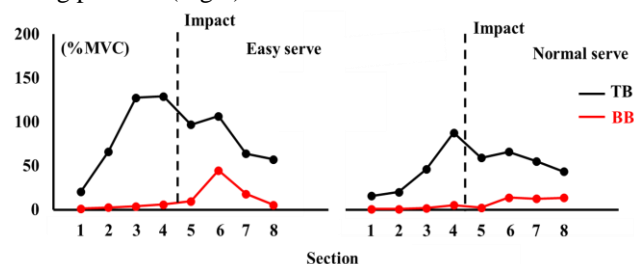
Figure 1 Elbow muscle activities for unskilled player.

CONCLUSION

The purpose of this research was to clarify the differences in muscle activity between unskilled and skilled players when they shot the serve at different levels of difficulty. Skilled player showed same muscle activity between the tasks, but unskilled players showed different type of muscle activities. These suggested that unskilled may better trying to know their own location of impact between racket and ball rather than practicing the serve swing.

REFERENCES

[1] Johnson C.D. et al. *Br J Sports Med* **40**(8): 696-699, 2006.

[2] Gribble PL et al. *J Neurophysiol* **89**(5):2396-2405, 2003.

MATHEMATICAL ESTIMATION OF MUSCLE CO-CONTRACTIONS DURING KNEE FLEXION

Masaru Higa[1], Yudai Nakagawa[1], Taiga Ishii[1] and Seita Inoue[1]

[1] Department of Mechanical Engineering, University of Hyogo, Himeji, Japan.

Email: higa@u-hyogo.ac.jp

INTRODUCTION

Joint moments can be calculated by inputting kinematics and external forces into a musculoskeletal computer model. This is called inverse dynamics. Then, individual muscle forces around the joint could be estimated from the calculated joint moments, however, we believe that there is a problem with this estimation method. Specifically, optimization procedures are performed to minimize the sum of squared or cubed muscle activities of all muscles. The minimization method eliminates co-contractions in the antagonist's muscles [1]. Although too much co-contraction in the antagonist's muscle is a waste of energy, a certain amount of co-contraction is necessary for stable joint motion. Therefore, the purpose of this study is to perform an exercise in which co-contraction is intentionally caused and to calculate the muscle activities with co-contraction.

METHODS

Knee joint flexions were repeated by one healthy adult subject. Reflective markers were attached to the lower limb and six infrared cameras were used to capture the marker trajectories. The sampling frequency was 100 Hz for the kinematics measurements. Surface EMG (Electromyography) was recorded by using pairs of surface electrodes applied over the belly of the muscles at a sampling frequency of 1 kHz. The main muscles involved in the knee flexion, rectus femoral and vastus medialis, biceps femoris and gastrocnemius muscles as antagonist muscles were selected. Finally, the EMG signals were normalized by the EMG values at maximum isometric contractions, and the root mean square with a moving average of 0.1 seconds was applied to the measured values. All measurements were repeated five times, and mean values were obtained. After the measurements, the motion data was inputted into a musculoskeletal computer model (OpenSim3.3), and muscle activities were estimated by the following optimization methods using MATLAB.

$$J_1 = min \sum_{i=0}^{n} [\omega_1 (\Delta\theta_{,i})^2 + \omega'_1 (a_{l,i})^2 + \omega''_1 (a_{s,i})^2$$
$$+ \omega'''_1 (a_{r,i})^2 + \omega''''_1 (a_{v,i})^2 + \omega'''''_1 (a_{g,i})^2] \qquad (1)$$

$$J_2 = min \sum_{i=0}^{n} [\omega_2 (\Delta\theta_{,i})^2 + \omega'_2 \frac{1}{(a_{l,i})^2} + \omega''_2 \frac{1}{(a_{s,i})^2}$$
$$+ \omega'''_2 \frac{1}{(a_{r,i})^2} + \omega''''_2 \frac{1}{(a_{v,i})^2} + \omega'''''_2 \frac{1}{(a_{g,i})^2}] \qquad (2)$$

where, ω_i: weighting factors, $\Delta\theta_i$: differences of the knee flexion between measurements and calculations, a_i: muscle activations. We used two cost functions; for minimizing the sum of squared muscle activations (J1) and maximizing them (J2).

RESULTS AND DISCUSSION

During the knee flexion, mean EMGs are shown in Fig.1 and Fig.2. When the exercise was performed in a relaxed manner, no co-contraction was observed, while co-contraction was observed when the exercise was intentionally co-contracted. Mathematical estimation of the EMGs using J2 function is shown in Fig.3.
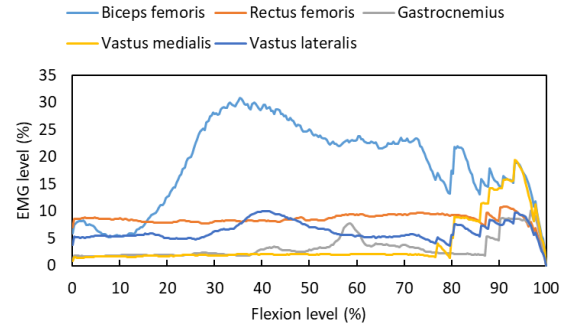
Figure 1 EMG levels when relaxed.
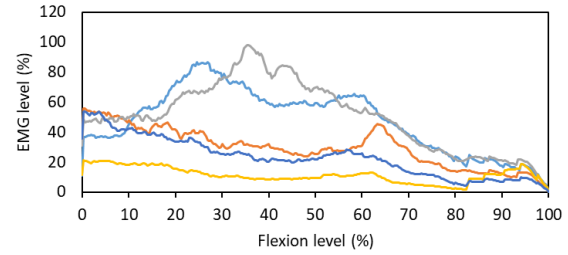
Figure 2 EMG levels when intentionally co-contracted.
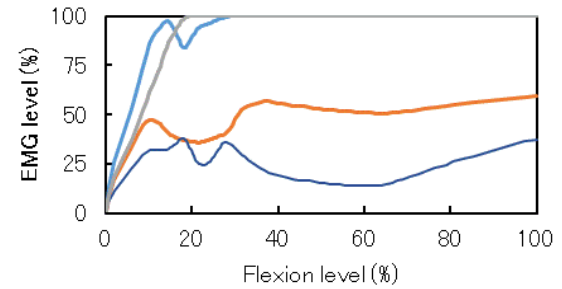
Figure 3 EMG estimated using the J2 function.

CONCLUSION

If the objective function is to minimize the sum of squared EMGs, co-contraction was not obtained, but when maximization was used as the objective function, co-contraction was computationally obtained. In fact, it is thought that the movement is performed between these two objective functions.

REFERENCES

[1] Higa M et al. *J Biomech Science Eng.,* **17**: (3), 22-00060, 202

MUSCLE EXERTION AROUND THE UPPER ARM DURING PLAYING TREMOLO ON MANDOLIN

Michihiko Fukunaga[1] and Ryoga Fujioka [2]

[1] Faculty of Science and Technology, Oita University, Oita, Japan.

[2] Division of Mechanical and Energy System Engineering, Oita University, Oita, Japan.

Email: fukunagam@oita-u.ac.jp

INTRODUCTION

Tremolo is the continuous production of the same note and is frequently used as a sustained note on plucked string instruments. It is a major technique in mandolin playing [1], however, there is no unified view on how to play and practice tremolo. Tremolo motion of the mandolin is a repetitive motion of downstroke and upstroke, mainly by flexion/extension of an elbow. We measured electromyograms around the elbow and discussed how the muscles were used, targeting a goal to establish teaching or practice methods.

METHODS

The test subject was an amateur mandolin player. He was asked to play tremolo in five ways listed below. All the conditions were played sul A, and conditions (a) to (d) were the tremolo of the same note using the open string. Conditions using a metronome assumed the basic training and playing melody assumed the actual performance.

(a) Fast tremolo with a metronome
(b) Slow tremolo with a metronome
(c) Fast tremolo without a metronome
(d) Slow tremolo without a metronome
(e) Playing melody without a metronome

The electromyograms of the biceps and triceps brachii were measured. We predicted each muscle would work during upstroke and downstroke respectively. First, the rectified and bandpass filtered EMG of the biceps between 0.1 to 6 Hz to divide the motion cycles. The EMGs of both muscles were then smoothed with a 60 Hz low-pass filter and the average of all cycles was calculated. These were normalized by the maximum voluntary contraction.

RESULTS AND DISCUSSION

The results were shown in Fig.1. The faster the tremolo motion, the more the muscle was exerted. The triceps did not exert during slow tremolo, which indicated the downstroke might be driven by a gravity force. EMG of the biceps was larger using a metronome, which would adjust the motion speed. Moreover, there showed the simultaneous contraction of antagonistic muscles during down stroke in case of fast tremolo with a metronome. In case of playing melody, the EMG of the triceps during downstroke was large. In summary, the tremolo of the same note without a metronome could be played without large muscle exertions, the biceps were exerted to control the tremolo speed, and the triceps might be exerted for some musical representation. Generally, it is better to be relaxed while performing, and it might be useful to recognize muscle control by comparing the tremolo with and without a metronome.
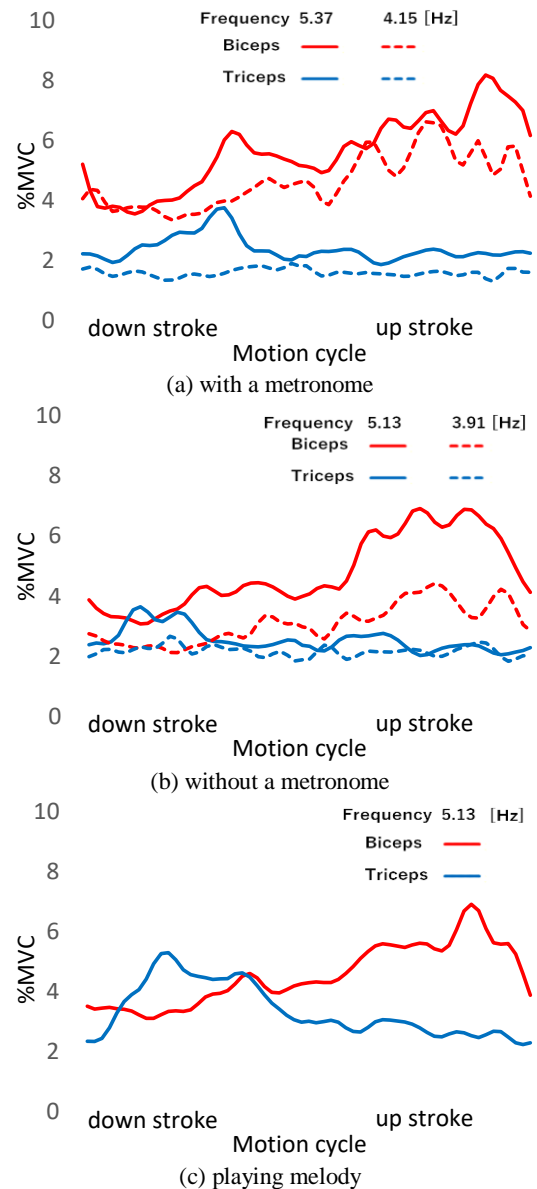
Figure 1 EMGs during the motion cycles of tremolo.

CONCLUSION

We measured the EMG of the biceps and triceps during playing tremolo on a mandolin. As a result, the tremolo of the same note was performed by the smaller muscle exertions.

ACKNOWLEDGEMENT

REFERENCES

[1] Yasui N et al. *J Acoust. Sci. & Tech.* **33**: 160-169, 2012.

DETERMINING THE OPTIMAL CLASSIFICATION FOR IMPROVING GRF ESTIMATION: GENDER, WEIGHT, AND SPEED ANALYSIS

Ji-Ting Lin[1], Ning Tung[1], Bing-Shiang Yang[1,2,*]

[1] Department of Mechanical Engineering, National Yang Ming Chiao Tung University, Hsinchu, Taiwan.
[2] Mechanical and Mechatronics Systems Research Labs, Industrial Technology Research Institute, Taiwan
Email: bsyang@nycu.edu.tw

INTRODUCTION

Ground Reaction Force (GRF) is an important indicator for evaluating pedestrian fatigue. Traditional methods are limited to lab settings. Therefore, our goal is to develop a portable sensor capable of measuring GRF in real life. Some studies have utilized IMUs to estimate GRF by measuring vertical acceleration ($\ddot{x}_v$) at either the 7th cervical vertebra (C7) [1] or the center of mass (CoM) [2] could achieve our goal. However, these studies have overlooked important factors like gender, weight, and walking speed, resulting in inconsistent estimation errors and limited practical applicability. Thus, our study aims to consider and compare the impact of these factors within the estimation model to overcome these limitations.

METHODS

Eight healthy participants (four males and four females) with an average age of 23.25 ± 0.46 years, were recruited. Used an instrumented treadmill (QQ-mill, Motekforce Link, Amsterdam, Netherlands) and an IMU (MTw Awinda, Xsens Technologies, USA) attached to C7, since the correlation of GRF and $\ddot{x}_v$ is the highest [1] . The procedure consisted of three test stages, each with different speeds (0.8, 1, and 1.2m/s) for three minutes.

Analysis procedure: The aim is to identify the optimal scaling function for GRF estimation.

The calculation process and parameters:

A. GRF_m: Measured GRF by treadmills; $\ddot{x}_{v,C7}(t)$: Vertical acceleration measured by IMU.
B. Classify data by gender, body weight and speed.
C. $\gamma(t)$(Scaling function for each gait cycle (gender: $\gamma_g(t)$, weight: $\gamma_w(t)$, speed: $\gamma_s(t)$))= $(GRF_m(t) - m_{total} \times g)/ (m_{total} \times \ddot{x}_{v,C7}(t))$.
D. $\gamma_T(t)$: Template $\gamma(t)$: the average line of all $\gamma(t)$ (including $\gamma_{g,T}(t)$, $\gamma_{w,T}(t)$, and $\gamma_{s,T}(t)$).
E. $GRF_{est,w/}$(Estimated GRF with $\gamma_T(t)$) = $m_{total} \times ((\gamma_{g,T}(t),\gamma_{w,T}(t),\gamma_{s,T}(t)) \times \ddot{x}_{v,C7} + g)$.
F. Compare the Normalized Root Mean Square Error (NRMSE) between $GRF_{est,w/}$ and GRF_m.
G. Identify the optimal $\gamma_T(t)$ and employ it as the final estimation modal.

To test for significant differences between conditions, we employed the Student t-test and set the level of statistical significance at p<0.05.

RESULTS AND DISCUSSION

Table 1 displays NRMSE results with and without $\gamma_T(t)$ across different categorizations, enabling us to evaluate their suitability. Comparing the categorizations, the speed category shows a significant error reduction (p<0.0001), closely approaching the gold standard. Furthermore, significant differences in errors without $\gamma_T(t)$ only occur within the speed category (fast, medium, slow) (p<0.01), suggesting that

combining different speeds in one model is inappropriate. Thus, the scaling function of the speed is optimal, yielding the model: $GRF_{est} = m_{total} \times (\gamma_{s,T} \times \ddot{x}_{v,C7} + g)$. By selecting the closest $\gamma_{s,T}(t)$ based on the subject's speed (Figure 1 right), it can be applied to the GRF estimation model, and the error differences within the speed classification to < 1%.

Table 1: NRMSE for GRF estimation among three categories.

		$GRF_{est,w/o}$	$GRF_{est,w/}$	Error reduction
Gender	Male	19.6±3.4%	14.0±4.6%	5.6%
	Female	18.8±2.7%	12.6±4.2%	6.2%
Body weight	Light	18.1±2.4%	11.5±3.9%	6.6%
	Med	19.7±3.0%	13.9±5.5%	5.8%
	Heavy	19.7±3.4%	13.5±4.4%	6.2%
Speed **	Slow	22.2±2.0%	11.6±3.1%	10.6%
	Normal	19.0±2.8%	12.6±4.3%	6.4%
	Fast	17.4±2.3%	11.3±3.7%	6.1%
Gold standard		-	9.3±4.0%	

$\gamma(t)$: Scaling function for each gait cycle; $GRF_{est,w/o}$: Estimated GRF without $\gamma_T(t) = m_{total} \times (\ddot{x}_{v,C7} + g)$; $GRF_{est,w/}$: Estimated GRF with $\gamma_T(t)$; *p<.05; **p<.01
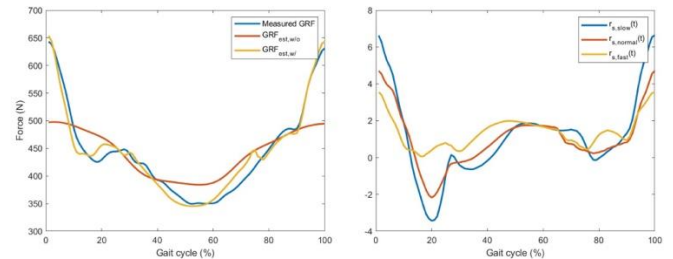
Figure 1 The left is GRF in a gait cycle (measured value, with and without $\gamma_T(t)$), the right is the $\gamma_T(t)$ for three different speeds.

CONCLUSION

This study found that speed plays a crucial role in reducing errors when estimating GRF (statistical power > 0.999). By incorporating the speed factor, the study improved the limitations of the original model, resulting in a consistent pattern in GRF estimation errors and better estimation of individual differences. These findings bring us closer to our target.

ACKNOWLEDGEMENT

REFERENCES

[1] Shahabpoor E., et al. J Biomech, 79, 2018.
[2] Refai. *IEEE Tran Neural Syst Rehabil Eng*, **28**(6),2020.

INFLUENCE OF FOOTWEAR ON MRI T2 RELAXATION TIME OF LOWER EXTREMITY MUSCLE IN ELITE RACE WALKERS: A CASE STUDY

Lee Rou You[1], Hiroaki Noro[3], Yohei Yamazaki[1,2], Keiichiro Hata[3] and Toshio Yanagiya [1,2]

[1] Graduate School of Health and Sports Science, Juntendo University, Chiba, Japan
[2] Institute of Health and Sports Science & Medicine, Juntendo University, Chiba, Japan
[3] Faculty of Health and Sports Science, Juntendo University, Chiba, Japan
Email: rouyoulee@gmail.com

INTRODUCTION

Race walking is one of the most regulated athletic events, that requires athletes to walk as fast as possible over long distance, while strictly adhering to specific motion restriction in order to comply with the rules set [1]. Previous studies have utilised motion analysis and electromyography to identify the primary muscle involved in race walking [2]. It is believed that muscle recruitment during race walking differs significantly from that observed during normal walking or distance running events. In recent years, race walkers have started to wear thick-soled shoes to increase their tolerance for fatigue and improve their walking pace with the assistance of the resilient midsole materials. Therefore, this study aims to identify the key active muscles during race walking and investigate the effects of wearing thicker-soled shoes on the distribution of muscle activities in the lower limb of elite representative walkers using T2-weighted magnetic resonance imaging (MRI) as a case study. This technique will provide us valuable insights into the extent of muscular fatigue.

METHODS

Two Japanese representative race walkers (age: 23 y, height: 167 cm and 174 cm; weight:52.0 kg and 58.5 kg; personal best record: 20km 1:21.21 and 20km 1:20.14) performed in treadmill race walking at 15 km·h^{-1} for a distance of 2 km under two shoes conditions (Table 1) in a random sequence. T2-weighted MRI scan was performed in semimembranosus (SM), semitendinosus (ST), bicep femoris long head (BFL), rectus femoris (RF), vastus lateralis (VL), vastus medialis (VM), vastus intermedius (VI), adductors (AD), sartorius (SA), gracilis (GR), medial gastrocnemius (MG), lateral gastrocnemius (LG), soleus (SOL) and tibialis anterior (TA) muscles before and immediately after race walking using 0.3-T scanner (AIRIS Hitachi Medical Japan). From the scan, transverse relaxation (T2) time of the right thigh and calf was calculated. The T2 value of each muscle in the thigh and calf were averaged over three images respectively.

Shoes Condition (sole)	Shoes Name	Mass (g)	Heel Stack (mm)	Toe to Heel (mm)
Thin	Mizuno Wave Cruise	191	24	3
Thick	Asics Metaracer	206	28	8

RESULTS AND DISCUSSION

Individual differences in muscle usage during race walking was observed from the result of T2 relaxation time. Subject A exhibited lower T2 values in the thigh, particularly in the VM, AD and SM muscles, while demonstrating a higher T2 value in the calf, specifically in the MG and SOL, compared to thin shoes (Figure 1). On the other hand, subject B exhibited minimal differences in T2 values between shoes conditions, with lower T2 values observed in SA muscles and higher T2 values in the GR muscles compared to thin shoes when compared to thin shoes. These results indicate that the muscles response to different shoes conditions vary individually. The rate of change in T2 was particularly high in AD, SM, TA and SOL muscles in both shoes condition. These findings suggest that race walker heavily rely on these muscles during race walking.
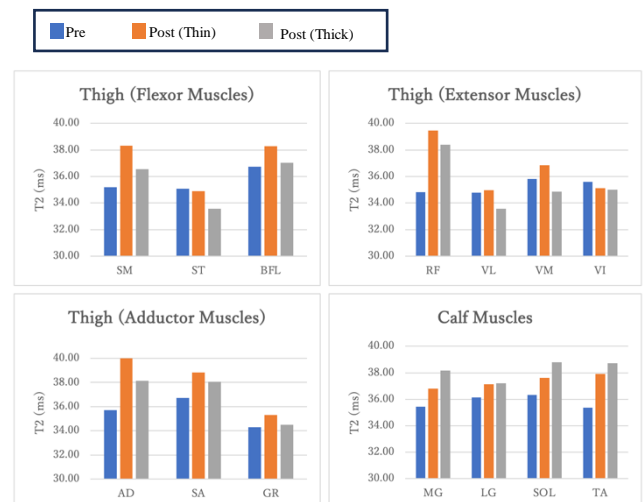
Figure 1 T2 value of each thigh and calf muscle before and after running with thin (orange) and thick (grey) shoes in subject A.

CONCLUSION

The observed individual differences in the muscle usage of the lower extremities among elite race walkers, as measured through the MRI T2 method, suggest that each athlete employs distinct muscle recruitment patterns to adapt to the restricted motion imposed by race walking regulations. In addition, the use of thicker sole shoes during race walking may induce changes in the distribution of muscle usage in the lower limb.

REFERENCES

[1] IAAF. *Competition Rules* 2012-2013, 2011.
[2] Hanley et al. *J Sports Science* **31**: 1222-1232, 2013.

A VALIDATION METHOD FOR ESTIMATING THE REACTION FORCE FROM THE ICE SURFACE DURING FIGURE SKATIHG JUMP MOVEMENTS

Yuse Hara[1], Kazunori Hase [2], Naoto Haraguchi[1], Tatsuki Koshio[1] and Takayoshi Takahashi[2]
[1] Graduate School of Systems Design, Tokyo Metropolitan University, Tokyo, Japan.
[2] Faculty of Systems Design, Tokyo Metropolitan University, Tokyo, Japan.
Email: hara-yuse@ed.tmu.ac.jp

INTRODUCTION

Ground reaction force is one of the most important evaluation indices in the analysis of figure skating technique [1]. The center of pressure is an indicator of stability and balance, and since the jumping motion includes rotational motion, it is also important to measure the moment around each axis. For these measurements, a device called force plate is generally used, but it is technically difficult to install on the ice. Therefore, A method was focused on to measure kinematic factors such as acceleration and angular velocity, and to estimate the reaction force from the ice surface, which is a mechanistic factor [2]. Using this system, it is possible to estimate the reaction force from the ice surface, an environment where it is difficult to measure the reaction force, and to estimate the body load.

In this study, the measuring figure skating shoe using wearable force plates was manufactured with the aim of validating the estimation method of reaction force from the ice surface and body load during figure skating jump movements based on inertial sensors and a body dynamics model. In addition, several experiments were conducted in which static loads were applied using weights with known values were conducted to evaluate the validity of the data obtained by this measurement system.

METHODS

The measurement system consists of five elements: three wearable force plates (M3D-FP-EL-U, Tec Gihan), used to measure three-axis reaction forces, moments around each axis and the center of pressure, a skate shoe (RF3pro, Risport), a blade (CoronationAce, JohnWilson), a jig mounting wearable force plates between the skate shoe and the blade, and a device with control software for wearable force plates (Figure 1, total weight: 2482 g, left foot only). The measured forces allow the calculation of torques and the center of pressure by using the distance between the wearable force plates.

To verify the validity of the data obtained with this measurement system, experiments were conducted in which static loads were applied using weights with known values. The measuring figure skating shoe was fixed in a vice avoiding force acting on the blades and wearable force plates, and a load was applied to each axis direction in the coordinate system defined for the measurement system, and the true values and measured values were compared. The moments around each axis direction were calculated theoretically from the positional relationship between the origin of the coordinate system defined for the measurement system and the load point, and compared with the measured values.

Figure 1 Measuring figure skating shoe with wearable force plates.

RESULTS AND DISCUSSION

The relative measurement errors in the vertical static loading experiment were 0.05 ± 0.43 % and 4.69 ± 0.15 % for the vertical reaction force and the sagittal moment, respectively. The absolute errors of the center of pressure were 7.56 mm in the medial-lateral direction and 6.71 mm in the antero-posterior direction. In the medio-lateral static loading experiment, they were 3.67 ± 0.09 %, 104 ± 0.03 % and 3.17 ± 0.03 % for the medio-lateral reaction force and the frontal and transverse moments, indicating a larger error in the frontal moment. In the antero-posterior static loading experiment, they were 0.76 ± 0.10 % and 150 ± 0.04 % for the antero-posterior reaction force and the sagittal moment, indicating that the errors of moments were large. Whereas the reaction forces were simply a composite of each data in each axis direction obtained from of three wearable force plates, the moments were calculated from the reaction forces and the distance between each wearable force plate. Therefore, it is possible that the accuracy was affected by measurement errors at the load points and distance uncertainties due to deformation.

CONCLUSION

Static loading experiments were conducted to verify the validity of the manufactured figure skating shoe for measurement. The reaction force measurement was sufficiently accurate, but the moment measurement had large errors due to the calculation methods.

REFERENCES

[1] King DL . *Biomech Sport* **15**: 312-325, 2000.
[2] Dorschky E . *J Biomech* **95**: 109278, 2019.

KINEMATICS AND STABILITIES OF THE INTER-SEGMENTAL LUMBAR SPINE: MEASUREMENT AND ANALYSIS USING 3D FLUOROSCOPY

Chung-Hua Chu[1,2], Chia-Ying Shen[1], Kuan-Hsien Wu[1] and Tung-Wu Lu[1]

[1] Department of Biomedical Engineering, National Taiwan University, Taiwan, R.O.C.

[2] Department of Orthopedic Surgery, Taipei Tzu Chi Hospital, Buddhist Tzu Chi Medical Foundation, New Taipei City, Taiwan, R.O.C.

Email: acold5@icloud.com

INTRODUCTION

Kinematics measurement of the spine has been one of the key approaches to understand the biomechanics of the spine in healthy and diseased population. Before 2000s, 3D motions measurements via infrared cameras (i.e. motion capture system) was the main approach to study spine kinematics in various population. However, it is limited to provide subtle information in the diseased spine joints, since the spine vertebrae are too small to put sufficient markers and the soft tissue artefacts are huge in the back. Several simplified models are used to minimize the complexity and soft tissue artefacts, and applications therefore have been limited. A developed the 3D fluoroscopy technique and successfully used it in measuring kinematics of the cervical spine [1]. Thus, it is confident that the model-based 3D fluoroscopy method needs a significant modification to be able to apply on the lumbar spine. Furthermore, knowledge on the kinematics of the lumbar region in the healthy controls during activities is still unclear due to limitations of measurement in the past. The purpose of the current study is to investigate the kinematics of the lumbar joints in the healthy subjects during functional activities using 3D fluoroscopy method.

METHODS

We recruited 15 healthy controls (age: 27±4 years, height: 170±4 cm, mass: 60±10 kg) in the current study with written informed consent as approved by the Institutional Review Board. CT and 3D fluoroscopy scan of the lumbar spine region of the subject were obtained for advance diagnosis and subsequent spine vertebrae models reconstruction. In the 3D fluoroscopy test, each subject was performed isolated spine exercise including lumbar flexion/extension, side bending, and axial rotation under the measurement of the bi-plane fluoroscopy system. Descriptive statistics will be carried out to quantify the kinematic parameters.

RESULTS AND DISCUSSION

A customized 3D fluoroscopy software was developed and specialized for lumbar spine registration and kinematics analysis. The lumbar spine DRR models, including the 3rd, 4th, and 5th lumbar spine, were imported into the software, and located in a proper position in the reconstructed 3D space. With the developed software, the pose of each component and kinematics and of the lumbar spine joints were able to be determined (Figure 1).

CONCLUSION

The 3D fluoroscopy technique has developed and successfully applied in measuring kinematics of the lumbar spine in the current study. The results from healthy adults can be used as baseline data in diseased population, which will be helpful for the planning of rehabilitative interventions and decisions of operations [2].

ACKNOWLEDGEMENT

REFERENCES

[1] Lin CC et al. *J Biomech* **47**: 3310-3317, 2014.
[2] Akuthota V et al. *Curr Sport Med Rep* **7**: 39-44, 2008.
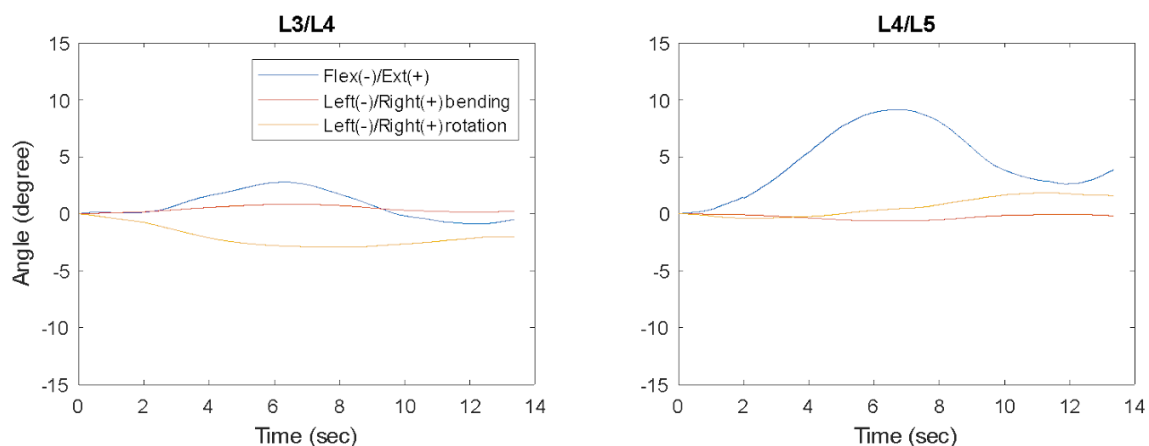
Figure 1 The curves of the angles of the L3/L4 and L4/L5 joints in the sagittal, frontal, and transverse planes of typical subject of the Control group when lumbar extension at sitting posture.

INSERTING A CURVED CARBON PLATE INTO THE MIDSOLE ENHANCES RUNNING MECHANICAL EFFICIENCY AT THE ANKLE JOINT

Tomohiro Miyazaki[1], Takayuki Aimi[1,2], Yugo Yamada[3] and Yasuo Nakamura[4]
[1] Graduate School of Health and Sports Science, Doshisha University, Kyoto, Japan
[2] Research Fellow DC1 of Japan Society for the Promotion of Science, Tokyo, Japan
[3] School of Environment and Society, Tokyo Institute of Technology, Tokyo, Japan
[4] Faculty of Health and Sports Science, Doshisha University, Kyoto, Japan
Email: yanakamu@mail.doshisha.ac.jp

INTRODUCTION
Carbon plate inserted shoes have gained popularity in long-distance races, due to their ability to improve running economy [1]. A previous study suggested that the improved running economy could be attributed to the "teeter-totter effect" resulting from the curved carbon plate [2]. However, the biomechanical aspects of this "teeter-totter effect" remain relatively unexplored. Therefore, the current study aims to examine the biomechanical advantages of the "teeter-totter effect," particularly in terms of mechanical efficiency, by inserting a curved carbon plate into the midsole.

METHODS
Two types of shoes made by a 3D printer were prepared: one with a curved carbon plate (**Carbon[+]**) and the other without (**Non-carbon**). Both shoes have 40 mm heel thickness and 8 mm drops. The curved carbon plates made by a 3D printer were inserted into the midsole to induce the "teeter-totter effect." Ten healthy male long-distance athletes (1.71 ± 0.05 m, 57.30 ± 4.11 kg, and 20.30 ± 1.25 years) were recruited for this study. Written informed consent was obtained from all participants (application number: 22013). Reflective markers were placed on their entire body. Participants were instructed to run three times in each shoe at $3 m/s \pm 5\%$. Their running motion and ground reaction forces were recorded using a motion capture system. The right leg in the stance phase was evaluated. We calculated the mechanical energy expenditure (MEE) and mechanical energy compensation (MEC). MEE represents the energy expenditure at the joint, while MEC indicates the efficiency of energy transfer between segments at the joint [3]. These calculations were performed for each energy transfer phase, which are concentric, eccentric, and non-transfer phases [3]. Wilcoxon signed-rank tests were used for statistical analysis ($\alpha = 0.05$).

RESULTS AND DISCUSSION
The ankle joint concentric and eccentric MEC were significantly higher in the **Carbon[+]** than in the **Non-carbon** (Table 1). However, no significant differences were found in the concentric, eccentric, or non-transfer MEE between the shoes. The mean power curves for all participants are plotted in Figure 1.

The greater ankle joint concentric and eccentric MEC in the **Carbon[+]**, without an accompanying increase in MEE, implies that the insertion of a curved carbon plate enables runners to absorb and generate energy more efficiently at the ankle joint, which indicates reduced effort from the plantar flexor muscles [3]. The "teeter-totter effect" resulting from the insertion of a curved carbon plate refers to the rolling function of the shoe, where the shoe rolls forward, causing the heel portion of the shoe pushes the runner's heel and lower thigh up [2]. This forward-rolling effect of the shoe appears to induce more efficient exertion of ankle plantarflexion force during the running stance phase.
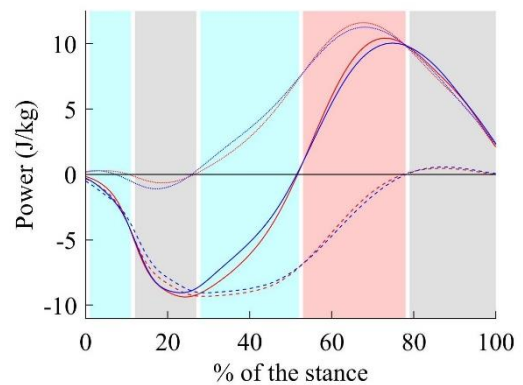
Figure 1 The power curve of ankle joint power (solid line) and segment torque power of the shank (dashed line) and foot (dotted line). Red lines refer to **Non-carbon** and blue lines to **Carbon[+]**. The different colored areas refer to different phases of energy transfer (pink: concentric, light blue: eccentric, grey: non-transfer).

CONCLUSION
Our results indicate that inserting a curved carbon plate into the midsole enhances the concentric and eccentric energy transfer efficiency at the ankle joint during the stance phase.

REFERENCES
[1] Hoogkamer W et al. *Sports Med* **48**: 1009-1019, 2018.
[2] Nigg B et al. *Footwear Science* **13**: 133-137, 2022.
[3] Mcgibbon C et al. *J Biomech* **34**: 481-490, 2001.

Table 1 The results of ankle joint concentric and eccentric MEC (median [25% tile value–75% tile value])

	Non-Carbon	**Carbon[+]**	p-value
Ankle concentric MEC	0.43 [0.34 - 0.50]	0.50 [0.39 – 0.57]	p = 0.037
Ankle eccentric MEC	0.48 [0.42 – 0.55]	0.52 [0.50 – 0.56]	p = 0.049

ELECTROMYOGRAPHIC ACTIVITY DURING THE LATERAL STEP-UP, LUNGE AND SINGLE LEG SQUAT EXERCISES WITH STANDARD BARBELL AND SAFETY SQUAT BAR

Ying-Ying Chen[1], Yu-Lin Yo[2], Chin-Dar Tseng[1], Lan-Yuen Guo[1]

[1] Department of Sports Medicine, Kaohsiung Medical University, Kaohsiung, Taiwan.
[2] Department of Sports Medicine, China Medical University, Taichung, Taiwan. Taiwan.
Email: yuen@kmu.edu.tw

INTRODUCTION

The safety squat bar can be used for those who have shoulder joint insufficient range of motion or injury [1,2]. However, we want to know whether existed difference between it and the standard barbell. In this study, we compare of electromyography activity during step-up, lunge and single leg squat with standard barbell and safety squat bar. It can be applied for helping in training more effective and lowering the necessary for injuries rehabilitation.

METHODS

We recruit 20 healthy adults who have at least 6 months of experience in resistance training. Electromyography activity were collected during step-up, lunge and single leg squat with standard barbell and safety squat barbell (Figure 1). The weight is 60% of 5RM. The EMG activation of gluteus medius, gluteus maximus, biceps femoris, vastus lateralis, vastus medialis, rectus femoris and erector spinae were analysed to compare the difference in muscle activation between standard barbell and safety squat bar. The statistical method was adopted the paired t-test and two-way ANOVA. The significant level was set as $p < .05$.

(a)　　　　(b)　　　　(c)
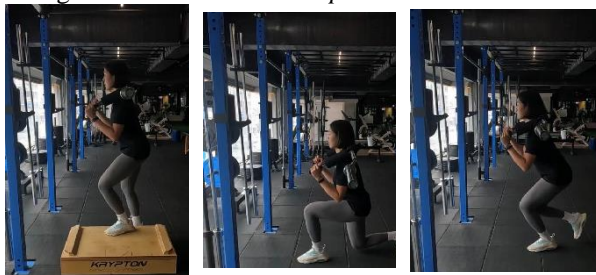
Figure 1 Electromyography activity were collected during (a) step-up (b) lunge (c) single leg squat

RESULTS AND DISCUSSION

Compared with the standard barbell and the safety squat barbell, there were significant differences in the erector spinae in step-up ($p < .05$); significant differences in the vastus medialis muscles in lunges ($p < .05$). Also, there is significant differences in the rectus femoris and erector spinae in single-leg squat (($p < .05$), Table 1).

Despite of using standard barbell or the safety squat barbell, single-leg squats have greater overall muscle activation than step-up and lunges ($p < .05$). Among the three movements, the vastus lateralis and vastus medialis had the greatest activation, and the biceps femoris had the least activation ($p < .05$).

CONCLUSION

Erector spinae has greater muscle activation in step-up and single leg squat using safety squat bar compared with standard barbell. Meanwhile, single leg squat having the greatest overall activation than the other two movements.

ACKNOWLEDGEMENT

REFERENCES

[1] Appleby, B.B., et al. *J Strength Cond Res 33*: 318-326, 2019.
[2] Keeves, R., et al. *Am J Sports Med* **27**: 545-546, 1999.

Table 1: EMG of single leg squat with normal barbell and safety squat barbell.

MVC%	Normal barbell	Safety squat barbell	*p-value*
Gluteus medius	74.34 ± 23.24	75.88 ± 22.56	*0.583*
Gluteus maximus	70.06 ± 24.73	68.58 ± 24.97	0.700
Biceps femoris	27.91±14.12	28.88 ± 14.49	0.507
Vastus lateralis	133.92 ± 37.15	123.14 ± 35.70	0.088
Vastus medialis	128.65 ± 31.56	123.31 ± 33.01	0.201
Rectus femoris	87.03 ± 21.33[a]	73.51 ± 27.07	0.029[*]
Erector spinae	40.06 ± 14.98	44.88 ± 19.88[b]	0.032*

Note: [*]$p < .05$ significant difference. [a]: $p < .05$ for the same muscle group compared to safe squat barbell. [b]: $p < .05$ for the same muscle group compared with normal barbell.

THE RELATIONSHIP BETWEEN TRUNK TWIST AND DISTANCE OF BATTED BALLS IN BASEBALL HITTERS

Taku Kawamura[1], Michihiko Fukunaga[2]
[1] Graduate School of Engineering, Oita University, Oita, Japan.
[2] Faculty of Science and Technology, Oita University, Oita, Japan.
Email: v22e1007@oita-u.ac.jp

INTRODUCTION

Understanding torso rotation in baseball hitting is important for improving technique and instruction. Previous study has shown that prior rotation of the hip leads to trunk twist, as demonstrated by three-dimensional analysis using the DLT method [1]. However, measurements using the DLT method are expensive due to the requirement of multiple cameras and synchronization equipment, making it difficult for amateur baseball teams to adopt this method. Therefore, this study utilized inertial sensors to analyze the trunk twist.

Methods

The subjects for this study included ten members from a university baseball team and ten inexperienced baseball players. We attached inertial sensors to the back and hip of the subjects. Each subject hit the ball placed on the tee five times with maximum effort, and we used the data from the trial with the longest distance. We adopted the method proposed by O'Donovan et al. [2] to estimate the position of the inertial sensors. The maximum value of the angular velocity of the back was used to evaluate the rotational velocity of the torso. The maximum angular velocity of hip and trunk twist, back rotation minus hip rotation, were normalized by the maximum angular velocity of the back to evaluate how the trunk twist. Additionally, the time by which the hip preceded the back was measured.

Results and Discussion

The correlation coefficients and significant differences between distance and swing characteristic quantities are shown in the table (Table 1). The timing of hip and back rotation, focusing on the maximum value of angular velocity, was not clearly preceded by the hip, and there was no correlation between the timing and the distance. There was a significant correlation between the angular velocity of the back and the distance in the inexperienced subjects (Figure 1-a). There was also a significant correlation between the maximum value of the angular velocity of normalized trunk twist and the distance in the experienced subjects (Figure 1-b).

These results suggested that the angular velocity of trunk twist was not caused by the earlier rotation of the hip, as shown in previous study, but rather by the faster rotation of the back relative to the hip.

(a) Angular Velocity of the Back

(b) Normalized Angular Velocity of the Trunk Twist
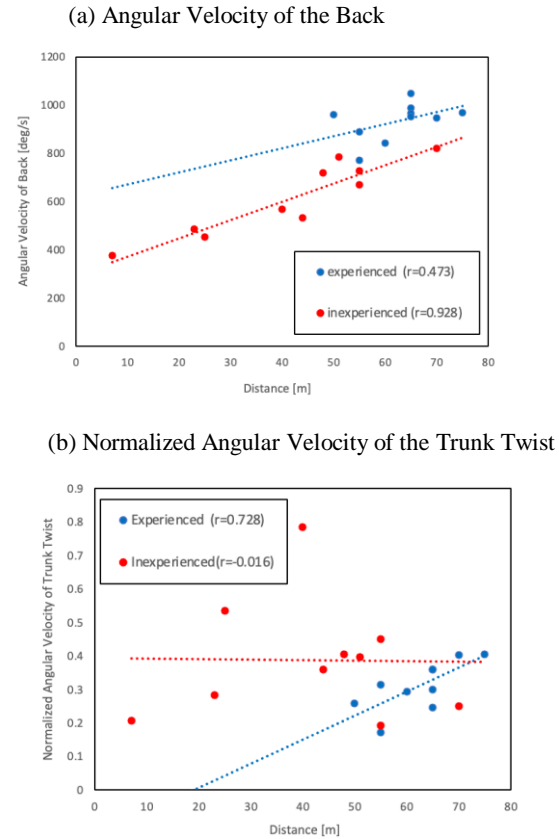
Figure 1 Relationship Between Distance and Torso Rotation

CONCLUSION

This study measured torso rotation during the baseball swing using inertial sensors. As a result, the hip and back rotated almost simultaneously, and the angular velocity of trunk twist contributed to the hitting distance of experienced players.

REFERENCES

[1] Tauchi K., et al. *J Coaching Studies* **1**: 1-9, 18.
[2] O'Donovan K.J., et al. *J Biomech*, **40**:2604-2611.

Table 1: Relationship Between Distance and Swing Characteristics

	Distance [m]	Hip-Back Time Difference [s]	Angular Velocity of Back [deg/s]	Normalized Hip Angular Velocity	Normalized Angular Velocity of Trunk Twist
Experienced	62.5±7.5	0.025±0.025 (-0.045)	931.1±79.4 (0.473)	0.779±0.055 (-0.321)	0.311±0.074 (0.728)*
Inexperienced	41.8±18.6	0.019±0.027 (0.306)	613.5±152.1 (0.928)*	0.915±0.057 (-0.475)	0.387±0.178 (-0.016)

* : Significant difference (p < 0.05) between experienced player and novice.

TRUNK AND LOWER LIMB LANDING KINEMATICS FOLLOWING A FOREHAND JUMP SMASH

Yeap Ming Wei[1], Yuvaraj Ramasamy[2], Juliana Usman[1] and Rizal Razman[3]
[1] Faculty of Biomedical Engineering, University of Malaya, Kuala Lumpur, Malaysia.
[2] Sports Biomechanic Centre, National Sports Institute of Malaysia, Kuala Lumpur, Malaysia.
[3] Faculty of Sports and Exercise Science, University of Malaya, Kuala Lumpur, Malaysia.
Email: rizal@um.edu.my

INTRODUCTION

It is now known that Anterior Cruciate Ligament (ACL) injury also occurs in non-contact conditions (e.g., jump-landing) and is a common sports injury among the youth [1]. However, studies investigating landing movement following a jumping smash are scant, and most jump-landing studies adopted landing tasks or tests rather than the actual sporting movement. The present study aimed to examine the relationship between the trunk and lower limb landing kinematics and the relative ground reaction force (GRF) associated with ACL injury risk.

METHODS

Twenty-one junior male full-time athletes (age 14.7 ± 1.4 years, mass 57.3 ± 8.7 kg, height 1.68 ± 0.07 m) who train at least five days a week at a professional badminton club or national sports school were recruited. Anthropometry data were measured, and the kinematics and kinetics of the smash trials were recorded using a Qualisys motion capture system and three Kistler force plates on an instrumented standard badminton court (Figure 1). A shuttle launcher was used to replicate the high serve/lift [2]. Five successful trials for each participant with single-leg landing were used for further analysis. Position data were labelled using Qualisys Track Manager while a 15-segment model in Visual 3D was used to calculate descriptive kinematic parameters. Correlational analyses were performed to identify the variables which potentially contribute to the knee impact loading.
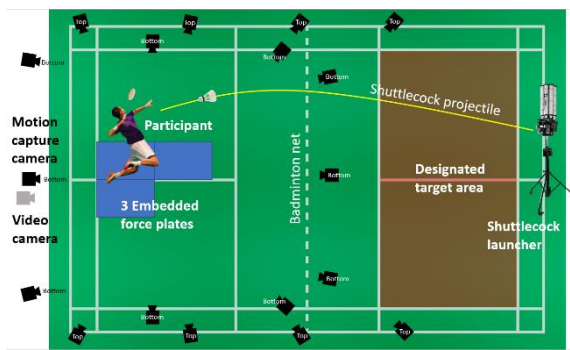
Figure 1 Laboratory setting layout.

RESULTS AND DISCUSSION

Among the elite junior players tested, their mean jump height, shuttlecock and racket head speeds were recorded at 0.55 m, 75 and 53 m·s⁻¹ respectively. The mean vertical GRF (vGRF) generated from a single-leg landing following a forehand jumping smash is 1669.2 ± 391.7 N, with the peak value recorded at 2544.8 N. The mean landing time (0.14 ± 0.02 s) and time-to-peak vGRF (0.06 ± 0.01 s) were recorded, while the mean relative vGRF was 29.1 N·kg⁻¹ when normalised to body mass. Table 1 presents the results of the correlational analyses.

Table 1: Significant correlation coefficients between trunk and lower limb landing kinematics and normalised vGRF.

Kinematic variables	$r/(\tau_b)$
Trunk	
Lateral flexion angle at IC (°)	0.264**
Lateral flexion AV at peak vGRF (°·s⁻¹)	0.289**
Rotation angle at IC (°)	0.275**
Peak rotation angle (°)	0.263**
Lower limb	
Peak ankle plantarflexion angle (°)	0.158*
Ankle plantarflexion angle at peak vGRF (°)	0.220*
Ankle plantarflexion AV at peak vGRF (°·s⁻¹)	0.330**
Peak knee extension angle (°)	0.203**
Knee extension angle at peak vGRF (°)	0.357**
Knee extension AV at peak vGRF (°·s⁻¹)	0.269**
Peak knee external rotation angle (°)	0.201*
Knee external rotation angle at IC (°)	0.284**
Knee external rotation angle at peak vGRF (°·s⁻¹)	0.280**
Knee abduction angle at IC (°)	-0.341**
Knee abduction angle at peak vGRF (°)	-0.231*
Peak hip abduction angle (°)	0.168*
Hip abduction AV at peak vGRF (°·s⁻¹)	0.254**

AV = angular velocity, IC = initial contact. *$p < 0.05$. **$p < 0.01$.

The asymmetric posture of the players in dominating one arm holding the racket [3] likely causes a tendency of forward rotating and lateral tilting of the trunk away from the racket arm during a single-leg landing could contribute to ACL injury risk during badminton games. A moderate correlation identified between knee extension angle and relative vGRF suggests that landing with reduced knee flexion would place a greater impact on the knee joint. Surprisingly, a negative correlation was found between knee abduction angle and relative vGRF, which could be due to the setting that requires the players to perform the smash from a static position rather than a multi-directional jumping smash.

CONCLUSION

While striving for a faster jump-smash speed, we recommend players to land with more flexed knee, less lateral tilted and less forward rotated trunk, to avoid excessive knee joint loading and subsequent injuries.

ACKNOWLEDGEMENT

REFERENCES

[1] Pardiwala DN et al. *Indian J Orthop* **54**: 237-245, 2020.
[2] Ramasamy Y et al. *Sports Biomech* 1-16, 2021.
[3] Hung MH et al. *J Hum Kinet* **73**: 19-31, 2020.

COMPARISON OF MUSCLE ACTIVITIES OF THE LOWER LIMB AMONG DIFFERENT SHOOTING DISTANCES IN PETANQUE

Yi-Wen Chang[1], Hong-Wen Wu[2] and Guo-Xun Wu[1]

[1] Department of Exercise Health Science, National Taiwan University of Sport, Taichung, Taiwan.
[2] Department of Physical Education, National Taiwan University of Sport, Taichung, Taiwan.
Email: changyw@ntus.edu.tw

INTRODUCTION

Petanque is one popular boule sports, historically originated from Provence, France [1]. High attention and well body coordination are essential for the petanque players to accurately throw the boule to touch the target boule or jack in petanque shooting game. The athlete is standing by both feet on the ground that are not allowed to move or lift-off from the ground when throwing the boule. The stability of the lower limb and trunk is important for providing a good base of support. There are various levels of shooting difficulty defined by four different shooting distances. Therefore, the purpose of this study was to compare the differences of muscle activities in the lower limb and trunk among different shooting distances in petanque.

METHODS

There were fifteen male petanque players participated in this study (age: 26.0 ± 6.3 years; body weight: 70.1 ± 11.3 kgw; body length: 173.2 ± 5.6 cm). Vicon Nexus motion capture system and Noraxon wireless surface electromyography (EMG) recording system were used. The EMG signals were measured in four different petanque shooting distances (6, 7, 8 and 9 m). The measured muscles consisted of the gastrocnemius (GM), rectus femoris (RF), biceps femoris (BF) and lumbar erector spinae (ES). The outcome parameters were the peak EMG value of each muscle in backward and forward phases of petanque shooting. One-way ANOVA was used to compare the differences of muscle activities among four different shooting distances (SPSS, V22).

RESULTS AND DISCUSSION

Significant difference among different shooting distances were found on gastrocnemius and rectus femoris in backward and forward phases of petanque shooting (Figure 1, $p < 0.05$). Significant difference among different shooting distances was found on erector spinae in backward phase ($p < 0.05$). The biceps femoris showed no significant difference among different shooting distances.

In backward phase, the gastrocnemius showed significantly higher activities at the 9 m shooting distance than at the 6 m shooting distance. The rectus femoris showed significantly higher activities at the 9 m shooting distance than at the 6 m, 7 m and 8 m shooting distances. The erector spinae showed significantly lower activities at the 6 m shooting distance than at the 8 m and 9 m shooting distances. In forward phase, the gastrocnemius and rectus femoris showed significantly higher activities at the 9 m shooting distance than at the 6 m shooting distance.

CONCLUSION

Petanque shooting basically is a throwing movement in upper limb while the lower limbs are maintained at a semi-squat position. This study found that higher activities in ankle plantar flexor, knee extensor and lumbar extensor were shown in petanque shooting at the farthest shooting distance. The stance stability via the muscle contraction of the trunk and lower limb extensor might be crucial in petanque shooting.

ACKNOWLEDGEMENT

REFERENCES

[1] Loster R et al. *Eng Fail Anal* **18**: 633-648, 2011.
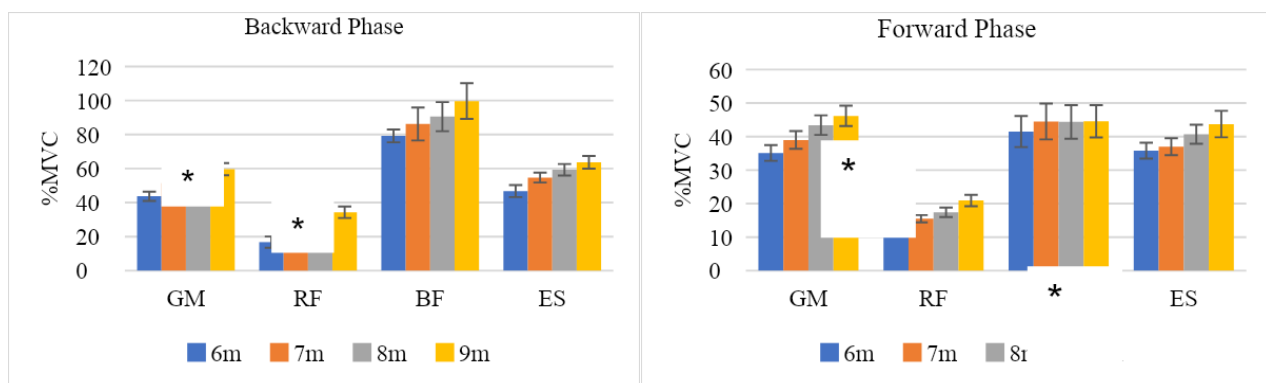
Figure 1 EMG activities in petanque shooting (*p<0.05)

EVALUATION OF 3D SURFACE SCANNING WITH HANDHELD 3D SCANNER FOR BIOMECHANICAL PRODUCT DESIGN

Muhammad Alfiyya Fajra[1], Harmein Khagi[2], Suprijanto[3] and Narendra Kurnia Putra[3]

[1] Engineering Physics Department, Institut Teknologi Bandung, Bandung, Indonesia.
[2] Human and Industrial Product Design Research Group, Institut Teknologi Bandung, Bandung, Indonesia.
[3] Instrumentation and Control Research Group, Institut Teknologi Bandung, Bandung, Indonesia.
Email: narend@itb.ac.id

INTRODUCTION

3D surface scans of the human body serve an important role in biomechanical product design, such as in sport equipment, orthotics, and personalized product design. Product design with 3D surface scans in hand are advantageous because it can be utilized to further optimize the product's fit to the human body.

One of the 3D scanners that can be used to perform such 3D surface scanning on the human body are handheld 3D scanners. They can be used to measure specific parts of the human body as needed and are relatively more affordable compared to full-body booth 3D scanners. At the lower end of the cost spectrums, full-body booth 3D scanners typically cost $10,000 while handheld 3D scanners typically cost $500 [1].

But unlike booth 3D scanners which is automated, handheld 3D scanners requires more effort from a measurer to manually scan the specific region of interest of the human body. The manual involvement of a measurer potentially contributes to more errors and variabilities within the result, thereby potentially making it less accurate and precise.

This inclined us to investigate the accuracy and precision of 3D surface scanning with handheld 3D scanners and find out whether or not it is acceptable for biomechanical product design. In this paper, we evaluate the accuracy of Sense™ 2 handheld 3D scanner (3D Systems, Rock Hill, SC) in performing 3D surface scanning on 10 subjects and 9 different body dimensions.

METHODS

The evaluation of the accuracy of performing full-body 3D surface scanning using Sense™ 2 handheld 3D scanner is done by comparing the result of anthropometric measurement performed on 3D surface model of a scanned human body with the result of anthropometric measurement performed physically on the same human body using anthropometers.

9 body dimensions defined at the torso and their subsequent conventional anthropometric measurement procedures were adopted from ANSUR II's defined body dimensions for 3D scan validation: A. biacromial breadth, B. bideltoid breadth, C. hip breadth, D. neck circumference, E. neck circumference, base, F. shoulder circumference, G. chest circumference, H. waist circumference, I. buttock circumference [2]

10 volunteers with BMI varying from 17.98 to 25.84 were recruited as subjects. Both conventional anthropometric measurement on each body dimension of each subject and full-body 3D surface scanning on each subject were done with five repetitions to minimize the dispersion of results caused by measurement uncertainty.
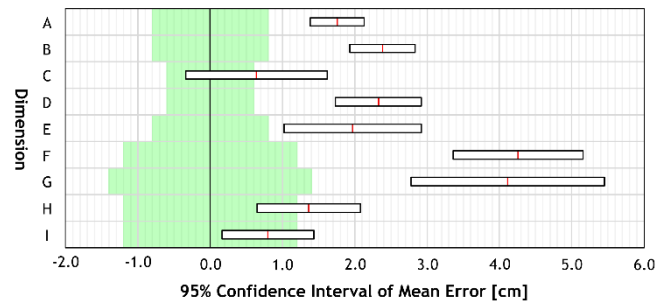
Figure 1 95% confidence interval of mean errors

RESULTS AND DISCUSSION

The 95% confidence interval of mean errors between the two anthropometric measurements results were calculated and plotted in Figure 1 relative to ANSUR II's allowable observer error (AOE) for each body dimension. No defined body dimensions satisfy the demanding criterions defined for comparing two conventional anthropometric measurement results, but almost all of them does satisfy the typical 5cm maximum error of the depth camera used in the handheld 3D scanner [2] [3]. The positive bias was bound to be found in the results as the conventional anthropometric measurements required skin contact, thereby causing the result to be less than it actually is.

CONCLUSION

On average, it was found that the mean errors of the measurements are found to be 2.18±1.7cm. It can be concluded that the handheld 3D scanners can be used in 3D surface scanning for biomechanical product design if the aforementioned errors are expected and tolerable in its respective use case.

REFERENCES

[1] Aniwaa Pte. Ltd. "3D scanner catalog" https://www.aniwaa.com/catalog/3d-scanners/, [Accessed 14 July 2023]
[2] Hotzman et al. *ANSUR II Measurer's Handbook*, 2011.
[3] Zabatani et al. *Transactions on Pattern Analysis and Machine Intelligence* **42**: 2333-2345, 2020

KINEMATICS OF A VISUALLY IMPAIRED RUNNING ON THE TREADMILL; A CASE STUDY

Pei Yi Cheah[2] and Rizal Razman[2],

[1]Centre for Sport and Exercise Sciences, University of Malaya, Malaysia.

[2] Centre for Sport and Exercise Sciences, University of Malaya, Malaysia.

Email: rizal@um.edu.my

INTRODUCTION

Running is a fundamental exercise that athletes need to engage in order to achieve cardiovascular endurance - visually impaired (VI) athletes are not exempt. However, running outdoors independently is challenging and dangerous for VI athletes. The treadmill presents an alternative method for the VI to train independently. The goal of this study is to explore and maximize the database of the kinematics of a VI athlete running on the treadmill while analyzing the asymmetry variability of discrete kinematic data collected.

METHODS

There are various categories of visual impairment and in this study, a healthy B1 (total blindness category; with no light perception in either eye and unable to recognize the shape of a hand at any distance or direction [1].) VI male athlete was recruited. The athlete was 20 years old with a height of 148cm, weighed 47kg, and was injury free upon measurement day. Qualisys motion capture system using eight cameras along with a motorized treadmill was used for data collection. The VI runner was required to sprint overground to obtain his maximal sprint speed. Then VI athlete moved on to treadmill running at 40% (3.4 mph) and 60% (4.5 mph) which were derived from his maximal velocity sprint taken on overground running.

RESULTS AND DISCUSSION

The VI's trunk flexion leaned towards the left side as the speed on the treadmill increased. The left leg at foot strike and toe-off constantly displayed a higher degree of flexion at both speeds. The pelvis rotation upon the left foot strike was much bigger than the right foot strike. The upper body was leaning to the left as well when the speed increased from 40% to 60% (Table 1). The alternate swinging of the legs exerts horizontal torque on the pelvis and transfers upwards, towards the shoulder girdle and arms. The stabilization of the muscles in the trunk and arm acts as an elastic element [2].

The interlimb asymmetry was most likely influenced by the grasping of the treadmill handrails with the left arm, leading to restrictions on the corresponding limb. Asymmetrical lower limb patterns may lead to muscular imbalance where one limb is required to work harder to compensate for the deficit [3]. asymmetry leads to a higher risk of injuries in

walking and running as gait stability is challenged [4]. Bilateral differences during a run will lead to overloading on one side causing excessive muscle contractions and compensation [5]

CONCLUSION

Running is essential for athletes to maintain their fitness and the treadmill needs to be seen as an alternative for VI to train indoors. From this study, it is evident there are asymmetrical issues seen when VI runs on the treadmill. Further investigation should be done with a bigger pool of VI athletes to gain more insights and recognize the issues to be overcome as injury prevention in the long run. Chronic injuries are built up from multiple joint loadings over time and it would end a career if not taken care of.

ACKNOWLEDGEMENT

REFERENCES

[1]USABA. Visual Classifications. United States Association of Blind Athletes. Available online: (accessed on 3 October 2022)

[2]Warrener A et al., *Hum Movement Sci*. **78**: 102817. 2021.

[3] Willwacher S et al., *Sports Med*. **52**(8):1863-1877, 2022.

[4] Gao Z et al., *Symmetry*, **12**:720, 2020.

[5] Glowinski S et al., *Sensors*. **20**:611. 2020.

Table 1: Kinematic parameters (angle in degrees) of the right and left leg at 40% and 60% speed.

Kinematic Parameter	Phase	40% Speed		60% Speed	
		Right	Left	Right	Left
		Mean ± SD	Mean ± SD	Mean ± SD	Mean ± SD
Pelvis, degrees					
Obliquity (R (+), L (-))	FS	-1.55 ± 0.36	3.56 ± 1.26	-2.42 ± 0.7	2.49 ± 0.70
Tilt (Fwd (+), Bwd (-))	FS	-0.04 ± 0.45	-1.44 ± 0.43	0.68 ± 1.49	3.07 ± 0.87
Rotation	FS	-0.12 ± 1.71	7.25 ± 4.82	-1.59 ± 2.75	8.66 ± 2.70
Knee Flexion (+) /Extension (-)					
Knee	Stride	114.07 ± 1.61	110.20 ± 1.42	145.98 ± 2.96	138.32 ± 0.92
Knee	FS	51.83 ± 2.03	47.54 ± 0.89	50.67 ± 2.62	47.37 ± 1.84
Knee	TO	14.02 ± 1.07	10.82 ± 2.19	15.93 ± 2.06	13.08 ± 1.80

FLOATING TOE SCORES OF ATHLETIC ATHLETES DURING STATIC STANDING POSTURE

Yohei Yamazaki[1,2], Hiyo Inaba[3], Hiroaki Noro[3], Keiichiro Hata[3], Shuta Matsui[1], Lee Rou You[1], Misato Ishikawa[1]
, Kazuhiko Yamazaki[3], Syunsuke Nagato[3], Takanori Sugibayashi[3] and Toshio Yanagiya [1,2]

[1] Graduate school of Health and Sports Science, Juntendo University, Chiba, Japan
[2] Institute of Health and Sports Science & Medicine, Juntendo University, Chiba, Japan
[3] Faculty of Health and Sports Science, Juntendo University, Chiba, Japan
Email: sh4222010@juntendo.ac.jp

INTRODUCTION

Floating toe score (FTS) is an index that measure the degree of foot contact between the toe digits and the ground during static standing posture with both legs. Previous studies have indicated that the floating toe condition can impair dynamic balance ability and/or physical activities such as walking, throwing and maintaining balance while standing [1,2,3]. However, to date, as far as we know, there is lack of evidence studying the relationship between running performance and floating toe scores. Therefore, we investigated the floating toe score of collegiate athletic athletes with the purpose of identifying the relationship between floating toe score and running performance. In this study, our hypothesis was that collegiate athletic athletes would exhibit a negligible presence of floating toes.

METHODS

The participants of this study were 204 collegiate athletic athletes (1.74±0.06 cm, 63.6±7.8 kg, 20.1±1.1 years) over 720 points in WA points. Of the participants 72 were sprinters, 64 were distance runners and 68 were jumpers. Their floating toe scores were evaluated using the foot printing apparatus (FootLook2, FootLook, Japan) according to the previous study [4]. Specifically, the participants were categorized into three conditions based on their digit contact: Normal (score over 18 points), Incomplete (score between 11 and 17 points) and Floating toes (score less than 10 points) according to their digit contact.

RESULTS AND DISCUSSION

The distributions of FTS of sprinters, distance runners and jumpers were shown in Fig. 1. The result of classification of participants by FTS showed that among sprinters, 12 participants (16.67%) exhibited floating toes, 42 participants (58.33%) demonstrated incomplete contact toes, and 18 participants (25.00%) had complete contact. On the other hand, among distance runners, 28 participants (43.75%) exhibited floating toes, 31 participants (48.44%)

demonstrated incomplete contact toes, and 5 participants (7.81%) had complete contact (Table 1). Moreover, among jumpers, 10 participants (14.71%) exhibited floating toes, 28 participants (41.18%) demonstrated incomplete contact toes, and 30 participants (44.12%) had complete contact. These results indicated that the percentage of floating toes was lower than of normal toes in sprinters and jumpers, whereas the percentage of floating toes was higher than the normal toes in distance runners. In addition, distance runners showed a higher percentage of floating toe compared to sprinters and jumpers. These results suggest that the incidence of floating toes in runners may vary depending on the type of athletic event.
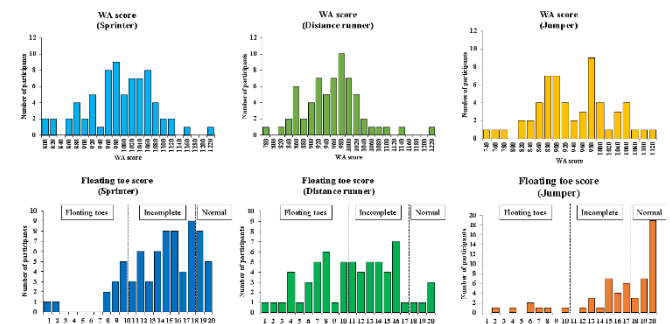
Figure 1. Distributions of WA scores (top) and floating toe scores (under) in sprinters, distance runners and jumpers.

CONCLUSION

Distribution of FTS differs in athletic event as distance runners exhibiting a higher prevalence of floating toes compared to others.

REFERENCES

[1] Uritani et al. *J Phys Ther Sci* **29**(2): 361-364, 2017.
[2] Nagamoto et al. *Res Sports Med:* 1-8, 2022.
[3] Fukuyama et al. *Rigakuryoho Kagaku* **24**(5): 683-687, 2009.
[4] Yanagiya et al. *J Phys Ther Sci* **32**(5): 342-347, 2020.

Table 1: Mean ± SD of floating toe score.

		Floating toes	Incomplete	Normal
Sprinter	n (%)	12 (16.67)	42 (58.33)	18 (25.00)
	Floating toe score	8.00 ± 3.00	14.76 ± 2.21	18.78 ± 0.85
Distance runner	n (%)	28 (43.75)	31 (48.44)	5 (7.81)
	Floating toe score	6.68 ± 2.48	13.77 ± 1.84	19.40 ± 0.80
Jumper	n (%)	10 (14.71)	28 (41.18)	30 (44.12)
	Floating toe score	5.60 ± 2.97	15.25 ± 1.48	19.50 ± 0.72

SILICONE ELASTOMER SOFT PNEUMATIC ACTUATORS FOR LOWER LIMB REHABILITATION

Hanisah Bakeri[1,2], Khairunnisa Hasikin[2], Nasrul Anuar Abd Razak[2], Rizal Mohd Razman[3], Abd Alghani Khamis[4], Muhammad 'Ammar Annuha[1], Abbad Tajuddin[2] and Darween Reza[5]

[1] Department of Biomedical Engineering, University Malaya, Kuala Lumpur, Malaysia.
[2] Medical Revolution Sdn Bhd, 10 Boulevard, Petaling Jaya, Malaysia.
[3] Faculty of Sport and Exercise Science, University Malaya, Kuala Lumpur, Malaysia.
[4] Department of Mechanical Engineering, University Malaya, Kuala Lumpur, Malaysia.
[5] My Conceptual Robotic Sdn. Bhd (MyCro), Selangor, Malaysia.
Email:khairunnisa@um.edu.my

INTRODUCTION

The prevalence of sports-related lower extremity injuries, particularly among active individuals, has resulted in millions of reported cases, frequently causing significant disruptions in training and competition [1]. Soft pneumatic actuators (SPAs) offer a promising technological solution for proactively delivering pressure to treat prevalent lower limb injuries, including venous-related diseases [2]. However, the most effective design and material selection of SPAs for dynamic pressure delivery has not been fully explored. This research aims to introduce a SPA chamber with two layers of elastomer, utilizing single-side inflation. The finite element method (FEM) was employed to anticipate the influence of the material selection of three silicone elastomeric rubber composed of commercial and food-grade silicone on SPA's deformation and conduct experimental testing to validate the SPA lower- limb system against simulation results.

METHODS

The conceptual model of the SPA was developed and designed using Solidworks. The SPA consisted of two silicone parts, the main body with several chambers driven by a pressure source, and the bottom layer. Three silicone elastomeric rubbers, namely Sylgard 184, A15 Shore, and A10 Shore, were studied for their properties and constitutive model parameters using the 3rd order Yeoh model. The deformation and pressure distribution of the proposed SPA, using three different silicone elastomers, were analysed through FEM simulations in ANSYS 2019 R3. The SPA chambers were fabricated for experimental analysis on a mannequin leg to validate the SPA system model and to resemble actual compression treatment. The deformation profile of the chambers concerning their inflation height was evaluated using a distance laser meter.

RESULTS AND DISCUSSION

The best SPA-compliant behavior was displayed by food-grade silicone A10 Shore, with a maximum deformation value of 25.34 mm. Figure 1 shows the behavior of three silicone elastomers. The findings align with A10 Shore's properties, as it has a lower Shore hardness compared to A15 Shore and Sylgard 184 [3]. Benjamin et al. [4] also emphasized that elastomers with lower Shore hardness are preferred to prevent high pressure. A10 Shore has the lowest Young's modulus among other elastomers. In a study on the characterization of pneumatic muscle actuators, Antonio et al. [5] discovered that materials with a low Young's modulus create greater deformation and force when stimulated. Bland-Altman analysis showed good agreement between simulated and experimental conditions, confirming the SPA's reliability for applying interface pressure on the skin within the desired range for compression therapy.
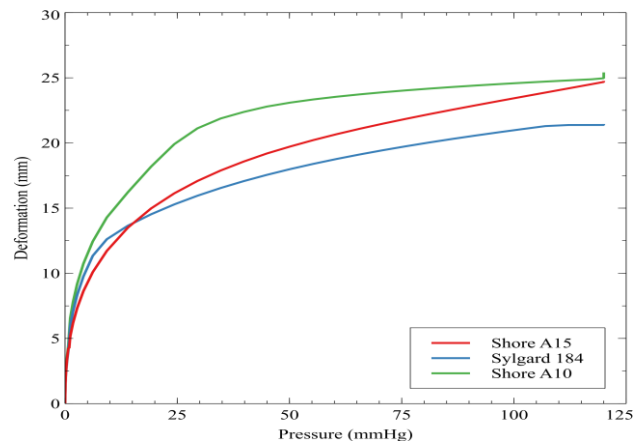
Figure 1 The behavior of three silicone elastomers from the simulation results

CONCLUSION

In this study, a SPA system was created to visualize interface pressure induced by the SPA chamber. FEM analysis helped identify appropriate design parameters with a minimum force of 1N. The A10 shore food-grade silicone demonstrates the material's potential as a major component for soft actuators. The simulation and experimental results showed excellent agreement in pressure transmission on the skin within the range of 0– 120 mmHg, confirming the suitability of food-grade silicone for SPA fabrication.

ACKNOWLEDGEMENT

REFERENCES

[1] McGuine, T. A. et al., *Am. J. Sports Med.*, **45**(12): 2706-2712, 2017.
[2] Youn Y. J. & Lee J., *Korean J. Intern. Med.*, **34**(2): 269-283, 2019.
[3] Smooth-On, "Durometer Shore Hardness Scale." https://www.smooth- on.com/page/durometer-shore-hardness-scale/ (accessed Nov. 20, 2022).
[4] Gorissen, B. et al., *Adv. Mater.*, **29**(43), 2017.
[5] Carvalho A. D. D. R. et al., *Sensors & Actuators Rep*, **4**, 100109, 2022.

A NEW DEVICE FOR DIAGNOSING AND TREATING HAND STIFFNESS AND INATTENTION CAUSED BY EXCESSIVE SMARTPHONE USE

Rui Gong[1,2], Kazunori Hase[2], Qian Li[2] and Sentong Wang[2,3]

[1] Organization of Liberal Arts Education, Mejiro University, Tokyo, Japan.
[2] Graduate school of Systems Design, Tokyo Metropolitan University, Tokyo, Japan.
[3] Department of Mechanical and Intelligent Systems Engineering, The University of Electro-Communications, Tokyo, Japan.
Email: r.gong@mejiro.ac.jp

INTRODUCTION

Since the beginning of the 21st century, there has been rapid development in mobile devices, particularly in the realm of mobile phones. The focus of mobile phone development has been on enhancing intelligence, leading to the emergence of smartphones. As a result, new smartphones are increasingly larger in size, heavier in weight, and richer in functionality [1]. According to a recent survey, the average smartphone user spends approximately three hours per day using their device due to the irresistible appeal of smartphones [2]. Prolonged smartphone use can have two primary consequences. Firstly, it can have a mental impact, resulting in decreased ability to concentrate effectively. Secondly, it can have a physical impact, causing significant stiffness in the soft tissues of the hand. In order to address the growing number of individuals experiencing these conditions and alleviate mild symptoms, this study has developed a new device.

METHODS

The device which shows in Figure 1 developed in this research comprises five deformation sensors and a high sensitivity triaxial acceleration sensor. The device operates as follows: it consists of five indicator lights, with each light corresponding to a specific finger. These indicator lights are controlled by a logic algorithm. When activated, the lights illuminate in a specific pattern or sequence. Participants are instructed to apply maximum force and exert pressure on the deformation sensor within a specified timeframe while the corresponding indicator light is illuminated.

The integrated Microprocessor Unit (MPU), memory, and sensors in the device allow for the calculation of various data. This includes measuring participants' reaction time to the illuminated lights and determining their correct response rate, which indicates their accuracy within the specified timeframe. These metrics serve as indicators of participants' concentration levels.

To assess the degree of stiffness in the finger soft tissue, the evaluation method relies on two factors. The first is the magnitude of instantaneous pressure applied to the deformation sensor, while the second is the stability of the palm during stress application. The magnitude of stress is determined by the deformation sensor's measurements, while the stability factor is based on readings from the integrated acceleration sensor.

Collected data is immediately displayed on the screen for feedback and can also be transferred to a computer for further analysis using the integrated SD card functionality. In addition, lifestyle information and clinical data will be collected through questionnaire surveys. This comprehensive approach allows for thorough analysis and interpretation of the data, providing insights into participants' conditions and enabling tracking of their progress over time. The combination of device-generated data and questionnaire responses contributes to a holistic understanding, supporting informed decision-making and tailored interventions.

Figure 1 An alpha version device

RESULTS AND DISCUSSION

As the device is currently undergoing reliability testing, the data and results will be disclosed and announced on the day of presentation.

CONCLUSION

Hands, being vital for human functionality, often face silent repercussions due to smartphone usage. Therefore, the development of this device holds great significance in preventing the further expansion of these issues. Simultaneously, it provides data support for analyzing the underlying mechanisms behind soft tissue verification in the hands. By understanding the occurrence mechanism, researchers and healthcare professionals can work towards developing preventive measures and tailored interventions to address these concerns effectively.

ACKNOWLEDGEMENT

REFERENCES

[1] GSMA HEAD OFFICE, "The Mobile Economy 2021," GSMA , London, Jul. 2021.
[2] Brent Cohen, "How Much Does a Smartphone Weigh?," Devicetests, Sep. 09, 2022.

DEVELOPMENT OF ASSISTIVE SURGICAL DEVICES FOR TOTAL HIP ARTHROPLASTY

Seita Inoue[1], Yu Goto[1], Hiromasa Tanino[2], Hiroshi Ito[2], Ryo Mitsutake[2] and Masaru Higa[1]

[1] Mechanical Engineering, University of Hyogo, Himeji, Japan.

[2]Orthopaedic Surgery, Asahikawa Medical University, Asahikawa, Japan.

Email: inoue.s0719@gmail.com

INTRODUCTION

Total hip arthroplasty (THA) is a surgical procedure to restore hip function in patients who have hip problems such as osteoarthritis, rheumatoid arthritis, osteonecrosis of the femoral head, or fractures. During the THA procedure, a "trial" is conducted to ensure appropriate tension of the soft tissues surrounding the joint. It is believed that the "trial" significantly influences the postoperative clinical outcomes. However, there is currently no device developed to quantitatively measure the appropriate tension in the soft tissues, and it relies on surgeon's skill. To address this issue, this study aims to develop a device that can quantitatively measure the tension of soft tissues during THA.

METHODS

In this study, we developed nine measuring devices. An example of one of the devices is shown (Figure 1). To keep surgical area clean, the measuring devices were developed to have wireless communication capabilities. To assess the accuracy of the developed measuring devices, calibration tests were conducted. In the calibration tests, applied load F [N] was set to F=0, 80, 160, 320, 560, 800, the cone angle θ [°] from the Z-axis to the Y-axis was set to θ=0, 15, 30, 45, and the polar angle φ [°] from the Y-axis to the X-axis was set to φ=0, 45, 90, 135, 180, 225, 270, 315 [1]. This resulted in a total of 25 combinations. The tests aimed to verify the error between the applied load and the load detected by the measuring devices. The results are presented (Table 1). In addition, we conducted validation experiments using a cadaver. The cadaver trial involved performing actual THA and measuring joint reaction forces using one of the developed measuring devices during the "trial" carried out. The measurements were taken during five different movements: flexion, abduction, extension with external rotation, flexion with internal rotation, and flexion with dislocation. For each of these movements, three repetitions were performed.
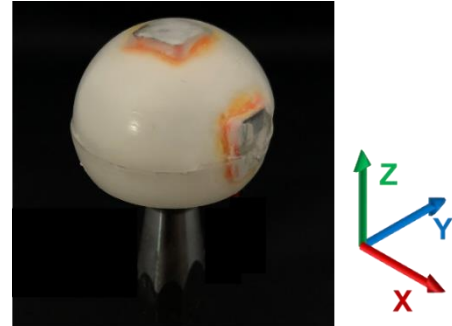
Figure 1 A measuring device.

RESULTS AND DISCUSSION

The variation in errors was calculated for the nine developed devices (Table 1). The results showed an average error of 8.61% in the X-axis, 8.86% in the Y-axis, and 8.10% in the Z-axis. Although there were no significant differences in error among the axes, there were different in errors among the sensors. This variation can be attributed to the fact that the measuring devices were developed by hand. On the other hand, the data obtained from the cadaver trial revealed that convective force values were observed during the movements (flexion, abduction, extension with external rotation, and flexion with internal rotation). This indicates that the measuring devices were able to successfully measure joint reaction forces without any problems during THA.

CONCLUSION

In this study, we developed measuring devices that resemble a part of an artificial hip joint with the aim of quantitatively obtaining the tension of soft tissues during THA. Calibration tests were conducted on the nine developed measuring devices. The average error of 8.61% in the X-axis, 8.86% in the Y-axis, and 8.10% in the Z-axis were obtained. In the cadaver trial using the developed measuring devices, we successfully measured joint reaction forces.

REFERENCES

[1] Standard Practices for Force Calibration and Verification of Testing Machines. *ASTM* **E4-08**: 13-22, 2008.

Table 1: Calculated errors of the nine sensors.

	1	2	3	4	5	6	7	8	9	average
X (%)	9.13	9.73	5.14	7.47	9.93	13.64	6.79	6.70	9.00	8.61
Y (%)	7.66	12.49	8.74	7.64	7.89	13.30	7.74	7.82	6.43	8.86
Z (%)	5.39	10.73	7.49	11.10	5.44	8.71	5.15	7.02	11.90	8.10

EFFICIENT DESIGN METHOD OF HANDWRITING SELF-HELP DEVICES FOR INDIVIDUALS WITH UPPER LIMB DISABILITIES

Qian Li[1], Kazunori Hase[1] and Jun Suzurikawa[2]

[1] Graduate school of Systems Design, Tokyo Metropolitan University, Tokyo, Japan.

[2] Department of Assistive Technology, Research Institute of the National Rehabilitation Center for Persons with Disabilities, Saitama, Japan.

Email: li-qian@ed.tmu.ac.jp

INTRODUCTION

Handwriting, though essential, poses a significant challenge to individuals with upper limb disabilities, often resulting from neck injuries. Self-help devices, comprising assistive apparatuses and welfare equipment, are designed to counter mobility complications arising from paralysis linked with disabilities, illnesses, or age-related physical degradation. Thus, for individuals contending with upper limb disabilities, these handwriting-aiding self-help devices become critical for a dignified and independent existence [1]. Primarily developed by care professionals and occupational therapists, self-help devices are tailored to accommodate the physical and mental capacities of the user. However, the predominantly empirical and trial-and-error methodology of their production introduces inefficiencies, spanning the measurement of hand parameters, to the fabrication and evaluation of these devices. In this study, we propose a more streamlined approach from measurement to fabrication of handwriting self-help devices.

METHODS

As shown in the figure 1, the handwriting self-help device under study comprises two rings and a pen holder-like main body. The thumb and index finger are secured using these rings, facilitating handwriting by holding the main body between these two fingers.

In this study, we engaged a healthy adult male as the participant, and simulated a cervical spinal cord injury by maintaining a relaxed posture of the fingers. Utilizing a 3D scanner (iReal 2E, Scantech, China), we captured the participant's finger shapes by rotating the scanner 360 degrees horizontally around the hand. The acquired point cloud data were then transformed into a triangular mesh, and the resulting three-dimensional shape data were preserved in an STL file format. Further, we employed the 3D hand pose estimation technique [2] to accurately estimate finger joint angles and extract essential parameters. Leveraging finger details of STL file format and these parameters, we could automatically generate the shape of self-help device models using Inventor (Autodesk, America).

The main parameters considered for designing these self-help devices are as follows:

1. Diameter of the main body (cylinder)
2. Height of the main body
3. Diameter of the two rings
4. Joining position between the ring and the main body
5. Angle of attachment of the ring to the main body

Upon inputting the main parameters, the self-help device model is archived in an STL file format via Inventor, and subsequently printed using a 3D printer (CR-10S Pro V2, Creality, China) with polylactic acid (PLA) material.
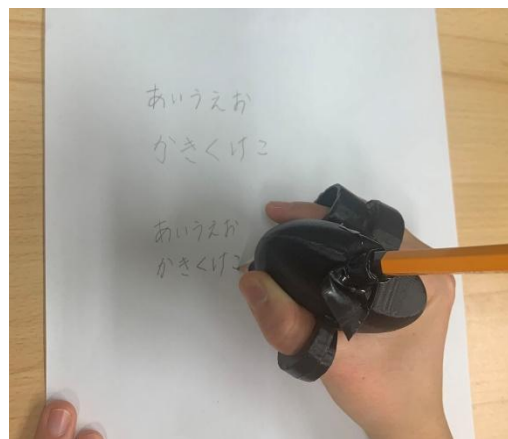
Figure 1 A handwriting self-help device using a 3D printer.

RESULTS AND DISCUSSION

Figure 1 depicts the participant undertaking subjective handwriting assessments with the aid of the self-help device. The device notably improves writing stability, thereby enabling more effortless handwriting. From measurement through design to fabrication, the entire procedure exhibits noteworthy efficiency. The self-help device is presently undergoing objective reliability testing, and the ensuing data and findings will be disclosed during the presentation.

CONCLUSION

This study presents an efficient design method, encompassing measurement to fabrication, for the design and production of self-help devices. The conceived model was realized using 3D printing technology. Initial subjective evaluations endorse the practicality and efficacy of the developed self-help device.

ACKNOWLEDGEMENT

REFERENCES

[1] Lowman E W et al. *Postgraduate Medicine* **34**(4): 425-427, 1963.
[2] Isaac J H et al. *Frontiers in Artificial Intelligence* **5**(4), 2022.

MEASUREMENT OF CONTACT STRESS BETWEEN HEEL AND SHOE

Takumi Agari[1], Kotaro Miura[2], Kazuhiko Sasagawa[2] and Kazuhiro Fujisaki[2]

[1] Faculty of Science and Technology, Hirosaki University, Hirosaki-shi, Japan.

[2] Graduate School of Science and Technology, Hirosaki University, Hirosaki-shi, Japan.

Email: k-miura@hirosaki-u.ac.jp

INTRODUCTION

The thin and flexible tri-axial stress sensors have been developed [1]. The sensors are capable of simultaneously measuring contact pressure and shear stress. The heel contact stress with regard to blister has not been measured because the lack of the thin and flexible sensors. In this study, we measured the heel contact pressure and shear stress during walking and investigated the effect of sock on the heel contact stress.

METHODS

The mechanism for measuring contact stress is shown in Figures 1(a) and (b). The sensor has a three-layer structure with a stress sensitive layer of conductive ink sandwiched by electrodes. The contact pressure is measured by the change in electrical resistance of the stress sensitive layer due to the compressive load. Shear stress can be measured by the change in electrical resistance due to the change in overlapping area between the upper and lower electrodes when shear stress is applied. The upper and lower electrodes were made from a copper-clad polyimide film by a wet etching process. The stress sensitive layer was made from conductive carbon ink by using a screen-printing method and sintered. The upper and lower electrodes were overlapped and covered with a polyurethane film. The sensor was coated by the human skin gel and the thickness of sensor is about 435 μm. The attached position and direction of fabricated sensor in the experiment was shown in Figure 1(c).

(a) Contact pressure

(b) Shear pressure

(c) Position and direction of sensor in experiment
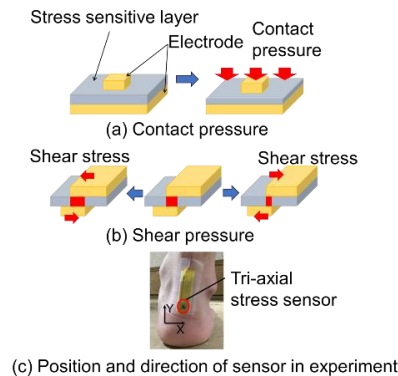
Figure 1 Measurement mechanism of contact stress and position of sensor in the experiment.

In this study, the contact interface between heel and the shoe were measured during the three steps walking without and with sock, respectively. The contact stresses were measured by the sensor attached on the position and direction as shown in Figure 1(c). The positive direction of X and Y-axis are set to the lateral direction and the proximal direction, respectively. The experiment was conducted for a 22-year-old male wearing the leather shoes. Walking motion in the experiment was recorded by the video camera. Two other pressure sensors were attached to toe and heel on the sole to synchronize stress data and the gait cycle.

RESULTS AND DISCUSSION

From the measured stresses data, contact pressure and Y-axis negative shear stress were detected at heel before heel contact (HC) in both cases of skin without sock and with sock. The Y-axis positive shear stress was detected in the standing phase. After that motion, Y-axis negative shear stress was also detected before the moment of toe off (TO). By comparing the results without and with sock, it is found that the duration time of contact pressure without sock was shorter than that with sock. Table 1 shows the average of peak-to-peak of stresses data in Y-axis around HC and before TO. The change of shear stress with sock was significantly higher than that without sock when p-value was chosen as 0.05. It is because that contact between heel and shoe was unstable without sock and instantaneous large shear stress occurred.

CONCLUSION

The heel contact pressure and shear stress were measured by thin and flexible triaxial stress sensors during walking without and with socks. There was a difference in the duration time and value change of shear stress without and with sock.

REFERENCES

[1] Kudo Y et al. *Mech Eng Letters* **9**: 22-00309, 2023.

Table 1 Average of peak-to-peak values in Y-axis shear stress.

	HC	TO
Without sock	54.5 ± 17.6 [kPa]	23.2 ± 8.13 [kPa]
With sock	36.1 ± 10.5 [kPa]	16.3 ± 6.00 [kPa]

SWEEP FREQUENCY IMPEDANCE MEASURES OF DIFFERENT EAR CONDITIONS

Hikaru Nakagawa[1], Teruki Toya[2], Risa Nagai[3], Hisashi Sugimoto[3], Michio Murakoshi[4]

[1] Division of Frontier Engineering, Graduate School of Natural Science and Technology, Kanazawa University, Kanazawa, Japan
[2] Faculty of Engineering, Yamanashi University, Kofu, Japan
[3] Department of Otolaryngology–Head and Neck Surgery, Graduate School of Medicine, Kanazawa University, Kanazawa, Japan
[4] Faculty of Frontier Engineering, Institute of Science and Engineering, Kanazawa University, Kanazawa, Japan
Email: hikaru-nakagawa@stu.kanazawa-u.ac.jp

INTRODUCTION

Tympanometry is widely used for the diagnosis of conductive hearing loss associated with middle ear disorders. However, the results often differ from actual conditions of the middle ear. We have developed a sweep frequency impedance (SFI) meter as a more accurate diagnostic device for conductive hearing loss [1, 2]. The conventional SFI meter is large and inconvenient to carry, so we developed a new SFI meter with a reduced size (Fig. 1) [3, 4]. In the present study, SFI measurements were performed on adults with normal middle ear condition and patients with conductive hearing loss using this new device. Here, we describe the measurements for different ear conditions.
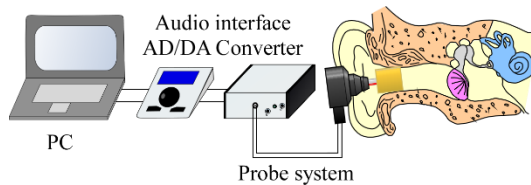
Figure 1 SFI meter configuration.

METHODS

The SFI inputs a sweep sound into the ear canal from a probe system, including a microphone and an earphone, and measures change in the sound pressure level (SPL) in the ear canal. The obtained result is called the SPL curve (Fig. 2). The SPL curve shows a large variation in sound pressure due to middle ear resonance at around 1 kHz in the normal ear. The frequency at this point is called the resonance frequency (RF), and the width of the increase in sound pressure level is called the ΔSPL. The middle ear condition is evaluated by these two parameters [1, 2].

SFI and tympanometry were performed to the ears with different middle ear conditions, including normal, fixation and separation.
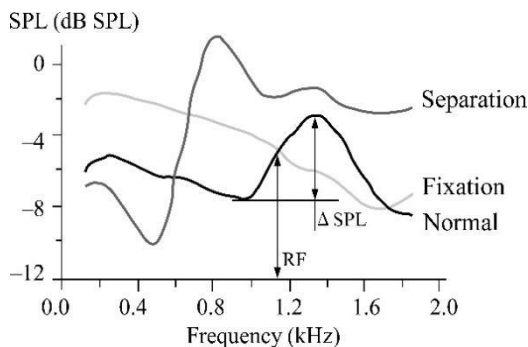
Figure 2 Examples of SPL curves.

RESULTS AND DISCUSSION

The SFI results obtained from normal ears were plotted on the distribution map, as shown in Figure 3 (a). All ears measured were within the normal range. These results indicate the equivalence of the new device to the conventional device. The SFI results showed that 49 ears were diagnosed as normal, with a sensitivity of 0.98. The sensitivity of tympanometry was 0.9, and 45 ears were found to be normal. These results indicate the superiority of SFI over tympanometry.

Figure 3 (b) shows the SFI result obtained from ears with ossicular-chain dysfunctions. The ears with separation/fixation were found to have lower/higher RF and higher/lower ΔSPL, respectively.
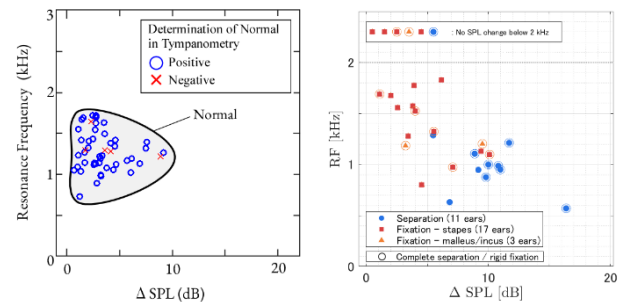
Figure 3 Distribution map of middle ear dynamic characteristics. (a) Normal ear distribution. (b) Distribution of ears with ossicular-chain dysfunctions.

CONCLUSIONS

SFI and tympanometry measurements were performed to the ears with different middle ear conditions. As a result, 98% of the results were within the normal range, indicating its equivalence to the conventional device. The sensitivity of SFI and tympanometry to the normal ear was calculated to be 0.98 for SFI and 0.9 for tympanometry, indicating the superiority of SFI over tympanometry. The different tendency was found in SFI measurements in ears with ossicular-chain dysfunctions.

ACKNOWLEDGEMENT

REFERENCES

[1] Wada et al, *Nippon Jibiinkoka Tokeibugeka Gakkai Kaiho* (in Japanese), **97** (8):1443-1455, 1994.
[2] Wada et al, *Ear Hear*, **19** (3): 240-249, 1998.
[3] Murakoshi, et al, *Int J Pediatr Otorhinolaryngol*, **77** (4): 504-512, 2013.
[4] Kanka, et al, *Int J Pediatr Otorhinolaryngol*, **134**: 110061, 2020.

THE EFFECT OF VIRTUAL REALITY-BASED AEROBIC DANCE EXERCISE PROGRAM ON CARDIOPULMONARY FITNESS IN OLDER ADULTS

Wan Yun Huang [1,2], Rong-Ju Cherng [1,3*], Yi-Chun Du [4]

[1] Institute of Allied Health Sciences, College of Medicine, National Cheng Kung University, Tainan, Taiwan

[2] Department of Physical Medicine and Rehabilitation, Kaohsiung Veterans General Hospital, Kaohsiung, Taiwan

[3] Department of Physical Therapy, College of Medicine, National Cheng Kung University, Tainan, Taiwan

[4] Institute of Biomedical Engineering, College of Engineering, National Cheng Kung University, Tainan, Taiwan

Email: rjc47@mail.ncku.edu.tw

INTRODUCTION

Frailty is one of the leading causes of fatal and nonfatal injuries in older adults. Decreased cardiorespiratory fitness is one of the key impairments that lead to frailty [1]. Therefore, to improve cardiopulmonary training is important. Virtual reality (VR) which offers a multifactorial approach showed potential effects on decreasing mobility, balance, and fall risk in the elderly [2]. However, the effect on cardiopulmonary fitness is unclear. The study was to examine effect of a VR-based aerobic dance exercise program on cardiopulmonary fitness in older adults

METHODS

Sixty older adults at the age of above 60 years were recruited from local community. They were randomly allocated into aerobic dance exercise group with VR (n=30) and aerobic dance exercise group without VR (n=30). The exercise program constitutes 5-min warm up stage, 20-min exercise stage and 5-min cooling down stage. It was executed for 30 min/day, 3 days/week and last for 8 weeks. Both groups of exercise were supervised by the same physical therapist. Physical function and quality of life were tested and measured at three time points: before intervention (WK0), immediate after intervention (WK8), and one month follow up (WK12). The outcome measures included 6-Minute Walk Test (6-MWT), Berg Balance Scale (BBS), The Chair Stand Test in 30-seconds (CST), Timed Up and Go Test (TUG), and Quality of Life Questionnaire by World Health Organization (WHOQOL-BREF).

RESULTS AND DISCUSSION

As shown in Table 1, the experiment group showed significant improvement in 6-MWT, BBS, CST, TUG and WHOQOL-BREF at WK8 and at WK12. The control group also showed significantly improvement in 6-MWT at WK8 and WK12, BBS at WK8, but not WK12, CST and TUG at WK12. No significant improvement in WHOQOL-BREF was noted at either WK8 or WK12. When comparing the improvement of above outcome measures between groups, the results showed that the experimental group had significantly larger improvement in 6-MWT at WK12, CST at WK8 and TUG at WK8.

CONCLUSION

Both aerobic dance exercise (with or without VR) are effective in improving certain outcome measures of cardiopulmonary fitness for older adults. However, aerobic dance exercise with VR system is more effective than without VR in 6-MWT, CST and TUG. Furthermore, it improves subjective feeling of quality of life which is not shown in the aerobic dance exercise without VR.

ACKNOWLEDGEMENT

REFERENCES

[1] Shema SR al. *Phys Ther* **94**: 1319-1326, 2014.

[2] Kamińska MS et al. *Clin Interv Aging* **14**: 2329-2338, 2018.

Table 1. Outcome measures scores of both groups at Week 0, Week 8, and Week 12

		Week 0	Week 8	Week 12	Week 0 vs. 8	Week 0 vs.12	EG vs.CG Week 0 vs. 8	EG vs.CG Week 0 vs.12
6-MWT								
	EG	359.07(63.34)	413.50(95.46)	431.53(93.27)	<0.001	<0.001	0.104	0.016
	CG	363.90(70.20)	393.60(71.56)	397.63(78.94)	0.018	0.008		
CST (??)								
	EG	10.73(3.02)	13.13(2.86)	13.03(3.00)	<0.001	<0.001	0.002	0.277
	CG	9.93(2.63)	10.33(3.34)	11.60(3.07)	0.388	<0.001		
BBS								
G	E	52.50(2.13)	53.27(1.74)	53.27(1.89)	0.001	0.001	0.234	0.181
G	C	52.93(2.15)	53.37(1.90)	53.30(2.02)	0.035	0.118		
TUG (seconds)								
	EG	8.71(1.70)	7.89(1.55)	7.77(1.59)	<0.001	<0.001	0.052	0.134
	CG	9.44(1.70)	9.22(1.74)	8.96(1.45)	0.387	0.032		
WHOQOL-BREF								
	EG	3.61(0.37)	3.85(0.30)	3.82(0.31)	<0.001	0.003	0.024	0.038
	CG	3.64(0.34)	3.72(0.37)	3.67(0.40)	0.180	0.586		

EG: Experimental group, CG: Control group, comparisons were shown with *p* values.

ELECTROMYOGRAPHY ANALYSIS OF THE HIP ADDUCTOR DURING BICYCLE ERGOMETER

Atsushi Iwashita[1], Yuto Konishi[2], Fujinaga takeshi[1], Tomoya Akakabe[1] and Kajiwara yosiyuki[1]

[1] Faculty of Health Sciences, Yamato University, Osaka, Japan.

[2] Faculty of Health Sciences, Butsuryo College of Osaka, Osaka, Japan.

Email: iwashita.atsushi@yamato-univ.jp

INTRODUCTION

Previous studies on muscle activity in bicycle ergometer exercise have mainly investigated hip extensor muscle groups such as the gluteus maximus and hamstrings, and knee extensor muscle groups such as the quadriceps. Only a few studies have focused on the hip adductor muscle group. Therefore, we focused on the muscle activity of the hip adductor muscle group during bicycle ergometer exercise. The hip adductor muscles, the greater adductor and longus adductor, extend the hip joint at deeper hip flexion angles. On the other hand, those muscles flex the hip joint when the hip joint is extended. Therefore, we performed bicycle ergometer exercise while varying two parameters and measured the muscle activity of the hip adductor muscles. The two parameters were hip angle and pedaling position.

Therefore, in this study, we aimed to clarify how muscle activity of the hip adductor muscles is affected by changing the position of the saddle and the position of the foot on the pedal during bicycle ergometer exercise.

METHODS

Subjects were 14 healthy adults (age: 20.3±0.6 years, height: 162.5±8.2 cm, weight: 83.0±9.0 kg) with no history of injuries to the joints of the lower extremities or trunk. The purpose and contents of the research were explained in writing, and consent was obtained from the participants. This study was approved by the Yamato University ethics review committee (approval number: 2021-3).

Electromyography was performed using a wireless electromyography sensor (active electrode). The target muscles were the adductor muscles of the right hip, the oblique head of the vastus medialis, the semitendinosus, the medial head of the gastrocnemius, and the tibialis anterior. The sampling frequency was 2000 Hz. The RMS value was obtained. Inertial sensors were used to measure the triaxial angles of the hip, knee, and ankle joints. The sampling frequency was 280 Hz and synchronized with electromyography.

The posture setting is two types of 90° hip flexion (high) and 110° (low) hip flexion at the top dead center of the saddle, with the foot position on the pedal as the front position. The second metatarsal bottom line was placed on the pedal shaft, and the rear position was 10 cm behind the front position. The exercise load setting was a power of 100 W and a pedal rotation speed of 50 rpm. Three cycles of electromyographic data obtained were used as data and were divided into flexion phase and extension phase based on the joint angle. The maximum isometric contraction time of each muscle was normalized as 100% to obtain %MVC. For statistical analysis, repeated measures three-way analysis of variance (Origin) was performed on the effects of the three factors of flexion-extension phase, saddle height, and foot position.

RESULTS AND DISCUSSION

As a result, the hip adductor muscle group exhibited muscle activity of 12.0% to 33.6%. In addition, there was no significant difference in the range of activity between the flexion and extension phases, suggesting that it is active in a wide range of bicycle ergometer exercise. In the flexion phase of the hip joint, it is necessary to suppress the movement in this abduction-external rotation direction, and it is thought that the adductor muscles of the hip joint are involved. In the extension phase, since the extension moment is generated from the relationship between the origin and stop at positions where the hip joint flexion angle is deep, it was suggested that it is involved in the generation of the hip joint extension force at least. The adductor muscles of the hip joints are thought to assist while performing proper positioning of the lower extremities during bicycle exercise.

Table 1 %MVC

	Flexion Phase				Extension Phase	
	Hip Abductor				Hip Abductor	
	Saddle Position				Saddle Position	
	High	Low			High	Low
Foot Ant.	20.8±16.1	18.7±11.9		Foot Ant.	20.8±18.0	20.5±16.7
Foot post.	17.7±13.3	17.7±8.0		Foot post.	19.4±14.5	21.5±16.2
	Semitendinosus				Semitendinosus	
	Saddle Position				Saddle Position	
	High	Low			High	Low
Foot Ant.	9.4±5.1	11.1±5.9		Foot Ant.	15.6±11.1	13.9±7.9
Foot post.	10.8±6.8	9.8±7.9		Foot post.	15.5±11.8	14.1±10.4
	Vastus Medialis				Vastus Medialis	
	Saddle Position				Saddle Position	
	High	Low			High	Low
Foot Ant.	14.6±8.7	19.6±11.1		Foot Ant.	43.1±27.6	52.6±29.3
Foot post.	14.7±7.3	18.6±9.2		Foot post.	52.5±34.2	60.8±37.4
	Gastrocnemius Medialis				Gastrocnemius Medialis	
	Saddle Position				Saddle Position	
	High	Low			High	Low
Foot Ant.	6.9±2.6	6.1±3.6		Foot Ant.	20.5±12.0	16.1±7.4
Foot post.	6.5±3.3	6.1±2.8		Foot post.	18.1±10.4	12.5±6.6
	Tibialis Anterior				Tibialis Anterior	
	Saddle Position				Saddle Position	
	High	Low			High	Low
Foot Ant.	21.2±10.2	18.8±9.3		Foot Ant.	6.9±3.7	7.4±3.6
Foot post.	24.8±13.1	24.6±9.1		Foot post.	7.6±4.8	9.5±6.5

(%MVC)

CONCLUSION

It was suggested that the hip adductor muscle group is active in a wide range of bicycle ergometer exercise, and that the leg is positioned appropriately during the hip flexion phase, and that the hip extension force is generated during the extension phase.

ACKNOWLEDGEMENT

EVALUATION OF THE RELATIVE RELATIONSHIP BETWEEN THE SCAPULA GLENOID AND HUMERAL HEAD BEFORE AND AFTER ARTHROSCOPIC ROTATOR CUFF REPAIR

Sayaka Matsuguma[1], Takeshi Shimoto[1], Kazuki Noda[1], Satoru Ikebe[2], Eiji Tashiro[3], Naoya Kozono[3], Naohide Takeuchi[3], Satoshi Hamai[3], Yasuharu Nakashima[3] And Hidehiko Higaki[4]

[1] Fukuoka Institute of Technology, Fukuoka, Japan.
[2] National Institute of Technology, Kitakyushu College, Fukuoka, Japan
[3] Kyushu University, Fukuoka, Japan
[4] Kyushu Sangyo University, Fukuoka, Japan
Email: mhm22109@bene.fit.ac.jp

INTRODUCTION

A rotator cuff tear (RCT) is a common disorder of the glenohumeral joint. An arthroscopic rotator cuff repair (ARCR) is one of the surgical treatments for patients with severe RCTs who are unable to perform daily activities. However, the larger the tear in RCT, the more frequent rotator cuff re-tears are reported after ARCR [1]. Therefore, it is important to visualize how the scapula and humeral head are displaced to understand the shoulder condition in detail. The purpose of this study was to visualize and evaluate the trajectories of the scapular glenoid center and humeral head center in three dimensions (3D) by applying our original 2D-3D registration technique.

METHODS

The subject was one male patient (65 years old, BMI: 25.6) who had a massive RCT with a postoperative period of about one year after the surgery. The movement of subject was the scapular plane in full abduction. Before and after the ARCR, periodic X-ray images of the movement of subject were taken using a flat-panel detector. 3D position and orientation were measured by comparing the solid model reconstruction from the CT data with the serial X-ray images [2]. The relative relationship between the scapula and humerus before and after the ARCR was reproduced on 3D-CAD based on the analysis results. The trajectories of the scapular glenoid center and humeral head center were then visualized and evaluated in 3D. Anatomical coordinate systems of the humerus and scapula were defined according to the International Society of Biomechanics standard [3].

RESULTS AND DISCUSSION

The trajectories of the scapula glenoid center and humeral head center at each abduction position from a glenohumeral joint abduction angle of 15 degrees to the maximum were obtained (Figure 1). Both before and after the ARCR, the trajectory of the humeral head center at the scapula humeral joint abduction angles greater than 90 degrees oscillated back and forth and side to side. During full abduction of the scapular plane, the humerus was pushed down by the rotator cuff. Before the ARCR, the humeral head was unstable because of rotator cuff dysfunction, and it was considered that this effect caused the humeral head to move upward. After the ARCR, the humeral head was pushed down by the rotator cuff due to restoration of rotator cuff function, but it moved anteriorly and laterally. The short postoperative period may have resulted in insufficient repair of the rotator

cuff and instability of the shoulder joint. The distance between the scapula glenoid center and the humeral head center was calculated for each glenohumeral joint abduction angle before and after surgery. The postoperative distance between the scapula glenoid center and the humeral head center was shorter than the preoperative distance. It was considered that the surgery may have improved the afferent nature of the glenohumeral joint.
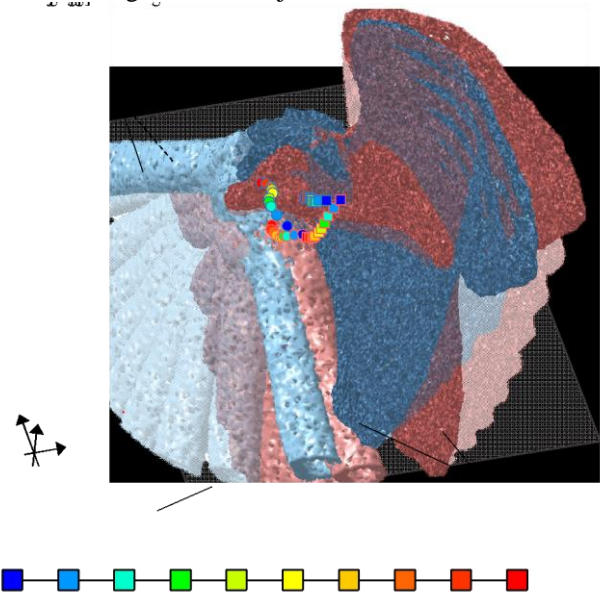
Figure 1 Trajectories of scapular glenoid center and humeral head center before and after ARCR

CONCLUSION

The trajectories of the scapula glenoid center and humeral head center were derived for the glenohumeral joint before and after ARCR in 3D. As a result, different trajectories were identified, predicting scapulohumeral joint instability before and after ARCR. This study can be applied to quantitative dynamic evaluation before and after ARCR and further consideration of the influence of muscle may contribute useful information.

REFERENCES

[1] Makihara T et al. *J Minimally Invasive Orthopaedic Surgery* **97**: 2-8, 2020.
[2] Kozono N et al. *J Orthopaedic Surgery* **28**(3): 1-7, 2020.
[3] Wu G et al. *J Biomech* **38**: 981-992, 2005

STABILIZING ROLE OF THE ACROMIOCLAVICULAR JOINT LIGAMENTS ALLOWS THE CONTRIBUTION OF CLAVICULAR MUSCLES TO ARM ELEVATION

Takayuki Aimi[1,2], Atsushi Ueda[3], Yasuo Nakamura[1]
[1] Doshisha University, Kyoto, Japan. [2] Japan Society for the Promotion of Science, Tokyo, Japan.
[3] Kansai University of Welfare Sciences, Osaka, Japan.
Email: aimibiomechanics@gmail.com

INTRODUCTION

The acromioclavicular joint (AC) links the scapula to the clavicle. It is stabilized by the acromioclavicular and coracoclavicular (AC/CC) ligaments, which restrict specific movements to facilitate shoulder-related tasks [1]. As young athletes often injure the AC joint [2], understanding the role of the ligaments is necessary for effective injury prevention and rehabilitation. However, most previous studies on the AC/CC ligaments have used cadaver data; thus, the effect of these ligaments on muscle function during active movements in living humans remains unelucidated. Therefore, this study aimed to determine the effect of AC/CC ligaments on muscle function during arm elevation. We calculated the muscle work using musculoskeletal simulation with and without the ligaments and compared the results.
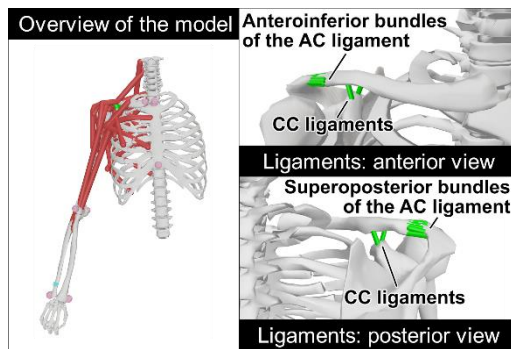
Figure 1 Shoulder musculoskeletal model used in this study.

METHODS

Doshisha University approved the experimental protocol (no.21022). We used a previously validated shoulder model with AC/CC ligaments added to the general shoulder model [3] as nonlinear springs based on cadaver data (Figure 1). Five healthy male volunteers (mean age: 24.8 ± 2.6 y, height: 168.8 ± 6.6 cm, weight: 62.0 ± 9.3 kg) were required to elevate (3 s) and lower (3 s) their right arm six times in the scapular plane. We attached ten reflective markers to the participants' upper extremities and trunk, and obtained marker trajectories via a motion capture system (Motion Analysis, USA). We calculated the joint motions using Butterworth 6 Hz low-pass filtered trajectories through inverse kinematics. Muscle forces were estimated from the joint kinematics via static optimization, both with and without ligaments. We calculated muscle work by time integrating the absolute muscle power during each elevation phase, averaging the six elevations, and normalizing by body weight. After verifying data normality by the Shapiro–Wilk test, we performed a two-tailed paired t-test ($\alpha = 0.05$) for each muscle to identify differences in muscle work between the models with and without ligaments.

RESULTS AND DISCUSSION

In the model with ligaments, the clavicular muscles (anterior deltoid, upper trapezius clavicular part, and pectoralis major clavicular part) performed significantly more work than those without ligaments. Alternatively, the surrounding muscles (the upper trapezius scapular part and middle deltoid) performed significantly less work (Table 1). The AC/CC ligaments stabilized the clavicular axial rotation, thus allowing the clavicular muscles to exert force effectively, which is probably the reason for the increased work of these muscles; as a result, the surrounding muscles were less demanding. By contrast, without ligaments, the clavicular muscles were unable to exert force since the clavicle posture was extremely sensitive to these forces. Conservative therapy is often employed for AC/CC ligament injuries; however, attention should be paid during the treatment and rehabilitation processes because such conditions may increase the load on certain muscles.

CONCLUSION

The presence of the AC/CC ligaments significantly increased the work of the clavicular muscles while decreasing the work of the surrounding muscles during arm elevation. This finding highlights the role of the AC/CC ligaments in efficiently exerting clavicular muscle forces by stabilizing the clavicular rotation.

ACKNOWLEDGEMENT

REFERENCES

[1] Sahara W et al. *J Orthop Res* **24**: 1823-31. 2006.
[2] Pallis M et al. *Am J Sports Med* **40**: 2072-7. 2012.
[3] Seth A et al. *Front Neurorobot* **13**: 90. 2019.

Table 1: Work done by the clavicular muscles and their surrounding muscles during arm elevation

Muscle	Part	Mean muscle work (±standard error) [J/kg]		Mean difference (±standard error) [J/kg]	t ratio	P value
		with ligaments	without ligaments			
Superior Trapezius	Scapula	0.084 (±0.021)	0.113 (±0.030)	−0.030 (±0.009)	3.43	0.026
Superior Trapezius	Clavicle	0.091 (±0.020)	0.004 (±0.001)	0.087 (±0.010)	8.68	<0.001
Anterior Deltoideus	Clavicle	0.413 (±0.112)	0.008 (±0.003)	0.405 (±0.056)	7.29	0.002
Middle Deltoideus	Scapula	0.288 (±0.129)	0.409 (±0.117)	−0.121 (±0.036)	3.32	0.029
Pectoralis Major	Clavicle	0.067 (±0.036)	0.004 (±0.003)	0.064 (±0.017)	3.86	0.018

MUSCULOSKELETAL SIMULATION TO ESTIMATE MUSCLE ACTIVITY AND REACTION FORCES OF KNEE OSTEOARTHRITIS PATIENTS WHILE WALKING

Takahiro Gempei[1], Daisuke Tawara[2] and Masaya Anan[3]

[1] Graduate School of Science and Technology, Ryukoku University, Otsu, Japan.
[2] Department of Mechanical Engineering and Robotics, Ryukoku University, Otsu, Japan.
[3] Faculty of Welfare and Health Sciences, Oita University, Oita, Japan.
Email:datawara@rins.ryukoku.ac.jp

INTRODUCTION

Knee osteoarthritis (KOA) is a disease in which joint cartilage is degenerated and destroyed, causing joint function deterioration due to pain[1]. One of the treatments for KOA is rehabilitation. Because KOA is closely related to the mechanical aspects of the knee joint, such as stress concentration and changes in muscle forces due to abnormal walking, it is necessary to evaluate and elucidate the specific loads around the knee in the treatment process. In this study, to assess the mechanical loads around the knee in KOA patients, muscle forces and joint reaction forces while walking were calculated, reflecting the height, weight, and walking motion of patients. Then, differences of muscle activity and joint reaction forces between KOA and healthy subjects were compared and the potency of the musculoskeletal analysis was discussed.

METHODS

The walking motions of KOA patients A (155.6cm, 49kg, bilateral affected), B (150cm, 58kg, right side affected) and C (154cm, 53kg, right side affected), and a healthy subject (174.5cm, 68kg), were captured using the Vicon (with 60 markers throughout the body). Then, using the AnyBody Modeling System, we performed inverse dynamics analysis on each model (Fig.1(a)), and assessed changes in muscle activity, knee joint reaction force and ankle joint reaction force in the right leg in a one-gait cycle.

RESULTS AND DISCUSSION

Figure 1(b) shows changes in muscle activity of the triceps surae muscle of the right leg during a one-gait cycle. At 30%-50% of the one-gait cycle, the muscle activity of the lateral soleus muscle and the medial gastrocnemius muscle in the healthy subject were almost the same. However, the lateral soleus muscle force was greater than that of the medial gastrocnemius muscle in the patients, suggesting that the balance of the exerted amount of the triceps surae muscle

force of the lower extremities of the KOA patients was biased toward the outside compared with that of the healthy subject. The gastrocnemius muscle acted to flex the knee joint and the activity of the inner gastrocnemius muscle in patients was lower than that in the healthy subject. This means that the knee flexion function of patients was reduced. In addition, considering that the soleus muscle is a muscle which acts on the plantar flexion of the ankle joint, the result that the muscle activity of the lateral soleus muscle force was greater in patients than in the healthy subject indicates that the plantar flexion function of the patients was increased, and patients walked in such a way to protect their knees[2]. In the comparison of the joint reaction forces of the knee and the ankle between the patients and the healthy subject, we found that the reaction force in the anteroposterior direction of KOA patients was greater than that in the healthy subject, meaning that the patients walked with more load on the joints. Thus, we were able to obtain patient-specific tendency in muscle activity and joint reaction forces of KOA.

CONCLUSION

We performed musculoskeletal analysis of KOA patients and healthy subjects, and differences in muscle activity and joint reaction forces were demonstrated. We discovered the potency of musculoskeletal analysis in assessing the specific loads around the knee.

ACKNOWLEDGEMENTS

REFERENCES

[1] Yuzi Kuroki. *Japanese Physical Therapy Association,* **38**(8): 637~638, 2011.
[2] Zehua Chen. *Frontiers in Bioengineering and Biotechnology* **9**, 2021.
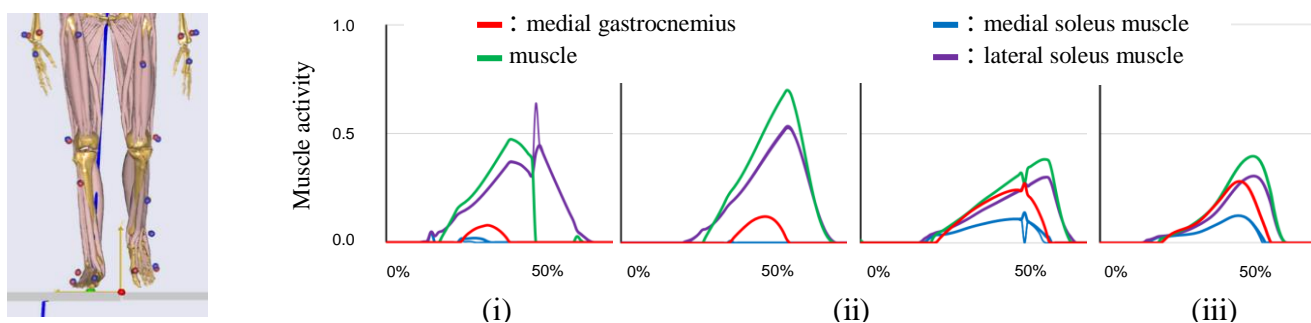
Figure 1 Musculoskeletal model and changes in muscle activity in the right triceps surae (i: Patient A, ii: patient B, iii: patient C, iv: healthy

NONINVASIVE DIAGNOSTIC SYSTEM FOR KNEE OSTEOARTHRITIS USING VIBRATION RESPONSE

Takeshi Tokoshima[1], Kazunori hase[1], Rui Gong[1], Makoto Yoshida[1] and Susumu Ota[2]
[1] Department of Mechanical Systems Engineering, Tokyo Metropolitan University, Tokyo, Japan.
[2] Physical Therapy Course, Seijoh University, Aichi, Japan.
Email: tokoshima-takeshi@ed.tmu.ac.jp

INTRODUCTION

Knee osteoarthritis currently affects over 300 million individuals worldwide, positioning it as one of the most prevalent arthropathies both domestically and internationally [1]. Knee osteoarthritis is characterized by knee pain and aberrant load distribution within the knee joint, which can impede walking in severe cases. Early detection of asymptomatic or mildly symptomatic knee osteoarthritis is crucial in order to prevent grave complications; however, this necessitates the availability of diagnostic tools that can readily identify knee osteoarthritis.

Recent studies pertaining to knee osteoarthritis diagnosis have explored the examination of joint sounds elicited during activities such as walking and squatting, as well as assessing joint instability and comparing it with that of a healthy knee. Nevertheless, a conclusive method for diagnosing knee osteoarthritis without relying on knee joint motion remains elusive.

In a prior investigation, the influence of meniscus injury/tear on frequency was confirmed using a cadaveric limb with an artificially induced meniscus tear [2]. The objective of this study is to apply this methodology to ascertain the effect of knee osteoarthritis on frequency. By utilizing a manipulable knee model, we will assess the alterations in vibration analysis resulting from modifications to the soft tissue of the knee within the same individual.

METHODS

In order to noninvasively diagnose knee osteoarthritis without requiring patient movement, we exposed porcine knees to vibration and measured the degree of vibration attenuation by the joint's soft tissue. To simulate a seated human subject, the femur was supported parallel to the ground by a pillar, with the knee flexed at 90 degrees and the tibia positioned perpendicular to the ground. Accelerometers were placed on the rough surface of the tibia and above the patella, areas with relatively less soft tissue. Accelerometers with a sampling frequency of 9,000 Hz were used, focusing on the previously identified significant frequency range of approximately 3,000 Hz. An inertial-type compact shaker (Model 2002E, manufactured by Modal Shop Corporation) was utilized to transmit the vibration, employing a sweep waveform that considered the magnitude of the vibration. In this study, a sweep waveform ranging from 20 Hz to 3,000 Hz, within the shaker's excitation capability, was used. The experimental procedure involved knee processing, measurement, and subsequent knee processing. The measured knee conditions followed the order of initial, Sham, meniscus tear, chondromalacia, cartilage wear, and total knee removal, based on the KL classification [3].

The measured accelerations were filtered and subjected to vibration analysis to determine whether there were any frequency variations before and after processing. Structural health monitoring methodology was applied for vibration analysis, where the frequency spectrum was averaged within each frequency band, and frequency analysis was performed on a matrix created based on the position and length of the data. The obtained matrix was then used to evaluate significant differences using two-sample t-tests and effect sizes [1].

RESULTS AND DISCUSSION

Results will be presented during the presentation. It is expected that there will be at least a significant difference in soft tissue removal.

CONCLUSION

Conclusion will be presented during the presentation.

REFERENCES

[1] Safiri S et al. *Ann Rheum Dis.***79**: 819-828, 2020.
[2] Safaei M et al. *in IEEE Transactions on Neural Systems and Rehabilitation Engineering* **29**: 350-359, 2021.
[3] Kellgren JH. et al. *Ann Rheum Dis* **16**: 494-502, 1957.

HIGH TIBIAL OSTEOTOMY INCREASES MEDIAL COMPARTMENT ARTICULAR DISTANCES IN MEDIAL KNEE OSTEOARTHRITIS DURING STAND-TO-SIT USING 3D FLUOROSCOPY

Kao-Shang Shih[1], Pei-Ling Weng[2], Chia-Ling Fan[2], Yi-Chen Wu[2], Cheng-Chung Lin[3], and Tung-Wu Lu[2,4]

[1] Department of Orthopedic Surgery, Shin Kong Wu Ho Su Memorial Hospital, Taiwan, R.O.C.
[2] Department of Biomedical Engineering, National Taiwan University, Taiwan, R.O.C.
[3] Department of Electrical Engineering, Fu Jen Catholic University, Taiwan, R.O.C.
[4] Department of Orthopedic Surgery, School of Medicine, National Taiwan University, Taiwan, R.O.C.

Email: twlu@ntu.edu.tw

INTRODUCTION

Knee osteoarthritis (OA) is a prevalent condition resulting from the degeneration of articular cartilage, which leads to joint discomfort and rigidity, impacting the joint's mobility and daily functions, such as stand-to-sit. High Tibial Osteotomy surgery (HTO) has recently been widely used for patients with medial compartment OA [1]. The surgery aims to shift the contact load in the medial compartment towards the lateral and increase the medial articular gap. However, owing to technical difficulties, no study reported the effects of HTO surgery on the articular kinematics of the knee during stand-to-sit in terms of the measured inter-articular distances *in vivo*. Therefore, the current study aimed to identify the inter-articular distances during functional activities before and after HTO surgery.

METHODS

Eight patients with knee OA (age: 58.07 ± 9.51 years; BMI: 28.56 ± 5.27 kg/m^2) performed stand-to-sit before and after the HTO surgery with the 3D motions of bones measured by a biplane fluoroscopy system. Subject-specific bone models of the femur and tibia were reconstructed from computed tomography images, and the motions of the bones were measured by the 3D fluoroscopy image registration method [2]. The angles of the tibiofemoral joint and the inter-articular distances of the medial and lateral compartments of the joint during stand-to-sit were calculated to quantify the efficacy of HTO surgery. A paired-T test was used to compare pre and post-HTO conditions with $\alpha=0.05$.

RESULTS AND DISCUSSION

The pre-surgery inter-articular distance in both medial and lateral compartments of the joint was compared with the post-surgery inter-articular distances (Figure 1 (a), (b)). The patients who underwent HTO surgery showed significantly greater inter-articular distance in the medial compartment for knee flexion between 35° and 65°, and there was no significant difference in the lateral compartment in all degrees. These results showed that after the HTO surgery, the change of the tibial alignment led to medial condylar lift and increased the distance between the medial compartment articular surfaces, which may help stop the deterioration of cartilage degeneration in the medial compartment. The current results suggested that patients with medial compartment knee OA can expect improved clinical outcomes after HTO surgery.
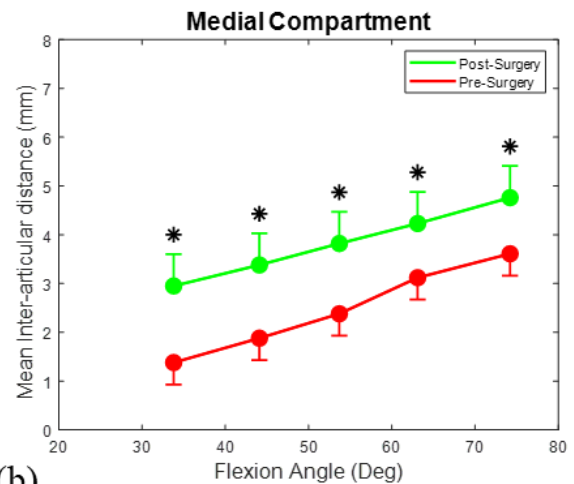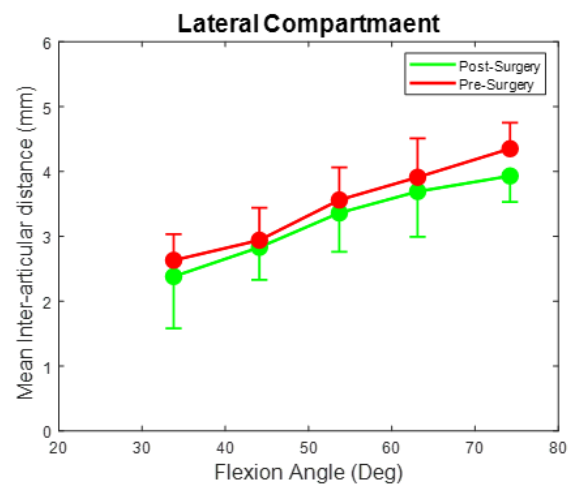
Figure 1 Mean values (standard deviations) of the inter-articular distances of the (a) medial and (b) lateral compartment of the tibiofemoral joint against the knee flexion angle during stand-to-sit pre (red) and post (green) HTO surgery. * Significant difference between pre-surgery and post-surgery groups.

CONCLUSION

The HTO surgery effectively partially unloaded the affected compartment of the tibiofemoral joint, as evidenced by a statistically significant increase in the inter-articular distances within the medial compartment. These findings provide valuable insights into the underlying mechanisms of the current treatment approach for medial compartment arthritis.

REFERENCES

[1] La Prade RF et al. J. *Arthrosc. Jt. Surg.* **28**(3): 354-364, 2012.
[2] Lin, C. et al. *Appl. Sci.* **10**(23): 8426, 2020.

APPLICATION OF DYNAMIC TAPE ON SEMICONDUCTOR WORKERS WITH REPETITIVE LOW BACK PAIN

Tian-Hong Wang[1], Jing-Min Liang[1], and Wen-Lan Wu[1]

[1] Department of Sports Medicine, Kaohsiung Medical University, Kaohsiung, Taiwan

Email: wenlanwu@kmu.edu.tw

INTRODUCTION

Long duration, repetitive motions, and muscle endurance requirements often cause repetitive low back pain (LBP) problems for workers in the semiconductor industry. Dynamic Tape (DT) provides unique adhesive stretching properties to help absorb stress on joints or soft tissues during movement, which promotes motor performance and improves work efficiency [1]. The aim of this study was to investigate influence of the application of DT on muscle strength, endurance, electromyographic activity (EMG) of lumbar extensor muscles, Visual Analogue Scale (VAS) scores of severity of pain, and the scores of the questionnaires Fear Avoidance Beliefs (FABQ 2).

METHODS

This study adopted a crossover study design. 28 manual laborers in the semiconductor industry who had repeated low back pain in the past three months were recruited in this study. Each participant was tested under two conditions, dynamic tape (DT) or no tape condition (no-DT), in random order, with each condition separated by more than 2 days. Participants were asked to complete a maximum isometric contraction test of the back extensors, three muscle endurance tests (Kneeling Forward Lean Test, Repetitive Lifting Test, and Biering-Sorensen test, **Figure 1**), and fill out two questionnaires (VAS, FABQ2) in each condition. A microFET®2 was used to record the back extensors maximum isometric muscle strength. For EMG analysis, the peak/mean value and median frequencies of the erector spinae muscle were analyzed in the pre- and post- periods of the three muscle endurance tests. The total performance time of each muscle endurance tests and VAS after testing were also recorded. Finally, the FABQ2 was measured after three days of taping to compare with the FABQ2 scores before the intervention.

RESULTS AND DISCUSSION

The application of the DT significantly prolonged the total performance time of the three muscular endurance tests, reduced the erector spinae muscle's activity, and maintained the median frequency in the post-periods of the endurance tests. In addition, VAS in the DT condition was significantly lower than in the no-DT condition after performing the

Repetitive Lift Test and Kneeling Forward Lean Test. Besides, the results also indicated that the maximum isometric strength and FABQ2 were significantly improved after the application of the DT.

Figure 1 Three muscle endurance tests, (A) Kneeling Forward Lean Test, (B) Repetitive Lifting, and (C) Biering-Sorensen test, Test.

CONCLUSION

For LBP workers in the semiconductor industry, applying the DT on the back extensor muscles prolongs endurance test performance without increasing muscle activity. It is also effective in increasing the maximum isometric strength of the back extensors and reducing the FABQ2 to improve work performance.

ACKNOWLEDGEMENT

None.

REFERENCES

[1] Alahmari KA et al., *PLoS One*, **15**(9):e0239505, 2020.

CLASSIFYING FUNCTIONAL DIFFERENCES BASED ON FUGL-MEYER ASSESSMENT FOR UPPER EXTREMITY (FMA-UE) USING MACHINE LEARNING AND MARKERLESS POSE ESTIMATION

Yu-Sheng Lin[1], Yu-Chih Tseng[1], Chieh-Hsiang Hsu[2], Yen-Po Huang[3], Chin-Chun Lin[4], Yu-Chen Lin[5] and Li-Chieh Kuo[2]

[1] Department of Mechanical Engineering, Southern Taiwan University of Science and Technology / Tainan, Taiwan.
[2] Department of Occupational Therapy, National Cheng Kung University / Tainan, Taiwan.
[3] Department of Medical Equipment Development and Application, Hungkuang University / Taichung, Taiwan.
[4] Department of Physical Therapy, I-Shou University / Kaohsiung, Taiwan
[5] Department of Occupational Therapy, Da-Yeh University / Changhua, Taiwan.
Email: yushenglin@stust.edu.tw

INTRODUCTION

In recent years, the field of remote rehabilitation has garnered considerable interest as a result of the epidemic's repercussions. Nevertheless, the accurate identification of stroke occurrence and the assessment of recovery progress generally necessitate therapist confirmation through visual observation. Emerging studies have demonstrated the viability of employing OpenPose, a sophisticated gesture detection technology, for monitoring human activities including running, walking, and ball throwing [1, 2]. Diverging from conventional approaches such as VICON, OpenPose allows for markerless operation and affords users enhanced mobility within an unconstrained setting.

To discern disparities between healthy individuals and patients in the post-recovery phase, this study presents a novel approach grounded in machine learning techniques for classification. The primary objective is to investigate functional discrepancies for upper extremity based on the Fugl-Meyer Assessment (FMA-UE) guidelines. By adopting this approach, therapists can effectively evaluate the conditions of their subjects, thereby facilitating the assessment process.

METHODS

A. Methodology and Dataset

The methodology employed in this study involved capturing 6-second videos using the built-in cameras of mobile devices. Participants were instructed to perform various specified motions, while a total of 14 individuals (comprising 9 healthy subjects and 5 patients) were included. The selection of 6 different motions was based on the Fugl-Meyer Assessment (FMA) guidelines. In total, 110 samples were obtained, encompassing both normal and patient cases. These videos were subsequently processed using the pose estimation OpenPose, which generated joint trajectories indicative of functional quality. Notably, when compared to the conventional motion capture method utilizing VICON, the mean absolute error resolution was approximately less than 20% maximum movement.

B. Data Processing and Classification Model

In order to assess the functional quality using markerless motion videos, the collected data underwent a series of processing steps. These included outlier removal, application of a Butterworth filter with a cutoff frequency of 6 Hz, resampling, and deduction of steady motion. Following these preprocessing steps, the feature data was statistically categorized into 11 distinct features. These features

encompassed parameters such as maximum displacement, velocity, and joint angle, with corresponding labels indicating whether the subject was classified as healthy or a patient. Subsequently, a K-nearest neighbours (KNN) model was employed to perform the classification task and determine the functional quality.

RESULTS AND DISCUSSION

Figure 1 shows the result of that the KNN model achieved an 85% accuracy in classifying normal and patient cases. A few misclassifications occurred due to similarities in movement integrity, but overall, the model effectively classified the majority of the test data, demonstrating its effectiveness in distinguishing between healthy individuals and patients.
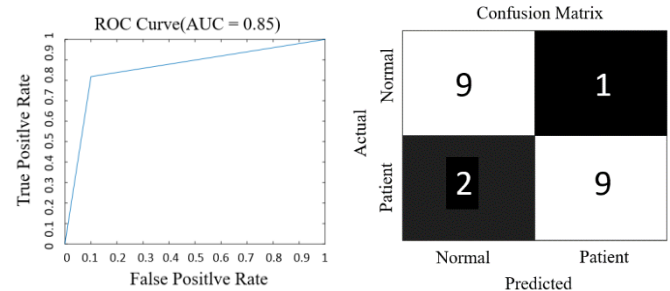
Figure 1 ROC curves and confusion matrix obtained by KNN model classification

CONCLUSION

This study utilized OpenPose as a motion capture system and achieved an 85% accuracy in classifying healthy individuals and patients. Future work aims to improve the assessment of patient movements and assist therapists in monitoring rehabilitation progress.

ACKNOWLEDGEMENT

REFERENCES

[1] Kim, W. et al., *Int J Industrial Ergon*. 2021
[2] Nakano, N. et al., *Front Sports & Active Living*, **2**, 50. 2020

ANALYSIS OF MUSCLE FATIGUE DURING A SIMULATED HEAVY TRAFFIC DRIVING: PRELIMINARY ANALYSIS

Jeevaraaj Vivekanandan[1], Juliana Binti Usman[1], Andri Andriyana[2], Goh Siew Li[3] and Lai Khin Wee

[1] [1] Biomedical Engineering, Universiti Malaya, Kuala Lumpur, Malaysia.
[2] Mechanical Engineering, Universiti Malaya, Kuala Lumpur, Malaysia.
[3] SEMREG, Faculty of Medicine, Universiti, Kuala Lumpur, Malaysia.
Email: juliana_78@um.edu.my

INTRODUCTION

Traffic jams and road accidents have been on the rise worldwide. Traffic jams causes prolonged sitting and repetitive pedal pressing action which leads to driver's fatigue. 20% of accidents in US are caused by driver's fatigue [1]. Muscle fatigue contributes to driver's fatigue, which is the most perceptual physiological state of drivers. Recently, generating Electromyography (EMG) based prediction models for muscle fatigue and computational models has been on the rise. In this paper, we would determine the primary muscles involved in pedal pressing and analyse the changes in the EMG signals before and after fatigue.

METHODS

7 participants were recruited, male drivers aged 20-25 years old with normal BMI and no previous musculoskeletal problems. 6 muscles are targeted, and surface electromyography (sEMG) are attached to rectus femoris (RF), vastus medialis (VM) and lateralis (VL), soleus (S), gastrocnemius medialis (GM) and lateralis (GL). Experimental procedure was adapted from Dimitrov et al [2]. Initially, participants would press the brake pedal with maximum voluntary contraction (MVC) for 20 seconds. Then, participants would press the pedal repetitively with 50% MVC with 20 pedal pressings per minute (Exp 1) until they are fatigue. Fatigue is determined using several questions from Swedish Occupational Fatigue [3]. Participants would press with MVC again. EMG and force will be taken before and after fatigue. 30 minutes' break will be taken, and the process would repeat with 40 pedal pressings per minute (Exp 2).

RESULTS AND DISCUSSION

The range of angle for knee joint was $112^\circ \pm 5^\circ$ and for ankle was $82^\circ \pm 3^\circ$. Both the angle of the knee and the ankle increased by 5° to 10° when depressing the pedal. The average durations taken for subjects to reach fatigue were 38 ± 6 minutes and 15 ± 3 minutes for 20 presses and 40 presses, respectively.

EMG signals was tested with multiple features, mean frequency (MNF), median frequency (MDF) and power spectrum density (PSD). We found that, PSD is not suitable for sustained contraction; it is used during the repetitive pressing and frequency spectrum shifts to the lower frequency during fatigue. During muscle fatigue, there is a drop in MNF and MDF similarly to Hosten [4]. Table 1 shows the results of paired t test which was done using MNF. The average change of gastrocnemius is higher compared to quadriceps muscles especially in Exp 2. It is much easier to contract smaller muscles compared to large muscles during a repetitive action.

CONCLUSION

Overall, there is no significant difference between fatigue and non-fatigue ($p>0.05$). Detection of driver fatigue is a major concern in vehicle design, road safety and transportation research. This paper would be beneficial for the studies in the mentioned fields.

ACKNOWLEDGEMENT

REFERENCES

[1] Sacco, M. & R.A. Farrugia. *International Symposium on Communications, Control and Signal Processing, IEEE.* 2012.
[2] Dimitrov, G.V., et al. *Med Sci Sports & Exerc* **38**(11): 1971-1979, 2006.
[3] Johansson, S., et al. *J of Rehabil Med* **40**: 737-743, 2008.
[4] Hosten, I. & H.Ramon, *J of Electromyography and Kinesiology*, **15**(3): 266-274, 200

Table 1: Paired t-test results of 6 muscles by comparing Mean frequency of participants during non-fatigue and fatigued conditions.

Muscles (Non Fatigue - Fatigue)	Mean		t value		p value	
	Exp 1	Exp 2	Exp 1	Exp 2	Exp 1	Exp 2
RF Non Fatigue - RF Fatigue	5.10 ± 7.28	0.33 ± 2.05	1.85	0.43	p>0.05	p>0.05
VM Non Fatigue - VM Fatigue	0.99 ± 3.68	1.52 ± 0.77	0.71	5.2	p>0.05	p<0.05
VL Non Fatigue - VL Fatigue	0.45 ± 6.26	0.09 ± 6.44	0.19	0.04	p>0.05	p>0.05
S Non Fatigue - S Fatigue	5.84 ± 16.28	1.69 ± 30.02	0.95	0.15	p>0.05	p>0.05
GM Non Fatigue - GM Fatigue	5.18 ± 11.22	1.21 ± 10.78	1.22	0.30	p>0.05	p>0.05
GL Non Fatigue – GL Fatigue	9.00 ± 16.56	6.03 ± 15.01	1.76	1.06	p>0.05	p>0.05

Effects of proximal-emphasized exercise equipment on balance for chronic stroke survivors

Yu-Lin You[1], Cheng-Feng Lin[2], Li-Chieh Kuo[3] and Fong-Ching Su [4,5]

[1] Department of Sports Medicine, China Medical University, Taichung, Taiwan.
[2] Department of Physical Therapy, National Cheng Kung University, Tainan, Taiwan.
[3] Department of Occupational Therapy, National Cheng Kung University, Tainan, Taiwan.
[4] Department of Biomedical Engineering, National Cheng Kung University, Tainan, Taiwan.
[5] Medical Device Innovation Center, National Cheng Kung University, Tainan, Taiwan.
Email: fcsu@mail.ncku.edu.tw

INTRODUCTION

Balance deficit is a common problem after stroke, which increased risk of falls [1]. Thus, the improvement of balance ability is a crucial goal for rehabilitation. The core (included the proximal lower limb) was the central part to the kinetic chain of movements, such as sports skill and balance ability [2], hence, the rehabilitation strategy that emphasized on the proximal lower limb for balance restoration is practicable. Pinnacle trainers (PT) is a pedal-type exercise equipment, in addition, the hip joint moments were greater than the knee and ankle joint moments during stepping on a PT which indicated the principal location for muscle force generation was the hip joint [3-5], therefore, PT is a proximal-emphasized intervention due to the greater hip joint muscle efforts. However, few studies compared the effects of PT with unweighting system on the balance ability restoration. Hence, the purpose of this study was to investigate the training effects of PT on the balance ability for individuals with chronic stroke.

METHODS

A commercially available PT (S776MA, SportsArt, Taiwan) (Figure 1a.) combined with a body weight support system (Figure 1b.) were used in this study to prevent falls during rehabilitation. Individuals with chronic stroke were enrolled in this study. Twenty-four participants were assigned in the PT group and the control group randomly. An 8-week intervention program was assigned for each group. Participants in the control group underwent an 8-week conventional therapy, for example, stretch exercise, strengthening exercise, and gait training for 60 minutes per session, and 3 sessions per week, while the PT group performed a total 60-minute intervention session, which included
30 minutes conventional therapy and 30 minutes exercise on the PT (Figure 1c). To assess the balance ability, participants were instructed to cross a 5-cm height obstacle. The center of pressure (COP) displacements during obstacle crossing.

(A)   (B)
Figure 1 The rehabilitation system.
(A) Pinnacle trainer, (B) body weight support system

RESULTS AND DISCUSSION

The displacement of COP in mediolateral direction was significantly decreased after PT intervention, however, no significant improvements were found in the control group (Figure 2). The lateral stability control ability was important for weight shifting movements, such as sit-to-stand [6]. The poor lateral stability was related to the risk of falls in the future [7]. Therefore, the improvement in the displacement of COP in the ML direction may thus be more crucial for the balance ability.
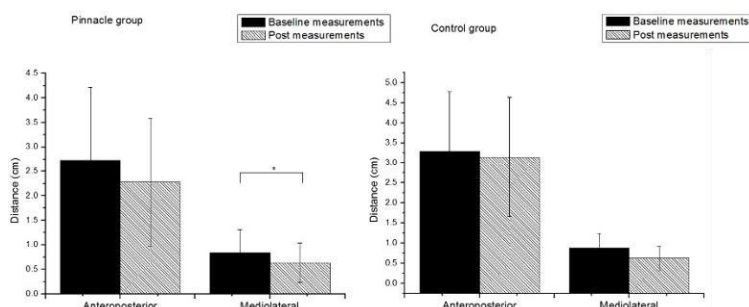
Figure 2 Comparison of posture sway during obstacle crossing between baseline measurements and post-intervention measurements for (A) Pinnacle trainer group; (B). Control group

CONCLUSION

The PT intervention could be effective on balance ability when crossing obstacles for individuals with chronic stroke.

ACKNOWLEDGEMENT

REFERENCES

[1] Ramnemark A et al. *Stroke* 31:1572-1577, 2000.
[2] Kibler W.B et al. *Stroke* 8:92-95, 1998.
[3] Tsai Y.J et al. *Int J Sports Med* 32:189-198, 2012.
[4] You Y.L. et al. *Gait Posture* 74: 45-52, 2019.
[5] You Y.L. et al. *Gait Posture* 77: 201-206, 2020.
[6] Mercer V.S. et al. *J Geriatr Phys Ther* 32: 6-15, 2009.
[7] Rogers M. et al. *Exerc Sport Sci Rev* 31:182-187, 2003.

ENHANCEMENT OF MASS TRANSPORT BY AN AGGREGATION OF SWIMMING MICROORGANISMS

Yu Kogure[1], Toshihiro Omori[2] and Takuji Ishikawa[1,2]

[1] Department of Biomedical Engineering, Tohoku University, Sendai, Japan.
[2] Department of Finemechanics, Tohoku University, Sendai, Japan.

Email: yu.kogure.s1@dc.tohoku.ac.jp

INTRODUCTION

Swimming microorganisms are often observed as aggregates in nature, for example, microalgae accumulated near free surfaces and biofilms constructed by bacteria. They play important roles as the base of food chains while they also inflict harm on our health as medical device fouling, so understanding and controlling their ecology is crucial for new technologies applications and harmful problems suppressing. Mass transport is one of the most essential factors related to microbial ecology since the transport of nutrients is involved in cell growth and their increase. Although previous studies have analysed the effect of hydrodynamic interactions on mass transport and clarified that diffusivity increased with higher cell concentration, they have only been performed up to a semi-dilute suspension of microswimmers [1]. Therefore, we aim to quantify the diffusivity and elucidate the mechanism in a packed suspension of swimming microorganisms using simulation.

METHODS

Swimming microorganisms were modelled by steady squirmers which swim generating slip velocities on their surfaces [2] and a packed suspension was represented by randomly configured squirmers with a volume fraction of 47%. Their orientations were also random to reproduce general states. In the simulation, we arranged 24 squirmers in a unit domain and applied the 3D periodic boundary condition to squirmers and the flow field, resulting in an infinite suspension. The net fluid velocity was set to zero. Additionally, squirmers were assumed to be stuck by external forces because they were highly packed.

The Reynolds number based on microorganisms' sizes and swimming speeds is small, so the flow field around them can be approximated as Stokes flow. The fluid velocity is given by the boundary integral equation (BIE),

$$\boldsymbol{u}(\boldsymbol{x}) - \langle \boldsymbol{u} \rangle = -\frac{1}{8\pi\eta} \sum_{n=1}^{24} \int_{A_n} \mathbf{J}^E(\boldsymbol{x}, \boldsymbol{y}) \boldsymbol{q}(\boldsymbol{y}) dA_y, \qquad (1)$$

where $\langle \boldsymbol{u} \rangle$ is the fluid velocity averaged over a plane in a unit domain, is the viscosity, $\mathbf{J}^E$ is the Green function based on the Ewald summation and $\boldsymbol{q}$ is the traction force exerted on a squirmer's surface by fluid. The BIE was solved with the boundary condition that the fluid velocity is equal to a surface velocity on a squirmer, and then fluid velocities at arbitrary position can be obtained. To quantify diffusion in a suspension, particles moving with fluid velocities and Brownian diffusion were tracked by Lagrangian manner and then diffusion tensors were calculated based on the mean-square displacement (MSD) of tracers. Moreover, we introduced the Péclet number which indicates whether mass transport is advection or diffusion dominated.

RESULTS AND DISCUSSION

Even though when advection was dominant, motion of particles was diffusive over long time duration (Figure 1(a)). This occurred when particles moving following one streamline were occasionally across to another streamline by Brownian motion. Figure 1(b) shows the ratio between this flow-induced diffusivity and the Brownian diffusivity when when $Pe = 1.0 \times 10^2$. D_{xx}^F, D_{yy}^F and D_{zz}^F are the diffusion components in each axis, respectively. Each diffusivity was enhanced by about 20 times, which was contributed by an aggregation of squirmers since the diffusivities increased as the squirmers' volume fraction became larger.

The isotropy of diffusion broke when the squirmers' orientation was the same. In that case, only the diffusivity in the orientational direction was largely enhanced, by about 100 times. Furthermore, the diffusivity increased depending on Pe in a high Pe regime. This indicates that even large molecules that would be difficult to transport only by thermal diffusion are facilitated by the aggregation of microorganisms.
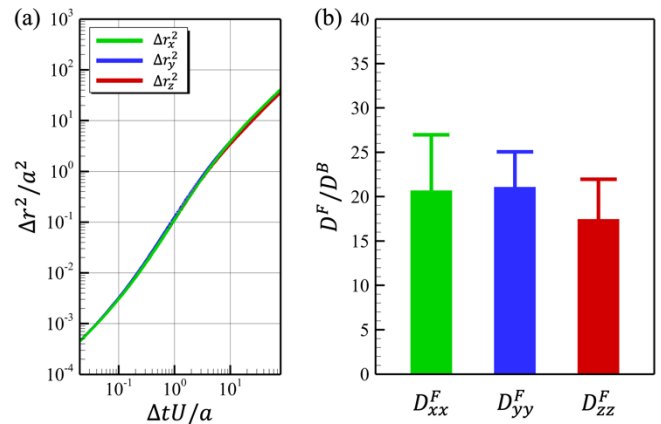
Figure 1 Flow-induced diffusion when $\phi = 0.47$ and $Pe = 1.0 \times 10^2$. (a) The MSD of tracer particles in each axial direction as a function of Δt. (b) The ratio of flow-induced diffusion components to the Brownian diffusivity. The values are the average of 16 independent cases and error bars are the standard deviations.

CONCLUSION

Swimming microorganisms promote mass diffusion by their aggregation. This enhancement leads to easier nutrient transport, which may improve their habitat environments.

REFERENCES

[1] Ishikawa T et al. *Phys Rev E* **82**: 021408, 2010.
[2] Blake J R *J Fluid Mech* **46**: 199-208, 1971.

SWIMMING SIMULATION OF ASCIDIAN SPERM CHEMOTAXIS

Sara Kamijo[1], Toshihiro Omori[1], Kogiku Shiba[3] and Takuji Ishikawa[1,2]
[1]Department of Finemechanics, Tohoku University, Sendai, Japan
[2]Department of Biomedical Engineering, Tohoku University, Sendai, Japan
[3]Shimoda Marine Research Center, University of Tsukuba, Shimoda, Japan
Email: sara.kamijo.s6@dc.tohoku.ac.jp

INTRODUCTION

Sperm chemotaxis plays an important role in the reproduction of organisms. An essential factor in chemotaxis is Ca^{2+}. It is known that a series of flagellar waveform changes in ascidian sperm that cause a swimming trajectory of repeated turns and straight paths is caused by an increase or decrease in intracellular Ca^{2+} concentration ($[Ca^{2+}]_i$) [1]. However, the mechanism that produces the asymmetric waveform and the relationship between the waveform change and $[Ca^{2+}]_i$ in the flagellum are still unexplained.

In this study, we developed a mathematical equation that links the waveform change and $[Ca^{2+}]_i$ and contribute to the elucidation of the mechanism of sperm chemotaxis.

METHODS

Since the size of ascidian sperm is very small (about 50μm), the Reynolds number around the sperm is very small. Therefore, the flow around the sperm can be described by the Stokes equation. The fluid motion of the flagellum of a sperm is described by Slender Body Theory [2].

We also consider the solid mechanics of the flagellum. The elastic force can be obtained by solving equilibrium equation with a finite element method.

Finally, we consider the internal driving force of the flagellum. The 9 doublet microtubules inside the flagellum are bending due to sliding of molecular motors called dynein. In this study, we assume that the 9 microtubules inside the flagellum are divided into two groups. Dynein sliding motion is assumed to be of two types: one is periodic sliding that produces propulsive force, and the internal driving force due to such sliding is defined as q_{a_0}. The other is a large slip of one microtubule section in one direction throughout the flagellum, and the internal driving force due to bending that occurs only near the neck is denoted q_{a_asym}. q_{a_asym} is controlled by the temporal variation of $[Ca^{2+}]_i$.

$$q_a = q_{a\_0} + q_{a\_asym}. \qquad (2)$$

The fluid force q_f, the elastic force q_e, and the internal driving force q_a are assumed to satisfy the following force balance equation.

$$q_f + q_e + q_a = 0. \qquad (1)$$

RESULTS AND DISCUSSION

By introducing q_{a_asym}, an asymmetric waveform could be produced. Furthermore, by changing the ratio of q_{a_0} to q_{a_asym}, we were successfully able to change the asymmetry index [1].

Figure 1 shows the results of the chemotaxis simulation. It shows that the sperm model is swimming toward the source of the sperm chemoattractant. This indicates that the model can exhibit chemotaxis by controlling the asymmetric force by time variation of $[Ca^{2+}]_i$.
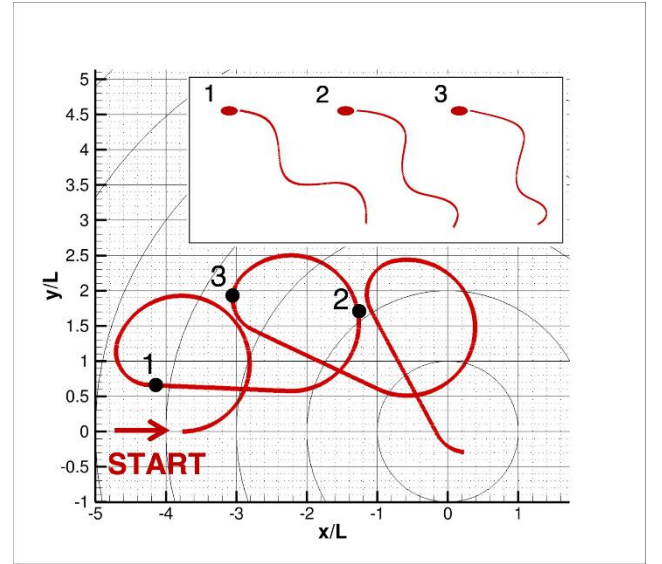
Figure 1 Sperm swimming trajectory introducing chemotaxis. The origin of the coordinates indicates the source of the sperm chemoattractant.

CONCLUSION

In this study, we developed a mathematical model linking waveform changes and $[Ca^{2+}]_i$ to clarify the mechanism of flagellar waveform changes in ascidian sperm that show chemotaxis.

We found that one possible mechanism that generates flagellar asymmetry is an asymmetric force acting on the sperm neck due to large dynein sliding. In addition, by controlling this asymmetric force with $[Ca^{2+}]_i$, we were able to simulate sperm chemotaxis.

REFERENCES

[1] Shiba K., et al. *PNAS* **105**: 19312-19317, 2008.
[2] Andersson HI., et al. *Phys. Fluids* **33**: 041904, 2021.

COLLECTIVE SWIMMING OF SPERMATOZOA
EMERGING FROM UNSTEADY HYDRODYNAMIC INTERACTIONS

Toshihiro Omori[1], Nanami Taketoshi[2], and Takuji Ishikawa[1,2]
[1] Department of Finemechanics, Tohoku University, Sendai, Japan.
[2] Department of Biomedical Engineering, Tohoku University, Sendai, Japan.
Email: omori@tohoku.ac.jp

INTRODUCTION

Genetically related individuals are more inclined towards altruism, and sperm from a single male may show cooperation and altruism to gain an advantage during sperm competition between males. Here, we report individual flagellar dynamics emerge collective swimming of spermatozoa [1]. Temporal fluctuations in flagellar beating, the driving force of sperm swimming, create unsteady fluid interactions between sperm, which in turn produce an overall ordered movement.

METHODS

Mammalian sperm are less than 100 μm in size and often have Reynolds numbers much smaller than 1. Fluid motion is therefore assumed to be viscous dominated, and fluid flow is governed by the Stokes equations. The flow field is described by a boundary-integral equation with Green's functions and the fluid motion is calculated by a boundary element method [2].

The flagellum of spermatozoa is highly elastic, and its deformation is analysed using a finite element method [3]. The flagellum is modelled as a Bernoulli-Euler rod as the radius is sufficiently small compared to the length, and the elastic force of the flagellum is calculated from the bending energy of the linear elastic body.

Flagellar beating is produced by the molecular motor dynein connected to axonemal microtubules; hydrolysis of ATP alters the structure of dynein, causing shear stress in the microtubules and flagellar flexion. The driving force produced by the coordinated motion of the dynein is expressed as an external force (force per unit length) at the continuum level acting on the microtubule. Since the total force on the flagellum is always zero under quasi-static motion without inertia, a mechanical model is constructed to represent sperm motion under a balance of fluid viscosity, elasticity and driving force; $\mathbf{f}_{fluid} + \mathbf{f}_{elastic} + \mathbf{f}_{active} = \mathbf{0}$ [3].

RESULTS AND DISCUSSION

A computational domain of 200 x 200 x 200 μm is set up and 72, 144 and 216 spermatozoa are randomly placed within the computational domain. In this case, sperm density corresponds to 5, 10 and 15 million cells per mL, respectively (typical human semen is 15 million spermatozoa per mL). A three-dimensional periodic boundary was set up to simulate sperm swimming in the suspension. Sperm swimming in disordered directions changed their swimming direction by repeated fluid interference, and finally a polar order emerged in which the whole sperm moved towards the same direction (Figure 1). The time required for reorientation of movement depends on the sperm number density and scales with ln n/n with respect to the density n.

So how is the polarity order formed? To investigate the mechanism, we calculated the motion of a toy model of a steady swimmer and found that no order mechanism is formed, and that ordered motion is formed by the interaction between unsteady flow and flagellar motion due to the undulation of the flagellar stroke. These results indicate that time-averaged active stress cannot predict organised multicellular movements, and that the accumulation of individual cell interactions is important for tissue formation. Next, we analysed the advantages of collective swimming for sperm in terms of swimming speed, work and efficiency. Swimming in groups speeds up compared to solitary swimming, with a simple increase in swimming speed with the number density. For example, at 15 million sperm/mL, they swim 2.3 times faster than when solitary swimming. On the other hand, the work and efficiency per cell were found to change little and grouping mainly contributed to an increase in swimming speed.
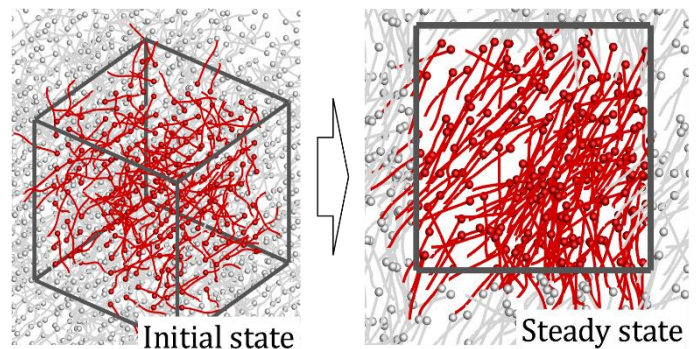
Figure 1 Emergence of collective sperm swimming

CONCLUSION

Simulations of sperm swimming show that the interaction between the unsteady flow produced by the sperm flagellum and cell motility results in the formation of a collective swim, with the whole group moving in the same direction. Collective swimming contributes to an increase in swimming speed and may be advantageous in winning the fertilisation competition.

REFERENCES

[1] Taketoshi N et al. *ArXiv*:2302.10572, 2023.
[2] Omori T et al. *PNAS* **117**: 30201-30207, 2020.
[3] Taketoshi N et al. *Phys Fluids* **32**: 101901, 2020.

FLYING YEAST: AEROSOL PARTICLES RELEASED DURING THE FERMENTATION

Ryoji Onishi[1], Kenji Kikuchi[2,1], Takuji Ishikawa[1,2]

[1] Graduate School of Biomedical Engineering, Tohoku University.
[2] Department of Finemechanics, Graduate School of Engineering, Tohoku University.
Email: ryoji.onishi.t1@dc.tohoku.ac.jp

INTRODUCTION

In this study, we use yeast as a model organism. In our previous research, Atul et al. (2021) revealed that top-fermenting yeast, which produces Ale beer, can move vertically in water for long distances by using the bubbles it produces [1]. In this study, we further developed the hypothesis that the bubbles generated by fermentation can burst, allowing yeast that do not have swimming ability to fly into the air. The objective of this study is to verify the hypothesis by observing the behaviour of bubbles on the surface of yeast culture media and capturing flying yeast.

METHODS

Firstly, an experiment was conducted to observe the behaviour of bubble-bursting at the water surface. Bubbles were released from a needle submerged in 60 mL of water in a culture test tube. The size of the bubbles was adjusted by changing the diameter of the needle. A metal halide light (LA-180Me , HAYASHI-REPIC Corporation , Japan) source was irradiated, and the moment the bubbles burst was captured by a high-speed camera (Phantom v.7.3, Vision Research, USA).

Secondly, we used Petrifilm to capture flying yeast. The baker's yeast *Saccharomyces cerevisiae* (SafAle™ S-04, Fermentis by Lesaffre, Co.) was used in the experiments. Petri-film (Petri-filmTM Aqua Yeast and Mold Count Plates, 3M Company, America) was used to verify whether the yeast was dispersed by the bursting of bubbles. Liquid medium was placed in a culture test tube, and baker's yeast Saccharomyces cerevisiae, cultured in advance to achieve an initial cell count concentration of 40 cells/mL, was added.

RESULTS AND DISCUSSION

The bubble-bursting on the water surface was captured by a high-speed camera and the results show that small droplets are sprayed upward at the time of bubble-bursting. It was found that the smaller the bubble radius, the higher the initial jet velocity, which was about 2 m/s.

A Petri-film was placed on top of the culture vessel after confirming that air bubbles appeared on the water surface of the culture medium. The results are shown in Figure 1: Two colonies were formed on the Petri-film. The same experiment was conducted four times, and the formation of a colony was confirmed in two experiments. On the other hand, no colonies were formed on the Petri film when the same experiment was performed three times using only YPD medium without yeast. These results demonstrated that the yeast flew and reached the Petri film, although the reproducibility was only one-half.
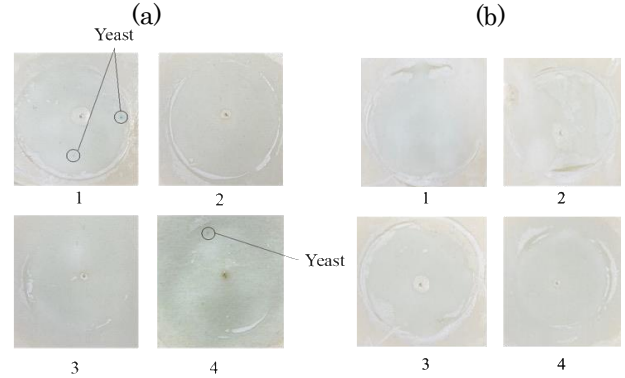
Figure 1 Yeast colonies on the upper Petri film. (a)For cultures with yeast. (b) For cultures without yeast.

We considered the jet velocity V at bubble burst and the maximum height z of flying droplets in yeast culture with yeast. From the study by Ghabache et al. (2017) [2], the jetting velocity V_{tip} due to bubble-bursting can be expressed as follows:

$$V_{tip}^2 = \sqrt[14]{\frac{\gamma^9 \mu^{16}}{g^3 \rho^{25}}} \frac{A}{R_b^2} \quad (1)$$

where γ is the surface tension, ρ is the density, μ is the viscosity, R_b is bubble radius and $A = 3.9 \times 10^4$ is a constant. The maximum height a drop can reach with a given initial velocity can then be captured by integrating the following differential equation:

$$\frac{4}{3}\rho\pi R_d^3 \frac{d^2z}{dt^2} = -\frac{1}{2}\rho_{\text{air}}\pi R_d^2 \left(\frac{dz}{dt}\right)^2 C_D - \frac{4}{3}\rho\pi R_d^3 g \quad (2)$$

where z is the drop height and C_D is the drop drag coefficient. We measured the density, viscosity, and surface tension of the yeast culture medium when the yeast fermented and derived the initial velocity from equation (1). Then, we solved equation (2) using that initial velocity and radius as the initial conditions. We observe that the droplet flying distance is the greatest when the bubble radius is close to 1 mm, indicating that the droplet flies about 13 cm.

CONCLUSION

In this study, we tested our hypothesis that yeast can be released into the atmosphere due to bursting bubbles generated by fermentation. This study verified the hypothesis, indicating that nonmotile yeast can travel from the bottom of liquid phase to up in the air.

REFERENCES
[1] Srivastava, et al. *J R Soc Interface* **17**, 20200735, 2020.
[2] Ghabache et al. *Phys. Rev. Fluids* **1**, 051901, 2016.

THERMAL CONDUCTIVITY MEASUREMENT OF SPIDER SILK USING THIN HOT WIRE

Daichi Sawada[1], Yoko Tomo[2], Takanobu Fukunaga[2], Kosaku Kurata[2], and Hiroshi Takamatsu[3]

[1] Graduate School of Engineering, Kyushu University, Fukuoka, Japan.
[2] Department of Mechanical Engineering, Kyushu University, Fukuoka, Japan.
[3] National Institute of Technology, Kumamoto College, Kumamoto, Japan.
Email: takamatsu.hiroshi.281@m.kyushu-u.ac.jp

INTRODUCTION

The development of materials with high thermal conductivity and low electrical conductivity is crucial to manage the increasing heat generation resulting from the increased integration and enhanced performance of electronic devices in recent years. In this context, spider silk, an insulating biopolymer, was reported to have a high thermal conductivity of 340~416 W/(m·K), which is comparable to that of metals [1]. However, measuring the longitudinal thermal conductivity of very fine spider silk is difficult, and therefore, the reported values of the high thermal conductivity is still controversial. In this study, we developed a new method, the ITX method consisting of spider silk threads suspended over a thin hot wire, and simultaneously determined the thermal conductivity of the spider silk and the contact thermal resistance between the hot wire and spider silk.

METHODS

The ITX method is based on the principle employed in the T-type sensor [2]. In this method, a platinum wire with a diameter of 10 μm was suspended between a pair of electrical terminals 20 mm apart, which also served as heat sinks (Figure 1). The average temperature of the electrically-heated wire was determined by measuring the electrical resistance of the wire in three different configurations: X-shape, where a spider silk is suspended between the heat sinks, making contact with the center of the wire; T-shape, where the connection to one of the heat sinks is removed while maintaining contact with the spider silk; and I-shape, where only the heated wire is present without any spider silk. By calculating the difference in the average temperature between the X- and T-shape configurations, the thermal resistance of the spider silk could be obtained. Similarly, the temperature difference between the T- and I-shape configurations gave the contribution of both the thermal resistance of the spider silk and the contact thermal resistance between the heated wire and spider silk. Therefore, by using the average temperatures of the heat wire in the three configurations, the thermal conductivity of the spider silk and contact thermal resistance could be simultaneously determined. To increase the accuracy of the measurement, six thermal paths were examined as shown in Figure 1, and the thermal conductivity and the contact thermal resistance were calculated by using the least-squares correction, effectively reducing the measurement error. In the experiments, spider silk threads collected from *Nephila clavata* were used. All experiments were conducted in a vacuum chamber of a scanning electron microscope (SEM),

and the average temperature was obtained while the spider silk was cut one by one by using electron beam irradiation of the SEM.
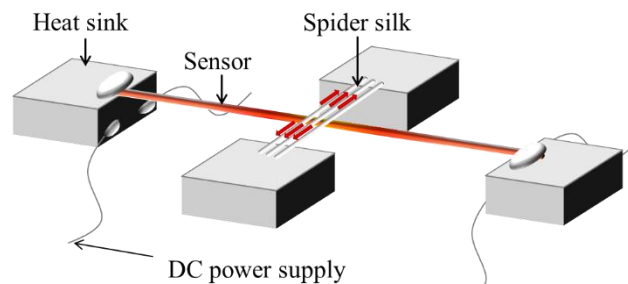
Figure 1 Schematics of experimental setup.

RESULTS AND DISCUSSION

The average diameter of the spider silk collected from *Nephila clavata* at a winding speed of 1.28 m/min was 3.95 μm.
Temperature measurements were performed at four different heating rates, *i.e.*, 7, 15, 22, and 31 μW, where the temperature rises of the hot wire up to 8.3 K were observed. The obtained thermal conductivity of the spider silk and the contact thermal resistance were 2.51 W/(m·K) and 4.43×10^7 K/W, respectively. The thermal conductivity measured for the spider silk was extremely lower than the highest value ever reported, but higher than the typical values of 0.1~0.5 W/(m·K) for conventional bulk polymers.

CONCLUSION

The longitudinal thermal conductivity of a spider silk was measured by using the ITX method proposed. The thermal conductivity of the spider silk measured excluding the effect of contact thermal resistance was 2.51 W/(m·K), which was considerably lower than the reported value, but still higher than conventional bulk polymers.

ACKNOWLEDGEMENT

REFERENCES

[1] Huang X, et.al. *Adv Materials* **24**: 1482-1486, 2012.
[2] Zhang X, et al. *J Thermophys* **21**: 965-980, 2000.

COMPARISON OF BIOMECHANICAL VARIABLES IN NURSES' WORK-RELATED TASKS BETWEEN HEALTHY AND CHRONIC NON-SPECIFIC LOW BACK PAIN NURSES

Nur Athirah Abd Rahman [1] and Shazlin Shaharudin [1,]

[1] Exercise & Sports Science Programme, School of Health Sciences, Universiti Sains Malaysia, Kota Bharu, Malaysia.
Email: athirah.rahman211@gmail.com

INTRODUCTION

Chronic non-specific LBP (CNLBP) is a common work-related musculoskeletal disorder among nurses due to their job scopes. Previous studies focused on the effects of LBP on subjective outcomes measured such as questionnaire and pain scale. This study aims to investigate nurses-related tasks and full body biomechanical outcomes through biomechanical comparison between healthy and CNLBP nurses.

METHODS

This cross-sectional study examined full body biomechanics, function and pain score in 4 female nurses (healthy=13 and CNLBP=13). They performed three dimensional (3D) full body kinematics and kinetics of carrying and transferring a standard load (5% of participant's body weight). 46 reflective markers (with 25-mm diameter) were placed on the participant's body by following IOR Gait method. Full body kinematics and kinetics was evaluated using the Qualisys Motion Capture Systems. Other outcomes include trunk muscle power, lower back and hamstring muscles flexibility measured by sit and reach, function measured by Roland-Morris Low Back Pain and Disability Questionnaire (RMQ) and visual analogue scale (VAS) pain scale. The independent T-test was used to evaluate differences across both groups by using Statistical Package for Social Science (SPSS) version 27 (IBM Inc., Armonk, New York, United States).

RESULTS AND DISCUSSION

Independent T-test showed there was no significant difference of anthropometrics data between both groups. However, pain (p=0.01), disability (p<0.00), trunk muscle power (p<0.00) and sit and reach (p<0.00) differed significantly across groups. There were significant differences of lumbar kinematics at start from ipsilateral side to contralateral side in sagittal plane, at initial contact during walking in frontal plane and at lean during sit-to-stand (STS) in sagittal plane (Table 1). Based on the results, CNLBP participants employed greater lumbar flexion during walking and STS and greater abduction during carry and transfer at start compared to healthy participants. This motion caused the upper body to move towards the load and decreased the vertical ground reaction force, hence, indirectly applied narrow base transfer technique [1]. Furthermore, increase in lumbar flexion during walking and STS among CNLBP participants was common as this pattern was manifested as the compensatory mechanism to avoid pain caused by increasing of trunk stiffness [2].

CONCLUSIONS

The biomechanical factors associated with CNLBP can be used as a screening tool for CNLBP among adults and assisted in developing customised exercise intervention targeting these factors.

REFERENCES

[1] Catena & Xu. *Ergonomics,* **58**(9), 1571-1580, 2015.
[2] Simonet et al. *J Biomech,* **108**, 2020.

Table 1: Kinematics and kinetics data during nurses' work-related tasks across healthy and chronic non-specific low back pain nurses

	Healthy	CNLBP	Effect size	*p-value*
Sagittal plane ipsilateral lumbar ROM (°) at start	165.42 ± 4.34	151.09 ± 1.8	4.31	
Sagittal plane contralateral lumbar ROM (°) at start	170.54 ± 0.65	159.88 ± 7.91	1.9	<0.05
Frontal plane lumbar ROM (°) at IC during walking	3.30 ± 0.23	11.2 ± 2.39	-4.65	
Frontal plane lumbar ROM (°) at MVGRF during walking	3.29 ± 0.34	10.77 ± 2.08	-5.02	
Sagittal plane lumbar ROM (°) at lean during STS	175.62 ± 2.35	167.9 ± 5.74	1.76	
Sagittal plane lumbar ROM (°) at momentum during STS	177.57 ± 2.69	166.93 ± 6.43	2.16	

ROM= Range of motion, IC= initial contact, MVGRF= maximum vertical ground reaction force, STS= sit-to-stand

A DEFORMABLE CAPSULE PROPELLED BY INSIDE MICROSWIMMERS

Zhihan Huang[1], Toshihiro Omori[1] and Takuji Ishikawa[2]
[1] Department of Finemechanics, Tohoku University, Japan.
[2] Department of Biomedical Engineering, Tohoku University, Japan.
Email: huang.zhihan.p4@dc.tohoku.ac.jp

INTRODUCTION

In nature, many organisms can propel themselves in fluid. Large organisms, like fish, use inertia in their motion, some organisms move at low Reynolds number (Re), where viscous forces dominate and inertia can be neglected, and they are called microswimmers. Among them, a lot of microorganisms, like bacteria, can move with the help of flagella or cilia, however, some other microorganisms, like *dictyostelium amoebas*, can swim by deforming their bodies. Self-propulsion by shape deformations requires the cell to move like a wave, the deformation at cell's surface moves back and forth along its swimming direction. Also, according to Purcell's theorem [1], this motion at low Re must break the reciprocal time symmetry. Previous research [2] developed a model of self-propelling capsule by directly applying active forces from its membrane. However, this can be difficult in practice. As a result, here we present a simpler model, a capsule propelled by shape deforming using inside microswimmers.

METHODS

In this study, we present a numerical simulation of a capsule propelled by two microswimmers. Assuming that the capsule and microswimmers are sufficiently small, thus the surrounding flow can be considered as Stokes flow where inertia is ignored, and the surrounding fluid is calculated by boundary element method [3]. We also assumed that there is only elastic deformation at the capsule membrane, which is calculated by using finite element method. As for the microswimmers, a mathematical model named squirmer model is adopted to simulate their motion and effect to the fluid. Also, in order to break the reciprocal time symmetry, external torque is applied to change the direction of inside microswimmers. Finally, position and velocity of both microswimmers and capsule are updated by solving the equation of motion using second order Runge-Kutta method.

RESULTS AND DISCUSSION

Result of our research is shown in Figure 1. Two spherical microswimmers are placed inside a deformable spherical capsule, where the radius of capsule is set to be four times of the radius of a microswimmer. Initial swimming direction of microswimmers are positive x-axis direction. Also, two external torque with same amplitude but opposite direction

are applied to microswimmers to propel the capsule to the x-axis direction. As the microswimmers swimming, capsule membrane deformed at its front and then the deformation occurs at its rear. At last, two microswimmers gather at the middle of capsule and then start a new cycle. We found that the capsule can move toward positive x-axis direction as we expected.
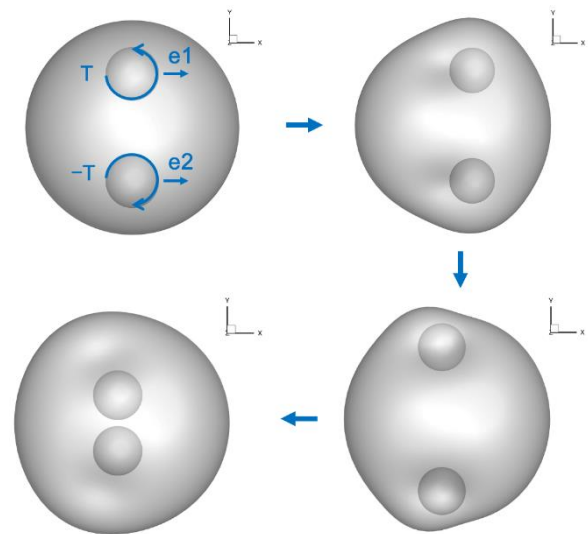
Figure 1 Initial condition of capsule and microswimmers.

CONCLUSION

In this research, we developed a model of a deformable capsule propelled by inside microswimmers and showed that the capsule locomotion can be generated by controlling the inside microswimmers. We also found how the amplitude of external can affect the velocity of the capsule.

ACKNOWLEDGEMENT

REFERENCES

[1] Purcell E. M. *Am. J. Phys.* **45**, 3, 1977.
[2] Farutin, A., et al., *Phys. Rev. Lett*. **111**, 228102, 2013.
[3] Morita, T. et al., *Phys. Rev. E*, **101**, 063101, 2020.

VISCOELASTIC ANALYSIS OF FERMENTING PUFFING DOUGH

Kenji Kikuchi[1,2], Kyosuke Kimura[1], Keiko Numayama-Tsuruta[2] and Takuji Ishikawa[2,1]
[1] Department of Finemechanics, Tohoku University, Sendai, Japan.
[2] Faculty of Biomedical Engineering, Tohoku University, Sendai, Japan.
Email: k.kikuchi@tohoku.ac.jp

INTRODUCTION

Bread has an elementary process in which the original mixed dough is inflated with some ingredients, including fermenting yeast cells, making it soft and malleable in a mold. This also affects the strict texture of the bread, which is controlled by the experience and skill of the baker. Interestingly, one bakery textbook says that the best time to ferment bread dough is to imitate the texture of the human ear lobe. We would like to report on the relationship between the spatiotemporal distribution of air bubbles in the rising dough and its viscoelasticity measured by micro X-ray CT and dynamic mechanical analysis (DMA).

METHODS

The dough samples were made by following the previous research (4). We used 150 g of strong flour (Nissin, Super King 5 kg, Japan), 87 g of water and 3 g of salt as a main ingredient of bread dough. We changed yeast addition amount (Nissin, Super Camellia Dry Yeast 50 g, Japan) to 1%, 2%, 3% and 4% (w/w flour basis). In the kneading process, we stirred the bread dough at 60 rpm for 10 minutes using a mixer (Kai, Stand Auto Mixer DL7523, Japan). After kneading, we weighed 3 g of the dough using an electronic balance and packed it to the bottom of a polystyrene sample tube bottle (AS ONE, PS-15, Japan). We used X-ray Computer Tomography (XRT) (Comscantecno, ScanXmate-E090, Japan) to obtain the 3D data of bread dough. In XRT, the sample was rotated to obtain a projected image and a cross-sectional image was constructed (Fig.1 right). We set the irradiate X-ray to 90 kV, 90 μA and the number of view (number of projected images per round) to 300. We used a temperature controller (Vivaria, Multi panel heater, Japan) and battery (Fujikura, 120 Ah power portable battery BA-450, Japan) to keep a constant temperature (30°C). We used MorpholibJ (a plugin for Fiji to detect the number and volume of bubbles from 3D image data). We discussed the relationship between yeast addition amount and bubble structure in the results section.

RESULTS AND DISCUSSION

Different size bubbles were distributed in the dough and many bubbles grew and generated over time. It was clarified that we can visualize the internal structure of the bread dough as shown in Fig.1. The bubbles were automatically labeled using MorpholibJ, and the bubbles are colored with a random. In the data 10 minutes after fermentation, the number of bubbles and the volume of bubbles

after fermentation, the total number of bubbles increased, and the number of large bubbles also increased.
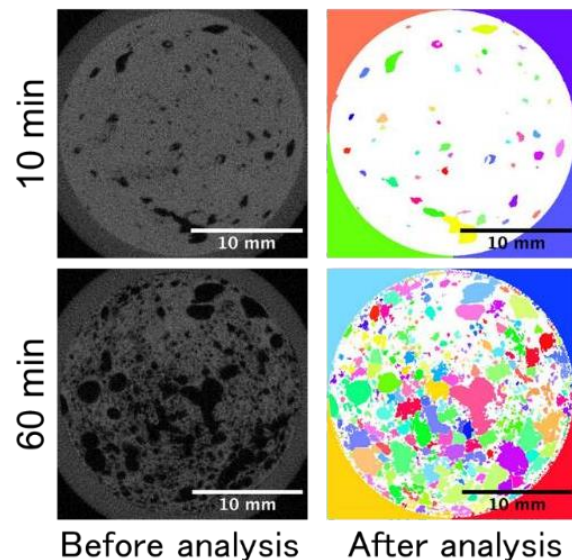
Figure 1 Bubble distribution in the fermenting dough. Cross-sectional views of fermenting bread dough after kneading 10 and 60 minutes later by XRT.

CONCLUSION

In this study we investigated the effect of yeast addition on puffing and analysed the internal bubble structure. It was clear that the amount of yeast added had a significant effect on the puffing rate of the dough. It was also clear that XRT is an effective method to visualise the bubble structure inside the bread dough. The analytical results confirmed that bubbles are formed and grow during fermentation, and that MorpholibJ is a powerful method for detecting bubbles.

We will investigate the effect of the amount of yeast added on the formation of the bubble structure. The relationship between the bubble structure and the mechanical properties of the dough using dynamic mechanical analysis will be reported in the presentation.

REFERENCES

[1] Ohashi A. & Fukuyama K. *The Hiyoshi Rev Nat Sci* **45**: 1-13, 2009.
[2] Inoue Y. *J Cookery Sci Japan* **49**: 4, 280-284, 2016.
[3] Zghal M.C., et al. *J Cereal Sci* **36**: 167- 176, 2002.
[4] Chevallier S., et al. *Food & Bioprocess Tech,* **5**: 609-617, 2012.

STUDY OF THE EFFECT OF MODIFICATION OF MECHANICAL PROPERTIES BY PLASMA NITRIDING TREATMENT ON THE STRAIGHT-LINE STABILITY OF RADIOTHERAPY NEEDLES

Keita Ito[1], Yasumi Ito[2], Ryuichi Yamada[2], Kensuke Hattori[1], Masahide Saito[3] and Hiroshi Onishi[3]

[1] Integrated Graduate School of Medicine, Engineering, and Agricultural Sciences, University of Yamanashi, Kofu, Japan

[2] Graduate Faculty of Interdisciplinary Research, University of Yamanashi, Kofu, Japan

[3] Department of Radiology, University of Yamanashi, Chuo, Japan

Email: g22tm004@yamanashi.ac.jp

INTRODUCTION

In cancer radiotherapy, a gold marker must be implanted in the body to locate the irradiation site, and an implantation needle is used for this purpose. From the viewpoint of invasiveness, a minimally invasive and straight needle is required. We have focused on the material of the needle and have improved the straightness of the needle by changing from stainless steel to tungsten, which has high rigidity. However, tungsten has problems of cost and workability. Therefore, we focused on the mechanical properties of stainless steel and applied plasma nitriding treatment. Surface hardening treatments such as nitriding can improve mechanical properties such as hardness and wear resistance without changing the design or materials of medical devices, and surface treatment can be performed on products [1]. In this study, plasma nitriding, XRD analysis, cross-sectional observation using an optical microscope, and Vickers hardness tests were conducted on small-diameter stainless steel as a basic study to improve the straight-line stability of the needle.

METHODS

Commercially available stainless-steel wear (φ1.0 mm) were used as experimental specimens. Nitriding was performed using a dipole plasma system. XRD analysis and cross-sectional observation using an optical microscope were conducted to examine the microstructural changes caused by the nitriding treatment. Vickers hardness was measured to investigate the change in mechanical properties after nitriding. The hardness distribution of the cross section of the nitrided layer was measured at intervals of about 2.5 μm from the surface of the specimen with the indentation load of 98.07 mN and the loading time of 15 s. The hardness distribution of the cross section of the nitrided layer was measured at intervals of about 2.5 μm from the surface of the specimen.

RESULTS AND DISCUSSION

XRD measurement of the surface revealed two distinct peaks at diffraction angle (2θ) of 44°, 51°, and 75° for the untreated material. The peak of lower angle corresponds to the austenite phase (γ-Fe) and the higher angle corresponds to the strain-induced α′-martensite phase (α′-Fe), which is thought to had been transformed during the drawing process of the wire [2]. In the nitrided material, diffraction peaks existed at the same 2θ as in the untreated material, however, the low angle peaks disappeared. This suggests that the structure of the austenite phase changed during the nitriding treatment, although the strain-induced α′-martensite phase was maintained [3]. A cross-sectional micrograph of the nitrided material using an optical microscope is shown in Figure 1. A layer with a thickness of 7.0 to 7.5 μm was observed on the surface of material. Vickers hardness tests were conducted at six locations near the surface of material (see Figure 1). The hardness of layer showed approximately 1100 HV (position 1), while the base material (position 6) showed approximately 580 HV. This result shows the formation of a hard nitrided layer on the surface of the nitrided material. The hardness of austenitic stainless steel is generally 200 HV, however, it is thought that the work hardening due to the drawing is thought to have increased the hardness of the wire.
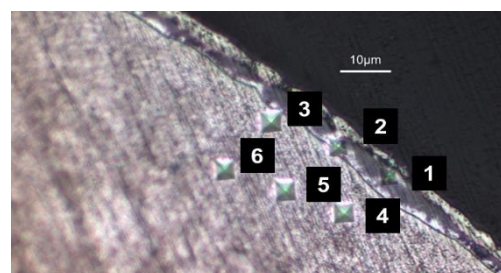
Figure 1 Cross-sectional micrographs of the nitrided material and indentation of Vickers hardness test

CONCLUSION

In this study, as a preliminary experiment to improve the straightness of the needle, plasma nitriding was performed on a stainless-steel wear with a diameter of 1.0 mm, and the formation of a nitrided layer was observed, and hardness was tested. In the future, we will conduct nitriding and puncture tests on needles with a diameter of 0.5 mm, which are used in clinical practice, to investigate whether surface treatment affects straight-line stability of the needle improvement.

REFERENCES

[1] Sumiya, K. et al. *Metals*, **11**: 366, 2021.

[2] Tsuchida, N. et al. *J Japan Inst Metals*, **72**-9: 769-775, 2008.

[3] Onoe, T. et al. *J. Japan Inst. Met. Mater*, **80**-8: 521-528, 2016.

ESTIMATION OF PULL-OUT FORCES OF AN ARTIFICIAL HIP JOINT WITH A STRUCTURE FOR PREVENTING DISLOCATION

Ei Yamamoto[1] and Yuki Kawamura[2]

[1] Department of Biomedical Engineering, Kindai University, Wakayama, Japan.
[2] Department of Clinical Engineering, Morinomya University of Medical Sciences, Osaka, Japan.
Email: ei@waka.kindai.ac.jp

INTRODUCTION

Total hip arthroplasty (THA) is an effective treatment for osteoarthritic patients [1]. In THA, diseased human hip joint is replaced using an artificial hip joint. A number of scientific and clinical studies have been performed to develop the effective treatments. However, there are still various problems with the artificial hip joint. For example, joint dislocation frequently occurs due to the weakness of muscles surrounding the hip joint. In order to prevent the dislocation, the movement or activity is limited in the patients with the artificial hip joint. Therefore, this limitation is a reason why an ideal rehabilitation cannot be conducted after the join replacement surgery. In the present study, we newly proposed an artificial hip joint which has the structure to prevent joint dislocation. Pull-out forces of the joint were estimated using a finite element method. Specifically, the effects of outer shell thickness on the pull-out forces were determined by contact stress analysis.

METHODS

We proposed a novel type of artificial hip joint with a preventing structure from joint dislocation. Its acetabular cup has a shape with over the half of sphere as illustrated in Fig. 1. Due to this geometric configuration, the joint dislocation does not easily occur in the artificial hip joint. Three-dimensional model of one part in twelve equal parts of femoral head and acetabular cup in the artificial hip joint was built using computer-aided design software. Femoral head diameter was set at 6 mm. The inner and outer shell thickness of the acetabular cup was 1 and 2 mm, respectively. Finite element models were constructed to estimate the pull-out forces of the joint using finite element analysis software (ANSYS). The outer parts of the cup and femoral head were made of titanium alloy and the inner part of the cup was made of ultra-high molecular weight polyethylene. Behavior of these materials was represented with a linear isotropic elastic material model. The bottom area of the outer shell of acetabular cup was fully restrained. The femoral head was vertically pulled out from the acetabular cup and the pull-out displacement was set at 2 mm. The maximum outer thickness was 1.0 mm. Then, we removed the parts of the outer shell and thinned dawn the shell to construct the model with the thin outer part. The thickness of the outer shell after the removal was 0, 0.1, 0.2, 0.3, 0.4, 0.5, and 0.6 mm. The pull-out forces were determined for each model of the artificial hip joint.

RESULTS AND DISCUSSION

Figure 2 shows the relationship between the outer shell thickness and pull-out forces in the artificial hip joint model without the slit. There was a clear reduction in the force with decrease in the outer shell thickness. In particular, a remarkable decrease in the force was observed in the case of the outer shell less than 0.1 mm in thickness. The pull-out force was 41.6 and 27.3 N in the case of the outer shell of 1.0 and 0.1 mm in thickness, respectively. Therefore, we can say that the outer shell made of titanium alloy plays an important role to prevent the dislocation of the artificial hip joint.
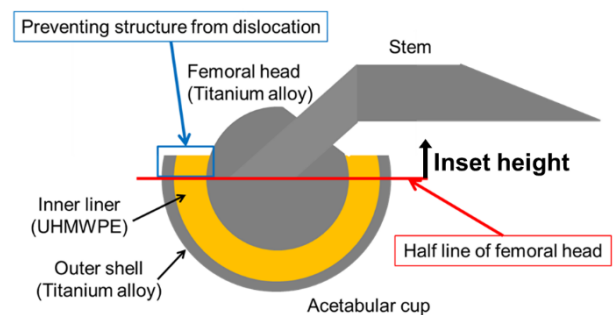
Figure 1 Artificial hip joint with a structure to prevent dislocation.
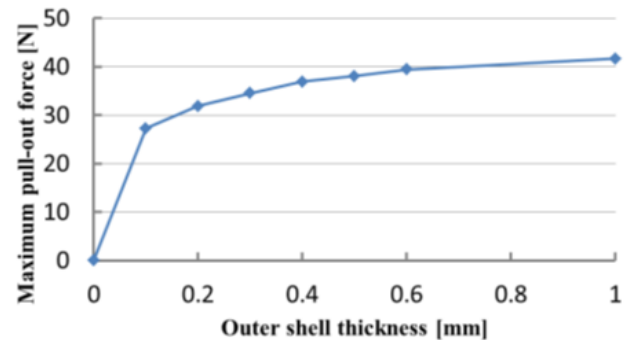
Figure 2 Relation between outer shell thickness and pull-out force.

CONCLUSION

The effects of outer shell thickness on the pull-out forces were determined using finite element analysis. From the results, we understood the characteristic of the joint to prevent the dislocation and suggested a concept of its optimal design.

REFERENCES

[1] Colic, K. & Sedmak, A., *Rheumatology & Orth Med* **1**, 1-7, 2016.

3D PRINTING AND MECHANICAL CHARACTERIZATION OF DYNAMIC BONE TISSUE SCAFFOLDS WITH COMMERCIALIZED FILAMENTS

Hatice Kübra Bilgili[1], and Masahiro Todoh [2]

[1] Human Mechanical Systems and Design, Hokkaido University, Sapporo, Japan.

[2] Mechanical and Aerospace Engineering, Hokkaido University, Sapporo, Japan.

Email: haticekubra.bilgili.q9@elms.hokudai.ac.jp

INTRODUCTION

Bone tissue scaffolds are three-dimensional structures that provide support and an environment for cells to attach, proliferate, and differentiate [1]. In literature there are various types of production techniques such as solvent casting, freeze drying, phase separation and 3D printing [2]. Each of these strategies has benefits and drawbacks. However, due to their capacity to create geometries with adjustable structural and mechanical properties, as well as changeable porosity and architecture, 3D printing and bioprinting have emerged as one of the most promising scaffold production processes in recent years. Thus, researchers have been focusing on improving 3D printing methods in bone tissue regeneration such as producing dynamic scaffolds. In this study we focused on advancing the phase segregation based "dynamic scaffold" [3] concept via using commercial filaments. Furthermore, we are focusing on the effect of different porosity and scaffold geometry in the dynamic nature of proposed scaffolds.

METHODS

For initial investigation of the dynamic nature of proposed scaffolds, ultrasonic wave propagation in COMSOL Multiphysics (in "Pressure Acoustic, Frequency Domain") [4] and MATLAB software is used. Based on the Helmholtz equation, different material parameters and boundary conditions simulations are conducted. To produce phase segregated filaments, commercial use PLA was cut into small sizes with the filament cutter and mixed with PCL (Sigma Aldrich) in single screw extruder. Due to the difference in MW between commercial PLA and PCL, they are mixed in percentages of PLA-PCL & PCL-PLA at 20:80 ,30:70 ,40:60 and 50:50, respectively. Raise3D Pro2 FDM printer is used for 3D printing uniform and non-uniform bone tissue scaffolds. For initial characterizations of produced filaments and 3D printed structures SEM (for phase segregation) and UTM (for mechanical characterization) is used. For SEM analysis samples were moulded into the resin structure and cut with a rotary cutter for thorough observation.

RESULTS AND DISCUSSION

The initial results of the mathematical approach to dynamic scaffolds in COMSOL Multiphysics are still being investigated. The outputs will be compared to current literature and presented during the conference. For 50:50 and 40:60 PLA-PCL mixed filaments, initial SEM characterization of prior to printing showed no phase segregation, supporting the existing literature [3]. For 3D printed structure of 40:60 PLA-PCL (Figure 1 A, B and C)

compared to PLA (Figure 1 D) 3D printed structures, as it's seen on section B and C, lack of major nonhomogeneous dispersity was observed, converging with the current literature [3].
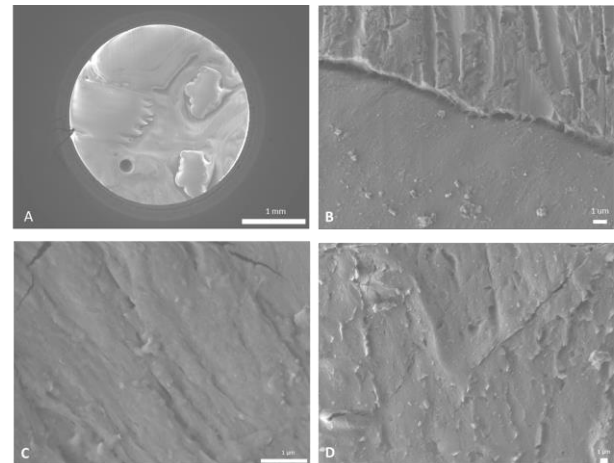
Figure 1 SEM images of PLA/PCL (A, B, C) and PLA (D) printed samples.

However, as seen from Figure 1(B, C) phase segregation wasn't apparent significantly. As a result of these observation, a new mixture in between 40:60 and 50:50 is decided to be investigated next. Further investigation of mechanical and compositional characterization of new proposed percentage and before decided percentages are still in process.

CONCLUSION

In conclusion, from a theoretical and experimental standpoint, the dynamic scaffold concept opens a new area for using commercial filaments and 3D printing techniques in bone tissue biomechanics. Furthermore, already existing potential of dynamic scaffolds in bone tissue regeneration will improve in correlation with ongoing research.

ACKNOWLEDGEMENT

REFERENCES

[1] Tesfa M et al. *Regen Ther* **18**: 102-111, 2021.

[2] Sakchi B et al. *Bioengineering* **9 (12)**: 728, 2022.

[3] Sandra C-E et al. *Nat Commun* **12**: 1031, 2021.

[4] Marysol G-P et al. *Annu Int Conf IEEE Eng Med Biol Soc*. **Nov**: 43-62.

CELL MORPHOLOGICAL CONTROL USING GEL-MICROMACHINING TECHNIQUE AND CELL DIFFERENTIATION INDUCTION

Haruhiko Takemoto[1], Yoichi Saito[2], Yoshitaka Nakanishi[2,3] and Yuta Nakashima[2,3,4,5]

[1] Graduate school of Science and Technology, Kumamoto University/ Kumamoto, Japan.

[2] Faculty of Advanced Science and Technology, Kumamoto University / Kumamoto, Japan.

[3] Institute of Industrial Nanomaterials, Kumamoto University / Kumamoto, Japan.

[4] International Research Organization for Advanced Science and Technology, Kumamoto University / Kumamoto, Japan.

[5] Fusion Oriented Research for disruptive Science and Technology, Japan Science and Technology Agency, Japan.

Email: 222d8470@st.kumamoto-u.ac.jp

INTRODUCTION

The major problem that hinders the realization of regenerative medicine is tumor formation originating from undifferentiated stem cells after transplantation. One of the solutions to solve this problem is to develop a technology to induce homogeneous differentiation of stem cells *in vitro*. We focused on cell morphology control for homogeneously differentiation induction to stem cells into desired types of cells. We previously developed the gel-micromachining technique for creating cell micropattern [1]. In this research, the objective is to control cell morphology by gel-micromachining technique so that cells differentiate into desired types of cells.

METHODS

Figure 1 shows the schematic of gel-micromachining technique. Photoresist was patterned on a glass plate by photolithography (a). Then, sodium alginate solution was spin-coated and gelated in the calcium chloride solution (b). The alginate gel was lift-offed by removing the patterned photoresist (c). When the cells were seeded on the fabricated device, cells were adhered only to glass surface by cell adhesion inhibition effect of alginate gel (d).

To evaluate the relationship between cell morphology and differentiation, osteoblasts were cultured in 20 and 100 μm width slit patterns, and the expression of osteogenesis marker genes was evaluated by qPCR after 3, 7, and 14 days.
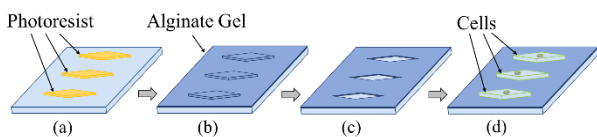
Figure 1 Schematic of morphology control of cells using gel-micromachining technique.

RESULTS AND DISCUSSION

Figure 2 shows the photographs of created gel-micropattern (a) and adhered cells to the patten. Cells did not adhere to the alginate gel areas and formed 20 and 100 μm width slit patterns (b, c). In addition, single cell patterns that shape were pentagon (d, e), triangle (f) and rhombus (g) were able to created using the same method. Cells cultured on 20 and 100 μm width slit pattern for two weeks were carried out the gene expression analysis by qPCR (Fig.3). In cells cultured in a 20 μm width slit pattern, the relative expression of OCN increased and RUNX2 decreased from the early to late stages of culture. Cells cultured in 20 μm width slit pattern had higher expression of OCN and lower expression of RUNX2

after 7 and 14 days of culture than those cultured in 100 μm width slit pattern. This is consistent with the trend in gene expression for osteogenesis, indicating that osteogenesis is induced in cells that are morphologically controlled to be finer in shape.
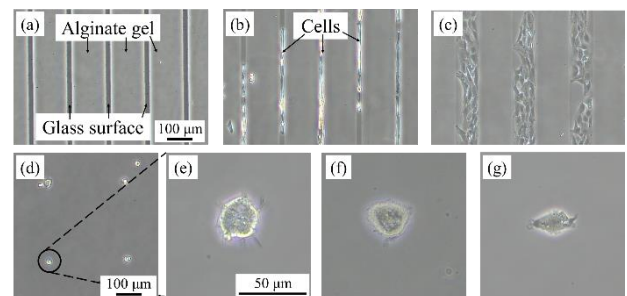
Figure 2 Photographs of created cell micropattern and single cell morphologically controlled.
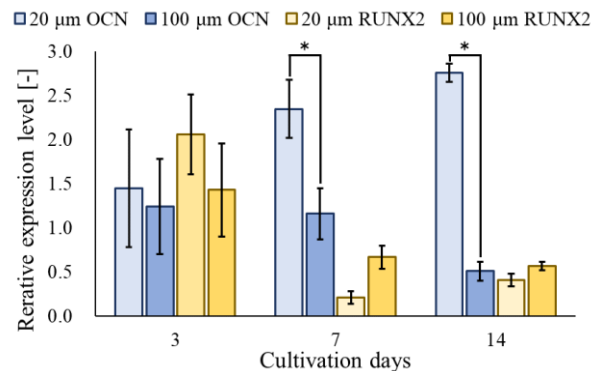
Figure 3 qPCR analysis of osteogenesis marker genes of cells cultured on 20 and 100 μm width slit pattern for 2 weeks. All results were normalized against GAPDH and the comprarative threshold cycle method was used to determin the relative DNA levels. n=3. *p<0.001.

CONCLUSION

In this study, morphology of single cells was able to control the various shapes using gel-micromachining technique. In addition, osteogenesis was successfully induced by controlling cell morphology to thin slit pattern. These results indicate the differentiation can be controlled by regulating cell morphology.

REFERENCES

[1] Nakashima Y. et al. *Biofabrication*, **8**(3):035006. 2016.

TRIALS ON MEMS SENSOR UTILIZATION ON 3D PRINTED INTRAVASCULAR FLOW MODEL

Narendra Kurnia Putra[,1], Fara Azzahra Dinata[2], Muhammad Iqbal[3], Muhammad Ihsan Maulana[2], and Muhammad Salman Al Farisi[4]

[1] Instrumentation and Control Research Group, Faculty of Industrial Technology, Institut Teknologi Bandung, Bandung, Indonesia.

[2] Department of Engineering Physics, Faculty of Industrial Technology, Institut Teknologi Bandung, Bandung, Indonesia. [3]Advanced Functional Material Research Group, Faculty of Industrial Technology, Institut Teknologi Bandung, Bandung, Indonesia

[4] Department of Biomedical Information Sciences, Hiroshima City University, Hiroshima, Japan.

Email: narend@itb.ac.id

INTRODUCTION

Micro-electromechanical systems (MEMS) have been developed as novel measurement devices which provide more accuracy for measuring microscale mechanical phenomena such as Blood flow hemodynamics. Recent development of MEMS sensors has been applied in various biomedical applications such as breathing airway, drug delivery, and detecting body vital signs [1].

3D print manufacturing method has been popular recently. The 3D printed intravascular model, such as blood vessels, has been utilized to understand about the hemodynamic conditions of the blood vessel, including the evaluation method of in silico model, which is usually used for analyses starting from predicting the fluid dynamics behaviour on intravascular blood flow until the design improvement of treatment devices, e.g., stent, flow diverter, and balloon angioplasty.

In this study, we develop the flow circuit model, which utilizes the MEMS sensors to measure the flow conditions on the 3D-printed blood flow model with aneurysm geometry.

METHODS

This study aims to mimic the blood flow circulatory system, which is consisted peristaltic pump as a representation of the human heart, a 3D printed blood vessel model, and a MEMS flow sensor to measure the instantaneous flow rate. The illustration of the overall system used is shown in Figure. 1.

Water is used as a working fluid which was stored in an open tank and passed through a 5-7 mm diameter silicone tube using a peristaltic roller pump with a flow rate in the range of 70 – 180 mL/min to obtain the Reynolds number within the range of 300 – 500, normal ranges for blood flow on the intercommunicating artery (ICA).

ICA geometrical model is fabricated using 3D-printer Anycubic Photon Mono X, made from flexible resin (eResin Flex eSUN). Blood vessel with aneurysm geometry is acquired from the Aneurisk dataset repository (Emory University) [2]. The printing process has successfully performed with the necessary support and edited geometry to fit the flow setup specification.

A thermal anemometry MEMS flow sensor was utilized in this study. The sensing structure was fabricated on a polyimide thin film of 50 μm thickness through a standard microfabrication lift-off process. Au was used for the metallization. It was connected to the constant temperature driving circuit using a 0.1 mm enamel wires. The MEMS sensors are calibrated and successfully attached to the flow tube. For the liquid flow measurement trial in this study, three different attachment methods have been performed: indirect contact with putting a sufficient hole area for sensor contact, reverse alignment of the sensor, direct contact with the flow, and insulated coating of the sensor area.

RESULTS AND DISCUSSION

The flow circuit has been constructed as described in Figure 1 below. Fluid flow was set by 90ml/min.
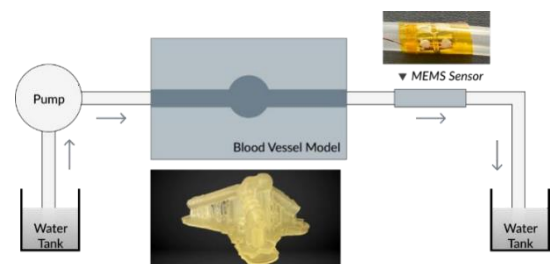
Figure 1 Flow systems with 3D printed blood vessel model and MEMS sensor

The MEMS sensor reading varies with each attachment method to the flow pipe. The indirect contact and reverse alignment resulting no measurement data since the sensor cannot sense the flow directly. Resistance and voltage differences were measured at 1.2 Ω and 10 mV on the direct contact method, respectively. However, the sensor has short after several minutes. In contrast, the insulated MEMS cannot sense any measurement.

CONCLUSION

It has suggested improving the MEMS sensor systems to improve the sensitivity and reliability of measurement under fluid flow conditions.

REFERENCES

[1] Shikida M et al. *Jpn J Appl Phys* **61**: SA0803, 2022.

[2] AneuriskWeb project website, http://ecm2.mathcs.emory.edu/aneuriskweb. Emory University, Department of Math&CS, 2012.

MODEL-BASED DESIGN AND OPTIMIZATION OF TAIL DEVICE FOR ASSISTING WORKERS: COMPUTATIONAL STUDY WITH HUMAN-DEVICE DYNAMICS SIMULATION

Naoto Haraguchi[1] and Kazunori Hase[1]

[1] Department of Mechanical Systems Engineering, Tokyo Metropolitan University, Tokyo, Japan.

Email: haraguchi-naoto1@ed.tmu.ac.jp

INTRODUCTION

Lower-limbs assistive devices that prevent lower-limb musculoskeletal disorders in workers have been developed [1]. The devices have the advantage of reducing lower limb loads of workers during prolonged standing [1]. However, the devices have some issues such as increasing lumbar loads of the wearer [2]. In the present study, we aim to design a tail device as a new lower-limbs assistive device. A tail device mimics a mammalian tail which is the notion of the tail being a "fifth limb" and has a wide variety of functions [3]. We focus on a mechanical function in supporting body mass and believe that the tail device with the mechanical function would be a new lower-limbs assistive device that resolves the issues such as increasing lumbar loads when wearing the device.

For developing a new tail device to replace the current lower-limb assistive devices, designers need to analyze the interaction between the device and the wearer and optimize the structure of the device. Hence, the present study proposed a model-based method for analyzing the human-device interaction and designed the tail device through optimization using the present method.

METHODS

We developed a model-based design method for optimizing the tail device structure and the wearer's posture. The present method analyzes the interaction between the tail device and the wearer using a dynamics simulation that accepts the user's body height and mass and working condition. This simulation consists of the multibody model for the forward dynamics calculations and the contact model of the wearer, device, and ground in order to compute the interaction such as ground reaction forces and joint torques. The present method defines a cost function that evaluates the physical load and the fitness for labor work, calculates the cost function based on the interaction computed by the simulation, and determines the optimal tail device structure and wearer's posture that minimize the cost function.

The present study constructed the human-device model combining a tail device model and a computational human model as the multibody model. The overall model has 28 rotational degree of freedoms (DOFs): the human model consists of 13 segments and 26 rotational DOFs, the tail device model consists of 2 segments, i.e., upper link and lower link, and 1 rotational DOF, and the human model and the tail device model are connected with 1 rotational DOF. The joint of the tail device has a passive mechanism for supporting the wearer's body mass which was modeled by a spring-damper system. In this study, the device structure, i.e., the segment length of the device and the elastic and damping coefficients of the joint in the device, and the wearer's

posture, i.e., the joint angle of the wearer, were optimized, and the physical loads such as ground reaction forces and joint torques when wearing the optimized tail device were calculated through the dynamics simulation.

RESULTS AND DISCUSSION

Figure 1 shows the human-device model with the optimized device structure and wearer's posture. The lumbar joint torque and the ground reaction force acting on the foot were 28.4 N·m and 35.2 % body weight (%BW), respectively. In a previous study, the lumbar joint torque of 31.1–33.8 N·m and the ground reaction force acting on the foot of 24.9–29.4 %BW have been observed when wearing a current lower-limbs assistive device [2]. Hence, although the new tail device is less effective in reducing lower limb load than the current lower-limbs assistive device, the new device can reduce the lower limb load with a lower lumbar load than the current device.
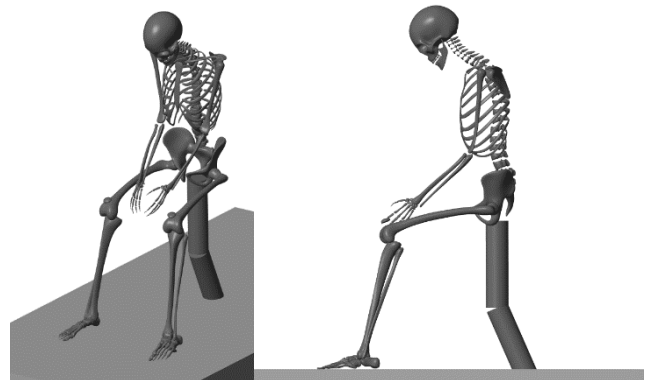
Figure 1 Human-device model with the optimized device structure, i.e., the segment length of the device and the elastic and damping coefficient of the joint in the device, and the wearer's posture, i.e., the joint angle of the wearer.

CONCLUSION

We developed a model-based design method for a new tail device and optimized the device structure and the wearer's posture. The present method could design the tail device that reduces the lower limb load with a lower lumbar load than the current lower-limb assistive device.

ACKNOWLEDGEMENT

REFERENCES

[1] Luger, T. et al., *Appl. Ergon.* **80**: 152-160, 2019.
[2] Haraguchi, N. et al., *arχiv.org*: **2205**.09910, 2022.

[3] Xie, H. et al., *Proc. 10th AHIC*: **35**, 2019.

COMPUTATIONAL MECHANICS OF THE KNEE JOINT LIGAMENT

Sentong Wang[1,2], Kazunori Hase[3], Rui Gong[2,4], and Tetsuro Funato[1]

[1] Graduate School of Informatics and Engineering, The University of Electro-Communications, Tokyo, Japan.
[2] Graduate School of Systems Design, Tokyo Metropolitan University, Tokyo, Japan.
[3] Faculty of Systems Design, Tokyo Metropolitan University, Tokyo, Japan.
[4] Organization of Liberal Arts Education, Mejiro University, Tokyo, Japan.
Email: sentongwang@gmail.com

INTRODUCTION

The mechanical properties of ligaments during movement are difficult to measure directly, making computer modeling methods a viable alternative for predicting ligament mechanics. However, simplistic joint models cannot accurately simulate real movements as they do not account for muscle activity. There is an interplay between muscle activity and joint motion *in vivo*. To address this, we have developed a musculoskeletal model that includes joint soft tissues, ligaments, and muscles to infer the mechanical properties of ligaments during movement.

METHODS

The study utilized a finite element musculoskeletal (FEMS) model of the right lower limb, including a healthy knee, which had been previously developed and analyzed using FEBio software (MRL Utah University, Salt Lake, UT, USA). The model's construction and validation were discussed in previous works by Wang et al. [1,2]. The FEMS model consisted of the geometries of all the bones in the right lower limb, as well as the articular cartilages and meniscus of the knee. These structures were manually segmented and reconstructed from computed tomography and magnetic resonance imaging scans.

To represent the bones, the femoral, tibial, and patellar bones were meshed using rigid triangular shell elements. The cartilage and meniscus were defined using elastic eight-node hexahedral elements. Various joints were included in the model: a spherical joint with three degrees of freedom represented the hip, joints with six degrees of freedom represented the tibiofemoral and patellofemoral joints, and a hinge joint with one degree of freedom represented the ankle joint.

The ligaments crossing the tibiofemoral joint, including the anterior cruciate ligament, posterior cruciate ligament, medial collateral ligament, posteromedial capsule, lateral collateral ligament, anterolateral structure, and oblique popliteal ligament, were modeled as nonlinear spring bundles. The force-strain relationship for each ligament was described by Equation (1), where the force sustained by the ligament depended on its current length, slack length, strain, and stiffness coefficients [3].

$$f_i = \begin{cases} 0 & \varepsilon_i \leq 0 \\ {}^1k_i(l_i - {}^0l_i)^2 & 0 < \varepsilon_i \leq 2^l\varepsilon \quad (1) \\ {}^2k_i[l_i - (1 + {}^l\varepsilon)^0l_i] & 2^l\varepsilon < \varepsilon_i \end{cases}$$

where f_i is the force sustained by the ith ligament, l_i is the current length of the ith ligament, ${}^0l_i$ is the slack length of the ith ligament, ${}^l\varepsilon$ is the strain assumed to be constant at

0.03, and ${}^1k_i$ and ${}^2k_i$ are the stiffness coefficients of the spring elements representing the ith ligament for the nonlinear and the linear regions, respectively.

The FEMS model also included 20 representative one-dimensional linear element muscles, such as the gluteus maximus, iliopsoas, pectineus, rectus femoris, and various muscles of the lower leg. Muscle wrapping around the femoral and tibial bones was considered to represent their paths. The mechanical properties of the muscles were represented using a Hill-type dynamic model, which incorporated both active and passive elements.
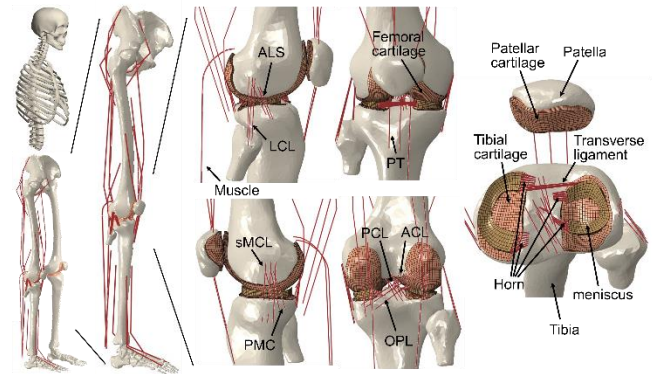
Figure 1 A musculoskeletal model containing a lower limb finite element musculoskeletal model includes a 12-DOF knee joint, along with 20 muscles, ligaments (ACL, anterior cruciate ligament; PCL, posterior cruciate ligament; MCL, medial collateral ligament; PMC, posteromedial capsule; LCL, lateral collateral ligament; ALS, anterolateral structure; OPL, oblique popliteal ligament; transverse ligament), cartilage, the meniscus, and meniscus horn attachments.

RESULTS AND DISCUSSION

The interaction between the muscle level and joint level that exists *in vivo* is an important relationship that influences the biomechanics of the musculoskeletal system and can only be described in the concurrent framework. Our model allows for accurate inference of the mechanical properties of ligaments during movement.

ACKNOWLEDGEMENT

REFERENCES

[1] Wang S et al. *Biomechanics* **1**: 293-306, 2021.
[2] Wang S et al. *J Biomech Eng* **144**: 051011, 2022.
[3] Abdel-Rahman EM et al. *Med Eng Phys* **20**: 276-290,

1998.

A NOVEL EVALUATION METHOD FOR THREE-DIMENSIONAL TOOTH AXIS AND DENTAL ARCH CURVE

Yoshihito Ishii[1], Makoto Sakamoto[2], Takashi Kameda[3], Koki Nagae[1], Koichi Kobayashi[2] and Kazuhiko Hiramoto[1]

[1] Graduate School of Science and Technology, Niigata University / Niigata, Japan.

[2] Department Health Science, Niigata University of Medicine / Niigata, Japan.

[3] Department of Orthodontics, Nippon Dental University School of Life Dentistry at Niigata / Niigata, Japan.

Email: sakamoto@clg.niigata-u.ac.jp

INTRODUCTION

The tooth axis represents the most fundamental morphological reference axis, and the dental arch represents the arrangement of teeth. These factors are crucial for dental treatment and orthodontic therapy as they involve the positioning of teeth. However, a coordinate system based on the intraoral space, which is essential in determining their spatial relationships, does not exist.

The objective of this study is to construct a world coordinate system within the oral cavity based on anatomical landmarks of the maxilla and mandible obtained from cone-beam computed tomography (CBCT) images. Furthermore, the study aims to quantitatively represent three-dimensional positioning of tooth axes and dental arches, considering the entire tooth including the root.

METHODS

In this study, 16 individuals with normal occlusion were included as subjects. The target area comprised 28 teeth, ranging from central incisors to second molars in both the maxilla and mandible. Three-dimensional tooth models, encompassing the maxilla, mandible, and tooth roots, were created using CBCT images. To establish a three-dimensional intraoral world coordinate system, three anatomical landmarks of the maxilla and mandible were used as follows:

First, the vector from the left mental foramen to the right mental foramen was temporarily designated as the X-axis. Next, the vector from the midpoint of both mental foramina to the incisive foramen of the maxilla was defined as the Z-axis. The origin of the coordinate system was set at two-thirds of the distance from the midpoint of the mental foramina along the Z-axis towards the incisive foramen. The Y-axis was determined by taking the cross product of the Z-axis and the temporary X-axis. Finally, the X-axis was defined by taking the cross product of the Y-axis and the Z-axis.

The tooth axes were defined as the first principal component that passes through the tooth root to the crown by conducting principal component analysis of each three-dimensional tooth model. These tooth axes were then projected onto the coordinate system.

The dental arch, on the other hand, was represented by calculating the center of gravity of each three-dimensional tooth model, projecting it onto the coordinate system, regressing it into a curve in each plane, and expressing the dental arch curve using mathematical equations.

RESULTS AND DISCUSSION

A representative example of typical findings is shown (Figure 1). The tooth axis showed a similar trend to the results of Dempster et al. [1], which included the direction of the tooth root, in both the coronal and sagittal planes. Additionally, this study clarified the relationship for the previously unknown transverse plane.

For the dental arch, an even function of the fourth order in the transverse plane, an even function of the sixth order in the coronal plane, and a function of the third order in the sagittal plane were found to be optimal representations of the curves.

We believe that such a mathematical representation of the dental axis and dental arch based on a three-dimensional intraoral world coordinate system will be valuable in dental diagnosis and orthodontic treatment with the development of digital dentistry.
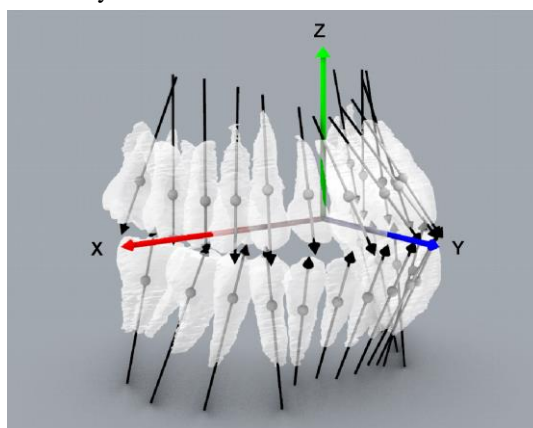
Figure 1 The teeth and tooth axes within the three-dimensional intraoral coordinate system.

CONCLUSION

A three-dimensional intraoral coordinate system was constructed using CBCT images and anatomical landmarks from 16 individuals with normal occlusion. The absolute three-dimensional positions of all teeth and tooth axes were determined. In addition, mathematical representations were used to describe the arrangement of the teeth within the dental arch curves.

REFERENCES

[1] Dempster WT et al. *J Am Dent Assoc* **67**: 779-797, 1963.

A MATHEMATICAL FORMULATION OF THE THREE-DIMENSIONAL OCCLUSAL PLANE BASED ON AN INTRAORAL WORLD COORDINATE SYSTEM

Koki Nagae[1], Yoshihito Ishii[1], Makoto Sakamoto[2], Takashi Kameda[3], Koichi Kobayashi[2], and Kazuhiko Hiramoto[1]

[1] Graduate School of Science and Technology, Niigata University / Niigata, Japan.
[2] Department Health Science, Niigata University of Medicine / Niigata, Japan.
[3] Department of Orthodontics, Nippon Dental University School of Life Dentistry at Niigata / Niigata, Japan.
Email: sakamoto@clg.niigata-u.ac.jp

INTRODUCTION

The occlusal plane is important in occlusal diagnosis, occlusal reconstruction, and in describing mandibular motion and position. The simplest definition of the occlusal plane is "the plane defined by the three points of contact between interincisal point of the upper central incisors and mesiobuccal cusps of the first upper right and left molars [1]". However, it is difficult to represent the three-dimensional (3D) position and direction of teeth in a world coordinate system for each individual, and there is no research that expresses the occlusal plane in mathematical equations. In this study, we proposed a new mathematical formulation of the 3D occlusal plane in the world coordinate system developed for each individual based on cone-beam computed tomography (CBCT) images.

METHODS

We used CBCT images of maxillary and mandibular bones and teeth from 17 normal occlusions. A 3D model of the teeth and jaws was constructed from the acquired CBCT images. The new 3D intraoral world coordinate system was established as follows [2]. The vector from the left mental foramen to the right mental foramen of the mandible is defined as the hypothetical X-axis, and the vector from the center of the hypothetical X-axis through the maxillary incisor canal is defined as the Z-axis. The origin is defined as the 2/3 position from the center of the hypothetical X-axis to the maxillary incisor canal. The Y-axis is defined as the outer product of the Z-axis and the hypothetical X-axis, and the X-axis is defined as the outer product of the Y-axis and the Z-axis to define a 3D Cartesian coordinate system. This coordinate system is defined for each subject and is independent of the CBCT equipment and the subject's posture during imaging, and its main advantage is that the Y-Z plane can be the sagittal plane, the X-Z plane can be the coronal plane, and the X-Y plane can be the axial plane. The occlusal plane was determined from the 3D mandibular tooth model in the coordinate system, i.e., the occlusal plane consisted of three feature points at the midpoints of the **mesioincisal** line angles of the bilateral central incisors and the distobuccal cusp of the bilateral second molar. From these three points, the equation of the 3D occlusal plane equation of the intraoral world coordinate system can be expressed as follows:

$$ax + by + cz + d = 0, \tag{1}$$

where the units for the x, y, and z position variables are in millimeters, and a, b, c and d are constants determined as individual subjects. In this study, the inclination angles of the occlusal plane in the coronal and sagittal planes were also examined and the angles were defined as α and β, respectively. In the coronal plane, a positive value of α was defined as the occlusal plane tilted upward on the right buccal side with respect to the X-axis. In the sagittal plane, a positive value of β was defined as the occlusal plane tilted upward on the mesial side with respect to the Y-axis.

RESULTS AND DISCUSSION

An example of the occlusal plane (#7) in 17 subjects is shown (Figure 1). The constants in equation (1) for the occlusal plane of this subject were $a = 29.80$, $b = 14.44$, $c = 2533.90$, and $d = 9283.76$, respectively. The angles of the occlusal plane of this subject were $\alpha = -0.7°$ and $\beta = -0.3°$. The occlusal plane of each individual can be quantitatively represented in the intraoral coordinate system, as described above. The mean and standard deviation of α and β for the 17 subjects were $\alpha = 0.9 \pm 2.0°$ and $\beta = -1.4 \pm 6.0°$, respectively. These results show that in the coronal plane, the 3D occlusal plane is nearly parallel to the X-axis with little angular variation, whereas in the sagittal plane, the occlusal plane is tilted up or down to the Y-axis, depending on the subject, with slightly more variation.
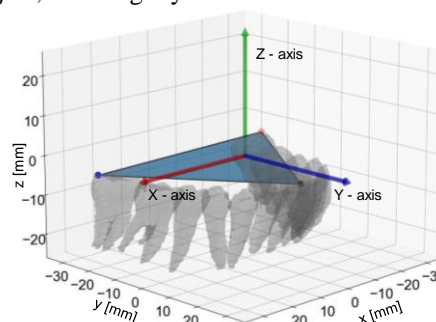
Figure 1 An example of the mandibular teeth and the occlusal plane in the 3D intraoral world coordinate system (#7).

CONCLUSION

We constructed a new intraoral world coordinate system based on the three-dimensional model of mandible and maxilla obtained from CBCT images of normal occlusion, and the 3D occlusal plane can be obtained from the three feature points of mandibular teeth and expressed by mathematical equations.

REFERENCES

[1] Rosati R et al. *Int J Oral Sci* **4**: 34-37, 2012.
[2] Sakamoto M et al. *Japanese J Clin Biomech* **39**: 207-216, 2018.

INVESTIGATION FOR THE ROLES OF BINDING OF AC REGIONS IN FORMING MESHWORK STRUCTURES OF FIBRIN AGGREGATION BY A MESOSCOPIC MECHANICAL MODEL

Takeya Ohno[1], Taiki Shigematsu[2], Satoshi Ii[1]

[1] Graduate School of Systems Design, Tokyo Metropolitan University / Hachioji, Tokyo, Japan.
[2] Graduate School of Engineering Science, Osaka University / Toyonaka, Osaka, Japan
Email: ohno-takeya@ed.tmu.ac.jp

INTRODUCTION

In the initial stage of blood coagulation, fibrin monomers combine to form protofibrils, which are protein complexes, followed by lateral polymerization of protofibrils through intermolecular interactions including binding their αC regions. This brings the formation of thick fiber bundles and branches, eventually leading to fibrin aggregation with meshwork structures [1]. Although understanding the detailed processes for the formation of fibrin aggregation is valuable in both the physiological and pathological senses, much is unknown for the relationship between fiber-level features and meshwork structures. For instance, increasing Zn^{2+} concentration makes the fibrin meshwork structures coarser [2], and it was speculated the stiffness of the bonded αC regions is decreased with increasing Zn^{2+} concentration that leads to loose polymerization of protofibrils and thick fiber bundles. However, it is unclear why such a loose polymerization also affects the meshwork line density. In this study, we investigate the effects of stiffness of the bonded αC region of protofibrils on the fibrin aggregation structures by a mesoscopic mechanical model.

METHODS

Several mathematical models have been proposed for addressing micro-scale meshwork structures of fibrin aggregation [3]. Here, we employed a mesoscopic mechanical model [4,5]. A protofibril is modelled with 25 nodes connected by elastic elements, and the motion is obtained by solving an overdamped Langevin equation. As the intermolecular interactions among protofibrils, the Morse potential is introduced for molecular interactions and harmonic potential is introduced for specific biding of αC regions [5].

2000 protofibrils were randomly placed in a cubic domain with a size of 3 μm per side under periodic boundary conditions. Using the Boltzmann constant k_b, temperature T (set to 300 K), and the radius of protofibrils a (set to 0.005 μm), we set parameters for the Morse potential as $\varepsilon^* = 1.5$ and $\alpha^* = 1.5$ and the stiffness of bonded αC regions as $k_\alpha^* = 0, 0.012, 0.12, 1.2$. We judged each system reached an equilibrium state when all the potential energies become almost plateau.

RESULTS AND DISCUSSION

The equilibrium structures of fibrin aggregation are shown in Figure 1. Except for $k_\alpha^* = 0$ (without considering the specific binding of αC regions), meshwork structures were formed.

As the decrease of k_α^*, thicker fiber bundles and coarser meshwork structures were formed. This tendency is consistent with that as the increase of Zn^{2+} concentration in the previous study [2]. Thus, strong binding of αC regions maintains fine meshwork structures. Interestingly, no meshwork structure and isolated thicker fiber bundles were formed when ignoring the bindings of αC regions.

These results suggest that the increases of flexibility of the αC binding lead to weaken constraints to maintain meshwork structures and enhance the formation of thick fiber bundles due to non-specific intermolecular interactions.
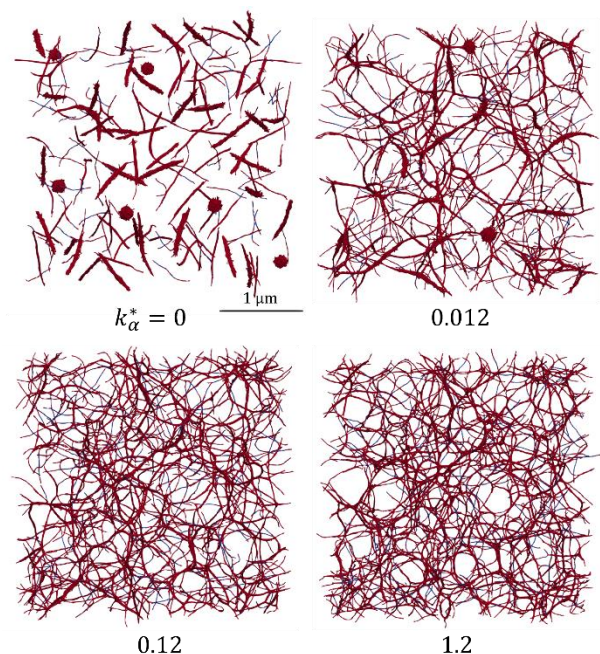
Figure 1 Equilibrium structures of fibrin aggregation with different stiffness k_α^* for stiffness of bonded αC regions.

CONCLUSION

The present study revealed that the binding of αC regions among protofibrils is required to form meshwork structures of fibrin aggregation, and its flexibility is an important role in both meshwork structures and the thickness of fiber bundles.

REFERENCES

[1] John, et al. *Blood* **121**: 1712-1719, 2013.
[2] Xia, et al. *PNAS* **118**: e2020541118, 2021.
[3] Francesco P., et al. *Curr Opin Biomed* **22**: 100369, 2022.
[4] Takeishi, et al. *J R Soc Interface*: **18** 20210554, 2021
[5] Shigematsu O., *9th World Congress of Biomechanics*, Taipei, July 10-14, 2022.

CELL-CENTERED DYNAMICS SIMULATION OF THREE-DIMENSIONAL EPITHELIAL SHEET DEFORMATION

Tomohiro Mimura[1], Yasuhiro Inoue [1]

[1] Department of Micro Engineering, Graduate School of Engineering, Kyoto University, Kyoto, Japan

Email: mimura.tomohiro.n2

INTRODUCTION

The shape of the epithelial monolayer can be represented as a curved tissue in three-dimensional (3D) space. The 3D morphogenesis of such tissues is governed by cellular dynamics. Various mathematical modeling and simulation studies have been conducted. One promising approach is the cell-center model [1]. The cell nucleus, which is considered to correspond to the cell center, can be observed experimentally. However, cell-center models specifically adapted to simulate the deformation of 3D monolayer tissues have been lacking. In this study, we developed a mathematical model based on the cell-centered model to simulate the deformation of 3D monolayer tissues. The model was validated by simulating out-of-plane deformation and invagination by apical constriction.

METHODS

As in the previous study [1], each cell of the epithelial tissue is represented as a cell point. Then, by connecting adjacent points with lines, the epithelial tissue is represented as a mesh of triangles. The polygon formed by the centers of mass of adjacent triangles is used as the 2D shape of cells in the neutral plane of the epithelial sheet.

The equation of motion for cell i is written as follows.

$$\eta \frac{dx_i}{dt} = -\nabla_{x_i} E$$

The energy function E consists of the mechanical energy E_{mech} and the constraint energy E_{Center} that reduces the inconsistency of the cell center and its polygonal center of mass.

The model can also represent cell division, cell rearrangement, and apical constriction. Cell division is represented by increasing the number of cell points in the triangular mesh and updating the adjacency based on Lomas model [2]. Cell rearrangement is a phenomenon in which the adjacency between cells is switched, and is represented by a flip operation to switch the adjacency. Apical contraction is a phenomenon in which the apical surface of a cell contracts and the cell becomes wedge-shaped, and is expressed by making two changes to the energy function E_{mech}.

RESULTS AND DISCUSSION

We prepared a 40×40 cell sheet in the xy-plane. First, we examined the differences in wrinkle patterns when the cells were divided in the specified direction from this condition (Figure 1 (A)~(C)). The results showed that wrinkles were formed in the direction orthogonal to the direction of cell division. Here, the wavelength of wrinkles behaves according to a power law in relation to the elastic modulus that suppresses out-of-plane deformation. According to continuum theory [3], this power index is 0.25. Upon examination in our study, this index was 0.23, closely aligning with the theoretical value (Figure 1 (D)).

Finally, simulation of concave formation due to apical constriction from the initial shape confirms that the concave formation occurs in the same orientation as in the previous study with the 3D vertex model [4] (Figure 1 (E)). These results indicate that the cell-center model can also represent 3D morphogenesis of epithelial monolayer sheets.
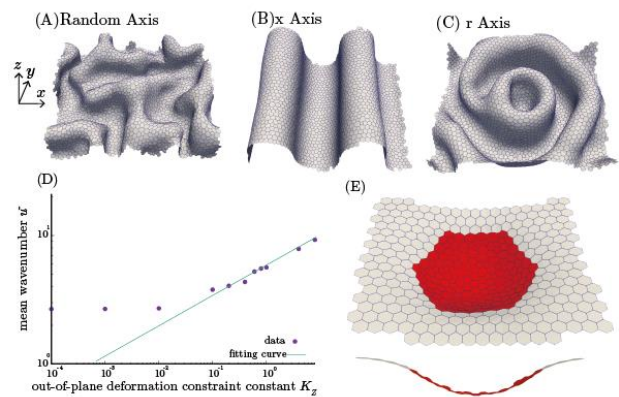
Figure 1 (A) to (C) show the wrinkle patterns when the cells were divided in the specified direction of cell division. (D) indicates the relationship between out-of-plane deformation constraint and wrinkle wavenumber. (E) shows concave formation due to apical constriction. Note that the red cells are those undergoing apical constriction.

CONCLUSION

Our model is a lightweight computational mechanics model compared to conventional multicellular mechanics models, while also describing movement at the cellular level. Therefore, it is capable of approaching phenomena on long time scales and is expected to be helpful in elucidating a new understanding of mechanisms based on cellular motion that has not been known before.

ACKNOWLEDGEMENT

REFERENCES

[1] Meineke et al. *Cell Proliferation* **34**: 253-266,2001.

[2] Lomas, *ACM SIGGRAPH 2014 Studio,* 2014.

[3] Cerda & Mahadevan, *Phys Rev Lett* **90**: 074302-074302, 2003.

[4] Inoue et al. *Development Growth and Differentiation* **59**: 444-454, 2017.

BAYESIAN APPROACH TO CHARACTERIZING ANISOTROPIC PROPERTIES OF SKIN FROM SUCTION TESTS

Taeksang Lee[1]

[1] Department of Mechanical Engineering, Myongji University, Yongin, South Korea.

Email: taeksanglee@mju.ac.kr

INTRODUCTION

In reconstructive surgery, understanding the mechanical properties of a person's skin is crucial for predicting its behavior and preventing wound complications [1]. However, characterizing skin properties in vivo using conventional methods is challenging. One possible non-invasive approach is the suction test, which involves deforming the skin inside a probe cavity and measuring the maximum height under negative pressure. Unfortunately, existing commercial suction devices like the Cutometer (Courage+Khazaka Electronic, Germany) offer limited metrics that are not enough for studying skin mechanics. To address this limitation, we propose using elliptical probes to capture anisotropic features and developing a Bayesian approach to characterize the mechanical properties of skin in computational simulations.

METHODS

Motivated by [2], we create 3D finite element (FE) models with circular and non-circular probe openings to characterize the anisotropic behavior of skin. The FE modeling of the Cutometer is performed using Abaqus Standard software. The skin is divided into anisotropic and isotropic layers, employing the Gasser-Ogden-Holzapfel model [3] for anisotropic behavior and the neo-Hookean model for isotropic behavior. The deformation of the skin under negative pressure is simulated, and the maximum height is recorded. The elliptical opening effectively captures anisotropy, resulting in different deformation profiles based on fiber orientations (Fig. 1**a**). Then, the FE analysis serves as a forward function, establishing the relationship between the mechanical properties of the skin and the observed deformation in the Cutometer test.

However, solving the inverse problem through Bayesian inference in FE analysis is computationally expensive. To address this, surrogate modeling is employed through Gaussian process (GP) regression, which defines probability measures over function spaces. We replace FE models with GP metamodels and assume the mean value from GP posterior as the point-wise prediction. By applying Bayes' rule, we obtain the posterior distribution over mechanical properties of skin given the training dataset. Sampling from the posterior distribution using the NUTS Hamiltonian Monte Carlo algorithm in PyMC3 [4] provides the solution distribution for the inverse problem.

RESULTS AND DISCUSSION

Given test dataset, Bayesian inference generates a solution distribution for predicting mechanical properties of the skin in the inverse problem. The values surrounding the peak point in the solution distribution closely align with the test input data, indicating that the proposed methodology can accurately infer anisotropic properties (each row in Fig. 1**b**).
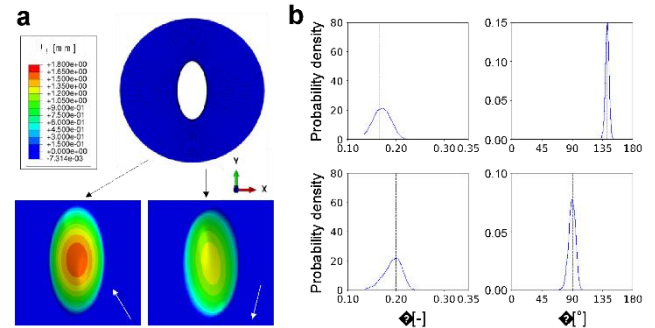
Figure 1. Finite element analysis with non-circular probe opening in the Cutometer shows the displacement values along the z-direction with respect to the fiber orientation (indicated by the white arrow) (**a**). Given two different test data, the solution of inverse problem is represented as posterior distributions, surrounding the true value (black dotted line) (**b**).

Additionally, the influence of measurement noise can be evaluated. By considering various noise variances, such as Gaussian distributions, the Bayesian inference becomes a fully Bayesian approach. The performance of the solution can be improved through this fully Bayesian approach as it considers individual noise values for each observation, which helps in determining the optimal solution.

CONCLUSION

The non-circular opening probe of the Cutometer allows us to characterize the anisotropic properties of the skin through computational simulation. Within the Bayesian framework, the prediction of skin properties is provided as a probability distribution, which also incorporates uncertainty quantification. Ultimately, our work aims to enable non-invasive determination of anisotropic skin properties, which is essential for accurate predictive modeling of skin biomechanics.

ACKNOWLEDGEMENT

REFERENCES

[1] Wong VW et al. *FASEB J* **25**(12): 4498-4510, 2011.

[2] Iivarinen JT et al. *Skin Res Technol* **19**(1): e356-e365, 2013.

[3] Gasser TC et al. *J R Soc Interface* **3**(6): 15-35, 2006.

[4] Salvatier J et al. *PeerJ Computer Science* **2**: e55, 2016.

PARAMETRIC STUDY OF ROTARY FILE INSTRUMENTS DURING ENDODONTIC TREATMENT THROUGH DYNAMIC FINITE ELEMENT SIMULATION

Satrio Wicaksono[1], Wandi Prasetia[1], Anna Muryani[2], Tatacipta Dirgantara[1], Andi Isra Mahyuddin[1]

[1] Faculty of Mechanical and Aerospace Engineering, Institut Teknologi Bandung, Bandung, Indonesia.

[2] Faculty of Dentistry, Universitas Padjadjaran, Bandung, Indonesia.

Email: satrio_wicaksono@office.itb.ac.id

INTRODUCTION

One of the critical steps in endodontic therapy is the shaping-cleaning process using a rotary file instrument. Nowadays, dentists adhere to minimally invasive endodontics as their paradigm, which may preserve more tooth structure and prolong its life. As a result, new instruments were produced, and the availability of new instruments may affect the success rate and durability of the treated tooth. Hence, it is important to understand which instrument is more suitable to prevent a defect or imperfection on the treated tooth. Current study objective was to evaluate the influence of material type, cross-sectional shape, and centricity variation on the material strength utility and cutting ability of rotary file instruments in root canal models with severe curvature through dynamic finite element analysis.

METHODS

Nine instrument models were designed based on the parameters evaluated: material type, cross-section shape, and centricity variation. The material types included in the current study were CM-Wire, NiTi from Protaper Gold, and NiTi from Trunatomy, while the evaluated cross-section shapes were convex triangular, parallelogram, and slender rectangular (Figure 1b). Additionally, centricity distance was varied on the parallelogram-shaped instrument into three variations: centered model, off-centered 1 (distance = 0.024 mm), and off-centered 2 (distance = 0.048 mm). Instruments were evaluated using dynamic finite element-based computational simulation in a root canal with a radius angle of 45 degrees and a hole radius of 4 mm. In the dynamic model, the loading condition employed was a vertical displacement of 5 mm together with a rotary speed of 500 RPM (Figure 1a). Additionally, a bending experimental test and simulation with a load of 1N were performed to validate the finite element model.

RESULTS AND DISCUSSION

The stress on the instrument was concentrated at different places during the shaping process (Figure 1c). In material type comparison, NiTi from Protaper Gold showed a higher strength utility and better cutting ability compared to CM-Wire and NiTi from Trunatomy. These occurred due to the value of material elastic modulus, where Protaper Gold was the stiffest, followed by Trunatomy and CM-Wire.

The strength utility, and cutting ability of triangular shape were higher compared to parallelogram and rectangular. The results showed that the geometrical design was one of the important factors, and a similar pattern in generated stress was found, as another study reported [1,2].

Furthermore, centricity did not significantly affect the stress or cutting ability of the parallelogram-shaped instrument. However, according to Ha et al. (2017), centricity significantly affected rectangular-shaped instruments [3]. The difference occurred due to the cross-section inertia area, where the rectangular area was drastically changed when the centricity changed, while the parallelogram still had a similar area.
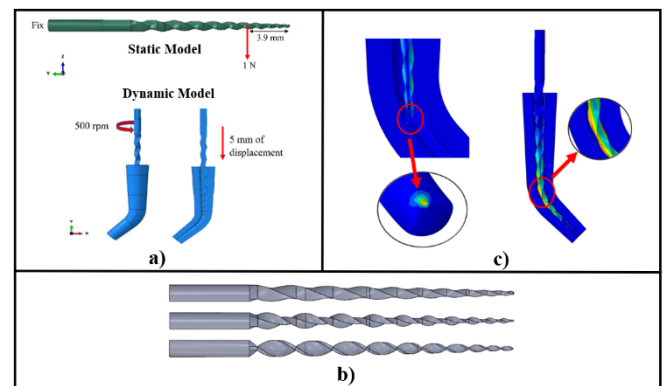
Figure 1. (a) Loading condition, (b) Instrument model with three different cross-section shapes, and (c) FEM stress result

CONCLUSION

The dynamic finite element model was able to predict the impact of different parameters on the instrument, where material types and cross-section shapes significantly influence the material strength utilization and cutting ability of the instrument. On the other hand, centricity variation in parallelogram-shaped instruments did not show any significant effect.

ACKNOWLEDGEMENT

REFERENCES

[1] Zhang Y, et al. *J Endodontics* **45**(3): 316-321, 2019.

[2] Galal M & Hamdy TM. *Bul Nat Res Centre* **44**(1): 1-11, 2020.

[3] Ha J-H, et al. *J Dental Sci* **12**(2): 173 178, 2017.

SIMULATION OF THE THROMBUS FORMATION IN STANFORD TYPE B AORTIC DISSECTION UNDER THE INTERACTION BETWEEN THROMBUS AND BLOOD FLOW

Shuta Imada[1], Kenji Komiya[1], Naoyuki Kimura[2], Yoshihiro Ujihara[1], Shukei Sugita[1], Masanori Nakamura[1]
[1] Department of Electrical and Mechanical Engineering, Nagoya Institute of Technology, Nagoya Japan
[2] Jichi Medical University Saitama Medical Center, Japan
Email: s.imada.079@stn.nitech.ac.jp

INTRODUCTION

An aortic dissection is a tear in the intimal layer of the aortic wall, causing blood to flow into a lumen (false lumen) between the tunica intima and media. Stanford type B aortic dissections are cases where dissections are confined to the descending thoracic aorta. For this case, conservative treatment is the first choice with hope of occlusion of the false lumen with thrombus. However, the risk of death rises by a factor of 2.7 in comparison with patients even with a completely patent false lumen [1] in case that the occlusion is incomplete and the false lumen remains partially patent. Our goal is to establish a way to predict complete occlusion of the false lumen with a thrombus via computer simulations. As a first step, we constructed a mathematical model of thrombus formation and applied it to a real case of the aortic dissection where thrombus was partially formed in the false lumen to see the validity of the proposed model.

METHODS

We developed a mathematical model of thrombus formation with consideration of the mechanisms of venous thrombus in reference to [2]. In brief, thrombus formation begins with the activation of resting platelets due to flow stagnation and their attachment to the wall at low wall shear stress. The activated platelets promote further activation of surrounding resting platelets, and those in low shear-rate region aggregate and bind each other to become thrombus (bound platelets). Transports of the resting, activated and bound platelets were described with advection-diffusion equations. Blood viscosity and fluid resistance were expressed as a function of the concentration of the bound platelets, and incorporated in the Navier-Stokes equation to account for effect of thrombus on blood flow.

We applied the above model to a clinical case of the Stanford type B aortic dissection in which the false lumen was partially thrombosed during follow-up. The aortic geometry immediately after the onset of dissection was used for the simulation, and the simulation results were compared with the data obtained at 4 years after the onset of dissection. While physiological flow conditions were applied as boundary conditions, parameters were tuned to accelerate thrombus formation. The simulations were implemented with scFLOW ver. 2022 (Hexagon).

RESULTS AND DISCUSSION

Figure 1 shows the thrombosed area (a) in the real case at 4 years after onset and the simulation results at (b) the 8th and (c) the 20th cardiac cycle. As shown in Fig. 1(a), in the actual case, thrombosis was found in part of the Fig 1 (a) Thrombus in a real patient with aortic dissection. Simulated thrombus at the peak systole of (b) the 8th and (c) the 20th cardiac cycle. (d) Plot of the total flowrate of each cardiac cycle and the thrombus volume in the true and false lumens.
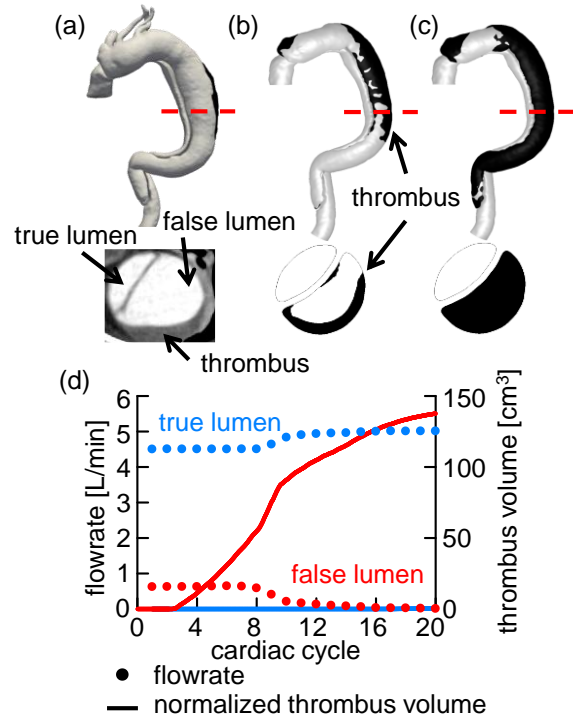
Figure 1 (a) Thrombus in a real patient with aortic dissection. Simulated thrombus at the peak systole of (b) the 8th and (c) the 20th cardiac cycle. (d) Plot of the total flowrate of each cardiac cycle and the thrombus volume in the true and false lumens.

false lumen, while the arch and true lumen were patent. The simulation demonstrated a qualitatively similar pattern of thrombus formation as shown in Fig. 1 (b); thrombi were formed on the posterior side of the false lumen, while no thrombus was on the border (flap) between the true and false lumens. Thrombus grew entirely in the false lumen and finally occluded with thrombus by the end of the 20th cardiac cycle (Fig. 1 (c)). In looking at the total flowrate of each cardiac cycle and the thrombus volume in the true and false lumens, we found remarkable reduction of the flowrate with the development of thrombus (Fig. 1(d)).

CONCLUSION

We successfully reproduced the thrombus formation in a case of Stanford type B aortic dissection by the developed mathematical model and simulations. Comparison with other patients, in particular the ones of long-term follow-up, will help further improvements of the mathematical model, and lead to establishment of thrombosis prediction technology of the aortic dissection.

REFERENCES

[1] Tsai TT et al. *N Engl J Med*, **357**:349-359, 2007
[2] Menichini C et al. *J Math Biol*, **73**: 1205-1226, 2016

INVESTIGATION OF CELL-MEMBRANE PROTRUSION DYNAMICS USING A COUPLING MODEL OF MEMBRANE AND ACTIN-CORTEX DYNAMICS

Kohsuke Tsukui[1], Hiromi Miyoshi[1], Naoya Sakamoto[1] and Satoshi Ii [1]

[1] Graduate School of Systems Design, Tokyo Metropolitan University / Hachioji, Tokyo, Japan.

Email: tsukui-kohsuke@ed.tmu.ac.jp

INTRODUCTION

Membrane protrusions occur frequently in cells in the early stages of adhesion and affect adhesion and extension [1]. Their generation and disappearance are associated with coupling dynamics of plasma membrane and actomyosin cortex including their linker proteins (ERM protein family). The actomyosin cortex is responsible for a mechanical feature of the membrane and adjusts its apparent stiffness by an active contractile force of the internal myosin. A local rupture of the ERM linkers weakens the local membrane stiffness that further leads to plasma membrane disconnection from the actomyosin cortex, and thus it is a key event for the membrane protrusion [2]. Recently, it has been shown that cortical gaps occur prior to ERM detachment and are associated with areas where myosin is localized [3]. However, the contribution of myosin localization to the formation of membrane protrusions is unclear. In this study, we propose a mechanical model for a bleb-like membrane protrusion that considers coarse-grained behaviors of plasma membrane and actomyosin cortex and their interaction.

METHODS

We propose a mechanical model of the cell membrane, including dynamics of the actomyosin cortex and plasma membrane. Actin, myosin, cross-link (CL) protein and ERM are modeled as elastic line elements, and the plasma membrane is modeled as a mesh capsule consisting of triangular elements (Fig. 1A). Actin filaments are placed as a network behind the membrane surface and connected to the plasma membrane via ERM filaments. For simplification, the myosin filaments are randomly bonded to any pairwise actin filaments, where the pairs are fixed over time, and a constant contractile force for each myosin is imposed. The numbers of actin and myosin filaments were determined based on a previous study [4]. The contractile force of the myosin was set to fact=100 pN.

RESULTS AND DISCUSSION

A bleb-like protrusion is focused in this study. A detachment area of the ERM with a diameter Dde was initially set, and then simulation was performed until reaching to an equilibrium state. Our simulation could generate a membrane protrusion around the ERM detachment area (Fig. 1B), and also could reproduce a dependency of size of the ERM detachment area that the protrusion height increases as the increase of Dde (Fig. 1C).

We then considered a case for the myosin localization, which is observed in the previous study, where the area of membrane protrusions formation coincided with the area of myosin enrichment [3]. The placement of myosin was set to be localized in the vicinity of the ERM detachment area. Here, the total amount of myosin filaments was fixed, namely the number density in the actomyosin cortex

becomes higher near the ERM detachment area compared with the non-localization (uniform) case. The results show that the myosin localization reduces the size of membrane protrusion, rather than enhancing formation of large membrane protrusion (Fig. 1D). The myosin localization strengthens the local contraction around the ERM detachment, whereas reduces the contraction area compared with the uniform case, inferring the latter fact is associated with the formation of membrane protrusion. This suggests the myosin localization around the ERM detachment area observed in the previous study may have a different role in the formation of large membrane protrusions (e.g., ERM ruptures).
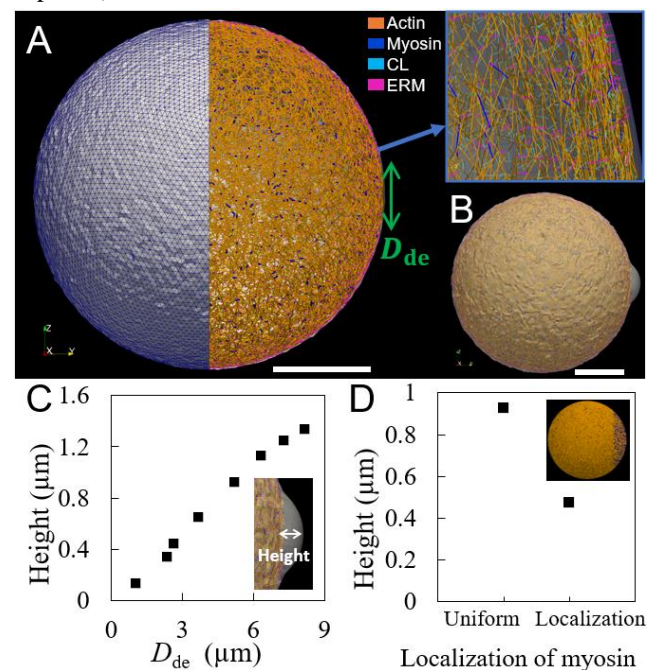
Figure 1 Cell membrane model and formed membrane protrusions. (A) A cortex network structure is constructed inside the plasma membrane. Scale bar is 5 μm. (B) Formed membrane protrusions. (C) Diameter of ERM detachment area vs. height of membrane protrusions. (D) Localization of myosin in cortex vs. height of membrane protrusions.

CONCLUSION

We have proposed a cell membrane model considering coupled dynamics of plasma membrane and actomyosin cortex that could reproduce the bleb-like membrane initiated from the local ERM detachment. Using this model, we suggested an effect of myosin localization on the protrusion formation.

REFERENCES

[1] Lee ST et al. *Adv. NanoBiomed Res.*, **2**: 2100100, 2022.
[2] Welf ES et al. *Dev. Cell*. **55**: 723-736, 2020.
[3] Asante-Asamani E et al. *PLoS. One*., **17**: e0265380, 2022.
[4] Chugh P et al. *Nat. Cell Biol.*, **19**:689-697, 2017.

DYNAMIC FINITE ELEMENT SIMULATION OF 3D FOOT DURING STANCE PHASE OF HUMAN WALKING

Kohta Ito[1], Takeo Nagura[2], Masahiro Jinzaki[3], Naomichi Ogihara[4]

[1] Artificial Intelligence Research Center, National Institute of Advanced Industrial Science and Technology, Tokyo, Japan.
[2] Department of Clinical Biomechanics, Keio University School of Medicine, Tokyo, Japan.
[3] Department of Radiology, Keio University School of Medicine, Tokyo, Japan.
[4] Department of Biological Sciences, Graduate School of Science, The University of Tokyo, Tokyo, Japan.
Email: k.itou@aist.go.jp

INTRODUCTION

Bipedal locomotion is a mechanical phenomenon that translates the center of mass forward by the precise control of reaction forces acting on the body from the ground. The human foot is the only body part that directly interacts with the ground during walking and running, thus the foot complex has been thought to be a crucial segment for the generation of robust bipedal locomotion. Previous research has revealed that the human foot possesses specific morphological features and mechanical functions that enhance the stability and efficiency of bipedal walking and running [1]. However, understanding the exact contribution of the human foot to bipedal locomotion has remained challenging due to difficulties in measuring the kinematic and kinetic data of the foot's internal structure. Fortunately, advancements in computational modelling and simulation techniques have provided valuable insights into the intricate mechanical behavior of the foot during human locomotion [2]. These computational approaches also enable us to predict changes in foot behavior resulting from foot diseases or footwear choices, thereby impacting clinical and ergonomic fields. In the present study, our objective was to develop a finite element (FE) model of the human foot and perform dynamic simulations to examine the three-dimensional (3D) behavior of the foot during walking.

METHODS

The 3D shape model of the foot bones and outer surface were reconstructed based on computed tomography (CT) images of one male adult right foot. These models were then meshed with tetrahedral elements. The foot bone models were connected to each other by ligaments and plantar fascia represented by tension-only truss elements. The bones and cartilages were modelled as isotropic linear elastic materials, while surrounding soft tissue and skin were modelled as hyperelastic Ogden materials. The contacts between the cartilages and between the foot plantar surface and ground were defined as frictionless and Coulomb friction contact, respectively. To replicate the human bipedal walking using constructed FE model, lower leg movement and ground reaction forces (GRF) during walking of the same subject of CT-scanned were measured. The tibia and fibula of the FE foot model were moved in accordance with the measured kinematic data. The muscle tension forces of the triceps surae, tibialis anterior, extensor hallucis longus and extensor digitorum longus were also applied with proper timing.
An explicit FE analysis was performed using RADIOSS 2019 (Altair Engineering, USA).

RESULTS AND DISCUSSION

We have successfully performed a dynamic FE simulation of 3D foot behavior during the stance phase of human walking (Figure 1). The GRF profile exhibited a close agreement with the measured data. Moreover, our precise FE model of the human foot allowed us to observe intricate kinematic and kinetic information, including the 3D movements of the foot bones, tension in the plantar fascia, and stress distribution.
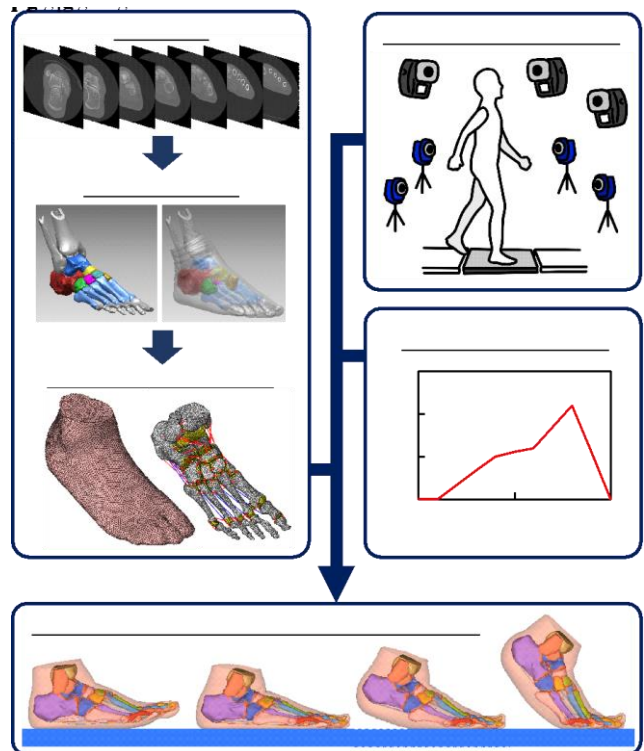
Figure 1 The flow of dynamic FE simulation.

CONCLUSION

We have developed a FE simulation framework for dynamically analyzing 3D foot behavior during human locomotion. The proposed framework holds significant potential not only in the field of foot biomechanics but also in various medical and ergonomics applications.

REFERENCES

[1] Holowka et al. *J Exp Biol* **221**: 174425, 2018.
[2] Ito et al. *Front Bioeng Biotechnol* **9**: 760486. 2022.

NUMERICAL STUDY ON PRIMARY CILIUM AND ITS MAIN MECHANICAL COMPONENTS

Do Tien-Dung[1], Mazalan Mazlee[2]

[1] Department of Computer Science, Faculty of Information Technology, PTIT, Hanoi, Vietnam.

[2] Faculty of Electronic Engineering and Technology, Universiti Malaysia Perlis (UniMAP), Perlis, Malaysia.

Email: dungdt@ptit.edu.vn

INTRODUCTION

The primary cilium is a non-motile cilium protruding from the apical cellular surface. It is found in multiple types of cells and functions as a mechanosensor to sense changes in surrounding mechanical environment such as fluid flow. The core of primary cilia is the axoneme of nine microtubule doublets. However, the cross-linking component which connect microtubutules together and connect the microtubules to ciliary membrane is believed to decide the mechanical properties of primary cilia [1].

In this study, for the first time, a 3D primary cilia model composed of main mechanical components such axoneme of nine microtubule doublets and cross-linking component is simulated by finite element method. In all cilia numerical, the primary cilia were modelled as the homogenous and elastic beam, there is no realistic model with main mechanical components of primary cilia studied so far. It is also shown that the mechanical properties of the cross-linking components being around 100 Pa - 1 kPa, is the first time reported here.

METHODS

Finite Element Modelling (FEM) analysis software (ANSYS Mechanical Multiphysics) was used to simulate the primary cilium model. The model was built up based on the 3D constructed information from Sun et al. [2]. The primary cilium model has 5 um in high, 0.2 um in diameter and is constructed from 7 sections (Figure 1) including two structures: the nine microtubule doublets structure and the cross-linking component (Figure 2).

Boundary conditions: The connection between nine microtubules and cross-linking structure is No separation type. The meshing study of tetrahydral element type was performed to mesh all components. Overall, the meshing size composed of 1.274.826 nodes and 697.738 elements. A static tensile load of 1 nN was chosen to apply force at one end of the primary cilium. Another end was set as the fix support. For the mechanical properties of nine microtubule structures, the Young's modulus of 1 GPa is assigned. The mechanical properties of cross-linking component are changed from 0 – 6 kPa to verify the dependence of properties of primary cilia on the properties of cross-linking component.
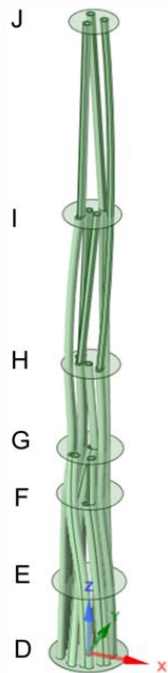
Figure 1 The 3D primary cilia model
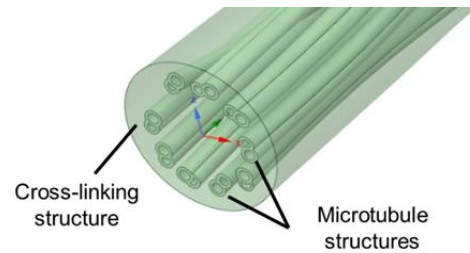
Figure 2 Two main components of primary cilia model

RESULTS AND DISCUSSION

Different Young's moduli of cross-linking component were assigned to investigate the effect of cross-linking structure on the mechanical properties of primary cilia. Figure 3 depicts that the equivalent Young's modulus of the cilia increases with the increasing of the Young's modulus of cross-linking component. According to Do et al. [1], Young's modulus of primary cilia varied from around 60 - 200 kPa (equivalent to the red section in Figure 3), which leads to the elastic properties of cross-linking components, being around 100 Pa - 1 kPa.
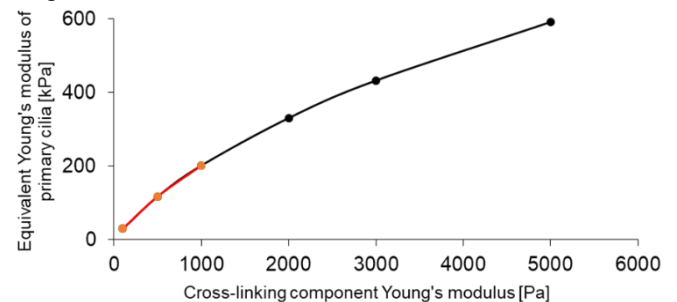
Figure 3 Dependence of equivalent Young's modulus of primary cilia on the Young's modulus of cross-linking component.

This study not only proved the mechanical properties of primary cilia depends mainly on cross-linking components, but also revealed the range of elastic moduli of this component, which is totally new and interesting discovery in this research field. However, these results still have some limitations since the assumption of cross-linking is the subtraction of cilium space to nine microtubule structures. It would be appropriate if there is the cilioplasm in the model as well.

CONCLUSION

For the first time, the proper primary cilium model with main mechanical components is investigated. Moreover, the mechanical properties of cross-linking component, for the first time, have been revealed.

REFERENCES

[1] Do et al. *Front. Bioeng. Biotechnol*. **9**, 753805, 2021.
[2] Sun et al. *PNAS* **116.19,** 9370-9379, 2019.

DEVELOPMENT AND BIOMECHANICAL EVALUATION OF AN ARTIFICIAL CERVICAL INTERVERTEBRAL DISC WITH COMPOSITE LATTICE STRUCTURE

Weng-Pin Chen, Jui-Hsien Chiu

[1]Department of Mechanical Engineering, National Taipei University of Technology / Institute of Mechatronic Engineering, Taipei, Taiwan.

Email: wpchen@mail.ntut.edu.tw

INTRODUCTION

Many studies have confirmed that as compared with traditional spinal fusion surgery, total disc replacement (TDR) can effectively preserve the range of motion of the operated segment and to reduce the risk of adjacent segment degeneration. The objective of this study was to develop a new biomimetic cervical disc with similar biomechanical properties of intact intervertebral disc. The new TDR was designed with components of core, artificial annular fibrosus (AF), upper and lower end plates. The artificial annular fibrosus was designed with a lattice structure in order to achieve the biomechanical properties similar to those of native intervertebral discs, as well as activities in all directions of motion.

Figure 1 (A) New artificial cervical disc design, (B) Baguera cervical disc

METHODS

In this study, an artificial intervertebral disc designed using a lattice structure was investigated by finite element analysis, and the biomechanical effects of the TDR on the multi-segment cervical spine C4-C7 model was evaluated. The endplate geometry was established according to the natural cervical endplate and Ti6Al4V material was used. The top surface of the core was designed as a semi-spherical shape to match the ball-and-socket design of the upper endplate and ultra-high molecular weight polyethylene (UHMWPE) material was used. The lattice structure of Octect [1] was adopted for the artificial annulus fibrosus and the composite material of TPU+PLA+GO was assigned. Finally, the biomechanical behaviors were compared between the newly-designed artificial cervical disc, the commercial product (Baguera cervical disc), (Figure 1), and the intact spine for the ranges of motion and the compression stiffnesses.

In the finite element analysis, a follower load of 100 N was applied to the superior endplate center of C4 to simulate the weight of head and a moment of 1.5 Nm to simulate the primary spinal motions (in flexion, extension, lateral bending and axial rotation, respectively). The inferior surface of C7 segment was fixed in all degrees of freedom.

RESULTS AND DISCUSSION

The finite element analysis results showed that the new TDR performed closely to the native cervical spine than the Baguera cervical disc in terms of compression stiffness, mobility of the surgical segment as shown (Table 1). The lattice structure was adjusted for a fixed wire diameter and space for the design of the artificial annulus fibrosus, and other parameters can be further adjusted in the future to achieve an optimal design in terms of compression stiffness, mobility and stress in order to meet the overall requirements. In summary, the new artificial disc with the lattice structure showed better biomechanical and kinematic properties as compared to the conventional ball-and-socket type artificial disc.

CONCLUSIONS

The annular fibrosus lattice structure design of the new biomimetic cervical disc can effectively improve the deficiencies of conventional ball-and-socket design, making it more resistant to axial rotation and can reduce compression stiffness and canprovide an alternative choice.

REFERENCES

[1] Ghannadpour et al. *Composite Structures* **281**:115113, 2022.

Table 1: Compression stiffness and range of motion in four different motions at C5-C6 segments for intact, new design, and Baguera models

	Stiffness (N/mm)	Flexion (°)	Extension (°)	Lateral Bending (°)	Axial Rotation (°)
Intact	1318	4.33	3.5	3.93	2.74
New design	2644.23	3.43	3.64	5.33	8.11
Baguera	3187.8	10.42	4.06	12.72	15.46

STATISTICAL AND MORPHOMETRIC ANALYSIS OF CEREBRAL MAJOR ARTERIAL SHAPES AND CORRESPONDING FLUID NUMERICAL INVESTIGATION

Yan Chen[1], Yanbo Liang[2] and Oshima Marie [1,2]

[1] Graduate School of Interdisciplinary Information Studies, The University of Tokyo, Japan.
[2] Graduate School of Engineering, The University of Tokyo, Japan.
[3] Interfaculty Initiative in Information Studies, The University of Tokyo, Japan.
[4] Institute of Industrial Science, The University of Tokyo, Japan.
Email: chenyan@iis.u-tokyo.ac.jp

INTRODUCTION

Medical imaging homogeneity in data science often results in unresolved inter-data variances compared to the data volume, creating challenges for data-driven methodologies in medical data analysis. One of the areas where imaging homogeneity is critical is the study of Intracranial Aneurysms, that this disease's etiology exhibits a clear correlation with distinctive hemodynamic features. Wall Shear Stress (WSS) is the frictional force exerted by the blood flow on the vessel wall, which plays a key role in the formation and rupture of cerebral aneurysms [1]. Abnormal high WSS can damage the endothelial cells and weaken the vessel wall, potentially triggering aneurysm formation. Therefore, this study aims to address these challenges by employing a statistical approach coupled with fluid dynamics simulation, thereby enhancing generalizability, and reducing time and computational resources.

METHODS

This study employs a Geometric Morphometrics approach for shape analysis of cerebral major arteries which is an amalgamation of high-incidence areas of cerebral aneurysms, comprised of the internal carotid artery and the middle cerebral artery.
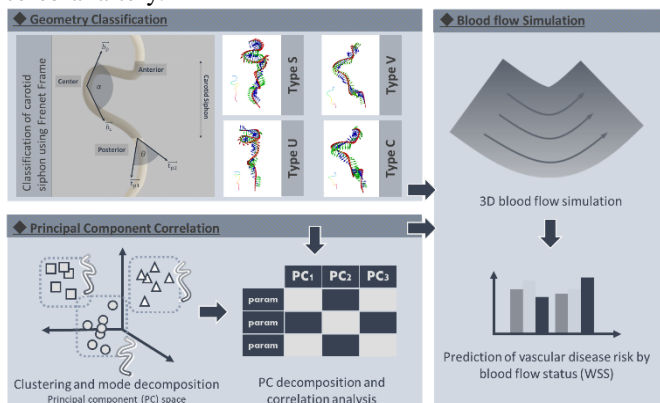
Figure 1 The flow of this study, which includes two shape analysis modules (Geometry Classification and Principal Component Analysis) and a fluid analysis module.

Our study is divided into two parts, the first part is called Geometry analysis, as shown in the left part of Figure 1. This part consists of two modules, the first module uses a criterion using a Frenet frame approach to classify the carotid siphon and the second module performs a principal component analysis on landmark models of vascular traits. We will combine the results of the two modules to generate a correlation matrix of principal components on vascular traits. In the second part which is shown in the right part, we will implement targeted blood flow simulations based on the correlation matrix obtained in the first part and explore the relationship between some meaningful vascular trait factors and the risk of cerebral aneurysm.

RESULTS AND DISCUSSION

In the results of this experiment, we observe that the trends obtained from classifying the dimensionally reduced features show a certain similarity to the vascular classification method introduced in [2]. This study strives to augment the understanding of vascular classification methods, thereby potentially contributing to blood flow simulation and risk prediction of vascular diseases. There was a statistically significant clustering of ICA shapes, and for v shapes with the highest risk of cerebral aneurysm, showed higher wall shear stress than other shape classifications, a phenomenon with the same trend as the odds of cerebral aneurysm development. The ability to parameterize and classify arterial shapes in the circle of Willis using geometric morphometrics introduces a new approach that is expected to improve both our understanding and predictive capabilities for cerebral vascular diseases. The ability to parameterize and classify arterial shapes in the circle of Willis using geometric morphometrics introduces a new dimension to the current methodologies.

The results derived from this study, especially the trends obtained from classifying the dimensionally reduced features, demonstrated a significant similarity to the vascular classification method. This highlights the effectiveness of geometric morphometrics in understanding the intricacies of ICA. Moreover, this approach purposes a novel method that combines geometric morphometrics and fluid dynamics simulation to analyse the geometry and WSS of cerebral arteries, with its potential applicability in predicting the risk of aneurysm development based on vascular shape and wall shear stress. Further research will be required to fully capitalize on these findings and refine the methods used. However, these findings represent an encouraging advancement in the quest to improve the detection and prevention of intracranial aneurysms.

REFERENCES

[1] Shojima, M. et al. *Stroke*, **35**(11): 2500-2505, 2004.
[2] Zhang, C. et al. *Surgical and Radiologic Anatomy*, **35**(5): 385-394, 2012.

AUTOMATED CENTERLINE EXTRACTION OF CIRCLE OF WILLIS USING DEEP LEARNING APPROACH

Zixuan Zhao[1], Yan Chen[1], and Marie Oshima [2,3]

[1] Graduate School of Interdisciplinary Information Studies, The University of Tokyo, Japan.
[2] Interfaculty Initiative in Information Studies, The University of Tokyo, Japan.
[3] Institute of Industrial Science, The University of Tokyo, Japan.
Email:zhao-mmhh@g.ecc.u-tokyo.ac.jp

INTRODUCTION

Circle of Willis (CoW), a crucial vascular structure in the brain, supplies oxygenated blood to over 80% of the brain. The existing automatic extraction method cannot provide vascular consistency because vessels are too sparse in the certain blocks. In this study, we propose a deep learning approach to automate the centerline extraction of CoW based on BraVa dataset [1] and Statistical atlas of cerebral arteries [2] to train the 3D Convolutional Neural Networks (CNN), enabling in-depth investigation of cerebrovascular biomechanics for enhanced biomedical fluid dynamics research.

METHODS

The methods combine Magnetic Resonance Angiography images (MRA) registration, point cloud deformation, and CNN training for generating consistent and accurate centerlines of CoW.

I. MRA registration

Brain Extraction (BET) involves skull removal from MRA in FMRIB Software Library (FSL) [3] to enhance the visibility of vascular features in MRA by eliminating non-brain tissues, such as the scalp and eye socket, which have highly variable contrast and geometry may obscure the blood vessels. Linear registration aims to align MRA in BraVa dataset with statistical atlas. This alignment process is achieved using the FIRLT (FMRIB's Linear Image Registration Tool), which enables a 12-degree-of-freedom transformation in a common 3D space. This alignment ensures that all MRA are spatially transformed to a standardized coordinate system.

II. Point cloud transformation of centerlines.

Centerline of CoW can be extracted from statistical atlas, while the centerline of CoW from BraVa dataset is obtained through the adjacency matrix.

To facilitate the accurate alignment of centerlines, points coordination involves obtaining the coordinates of 132 points on statistical atlas, as well as the corresponding points on 52 subjects in BraVa dataset. This step establishes the correspondence between points in statistical atlas and the respective points in BraVa, enabling a reliable alignment process.

A 4x4 affine transformation matrix is computed to align each point on the centerline of statistical atlas with its corresponding points on the centerline of each subject in BraVa dataset. The computed affine transformation matrix enables quantification of the transformation point cloud from statistical atlas to the centerlines of individual subjects, which can serve as training labels for CNN.

III. 3D Convolutional Neural Networks

To accomplish centerline extraction, firstly BraVa dataset is split into Training Set of 38 cases, Validation Set of 7 cases, and Test Set of 7 cases. Then, a 3D CNN architecture based on an encoder-decoder structure is designed, trained, and utilized to learn the intricate relationships between MRA and their corresponding affine transformation matrices.

RESULTS AND DISCUSSION

This research offers an automatic method for generating consistent centerlines of CoW. Figure 1 (a) shows an example transformation of each point from statistical atlas to its corresponding position of BG0002 subject through affine transformation matrices. Figure 1 (b) visualizes the ranges of distances are represented by the differences between the coordinates of several vessels on statistical atlas and their corresponding points in BraVa. It showcases the maximum and minimum values of these differences across all 52 subjects, as well as the overall range of variations from the maximum to minimum. This suggests that most of values falls within a narrow range. Additionally, the orange line indicates the average value of the differences for each vessel.
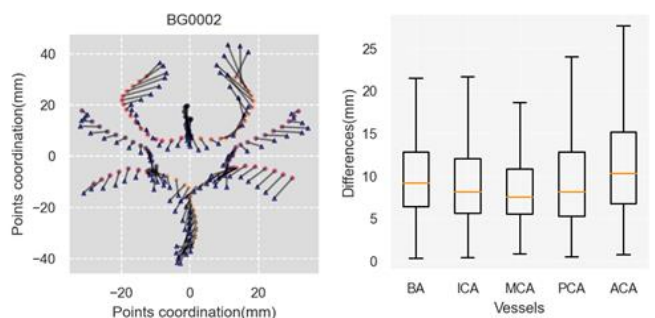
Figure 1 (a) Point cloud transformation of BG0002 in vertical view. (b) Difference of vessels points between statistical atlas and 52 subjects in BraVa dataset.

By transforming the point cloud of statistical atlas, the consistency of centerlines in each subject can be ensured. Additionally, optimizing network training in the future research will consider of reducing the complexity of learning parameters. This will improve the ability to accurately extract the CoW centerlines from any given subject. Furthermore, these findings have significant implications for fluid dynamics simulations and further advance our understanding of cerebral arterial flow.

REFERENCES

[1] Wright S., et al. *NeuroImage* **82** (2013), 170-181, 2013.
[2] Mouches P., et al. *Scientific Data* **6**, 1, 2019.
[3] Woolrich M.W., et al. *NeuroImage*, **45**: S173-86, 2009.

A SUPPRESSION EFFECT OF A MAGNETIC FIELD ON BREAKUP OF A FERROFLUID DROPLET IN SIMPLE SHEAR FLOW

Yuto Kawabata[1], Shunichi Ishida[1] and Yohsuke Imai[1]

[1] Department of Mechanical Engineering, Graduate School of Engineering, Kobe University, Kobe, Japan.

Email: 216t319t@stu.kobe-u.ac.jp

INTRODUCTION

A ferrofluid droplet is a droplet of colloidal dispersion of ferromagnetic particulates, and its unique characteristic has been applied to microfluidic devices. Controlling a droplet breakup in flows is essential to further development, but its method has not been established yet.

Here, we show that the breakup of a ferrofluid droplet in simple shear flow is supressed by imposing a magnetic field perpendicular to the shear plane, using a three-dimensional numerical analysis.

METHODS

Figure 1(a) shows the problem statement of this work. We consider a ferrofluid droplet with a radius a suspended in a non-magnetic fluid. This system is subject to unbounded shear flow $v = (\gamma z, \ 0, \ 0)$ with shear rate and uniform magnetic field $H_0 = (0, \ H_0, \ 0)$. The incompressible two-phase flow is governed by the Stokes equations:

$$-\nabla p + \eta \nabla^2 v + f = 0, \quad \nabla \cdot v = 0, \#(1)$$

where p is the pressure, is the viscosity, v is the velocity, and f is the resultant force of the surface tension and the magnetic force. The magnetic field in both the fluids is governed by the Maxwell's equations for non-conducting fluids [1]:

$$\nabla \cdot B = \nabla \cdot (\mu H) = 0, \quad \nabla \times H = 0, \#(2)$$

Where B is the magnetic flux density, μ is the magnetic permeability, and H is the magnetic field. We solve them on the droplet surface by using the boundary integral method [2, 3]. The capillary number is defined by $Ca = \eta_0 \gamma a / \sigma$, the Bond number is $Bo = a\mu_0 H_0^2 / 2\sigma$, and viscosity ratio is $\lambda = \eta_d / \eta_0$. Where the subscript 0 represents the ferrofluid droplet and d is the non-magnetic fluid, σ is the surface tension, and the Bond number is fixed to $Bo = 4$.

RESULTS AND DISCUSSION

We first investigated the ferrofluid droplets' shapes when the uniform magnetic field is absent and present for $Ca = 0.45$ and $\lambda = 1$. Figure 1(b) shows the typical shape of the droplet viewed from the *y*-direction in each case. When the magnetic field is not imposed, the droplet deforms drastically and results in its breakup (Figure 1(b) left). In contrast, the case imposing the magnetic field shows an ellipsoid-shaped droplet, and it goes into a steady state (Figure 1(b) right). These results indicate that imposing a magnetic field perpendicular to the shear plane can prevent the breakup of the ferrofluid droplet in simple shear flow.

We then summarized the critical capillary numbers Cacr as a function of the viscosity ratio in Figure 1(c). Note that the critical capillary number means the upper limit of the capillary number in which the droplet does not break up. The critical capillary numbers in all the viscosity ratios we examined is pulled up by imposing the magnetic field.

CONCLUSION

We investigated the suppression effect of a uniform magnetic field on the breakup of a ferrofluid droplet in simple shear flow using a three-dimensional numerical analysis. We showed that the breakup of a ferrofluid droplet in simple shear flow supresses by imposing a magnetic field perpendicular to the shear plane.

ACKNOWLEDGEMENT

REFERENCES

[1] Ishida S., & Matsunaga D., *Phys Rev Fluid* **5**: 123603, 2020.
[2] Pozrikidis C., *Boundary Integral & Singularity Methods*, **1991**.
[3] Erdmanis J., et al., *J Fluid Mech* **821**: 266-295, 2017.

COMPUTER SIMULATION OF RED AND WHITE THROMBI FORMATION DETERMINED BY BLOOD FLOW

Ken-ichi Tsubota[1] and Wataru Tokuno[2]

[1] Graduate School of Engineering, Chiba University, Chiba, Japan.

[2] Graduate School of Science and Engineering, Chiba University, Chiba, Japan.

Email: tsubota@faculty.chiba-u.jp

INTRODUCTION

A flow-related mechanism of thrombus formation has been investigated for many years. Recent clinical observations [1] suggest that fibrin formation occurs not only in veins (low flow velocity) but also in arteries (high flow velocity). Numerical simulations of the coupling of platelet (PLT) aggregation and blood coagulation [2] demonstrated that fibrin-rich (venous) and PLT-rich (arterial) thrombi form under low and high flow velocities, respectively. In this study, we performed a two-dimensional numerical simulation of blood coagulation in a large vessel due to a thrombin burst to clarify the thrombus formation process under the influences of flowing red blood cells (RBCs).

METHODS

Blood coagulation was modelled as a process of thrombin burst, diffusion and convection of thrombin under blood flow, and fibrin formation as a function of thrombin concentration. Thrombin burst was expressed by thrombin flux from the surfaces of activated platelets (PLTs) to blood plasma. A rate equation of fibrin concentration CF was assumed as a linear function of thrombin concentration. When CF reached a threshold value, blood plasma was assumed to be coagulated. This was expressed by changing the fluid phase of blood plasma to a solid phase. The blood coagulation was coupled with blood flow where the motion of RBCs and PLTs was directly solved using the particle method [3]. A PLT was assumed to adhere to an injured endothelium and coagulated blood, followed by the activation. The Couette flow between two parallel plates with shear rate was used to express blood flow near the vessel wall, in which the distance between the two parallel plates was set as large as several hundred microns.

RESULTS AND DISCUSSION

Simulated thrombus formation process depended on Peclet number $Pe = d_{RBC}^2/D$ as the blood flow velocity relative to the thrombin diffusion with the coefficient D [$m^2 s^{-1}$], where $d_{RBC} = 5$ μm is the characteristic length of an RBC. In the case of low blood flow velocity (Pe=2.5), a thrombus by blood coagulation was grown toward the inside of the blood vessel, involving PLTs and RBCs. Those PLTs released thrombin after their activation, which helped to continue blood coagulation. Ratios of thrombus component amounts at the final state of the simulation corresponded to experimentally measured venous thrombus whose mass was occupied mainly by RBCs and fibrin [1].

In case of high blood flow velocity (Pe=100), PLT aggregates trapped another PLT that moved along blood flow on the upstream side, and then grew large to form
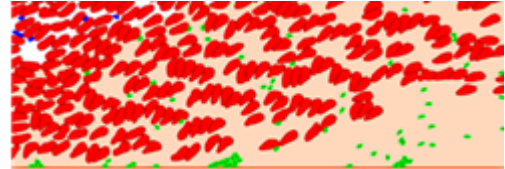
Red thrombus formed in low Peclet number (Pe = 2.5)
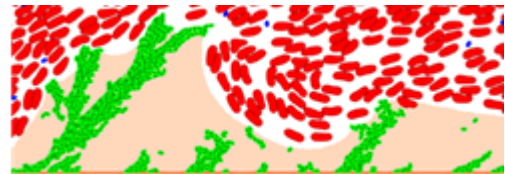
White thrombus formed in high Peclet number (Pe = 100)

Figure 1 Simulated thrombus formation depending on Pe.

"valley and mountain" shape [4]. Blood coagulation formed downstream of PLT mountains, the formation amount of which was much smaller than that in the case of low flow velocity (Pe=2.5) because thrombin released from PLTs was washed out by significant convection from both the upstream and downstream sides of the PLT mountains. Ratios of thrombus component amounts corresponded to experimentally measured arterial thrombus [1], whose mass was occupied mainly by PLTs and fibrin.

Ratios of thrombus components were quantitatively different between the current simulations and published experimental results. This might be due to a simple model used for blood coagulation, as well as to a two-dimensional model.

CONCLUSION

Our numerical simulations demonstrated that thrombus formation process was determined by blood flow velocity relative to the thrombin diffusion. Many and few RBCs were involved at low and high flow velocities, respectively, in a blood coagulation. The results suggest that velocity-dependent kinematics of RBCs relative to thrombin diffusion plays an important role in forming red and white thrombi.

ACKNOWLEDGEMENT

REFERENCES

[1] Chernysh I.N., et al. *Sci Rep* **10**: 5112, 2020.

[2] Bouchnita A., & Volpert V. *Comput Fluids* **184**: 10-20, 2019.

[3] Tsubota K., & Namioka K. *J Biomech* **137**: 111081, 2022.

[4] van Rooij B.J., et al. *Sci Rep* **10**: 1-11, 2020.

MOLECULAR INSIGHTS INTO ATPASE RELEASE PATHWAY OF CYTOPLASMIC DYNEIN

Pei-Cheng Li[1], Yu-Bai Xiao[1], Shu-Wei Chang[1,2]

[1] Dept. of Civil Engineering, National Taiwan University/ Taipei 10663, Taiwan, R.O.C.
[2] Dept. of Biomedical Engineering, National Taiwan University/ Taipei 10663, Taiwan, R.O.C.
Email:changsw@ntu.edu.tw

INTRODUCTION

Cytoplasmic dynein is a family of motor proteins with six AAA+ domains that move along microtubules in cells and is responsible for transporting intracellular cargos. It generates force through an ATP-consuming cycle in the AAA+ domains. The motility of dynein is coupled to the ATP hydrolysis cycle at AAA1, and the process requires AAA3 to be in a post-hydrolysis state (ADP-Pi or ADP) [1]. Although the mechanochemical cycle of dynein's movement has been concluded, it is still unclear how the hydrolysis products (ADP/Pi) are bonded and released. In this work, we utilize metadynamics simulations to understand the releasing mechanism of Pi ($H_2PO_4^-$) at AAA1 and AAA3 [2]. The collected potential of mean force (PMF) of Pi inside the AAA1/3 domain is used to explore the lowest cost path to deliberate the mechanism. Finally, a comparison in releasing path and the energy barrier between the two domains were conducted.

METHODS

A.   Model Setup

NAMD 2.14 was used for all the all-atom molecular dynamics simulations. To mimic the state just after ATP hydrolysis, ADP at AAA1 and AAA3 were first replaced with ATP and then separated into ADP and Pi ($H_2PO_4^-$). The system was energy minimized and equilibrated in the NPT ensemble for 25 ns, followed by the NVT ensemble for 45 ns. The pressure was set at 1 atm, and the temperature was set to 310 K.

B.   Metadynamics Simulation

Metadynamics simulations were conducted to find the Pi release pathway and estimate the energy profiles. The absolute Cartesian coordinates x, y, and z of Pi were used as collective variables and Gaussian potentials with 0.2 kcal/mol and width of 1.0 Å were added into the system to enhance sampling and estimate energy profiles of Pi release. Two stable CA atoms (RMSD < 4) at the object site were fixed during the simulation.

RESULTS AND DISCUSSION

According to NVT equilibrium simulations, the binding site for ADP and Pi at AAA1 is composed of ARG2358, ARG2091, and ARG2046, and made up of ARG2801, ARG3088, LYS2601, THR2800 at AAA3. It was found from the trajectories of metadynamics simulations that Pi at both units leave the binding site at the interface of the domain it is bounded and the neighboring subunit (Figure 1), and ADP could be brought out with Pi through MG, which is

unexpected and could be related to the number of water molecules in the protein [3].

After analyzing the hydrogen bonds in metadynamics simulations, we noted that most of the residues bound with ligands are Arginine, so we hypothesize that Arginine play an important role in the ligand release pathway. According to the lowest cost path calculated by energy profiles, we found that the energy required for both Pi release at AAA1 and Pi release at AAA3 are in the range of ~10 to 15 kcal/mol.
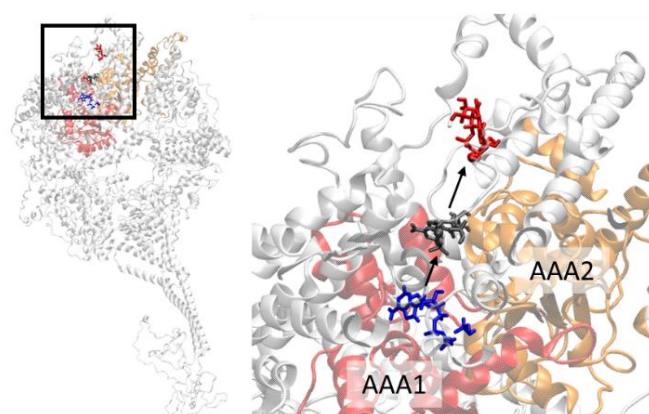
Figure 1 ADP and Pi release pathway

CONCLUSION

In this study, we first clarify the binding site of ligands at the two subunits based on equilibrium simulations, then implemented metadynamics to search for an approximate Pi release pathway. We found that the ligands came out together. On the other hand, many Arginine was involved in the release of ligands, indicating its importance in the process. The PMF data of the simulations were utilized to find the lowest cost path at the two domains, where it was shown that the energy barrier at AAA3 is higher than AAA1. Our results provide important molecular insights into the molecular mechanism of Pi release of dynein.

REFERENCES

[1] DeWitt, M.A., et al. *Nat Struct & Mol Biol* **22**(1): 73-80, 2015.
[2] Okazaki, K., & Hummer, G. *Proc Nat Acad Sci*, 2013, **110**(41): 16468-16473, 2013.
[3] Mugnai, M.L., & Thirumalai, D. *J Physical Chem B*, **125**(4): 1107-1117, 2021.

DEVELOPMENT OF A COMPUTATIONAL MECHANICAL MODEL OF BRAIN VOLUME CHANGE WITH CEREBRAL ATROPHY

Yuta Iijma[1], Shusaku Maeda[1], Tomohiro Otani[1], Shigeki Yamada[2], Mitsuhito Mase[2] and Shigeo Wada[1]
[1]Graguate school of Engineering Science, Osaka University, Toyonaka-shi, Osaka, Japan.
[2]Depatrment of Neurosurgery, Nagoya City University Graduate School of Medical Science, Nagoya-shi, Aichi, Japan.
Email: y.iijima@biomech.me.es.osaka-u.ac.jp

INTRODUCTION

The brain is a fluid-saturated poroelastic material and keeps its mechanical balance between solid and fluid phases in an intracranial space. It is known the cerebral atrophy progresses with degeneration of nerve cells in brain [1], which changes the mechanical balance of the brain tissues resulting in decrease of bulk volume of the brain containing interstitial fluid. However, these underlying mechanisms are poorly understood. This study aims to develop a computational mechanical model of cerebral atrophy with considering anatomical brain shape and the volume change of brain observed in clinics.

METHODS

A brain geometry was constructed from a statistical shape model of the human brain distributed in image format [2]. A three-dimensional (3D) brain shape containing ventricle space, white matter (WM), and grey matter (GM, thickness of 3 mm) was reconstructed from images using 3-matics (Materialise, Inc.), and tetrahedral volume meshes were created using HyperMesh (Altair Engineering, Inc) (Fig. 1). The mechanical balance state of the brain tissue was computed with Galerkin finite element method. Brain tissues were assumed as the compressible neo-Hookean material, in which the strain energy density function W is given by

$$W = \frac{\mu}{2}(I_c - 3) - \mu \ln J + \frac{\lambda}{2}(\ln J), \qquad (1)$$

where I_c is the first invariant of the right Cauchy-Green deformation tensor, J is the volume change ratio, and constants of μ and λ were set to 2 kPa and 64.67 kPa for WM, and 1kPa and 32.33 kPa for GM [3]. In this study, the decrease in bulk volume of the brain with cerebral atrophy was represented by changing the reference state of brain tissue. Here, the reference length was assumed to be isotropically decreased in the principal direction, which is expressed by the multiple decomposition of the deformation gradient tensor $\mathbf{F}$, given by

$$\mathbf{F} = \mathbf{F}_1(\mathbf{u}) \cdot \mathbf{F}_0(\lambda), \mathbf{F}_0(\lambda) = \lambda \mathbf{I} \qquad (2)$$

where $\mathbf{F}_1(\mathbf{u})$ is the deformation gradients defined by displacement $\mathbf{u}$ from initial to current states and $\mathbf{F}_0$ is the prescribed deformation gradient from the stress-free to the initial configuration defined by the initial stretch λ. Here, we set λ=1.0527 (15% volume loss) in GM only, based on clinical observation as aging [4]. Fixed displacement condition was assigned at the basal brain surface (Fig.1(right)).

RESULTS AND DISCUSSION

Fig. 2 (left) shows equivalent strain distribution on the axial plane in the WM by the volume loss of the interstitial fluids

in GM. High strain concentration was found near GM. Fig. 2 (right) shows the initial and deformed brain shape where the deformation was 10 times magnified to emphasize the deformation characteristics. Relatively large deformation to expand the subarachnoid spaces between left and right hemispheres was found in the upper region, which is qualitatively consistent with clinical brain atrophy [5].
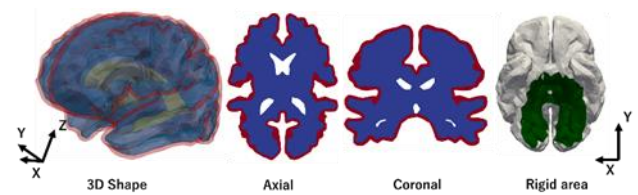
Figure 1 Brain shape model consisted of white matter (blue) and grey matter (red). The basal brain (green) is fixed for simulation.
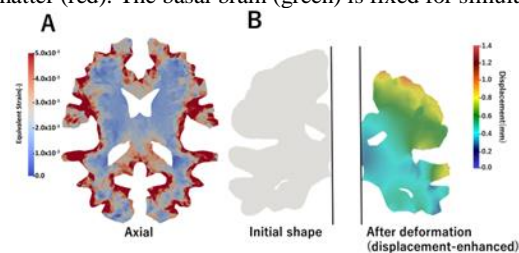
Figure 2 Equivalent strain distribution on the axial plane in the WM (A) and displacement distribution from the initial shape (B), in which the deformation was 10 times magnified.

CONCLUSION

This study developed a computational model of brain remodelling by cerebral atrophy. Numerical examples demonstrated that GM volume loss provided anisotropic, characteristic brain deformations, consistent with clinical knowledge. This finding suggests that mechanical balances would be one of the essential factors to understand the mechanism of cerebral atrophy.

ACKNOWLEDGEMENTS

REFERENCES

[1] Daners et al., *PLoS One*, 2012.
[2] Wichmann et al., *Front. Neurosci.*, 2011.
[3] Blinkouskaya et.al, *Front. Mech. Eng.*, 2021.
[4] Yamada et al., *Eur J Radiol*, 2023.
[5] Damasceno, *Dement Neuropsychol*, 2015.

SELF-ORGANIZED PATTERNS OF FERROFLUID DROPLETS IN WALL-BOUNDED SHEAR FLOW

Shunichi Ishida[1] and Daiki Matsunaga [2]

[1] Graduate School of Engineering, Kobe University, Kobe, Japan.

[2] Graduate School of Science Engineering, Osaka University, Toyonaka, Japan

Email: ishida@mech.kobe-u.ac.jp

INTRODUCTION

Ferrofluid droplets are magnetic emulsions that are immersed in a non-magnetic fluid, which can be magnetized under a uniform magnetic field and extend in the field direction. The ferrofluid droplet can be a practical material to control the suspension rheology by imposing the magnetic field [1]. However, the main scope of the previous works has been limited to manipulating a single ferrofluid droplet, and it would be useful as a metamaterial if collective motions of droplets could be controlled by the magnetic field. In this paper, we report that the spatial self-organization patterns of ferrofluid droplets in shear flow can be controlled by various direction of the external magnetic field [2].

METHODS

Consider ferrofluid droplets of radius a suspended between two parallel plates which are separated by a distance L_z as shown in Fig.1A. The domain size is $L_x \times L_y \times L_z = 18a \times 12a \times 3a$, and the number of the droplets $N = 16$. By relative movements of two plates, a simple shear flow with shear rate $\dot{\gamma}$ can be generated. For simplicity, we assume the viscosity η and the density ρ the same inside and outside of the droplets. The magnetic permeability inside the droplet μ_d is assumed to be $\mu_d/\mu_0 = 2$ where μ_0 is the vacuum permeability. An external magnetic field is applied: $H_0 = H_0(sin\theta cos\phi, sin\theta sin\phi, cos\theta)$, where θ and ϕ are the polar and azimuthal angle, respectively. $H = H_0$ is taken at both the top and the bottom wall as boundary conditions for the magnetic field. In the absence of electric currents, H satisfies the following magneto-static Maxwell's equations [3]:

$$\nabla \cdot (\mu H) = 0, \quad \nabla \times H = 0, \tag{1}$$

where μ is the magnetic permeability.

The two-phase flow hydrodynamics is governed by the following incompressible Navier-Stokes equation:

$$\nabla \cdot u = 0, \tag{2}$$

$$\rho \left(\frac{\partial u}{\partial t} + u \cdot \nabla u \right) = -\nabla p + \eta \nabla^2 u + f_s + f_m, \tag{3}$$

where u is the velocity field, p is the pressure, ρ is the density, η is the viscosity, f_s is the surface tension force, and f_m is the magnetic force. Equations (2) and (3) are solved by the lattice Boltzmann method. The front-tracking method is used to track the droplet interface.

RESULTS AND DISCUSSION

Figure 1B shows the phase diagram of the droplet patterns in simulations with changing values of θ and ϕ. As illustrated in the phase diagram, ferrofluid droplets can alter their organized patterns from the chain-like to a crystal-like pattern because of the repulsive magnetic interactions between the droplets. The droplets form a crystal pattern (Fig.

1E) when the magnetic field is perpendicular to the parallel plates ($\theta \sim 0$), while the magnetic field is nearly parallel to the plates ($\theta \sim \pi/2$), the droplets form a chain-like patterns as shown in Fig. 1C and 1D.
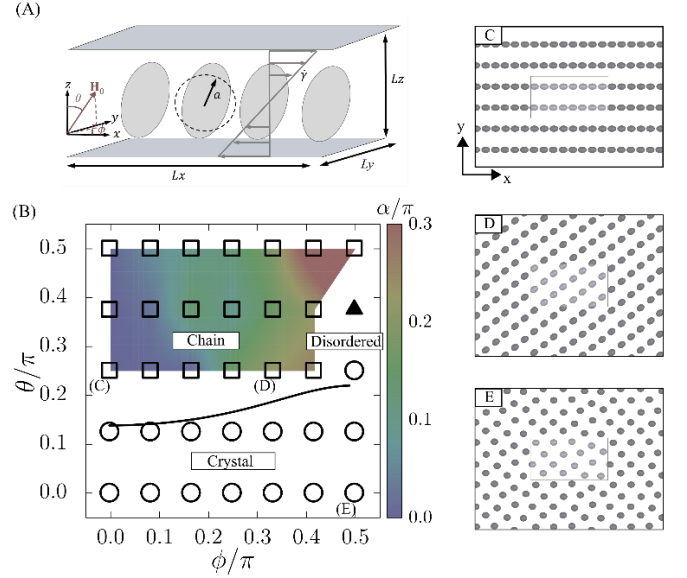
Figure 1 (A) Schematic illustration of the system setup. (B) Phase diagram of the spatial pattern under various magnetic field directions. The solid curve is the theoretical estimation of the chain-crystal transition [2]. In the phase diagram, each symbol denotes square (chain pattern), circle (crystal pattern), and triangle (disordered pattern), respectively. The contour shows angle of the droplet alignment in the chain pattern. (C-E) Snapshots from the simulation.

CONCLUSION

In this study, we analysed self-organized patterns of ferrofluid droplets suspended in a wall-bounded shear flow. By applying shear flow and magnetic field, we showed that various collective patterns of ferrofluid droplets can be realized by controlling the interplay of hydrodynamics and magnetic interactions. Our system demonstrates the potential of ferrofluids as a configurable and repressible metamaterial.

REFERENCES

[1] Ishida S and Matsunaga D, *Phys Rev Fluids* **5**: 123603, 2020.

[2] Ishida et al. *Phys Fluids* **34**: 063309, 2022.

[3] Rosenweig RE, Ferrohydrodynamics, *Cambridge University Press*, 1985.

DEVELOPMENT OF A NUMERICAL SIMULATOR OF PHASE CONTRAST MAGNETIC RESSONANCE IMAGING

Ellen Cavalcante Alves,[1], Yu Sato[1], Tomohiro Otano[1], Tetsuro Sekine[2] and Shigeo Wada[1]
[1] Department of Mechanical Science and Bioengineering, Osaka University, Toyonaka, Japan.
2 Department of Radiology, Nihon Medical University, Kanagawa, Japan
Email: ellen.cav.alves@gmail.com

INTRODUCTION

Phase-contrast magnetic resonance imaging (PC-MRI) is a non-invasive technique capable of providing biological flow velocity data. However, the nonnegligible artifacts intrinsic to the system, especially for unsteady and complex flow field measurements, limit its diagnostic capabilities [1]. Therefore, this study developed a computational model of PC-MRI capable of simulating the physical behavior and measurement process, from which the system response to certain parameters can be evaluated and understood.

METHODS

The PC-MRI simulation solves spin transport in background flow fields while performing an image reconstruction routine, including the appropriate magnetic field, radiofrequency pulse sequence, signal acquisition and image processing protocols (Figure 1). The spin transport is characterized by the magnetic moment **M** of the spins under a magnetic field **B** and periodic excitement from radio-frequency pulses. In the Cartesian domain, this behavior is described by the Bloch Equation [2], given by

$$\frac{\partial \mathbf{M}}{\partial t} + \mathbf{v} \cdot \nabla \mathbf{M} = \gamma \mathbf{M} \times \mathbf{B} - \frac{M_x}{T_2} \mathbf{e}_x - \frac{M_y}{T_2} \mathbf{e}_y + \frac{M_o - M_z}{T_1} \mathbf{e}_z \qquad (1)$$

where the gyromagnetic ration γ, the longitudinal equilibrium magnetization M_o, the spin-lattice and spin-spin relaxation times T_1 and T_2, and the flow velocity vector **v** are prescribed parameters. Equation 1 was solved over a uniform cartesian grid through finite difference method using a step-by-step approach.

The image reconstruction routine follows the spoiled gradient echo sequence through which flow velocities were computed by a balanced four-point method [2].

For the numerical example, a PC-MRI of a non-viscous Taylor-Couette flow was considered, with internal and external cylinders of 32 mm and 96 mm radius and tangential velocities of 1 m/s and 0 m/s respectively (Figure 1 top right image).

Furthermore, the parameters T_1, T_2, γ and M_o were set as 1000 ms, 200 ms, 42.6 10^3 kHz/T and 100 as a normalized value. Computational grids and MRI image size were set to 256×256 mm^2 and 128×128 voxels. The evaluation of the output was performed through the absolute and percent errors of the reconstructed velocity over the original value on each voxel, organized and averaged over different velocities ranges for better analysis.

RESULTS AND DISCUSSION

The PC-MRI simulation could recreate the velocity profile with a percent error of 4.3% in average. From that, over 45%

of the total error was observed on voxels associated with velocities between 0 and 0.1 m/s. This high concentration reinforces the understanding of PC-MRI limitations with slow flow mapping.
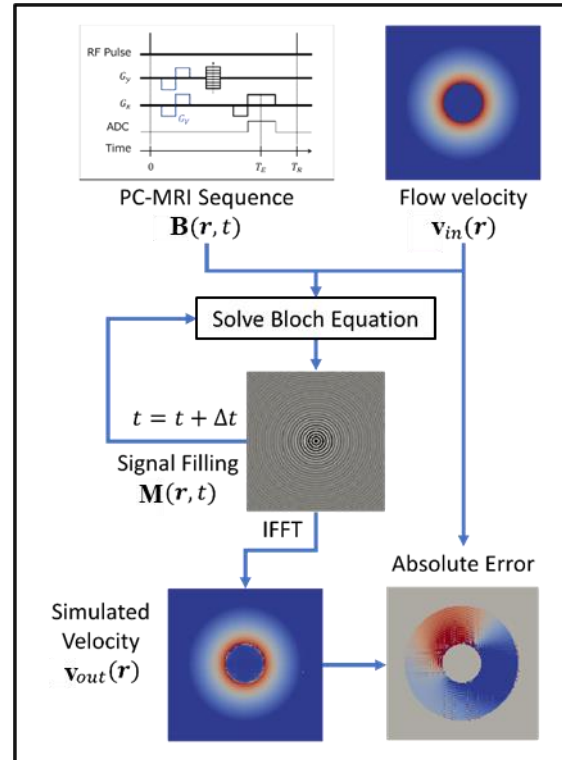
Figure 1 PC-MRI simulation flow

CONCLUSION

The computational model developed was capable of successfully replicating the PC-MRI routine and providing a velocity map in accordance to the inserted with the present errors also found in PC-MRI images. To further investigate the method, different velocities profiles should be observed.

ACKNOWLEDGEMENT

REFERENCES

[1] Zhuang et al. *Quant Imaging Med Surg* **11**:4193-4210, 2021.
[2] Brown R W et al. *John Wiley & Sons* **2**, 2014.

VERTEBRAL STRENGTH PREDICTION USING AUTOMATIC CT-BASED L1 MODELS WITH BONE INHOMOGENEITY

Yen Cheng[1], Po-Liang Lai[2], Mao-Chieh Su[3] and Hsiang-Ho Chen[2,3]

[1] Department of Biomedical Engineering, National Yang Ming Chiao Tung University, Taipei, Taiwan.
[2] Department of Orthopedic Surgery, Linkou Chang-Gung Memorial Hospital, Tauyuan, Taiwan.
[3] Department of Biomedical Eng., Center for Biomedical Eng., Chang Gung University, Tauyuan, Taiwan.
Email: hchen@mail.cgu.edu.tw

INTRODUCTION

Biomechanical computed tomography analysis can predict the bone strength and vertebral fracture risk in patients with low bone density. To automatically create a finite element model with inhomogeneous bone materials, a customized (MATLAB) program was designed for pre-processing CT images of each patient. This study compared the vertebral strain in human subjects generated by using a MATLAB program.

METHODS

When modeling with MATLAB, the CT images are first stacked into a 3D array, and the pixel values are converted into Hounsfield units based on the RescaleSlope and RescaleIntercept in the CT image tag. The PixelSpacing is used to determine the actual imaging size. Using the Volume Segmenter, the general location of the image is marked for cropping. The bone segment is then separated based on the Hounsfield units, and the largest voxel group is marked for isolation, to separate the vertebrae to be analyzed. According to the order of intensity values, the coordinates of each voxel's eight nodes are numbered and stored in a cell, which are then converted into three-dimensional coordinates. The intensity is converted into apparent density and elastic modulus using an empirical formula [1]. The maximum and minimum values of the y-coordinate are stored in an additional array to establish the node set for the upper and lower plane of the vertebral body. Strain calculation was conducted by LS-DYNA (LSTC, Livermore, CA, USA). A 5000N compression force was distributed perpendicularly on the upper endplate of the vertebral body. All nodes in the lower plane of the vertebral body are restricted. After renumbering the nodes, the solver can be utilized for computation. For comparison, L1 vertebral models were automatically established from 30 women recruited. Four hundred different levels of moduli were assigned in the trabecular area to meet the real inhomogeneity of the vertebral body. Subjects were divided into three age groups. The subjects were 30~39 years old in the young group(30s), 50~59 years old in the middle-aged group, and 70~79 years old in the elderly group. To predict the mechanical strength, their principal strains were estimated by finite element method.

RESULTS AND DISCUSSION

The models were generated by using the MATLAB program automatically (Figure 1). The computation time was less than 1.5 hours. Comparing the maximal 10 % of the 1st Principal Strain-Infinitesimal, the differences among the three age groups was significant by ANOVA test (Table 1). Regarding the 3rd Principal Strain-Infinitesimal, the difference among three age groups was also significant. The elderly group has the largest strain and possibly fail under 5000N loading [2].
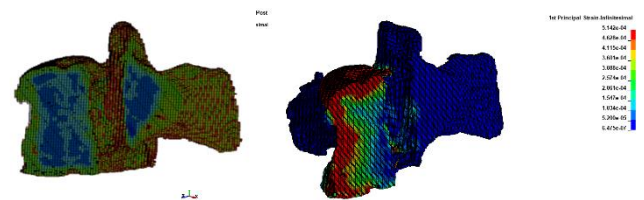
Figure 1 Left: E distribution; Right: strain distribution of vertebral model in sectional view.

CONCLUSIONS

The modelling process used in this study can perform pre-processing and model meshing tasks automatically and saves time and labor costs in pre-processing. This modelling method can be used to predict the mechanical strengths and fracture risks of vertebrae.

REFERENCES

[1] Rho, J., et al. *Med Eng Phys.* **17**:347-55, 1995.
[2] Bayraktar, H.H., et al. (*J Biomech* **37**:27-35, 2004.

Table 1 Vertebral Strain under 5000N loading in three age groups.

Age Group (n=30)	Young (30s)	Middle-Aged (50s)	Elderly (70s)
1st Principal Strain (tensile)	0.143± 0.025 %	0.207±0.061 %	0.389±0.446 %
3rd Principal Strain (compressive)	0.42±0.06 %	0.60±0.16%	1.16±1.16%
Yielding Strain of bone:	Tensile 0.73%	Compressive 1.04%	Bayraktar et al. (2004)

ISOGEOMETRIC BOUNDARY ELEMENT ANALYSIS OF WRINKLING AND CREASING OF A CAPSULE MEMBRANE IN A SHEAR FLOW

Hironori Takeda[1], Yusuke Asai[1], Shunichi Ishida[1] and Yohsuke Imai[1]
[1] Graduate school of Engineering, Kobe University, Kobe, Japan.
Email: takeda@people.kobe-u.ac.jp

INTRODUCTION

Wavy shapes of biological membranes are formed through the process of buckling [1]. The buckled membrane can be categorized into various types, such as wrinkles and creases. Wrinkles exhibit a smooth appearance, while a crease is post-buckled shape that lacks smoothness at its ridge. A capsule, which consists of a liquid enclosed by a membrane, can form wavy shapes due to the influence of external fluid flow [2]. When capsules are subjected in a shear flow, in addition to the elongation and rotation, buckling occurs as a result of flow-induced compression, leading to the formation of wavy capsule membranes. The objective of this study is to investigate the wavy pattern in the capsule under simple shear flow.

METHODS

To investigate the wrinkling and creasing of the capsule membrane, we developed a numerical method to calculate the geometry of the inner and outer surface. The deformation of the capsule was formulated by Kirchhoff--Love shell theory, taking into account the change in membrane thickness [3]. The material property of the capsule was modelled as the incompressible neo-Hookean material. The fluid flow was calculated by the boundary integral equation for Stokes flow. The shape of the capsule was represented by a T-spline surface. The capsule deformation induced by the shear flow was solved using isogeometric boundary element method.

RESULTS AND DISCUSSION

We simulated the deformation of the capsule in the shear flow with a shear rate $\dot{\gamma}$ (Fig. 1A). At the initial state ($\dot{\gamma}t = 0$), the capsule has the spherical shape with a radius a and a membrane thickness h_0. We defined a dimensionless parameter named the capillary number, $Ca = \mu\dot{\gamma}a/(Gh_0)$, where G is the elastic shear modulus of the capsule membrane.
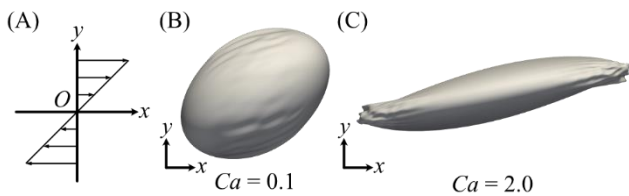
Figure 1 (A) Simulation condition of the simple shear flow. Deformed shapes of the capsule in the shear flow with (B) $Ca = 0.1$ and (C) $Ca = 2.0$ at non-dimensional time $\dot{\gamma}t = 20$. The thickness of the capsule membrane is $h_0/a = 0.001$.

Figure 1B and C shows the capsule shapes with $Ca = 0.1$ and 2.0 at time $\dot{\gamma}t = 20$. In both cases, the thickness of the capsule membrane was $h_0/a = 0.001$. When $Ca = 0.1$, the capsule formed wrinkles in the vicinity of the central to both tips of the elongated capsule. When $Ca = 2.0$, the wrinkles were formed in the vicinity of the tips. To investigate the deformation types of the capsule, we calculated the parameter of the geometrical consistency $|\kappa d|$, where the κ is the larger principal curvature of the mid-surface and d is the distance from the mid-surface to the outer or inner surface. $|\kappa d| < 1$ and $|\kappa d| = 1$ indicate the wrinkled and creased membranes, respectively (Fig. 2A and B). If $|\kappa d| > 1$, the surface has a geometrical inconsistency. We investigated the maximum value of $|\kappa d|$ during deformation by changing Ca and h_0 (Fig. 2C). When $Ca \geq 1.7$ and $h_0/a \geq 0.002$, $|\kappa d|$ reached 1, indicating that creasing occurred. This was because that increase in d with h_0 resulted in the ease of self-contact.
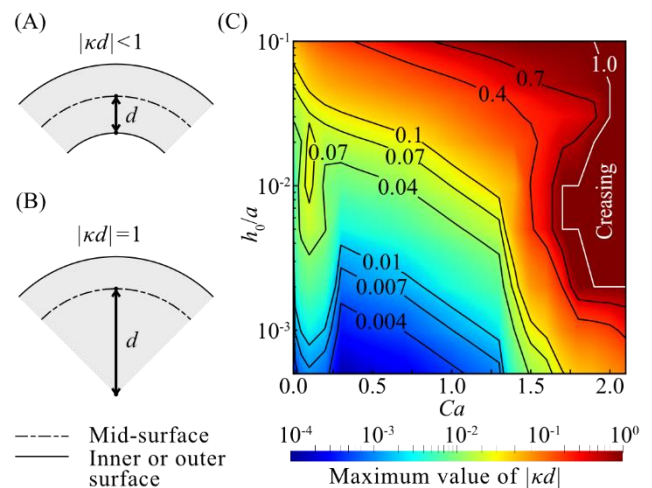
Figure 2 Wrinkling and creasing of the capsule membrane. (A, B) The parameter of geometrical consistency $|\kappa d|$. (C) The maximum value of the parameter of $|\kappa d|$ during deformation

CONCLUSION

The isogeometric boundary element analysis showed that the capsule in the shear flow formed wrinkles and creases. This study will be useful for investigating the geometrical consistency to further understand the post-buckling of capsules in Stokes flow.

REFERENCES

[1] Cerda E., & Mahadevan L. *Phys Rev Lett* **90**: 074302, 2003.
[2] Lac E., et al. *J Fluid Mech* **516**: 303-334, 2004.
[3] Takizawa K., et al. *Computational Mechanics* **63**: 681-700, 2018.

MULTI-CELL MODELLING OF THE SKELETAL MUSCLE MICROENVIRONMENT TO EXPLORE AGE-RELATED CHANGES IN SATELLITE CELL DYNAMICS

Stephanie Khuu [1] Andrew D McCulloch [1]

[1] Department of Bioengineering, University of California, San Diego.

Email: stkhuu@ucsd.edu

INTRODUCTION

The regenerative potential of skeletal muscle tissue depends on cell-cell and cell-matrix interactions in the muscle microenvironment. Satellite cells (SCs) are the muscle resident stem cells that play a pivotal role in muscle fibre repair; however, the ability of the muscle milieu to adapt following damage is attributable to regulation by many cell types as well as chemical and mechanical guidance cues. Ageing muscle shows a functional decline in stem cell dynamics, with changes to polarisation and integrin density leading to increased asymmetric (apicobasal) division relative to symmetric (planar) division [1]. Understanding the regulators of SC division in muscle fibre bundles is an important step in rescuing regenerative potential of muscle. In silico modelling offers a high throughput method to investigate chemical and mechanical regulators of cell-cell and cell-matrix interactions that is otherwise not possible. This preliminary study aims to recapitulate the effect of growth factors and cytokines, such as hepatocyte growth factor (HGF), on SC repair kinetics using multi-cell models of repair. Specifically, we evaluate the effect of increasing HGF concentration in recruiting SCs to the damage site.

METHODS

A 3D multi-cell model of the muscle microenvironment was created using CompuCell3D (CC3D), a virtual tissue modelling platform [2]. The simulation represented four cell types: muscle fibres, satellite cell, damaged tissue, and the ECM. These cells were represented as agents, with rules governing their behaviour. Agents were implemented in a 100x10x8 lattice. Physical properties such as volume, surface area, contact and adhesion molecule density are described in Table 1. Average SC diameter relative to muscle fibre diameter is represented in the model. Growth factors and cytokines are diffused in the space using the following equation:

$$\frac{\partial c}{\partial t} = D\nabla^2 c - kc + secretion$$

where k is a decay constant of concentration c and *D* is the diffusion constant.

Secretion of HGF from damaged tissue was varied from 0-50, and the time for SCs to reach the damage tissue location was recorded. Each time step represented one minute, and simulation end time was set to 3000 minutes. Initial SC distance from damage was set to ~20 pixels for all simulation conditions.

RESULTS AND DISCUSSION

Satellite cells did not reach the location of damage when HGF secretion was 10 or below. SCs time to reach damage location was decreased when HGF secretion from damaged tissue was increased. With secretion set to 50 or 40, distance to damage was comparable (~800 mins). Secretion level of

30 took 1000 min to reach the damage location, while 20 took 1750 min.

Table 1 Initial agent properties in 3D model of skeletal muscle microenvironment.

Agent	Volume	Surface Area
Muscle fibre	1971	1664
Damaged tissue	24	52
Satellite Cell	4	18
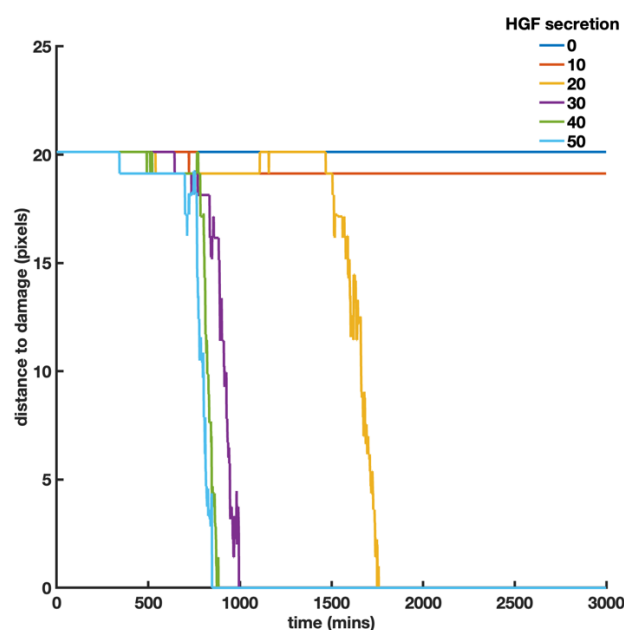
Figure 1 Satellite cell distance from damage over time at different HGF secretion levels. Single simulations shown only.

By changing the HGF secretion alone, this model can recapitulate the actions of known activators of SCs.

CONCLUSION

In silico models of the muscle microenvironment can recapitulate its complex composition. This model can be used to study pathways pertinent to the maintenance of regenerative potential of skeletal muscle.

ACKNOWLEDGEMENT

REFERENCES

[1] Feige P., et al. *Cell Stem Cell*. 2018
[2] Swat M.H., et al. *Methods in Cell Biology*. 2012

THE SIMULATION OF BLOOD VESSEL REVASCULARIZATION IN STENOSIS CASE WITH SPRING-DAMPER ANALOGY METHOD

Muhammad Ihsan Maulana[1], Bonfilio Nainggolan[2], Mikha Hilliard[1], Faqihza Mukhlish[1], and Narendra Kurnia Putra[1]

[1] Engineering Physics Department, Institut Teknologi Bandung, Bandung, Indonesia.
[2] Department of Physics, Arizona State University, Tempe, United States.
Email: narend@itb.ac.id

INTRODUCTION

Stroke ranked as the second disease cause of death worldwide [1]. Most stroke cases are caused by plaque accumulation inside the vessel walls, commonly known as stenosis. The method to treat stenosis is using balloon angioplasty (BA) to revascularize the stenosis area, then place the stent to maintain the opened vessel position. The importance of designing a good medical device plays a big role according to clinical regulation. To support the objective, we develop an *in silico,* or a computational simulation device, to represent the physical phenomenon during the revascularization treatment activity. Also, *in silico* simulation allows us to obtain physical parameters during the treatment activity represented.

METHODS

The computational simulation algorithm is virtually implemented using a spring-damper model analogy with the lineal and semitorsional spring approach [2]. The derived equilibrium system equation will be transformed into a discrete form to solve the derivative function problem iteratively by Euler's numerical method. The computation algorithm is used to rebuild two types of stenosis models, ideal and realistic models, to be each revascularized vessel model in a three-dimensional representation. Firstly, the model will be exploded and consecutively shrink to the boundary condition, that is, the Signed Distance Field (SDF) of the virtual BA used in the simulation. The exploding process is meant to prevent encountering the instability problem during the numerical simulation. After the final geometry configuration is obtained, the next step is to examine the physical information, which is pressure estimation along the blood vessel by the forces yielded from each evolutionary step. It was according to the actual condition when inflated BA pushed up the vessel. The pressure data regarding the standard clinical reference, such as Rated Burst Pressure (RBP) and maximum vessel pressure tolerance, can further be evaluated.

RESULTS AND DISCUSSION

The result of pressure estimation from the final revascularized model for each case, ideal and realistic blood vessel configuration, is depicted in Figure 1. The darkest red surface color implies a higher pressure on the specific area. The pressure profile focused on the middle of the revascularized region, caused by the deformation in the stenosis part is larger than on the other side.
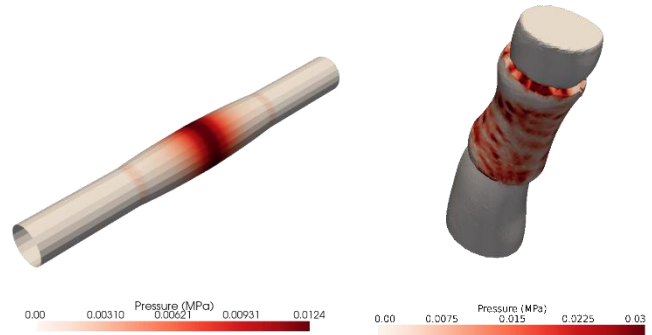
Figure 1 Pressure profile on the ideal and realistic revascularized vessel model.

The model was deployed with the particular BA parameters used as the simulation-stopping criteria. Referring to the BA's RBP data, the summary of the vessel's pressure compared to the RBP is shown in Table 1.

Table 1 Summary of pressure data compared with the RBP.

Case	Pressure (MPa)		RBP (MPa)
	Maximum	Average	
Ideal	0,012	0,0018	2
Realistic	0,245	0,004	2

As shown in Table 1 that the maximum pressure for both cases are still below the RBP. Therefore, treating actual stenosis similar to the virtual model can be done clinically securely with the used BA parameter.

CONCLUSION

The computational simulation algorithm gives the final desired configuration of the revascularized model of the ideal and realistic model. Thus, the pressure estimation shows that both cases' maximum pressure is still below the RBP. According to that, through this work, the BA configuration used to treat similar stenosis cases will not burst during the treatment or possibly fall into treatment failure.

ACKNOWLEDGMENT

REFERENCES

[1] Donkor, E. S. "Epidemiology, and Quality of Life," 2018
[2] Spranger K., & Ventikos Y., *IEEE Trans Biomed Eng*, **61**(7): 1998-2010, 2014.

DEVELOPMENT OF A 3D RECONSTRUCTION METHOD FOR RED BLOOD CELL SHAPES BY DEEP LEARNING AND FLUID-STRUCTURE INTERACTION ANALYSIS

Gakuto Nakaie[1], Shunichi Ishida[1], Yusuke Asai[1], Takuma Kaneoka[1] And Yohsuke Imai[1]
[1]Graduate School of Engineering, Kobe University, Kobe, Japan.
Email: 220t345t@stu.kobe-u.ac.jp

INTRODUCTION

Red blood cells (RBCs) deform into various shapes andpass through a capillary whose diameter is smaller thanthat of RBCs (~8μm). It is possible to take 2D pictures of RBCs and observe 2D RBC shapes. However, it is difficult to observe 3D shapes of RBCs in a capillary flow in an experiment. Our goal is to reconstruct 3D RBC shapes from 2D pictures taken in an experiment and observe them. The objective of this study is to develop a method of 3D reconstruction for RBCs from single 2D pictures using deep learning and fluid- structure interaction analysis as the first step of our goal.

METHODS

We simulated RBC flow in a capillary whose diameter is $D = 16$ μm. The volume fraction of RBCs called hematocrit is $Hct = 0.2$. Governing equations for fluid mechanics are the continuity and Navier-Stokes equations for incompressible and Newtonian fluids. Formembranes of RBCs, we used Skalak's constitutive law[1]. We used the isogeometric analysis [2] for membrane mechanics, the lattice Boltzmann method forfluid mechanics, and the immersed boundary method forthe coupling method.

We used numerical results of fluid-structure interactionanalysis for the dataset of deep learning. The dataset wasdivided into training dataset, validation dataset and test dataset (training dataset: 1024, validation dataset: 1024,test dataset: 512). The shape of RBCs can be reconstructed by control points. We developed deep learning model to predict the control points of RBCs from single 2D pictures. This model consists of two modules: a module that extracts the feature of a 2D picture and a module that moves the control points of the resting shape of RBCs. At first, the model extracts afeature vector from a picture by ResNet18. Next, it determines the position of control points of the predictedRBC shape using the extracted feature vector. We used mean square error (MSE) as loss function. After predicting control points by deep learning, we conducted smoothing using fluid-structure interaction analysis.

RESULTS AND DISCUSSION

We performed a test using the test dataset after learning.Figure 1 (a) shows the average of root mean square error(RMSE) of the test dataset. The average error was 0.044.Figure 1 (b) shows the example of the results of reconstruction. The predicted RBC shape well capturedthe ground truth, but has wrinkles. We conducted smoothing to remove wrinkles from the predicted shape.Smoothing by fluid-structure interaction analysis could keep the shape of the predicted and remove wrinkles from the predicted shape as shown in Figure 1 (b).
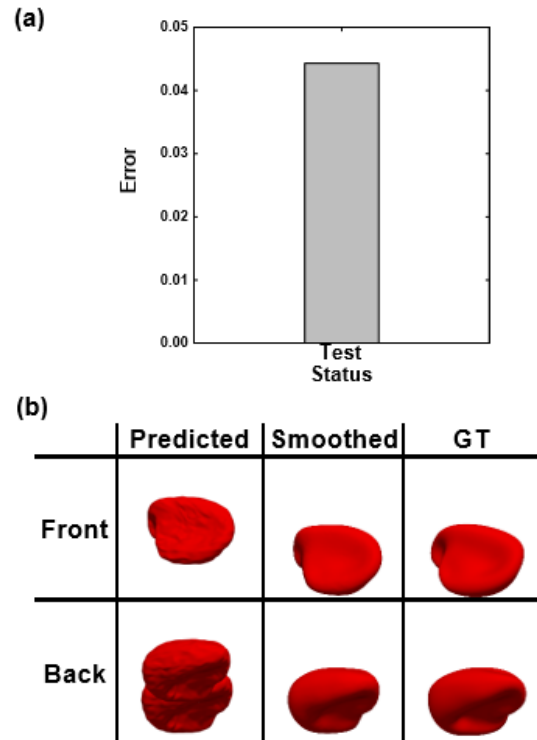
Figure 1 (a) The average of RMSE of the test dataset. (b) The example of the results of reconstruction of the test dataset. GT: Ground truth.

CONCLUSION

We developed the method of reconstructing 3D RBC shapes from single 2D pictures using deep learning and fluid-structure interaction analysis. The RBC shape reconstructed by our method well captured the ground truth. We used only numerical results as the dataset. Wewill use experimental results as the test dataset and try toreconstruct 3D RBC shapes from 2D pictures taken in anexperiment as the next step.

REFERENCES

[1] Skalak et al. *Biophysical journal* **13**: 245-264, 1973.
[2] Hughes et al. *Comp Met Appl Mech Eng* **194**: 4135-4195, 2005

2-DEOXY-ATP IMPROVES CARDIAC FUNCTION IN A MULTISCALE COMPUTATIONAL MODEL OF HEART FAILURE

Abigail E. Teitgen[1], Marcus Hock[1], Kimberly J. McCabe[2], Matthew C. Childers[3], Gary Huber[4], Daniel Beard[5], Michael Regnier[3] and Andrew D. McCulloch[1]

[1]Bioengineering, University of California San Diego / La Jolla, CA, USA.
[2]Computational Physiology, Simula Research Laboratory / Oslo, Norway.
[3]Bioengineering, University of Washington / Seattle, WA, USA.
[4]Chemistry and Biochemistry, University of California, San Diego / La Jolla, CA, USA.
[5]Molecular and Integrative Physiology, University of Michigan / Ann Arbor, MI, USA.
Email: ateitgen@eng.ucsd.edu

INTRODUCTION

2-deoxy-ATP (dATP), a candidate therapeutic for heart failure, improves cardiac contractility and lusitropy by acting on myosin to increase the rate of crossbridge binding and cycling, and by increasing the rate of Ca^{2+} transient decay [1,2]. However, the molecular mechanisms behind these effects and how observed therapeutic responses to dATP are achieved – even when it is only a small fraction of the total ATP pool – remain poorly understood, especially in models of heart failure, in which energy metabolism is impaired. We developed a novel multiscale computational modeling framework to address these questions (Figure 1).

METHODS

We conducted molecular dynamics (MD) and Brownian dynamics (BD) simulations to assess (d)ADP.Pi-myosin/actin association rates. We then utilized these association rates to constrain a sarcomere mechanics model, and combined this with experimental Ca^{2+} transient data to simulate the effects of dATP at the myocyte level. We then utilized a model of rat biventricular mechanics, energetics, and circulation to predict the effects of elevated dATP at the tissue and ventricular scale under heart failure conditions [3].

RESULTS AND DISCUSSION

MD and BD simulations showed that dATP increases the actomyosin association rate by 2.15 fold via optimization of myosin's actin binding interface. Model predictions indicated that dATP destabilizes the super- relaxed state of myosin, a state in which myosin motors cannot participate in crossbridge cycling, leading to large changes in force with small fractions of dATP. The integrative effects of dATP on improved Ca^{2+} handling and increased crossbridge binding and cycling augmented cardiac myocyte contractility and lusitropy, and could fully explain increases in myocyte shortening and relaxation observed experimentally. In a failing heart model, we predicted improvements in left ventricular function, including an 18% increase in ejection fraction, with no additional impairment of metabolic state with only 1% dATP. This was due at least in part to improved energy efficiency with elevated dATP.

CONCLUSION

In this work, we developed a novel multiscale modeling framework extending from the atomic to full ventricle scale. Our model predictions suggest that the combined effects of dATP on myocyte Ca^{2+} handling and myosin crossbridge
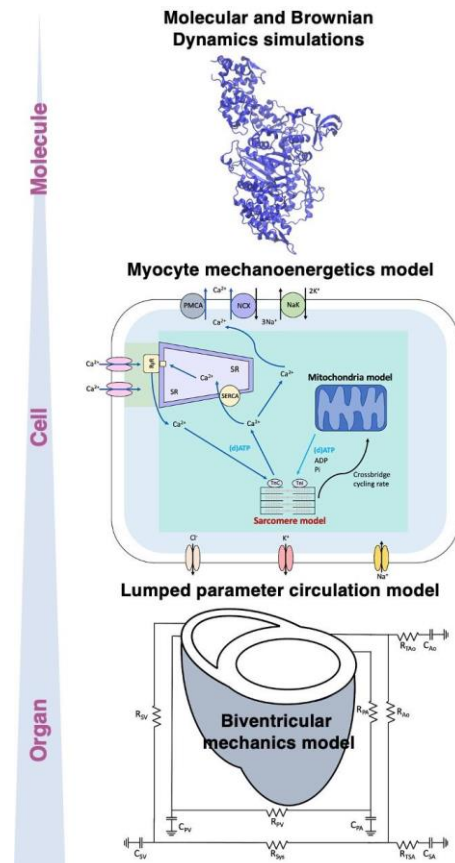
Figure 1 Multiscale modelling framework extending from molecular to ventricular biomechanics.

state transitions, including increased recruitment of myosin from the super-relaxed state, improve ventricular mechanics and energetics, especially under metabolically inhibited conditions of heart failure. This modeling framework can be extended in the future to further personalized medicine approaches and to investigate additional therapeutics for treating heart failure.

REFERENCES

[1] Thomson K.S., et al. *JACC Basic Transl Sci* **1**: 666-679, 2016.
[2] Powers J.D., et al. *PNAS* **116**: 11502-11507, 2019.
[3] Lopez R., et al. *Function* **1**: zqaa018, 2020.

DEVELOPMENT OF A PRACTICAL APPROACH FOR PREDICTING PATIENT-SPECIFIC INTRA-ANEURYSMAL FLOWS USING A DATA ASSIMILATION TECHNIQUE

Tsubasa Ichimura[1], Shigeki Yamada[2], Yoshiyuki Watanabe[3], Hiroto Kawano[4], Satoshi Ii[1]

[1] Graduate School of Systems Design, Tokyo Metropolitan University / Hachioji, Tokyo, Japan.

[2] Graduate School of Medicine, Nagoya City University/ Nagoya, Aichi, Japan [3]Department of Radiology, Shiga University of Medical Science / Otsu, Shiga, Japan [4] Faculty of Medicine, Shiga University of Medical Sciences / Otsu, Shiga, Japan

Email: ichimura-tsubasa@ed.tmu.ac.jp

INTRODUCTION

Ruptures of cerebral aneurysms give a high mortality rate that reaches approximately 35% [1]; however, the occurrence rate of the rupture is low known as around 2% [2]. Since surgical interventions for the cerebral aneurysm also have risks of infection and mortality, a quantitative evaluation of the rupture risk is a crucial issue in clinical sites. It is believed hemodynamics is an important factor for the formation, growth and rupture of the cerebral aneurysms [3], and therefore several quantification techniques have been attempted using a magnetic resonance imaging (MRI), computed tomography (CT), as well as computational fluid dynamics (CFD). However, medical observation has a limitation for spatiotemporal resolutions, while the CFD has a difficulty in setting appropriate boundary conditions for patient-specific analyses. Now a day, data assimilation (DA) techniques, which fuse the CFD and observed velocity, have been applied for hemodynamic analyses of the cerebral aneurysm [4]. However, in general, an analysis cost of the DA is much higher than that of original (direct) simulation, and thus it is still challenging for general use.

In this study, we propose a practical approach for predicting the patient-specific intra-aneurysmal flows using the DA method. An intra-aneurysmal region is only targeted as an analysis domain, and velocity profiles at an interface between the aneurysm and vessel branch is inversely estimated by solving a 4D variational problem. Results are validated through comparisons with three different samples.

METHODS

The vascular geometries including aneurysms were constructed from the TOF-MRA images using Mimics (Materialise, Belgium). The spatiotemporal velocity data (termed 4D-flow MRI) were extracted from the phase-contrast MRI images based on the constructed vessel shapes. For the DA, we employed a 4D variational method, in which the velocity profile at the boundary is inversely estimated through solving a minimization problem for velocity mismatch between observation and incompressible Navier-Stokes equations. For the sake of comparisons, we also performed direct simulations for each case that uses a vascular shape including both the aneurysm and main branch and employs the given inlet velocity. We applied the velocity data that a velocity encoding value is set to 40 cm/s for the DA and 120 cm/s for the direct simulations (as the given boundary condition for the inlet velocity).

RESULTS AND DISCUSSION

Figure 1 shows velocity fields at a systolic phase for the DA, direct simulation and 4D-flow MRI for three different

samples, A, B, and C. In all samples, the proposed DA analyses show a reasonable coincidence with the 4D-flow MRI compared to the direct simulation for the velocity magnitude and direction. Moreover, the proposed DA exhibits a clear swirling pattern in each aneurysm. For the sample B and C, observation noises in the 4D-flow MRI are seemed to be relatively large that show unphysical velocity fields, e.g., pointing to the wall near the inlet in the sample C, because the velocity magnitude is smaller than that of sample A. The proposed DA approach could automatically correct such data noise and would obtain physically-consistent flow fields.
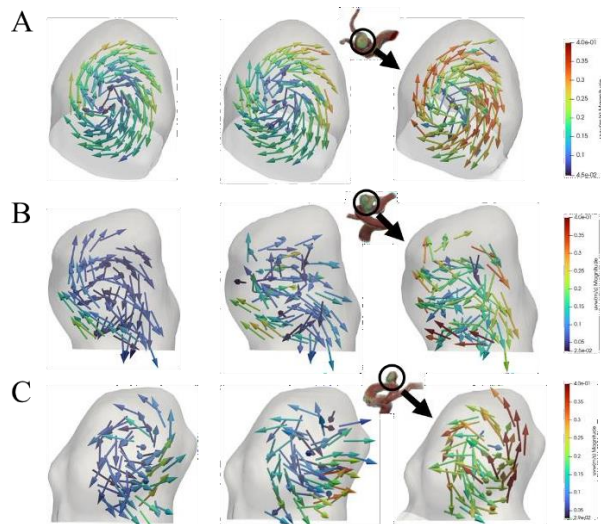
Figure 1 Comparison of velocity vectors in cerebral aneurysms in a systolic phase for the proposed DA, 4D-Flow MRI and direct simulation.

CONCLUSION

We have developed a practical approach for predicting the intra-aneurysmal flows using the DA method, in which intra-aneurysmal region is only targeted as an analysis domain. Through comparisons with three different samples, the proposed method would become a possible approach to evaluate the patient-specific hemodynamics in the aneurysm.

REFERENCES

[1] Donkor, E.S., *Stroke Res. Treat*. e3238165, 2018.
[2] Rinkel, G.J., et al., *Stroke*, **29**, 251-256, 1998.
[3] Meng, H. et al., *AJNR* (2014), **35**, 1254-1262, 2014.
[4] Funke, S.W., et al*., Int J Numer Method Biomed Eng*, **35**, e3152, 2019.

EFFECT OF CORRECTION ANGLES FOR DISCOID LATERAL MENISCUS ON DISTRIBUTION OF JOINT STRESS DURING BIPLANE OPEN-WEDGE HIGH TIBIAL OSTEOTOMY

Tae Soo Bae[1], and Bo Won Jung[2]

[1]Dept. of AI Biomedical Engineering, Jungwon University, Chungbuk, South Korea [2]Dept. of Convergence Engineering, Jungwon University, Chungbuk, South Korea

Email: bmebae@jwu.ac.kr

INTRODUCTION

Open wedge tibial osteotomy is well known as an operation performed to reduce the load due to osteoarthritis on the medial compartment of knee. Previous clinical studies reported that the correction angle should be reduced during tibial osteotomy since the discoid lateral meniscus is vulnerable to degenerative changes. However, biomechanical studies on joint load distribution for discoid lateral meniscus as correction angles are lacking. Therefore, this study attempted to analyze the biomechanical effect on the discoid lateral meniscus during open wedge proximal tibial osteotomy through computational analysis.

METHODS

C Three-dimensional knee joint models (femur, tibia, patella, and meniscus, respectively) with medial osteoarthritis were reconstructed by using CT and MRI images using image processing commercial program (Mimics, Materialise Inc., Belgium). Ligaments around the knee (ACL, PCL, MCL, LCL) were modelled with a spring. To apply the correction angle during proximal tibial osteotomy, three groups were set by a commercial editing program (3-Matic, Materialize Inc., Belgium) was used: under-correction (52.5%), acceptable- correction (62.5%), and over-correction (70%). The material properties of bone, cartilage(meniscus), and ligaments were set referred to previous studies. For the boneplate and screws, TomoFix (DePuy Synthes, USA) products were modeled with material properties of the Ti-alloy (Ti4V6Al). All finite element models were created using a 4-node tetrahedral element, contact conditions were given between femur and meniscus, and all other parts were set in a fixed state. A fixed boundary condition was set at cutting tibial base, a half of weight was applied as a load in the direction of the mechanical axis, and static analysis was performed.
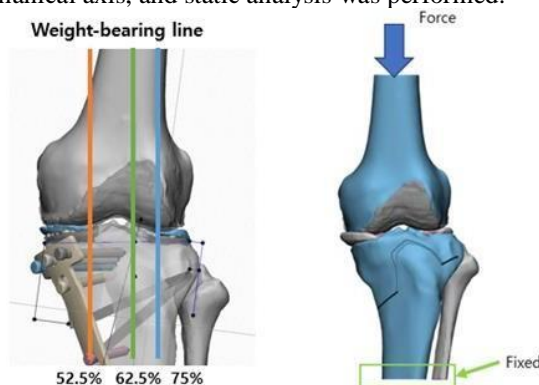
Figure 1 Three correction angle as weight-bearing line (left) and load and boundary condition (right)

Commercial software was used for finite element analysis, and the stress distribution for each correction angle was calculated and compared with each other.

RESULTS AND DISCUSSION

When three correction angles were applied to the discoid lateral cartilage model, the von-mises stresses on medial and lateral meniscus were calculated and compared with each other. In the allowable correction, the internal and external stresses were similar, and it was confirmed that a 14% larger load than the medial load moved to the lateral meniscus. In the under-correction, the load on the medial showed more than 3.5 times larger than that on the lateral meniscus. The ratio of the load on the medial to the lateral meniscus was significantly reduced. Finally, in the case of the overcorrection group, it was calculated that about 70% of the medial load moved to the lateral meniscus.
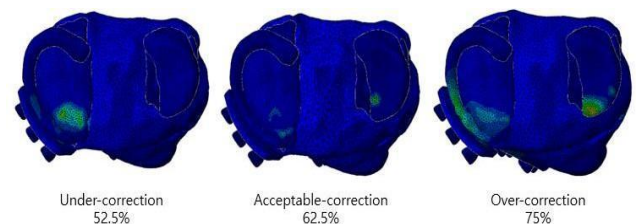
Figure 2 Comparison of von-mises stress on medial and lateral meniscus as correction angle

CONCLUSION

For a distoid lateral meniscus, the medial load was still not improved, and the medial load moved quantitatively to the lateral meniscus between the acceptable- and over-correction angle. Therefore, it is recommended to apply between the low-correction angle and the acceptable-correction angle according to the condition of the distoid lateral meniscus to avoid the shift of joint load on lateral meniscus.

ACKNOWLEDGEMENT

REFERENCES

[1] Fujisawa, K., et. al. *J Orthop Clin Res North America,* **10**:585-608, 1979.

[2] Atay O.A., et. al. *J Arthroscopy*, **19**(4):346-352, 2003.

BLOCK BUILDING TO FABRICATE TRANSPLANTABLE ORGANOIDS

Ayaka Kadotani[1], Gen Hayase[2], and Daisuke Yoshino [1]

[1] Graduate School of Engineering, Tokyo University of Agriculture and Technology, Koganei, Japan.
[2] International Center for Materials Nanoarchitechtonics, National Institute for Materials Science, Tsukuba, Japan.
Email: dyoshino@go.tuat.ac.jp

INTRODUCTION

The development of three-dimensional (3D) culture systems, organoids, has been one of the most exciting advances in related research fields in the decade since the invention of iPS cells [1]. The introduction of this organoid system has enabled the modeling of genetic, degenerative, and cancer diseases that were difficult to reproduce in vitro [2], and has led to innovative advances in establishing medical treatments. Organoids can express the higher order functions of organs [3], but are currently limited to a few millimeters in size, referred to as "mini organs". Therefore, one of the ultimate goals of regenerative medicine, "organ replication and transplantation using organoids", faces a major obstacle.

To address these problems, we conceptualize to establish a method to assemble organoid blocks like LEGO® (*i.e.*, block building), leading to a highly efficient and fast technique to fabricate full-size organoids that can withstand organ transplantation (Figure 1a). Here, we show how to fabricate and stack organoid blocks of various shapes of several millimeters in size as basic elements.

METHODS

Organoid fabrication: Monolithic porous bulk material with superhydrophobicity [4] was processed using a CNC milling machine (monoFab SRM-20, Roland DG) to manufacture molds for various shapes of organoids. Polytetrafluoroethylene was used as the mold material when necessary. After reaching 90 % confluence, the MDA-MB-231 cells (AKR-201, Cell Biolabs) were harvested with 0.25% trypsin-EDTA (25200-072, Gibco) and re-suspend in the culture medium at the concentration of 5.0×10^6 cells/mL. Cell-suspended collagen solution [4.0 mg/mL; native collagen acidic solution (IAC-50, KOKEN), 10× culture medium, 10 mM NaHCO3, 10 mM HEPES-NaOH (pH 7.5), and the cell suspension] was prepared on ice to give the final concentration of 5.0×10^5 cells/mL. The cell-suspended collagen solution was then dispensed onto the sterilized molds and incubated in a CO_2 incubator for 30–60 min. After gelation, the primary organoids were picked up from the molds and transferred to a 35 mm diameter dish.

Organoid assembly (block building): The collagen solution [2.5 mg/mL; the native collagen acidic solution, 10× culture medium, 10 mM NaHCO$_3$, 10 mM HEPES-NaOH (pH 7.5), and ultra-pure water] was treated with the surface discharge plasma [5]. The organoid blocks were bonded by applying a charged collagen solution between the organoid blocks and allowing them to sit in a CO_2 incubator for 2-5 minutes.
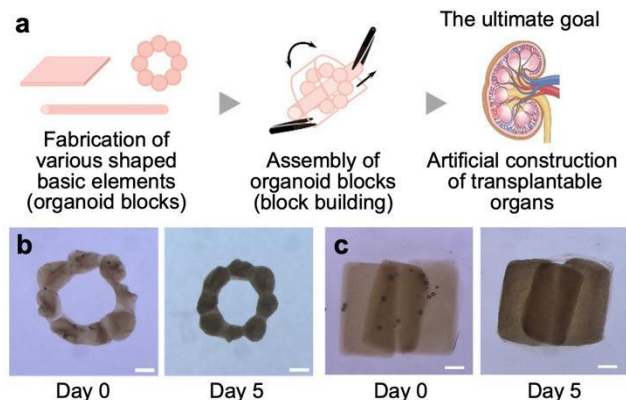
Figure 1 Block building to fabricate transplantable organoids. (**a**) Concept of block building. (**b**) Beaded-shaped organoid block. (**c**) Structures stacked with three rectangular blocks. Scale bars: 1 mm.

RESULTS AND DISCUSSION

We first selected and fabricated organoid blocks of the shapes needed to reproduce the different structures of the organs (Figure 1b). We found no problems releasing bead rings, cylinders, rectangles, sheets, and spheres of organoids from the molds and confirmed that they could be fabricated with high accuracy. organoids fabricated with MDA-MB-231 cells showed shrinkage in size as they matured. This phenomenon is known to be due in part to actomyosin contractility [4]. Notably, even complexly shaped organoids contracted while maintaining their overall shape.

We then assembled the various organoid blocks we had made. We confirmed that the blocks could be glued together and stacked by applying plasma-charged collagen solution to the appropriate areas with a micropipette (Figure 1c).

CONCLUSION

We proposed a block construction method with the ultimate goal of creating transplantable organs. We were able to fabricate and assemble various organoid blocks with the plasma-treated solution. Expression of higher organ function in the constructed organoids is an important step toward future organ transplantation.

REFERENCES

[1] Zhao Z et al. *Nat Rev Methods Primers* **2**: 94, 2022.
[2] Hofer M et al. *Nat Rev Mater* **6**: 402-420, 2021.
[3] Takasato et al. *Nature* **526**: 564-568, 2015.
[4] Hayase G et al. *ACS Appl Bio Mater* **3**: 4747-4750, 2020.
[5] Yoshino et al. June 2020, JP patent 6713795.

EFFECT OF CLUMP SIZE FOR iPS CELL PASSAGING ON PLURIPOTENCY AND PROLIFERATION

Koji Ishii[1], Koki Abe[2], Teiji Sakamoto[2], Takashi Kurihara[2], and Shogo Miyata[1]

[1] Faculty of Science and Technology, Keio University, Yokohama, Japan.
[2] Institute of Technology, Shimizu Corporation, Tokyo, Japan.
Email: miyata@mech.keio.ac.jp

INTRODUCTION

Induced pluripotent stem cell (iPSC) is one of promising cell sources because of their pluripotency and self-renewal ability. There are two types of iPSC passaging methods: single cell passaging in which cell colonies are enzymatically dispersed into a single-cell state, and clump passaging in which cell colonies are fragmented into small cell clusters. Single-cell passaging is a rapid and simple method for cell manipulation, whereas clump passaging is superior for maintaining pluripotency of iPSCs.

Therefore, clamp passaging has been a robust method for expanding iPSCs with maintenance of pluripotency. However, it is difficult to control the clump size in clamp passaging because the fragmentation of colonies is manually performed by pipetting the colonies detached from cell culture substrates.

The purpose of this study is to evaluate the effect of pipetting procedure on the fragmentation of iPSC colonies and to clarify the relationship between clump size and pluripotency of iPSCs.

METHODS

An automated cell-pipetting device was developed to precisely control the pipetting conditions such as flow rate and pipetting volume. The device consisted of motorized-stage and disposable syringe (Fig. 1).

Mouse iPSCs (iPS-MEF-Ng-20D-17, Riken BRC, Japan) were maintained on murine embryonic fibroblasts (MEFs) as feeder cells in DMEM high-glucose supplemented with 15% FBS, 1% antibiotic-antimycotic, 0.1 mM non-essential amino acid, 0.1 mM 2-mercaptoethanol and 1000U/mL leukemia inhibitory factor (LIF). The cell colonies were scraped from cell-culture substrates after reaching confluence. Colony-suspended solution was pipetted for 0, 3, 10, 20 times at the flow rate of 6.4×10^{-7} m^3/s using the custom-made pipetting device. The cells were also enzymatically dissociated into a single-cell state by 0.25% trypsin as a control experimental group.
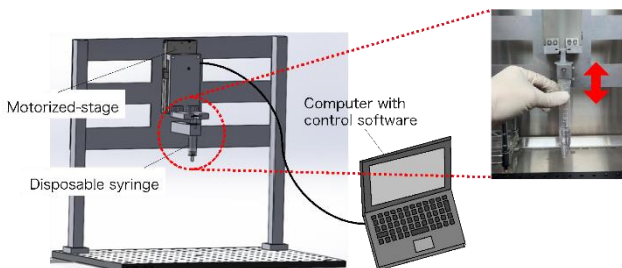
Figure 1 Automated pipetting device for iPSC passaging.

Phase-contrast images were obtained to evaluate the size of colony and cell clump as well as proliferation rate. The alkaline phosphatase (AP) activity was examined after 48 h of culture to evaluate the pluripotency. Sox2, one of the pluripotent markers, was also examined by a flow cytometry.

RESULTS AND DISCUSSION

The size of cell clump decreased as the number of pipetting cycles increased (Fig. 2). The proliferation rate of cells increased as clump size decreased. AP activity was confirmed in all experimental groups. Especially, the area of cells expressed AP activity was largest in the miPSCs with pipetting for 3 cycles. From the flow cytometry analysis, Sox2 expression was larger in the miPSC clumps fragmented with 3 and 10-cycle pipetting (Fig. 4). From these results, there could be a suitable condition appropriate for maintaining proliferation and pluripotency.
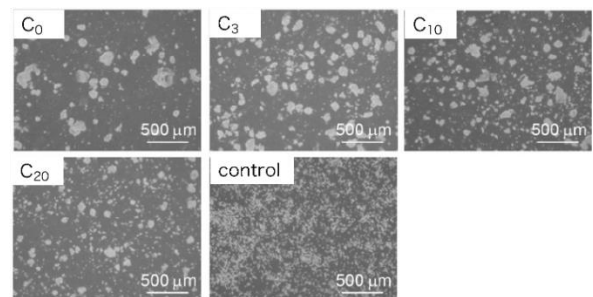
Figure 2 Phase-contrast images of miPSCs after pipetting with 0, 3, 10, 20 cycles (C_0, C_3, C_{10}, C_{20}).
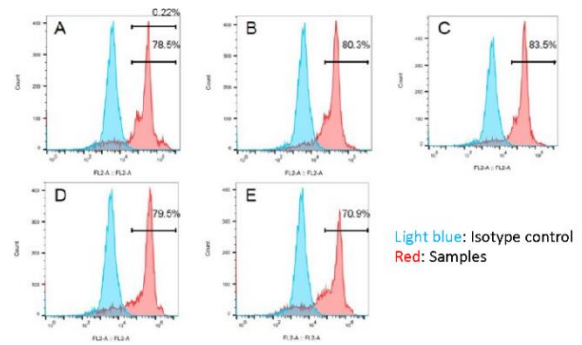
Figure 3 Sox2 expression of miPSCs cultured in (A) C_0, (B) C_3, (C) C_{10}, (D) C_{20}, and (E) control groups.

CONCLUSION

In this study, we developed the automated cell-pipetting device to fragment miPSC colonies into small clumps. As the result, the pluripotency of miPSCs could be maintained in appropriate clump size whereas proliferation was promoted in smaller clump.

INVESTIGATION OF QUANTITATIVE EVALUATION OF FUSION PROCESS BASED ON MORPHOLOGICAL ANALYSIS OF SPHEROIDS

Ginga Kinoshita[1], Xiu-Ying Zhang[2], Satone Taniguchi[1], Takahiro Oshio[1], Koharu Aoyama[1] and Takeshi Shimoto[1]

[1] Fukuoka Institute of Technology, Fukuoka, Japan.
[2] Kyushu University, Fukuoka, Japan.
Email: mhm23105@bene.fit.ac.jp

INTRODUCTION

In the field of regenerative medicine, the fabrication of cellular structures is attracting attention. For example, the KENZAN method can fabricate cellular structures with complex shapes by placing multiple types of spheroids at arbitrary positions [1]. The fusion process between spheroids has attracted much attention in the fabrication of cellular structures. Comparisons between fusing spheroids and simulations using numerical models have been attempted [2]. However, the differences in fusion characteristics among cell types, number of spheroids, and size of spheroids have not been clarified. Therefore, clarifying the differences in the fusion properties of spheroids will allow us to investigate the fabrication of new cellular structures. In this study, we quantitatively evaluated the fusion process based on morphological analysis of spheroids.

METHODS

Spheroids were prepared using Human mesenchymal stem cells (hMSC-AT). Cell culture to reach the number of cells required for spheroid production was performed by an operator with extensive culture experience. Cell suspensions were prepared and 100 μL were dispensed into each well of the well plate to make spheroids. After 2 days of spheroid culture after dispensing the cell suspension, the spheroids were subjected to fusion experiments. For the fusion experiment, 50 μL of culture medium was discarded from each well of the well plate and the spheroids were collected along with the remaining 50 μL. Spheroids were fused so that there were six wells with two spheroids and six wells with three spheroids. A fluorescence microscope was used for time-lapse photography. The carbon dioxide concentration in the microscope was maintained by an external device, and observations were made under the same conditions as in the culture environment. The center of gravity was detected from the contour of each spheroid, which included a straight line connecting the surfaces of the necks where the spheroids fused with each other. The radius of the neck was defined as r, the length from the center of gravity to the surface of the neck of each spheroid as R, and the parameter of the fusion process of spheroids as $\pi r^2/\pi R^2$ as the area ratio. The area ratio was quantitatively evaluated by calculating $\pi r^2/\pi R^2$ [2].

RESULTS AND DISCUSSION

Changes in the area ratio $\pi r^2/\pi R^2$ were observed from 48 to 120 hours after the spheroid fusion experiment (Figure 1). The change in $\pi r^2/\pi R^2$ for the case of two spheroids and the case of three spheroids increased from 48 to 72 hours after

the fusion experiment and then ceased to change. It is thought that the amount of change in the area ratio remains the same regardless of the number of spheroids. Therefore, it can be considered that fusion is more successful when the number of spheroids is 3 than when the number of spheroids is 2.
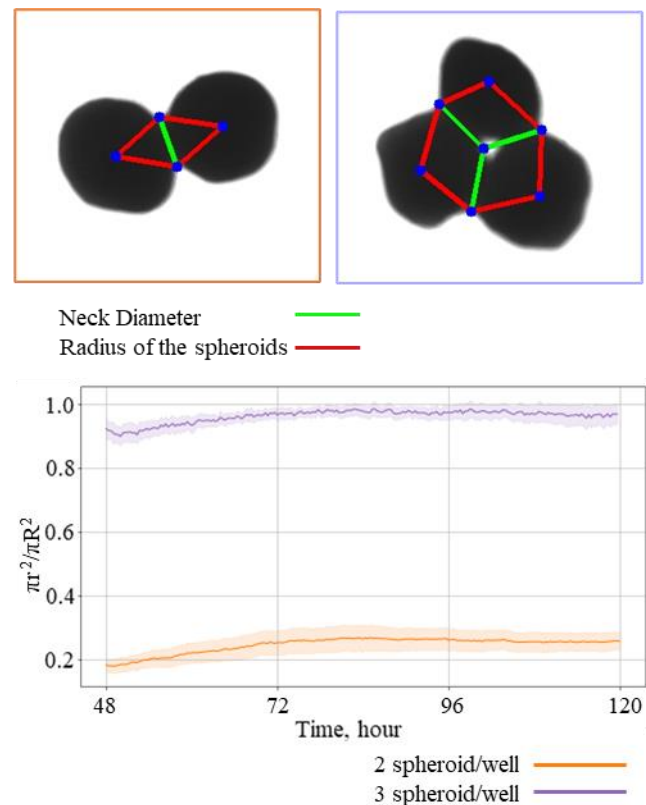
CONCLUSION

Changes in fusion of human adipose-derived stem cell spheroids over time were observed. By detecting the length of the spheroid neck radius and the center-of-gravity radius of each spheroid, the quantitative evaluation of the fusion process by the number of spheroids was examined. Based on this information, detailed fusion characteristics of the spheroids could be clarified and methods for creating new cellular structures could be investigated.

REFERENCES

[1] Yoshitaka N et al. *Regen. Ther.* **11**: 47-55, 2019.
[2] Nastasia.VK. et al. *Sci Rep* **10**: 12614, 2020.

TRANSTIBIAL PROSTHESIS ALIGNMENT AUTOMATION: A MACHINE LEARNING APPROACH FOR DATA ANALYSIS AND METHOD DEVELOPMENT

Taha Khamis[1], Hamam Mokayed[3], Nasrul Anuar Bin Abd Razak[1], Noor Azuan Abu Osman[1,2]

[1] Center for Applied Biomechanics, Department of Biomedical Engineering, Universiti Malaya, Kuala Lumpur, Malaysia.

[2] The Chancellery, Universiti Tenaga Nasional, 43000, Kajang, Malaysia.

[3] Department of Computer Science, Electrical and Space Engineering, Lulea University of Technology, Lulea, Sweden.

Email: azuan@um.edu.my

INTRODUCTION

Transtibial prosthesis alignment is a critical aspect of prosthetic rehabilitation for amputees [1]. Achieving proper alignment is essential for enhancing gait performance, stability, and overall comfort. However, the alignment process is often subjective and time-consuming, relying heavily on the expertise and experience of prosthetists. To address these challenges, this study proposes a machine learning approach for data analysis and method development in transtibial prosthesis alignment.

METHODS

To gather data for analysis, wearable sensors were employed in clinical trials involving amputees. These sensors included ground reaction force sensors from (OpenGo) and inertial measurement unit (IMU) utilizing OPAL system provided from "APDM Wearable Technologies" sensors. The OPAL sensors captured kinematic information, while the ground reaction force sensors provided gait parameters and weight distribution data. The OPAL sensors were attached to seven points as follows: two sensors on both sound and artificial feet, one sensor on the pylon-tibial, one sensor on the sound tibial, one sensor on the socket, and two sensors on both femurs. The OpenGo sensors were inserted into both shoes as insoles. Fig 1 shows a snippet of the collected gyroscope data for the left foot on the sagittal plane for post alignment. The participants were asked to stand for 60 seconds to collect static data then walk in a self-selected speed for another 60 seconds. All participants agreed and signed consent forms.

The data collected from these sensors underwent data clustering using artificial intelligence (AI) algorithms, such as machine learning and pattern recognition techniques. The data clustering process aimed to identify patterns and correlations within the collected sensor data. By detecting alignment discrepancies through the analysis of these patterns, the automated approach presented in this study aimed to enhance accuracy, reduce subjectivity, and improve efficiency in the transtibial prosthesis alignment process.

RESULTS AND DISCUSSION

The preliminary results show that the proposed system utilizing machine learning algorithms is effective in identifying misalignments and offering alignment guidance. Through data clustering, distinct clusters representing various alignment patterns and discrepancies were identified. These clusters provided valuable information about specific alignment issues, such as pressure distribution, gait deviations, and weight asymmetry. By integrating machine learning, the alignment process becomes less reliant on subjective judgment, leading to more consistent outcomes among different prosthetists. Moreover, the automated approach improves efficiency by streamlining the analysis, allowing prosthetists to focus on fine-tuning the alignment based on the generated insights.
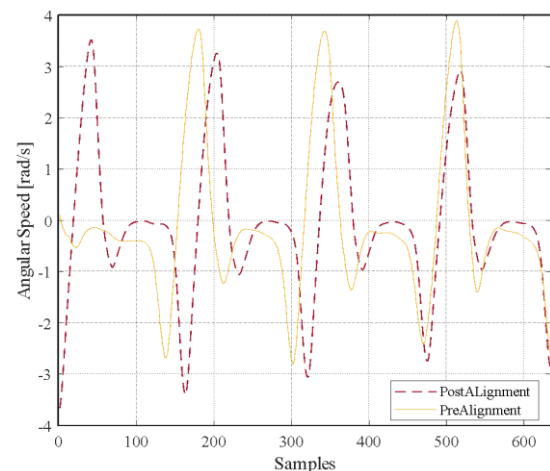
Figure 1 Gyroscope Data for Left foot on the sagittal plane for Pre-Alignment and Post-Alignment.

CONCLUSION

This research demonstrates the potential of using machine learning and wearable sensors for transtibial prosthesis alignment. The proposed system offers a data-driven analysis of alignment patterns and discrepancies, showing promising results in terms of accuracy, subjectivity reduction, and process efficiency. These findings have important implications for prosthetic rehabilitation, suggesting a valuable approach to advance current alignment practices. Further refinement of machine learning algorithms and larger-scale clinical trials are recommended for future research.

ACKNOWLEDGEMENT

REFERENCES

[1] Cárdenas A. M., et al., *Gait Posture*, **95**:76-83, 2022.

QUANTITATIVE EVALUATION METHOD OF BRAIN ACTIVITY AND AUTONOMIC FUNCTION USING HEART RATE VARIABILITY DATA

Miki Matsuhashi[1], Yasumi Ito[2], Ryuichi Yamada[2], Tetsuya Nemoto[2] Yoshiyuki Kagiyama[2] and Qin Xu[2]

[1] Integrated Graduate School of Medicine, Engineering, and Agricultural Sciences, University of Yamanashi, Kofu, Japan

[2] Graduate Faculty of Interdisciplinary Research, University of Yamanashi, Kofu, Japan

Email: g22tm027@yamanashi.ac.jp

INTRODUCTION

Serious accidents caused by human errors continue to occur in traffic and industrial accidents. To prevent human error, objective evaluation of the state of arousal is necessary. This study aims to assess the state of arousal with high accuracy by classifying it into four states: 1) high arousal, 2) relaxation, 3) stress and 4) low arousal, based on the analysis of both brain activity and autonomic nervous function using heart rate variability data that can be easily measured. Then, based on the classification into these four states, an attempt is made to establish evaluation criteria.

METHODS

The experiment was conducted on five young subjects (all males: 22 years old) and four elderly subjects (two males and two females: 71.5 ± 2.3 years old). Each test consisted of three tasks: a closed-eye rest task, and a relaxing movie task. Each test lasted for 3 minutes, with a minimum 10-minutes break between tests. A series of experiments were conducted twice with at least one week's interval. The R-R interval was measured using a fingertip pulse wave device, called BACS Advance (TAOS Laboratories, Inc.), and the following analyses were performed to calculate indices representing brain activity and autonomic nervous system function.

1) Brain activity: Chaos analysis

The Lyapunov exponent (LE), obtained by chaos analysis of biological signals, is considered to reflect the activity state of the upper centers and serves as an indicator of brain activity level. In this study, LE was calculated using the method proposed by Sano et al. [1]

2) Autonomic nerve function: Frequency analysis

Fast Fourier Transform was performed to calculate the ratio of the high-frequency component (HF: 0.04-0.15 Hz) to the low-frequency component (LF: 0.14-0.4 Hz) (denoted as LF/HF), which is known as a stress index.

RESULTS AND DISCUSSION

In the resting state with closed eyes, the mean LE and standard deviation LE showed significant interior-individual variations (Table 1). This observation indicates that the resting state with closed eyes, which was conventionally considered as the evaluation criterion for biometric measurements, is an unstable state with significant differences among individuals. Conversely, all subjects showed relatively similar values during relaxed video viewing, indicating that the subjects were in a stable state of low arousal and relaxation regardless of the subject. Similar findings were observed for LF/HF.

The computational task scores exhibited a positive correlation with LE (Figure 1). In addition, by setting the threshold (dotted line in Figure 1) as the value during the relaxed movie (LE = 2.35: average value of the entire group), which is a state of low arousal and relaxation, it would be possible to evaluate the younger group separately from the older group with low scores. Thus, it is hypothesized that setting the threshold values as LE = 2.35 and LF/HF = 2.68 enables evaluation of arousal state.
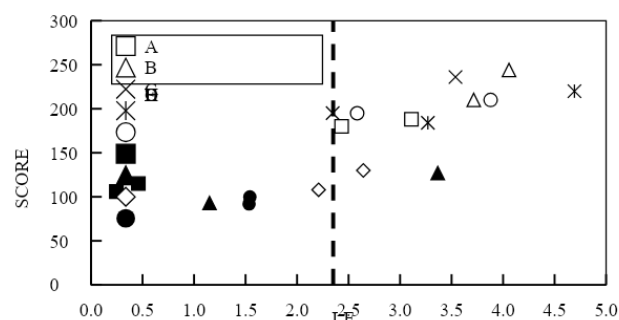
Figure 1 Relationship between LE and calculated score

CONCLUSION

In this study, experiments were conducted to establish a highly accurate evaluation method for arousal state based on two types of analysis using heart rate variability data. Moving forward, our focus will be on validating whether the threshold values obtained from this study can be used to predict and prevent accidents using heart rate variability data collected through a driving simulator.

REFERENCES

[1] Sano M., et al. Measurement of the Lyapunov spectrum from a chaotic time series, *Phys Rev Let* **55**(10): 1082-1085, 1985.

Table 1 Average LE at second inspection (S.D.)

Subject	Young subjects					Elderly subjects				Average
	A	B	C	D	E	F	G	H	I	
Closed eyes	3.43 (1.73)	4.91 (0.64)	4.48 (2.04)	2.65 (0.92)	5.23 (0.90)	0.54 (0.37)	1.95 (1.59)	1.51 (3.39)	2.52 (1.13)	3.02 (1.52)
Relax Movie	2.68 (0.56)	2.16 (1.17)	3.78 (0.78)	3.26 (0.96)	2.59 (0.60)	1.06 (0.73)	3.41 (0.62)	2.54 (1.42)	1.96 (0.61)	2.60 (0.78)

Subject	Young subjects					Elderly subjects				Average
	A	B	C	D	E	F	G	H	I	
Closed eyes	3.43 (1.73)	4.91 (0.64)	4.48 (2.04)	2.65 (0.92)	5.23 (0.90)	0.54 (0.37)	1.95 (1.59)	1.51 (3.39)	2.52 (1.13)	3.02 (1.52)
Relax Movie	2.68 (0.56)	2.16 (1.17)	3.78 (0.78)	3.26 (0.96)	2.59 (0.60)	1.06 (0.73)	3.41 (0.62)	2.54 (1.42)	1.96 (0.61)	2.60 (0.78)

GENERATING THE FOOT PATTERN WITH A RECURRENT NEURAL NETWORK USING MINIMAL FEEDBACK SIGNALS: APPLICATION FOR POWERED ANKLE-FOOT

Hamza Al Kouzbary[1], Mouaz Al Kouzbary[1], Hamam Author, Nooranida Arifin[1] and Noor Azuan Abu Osman [1,2]

[1] Center for Applied Biomechanics, Department of Biomedical Engineering, Universiti Malaya, Kuala Lumpur, Malaysia.

[2]The Chancellery, Universiti Tenaga Nasional, Kajang, Malaysia

Email: azuan@um.edu.my

INTRODUCTION

The rhythm in which robotic lower limb prosthesis evolving in the past few decades gives a promising anticipation of replacing the passive prosthesis which are the most prevailing devices in the market. Powered prosthesis can improve the symmetry of the gait cycle, reduce the metabolic cost, and increase the shock absorption during heel strike and provide net power during plantar flexion. Meanwhile, passive prosthesis effects on the amputee life not only associated with mobility restriction but it could contribute to osteoarthritis, joint disorder, back pain, and residual limb chronic pain. Although powered prosthesis improves amputees' quality of life, it is still not popular among prostheses users due to the hefty price tag and some limitations associated with the mechanical and control system of the prosthesis. Continuous control pattern generators for powered prosthesis are one of the alternative methods to the conventional intermittent three level controllers which become a trend in the last few years in the literature as it overcome some of the problems associated with the conventional controllers.

METHODS

In this conference we will present our developed RNN which generates continuous foot walking patterns over variant terrains with different walking pace using only data observed by an IMU attached to the tibia of the same leg. The introduce method use minimal number of sensors which reduce the computation load and the coast of the prosthetic device, also all the sensors required to control the prosthesis in the proposed control system can be embedded to the prosthesis so no invasive sensors or sensors attached to the amputee skin will give the amputees discomfort while using the prosthetic device. The developed pattern generator is an enhanced version of our previous method [1]. A Gated Recurrent Unit (GRU) was selected to form the pattern generator which consists of four layers three GRU layers each layer consisting of 10 neurons and one pure line output layer consisting of one neuron. The input signals of this RNN are the tibia angular position computed by a complimentary filter from the gyroscope and accelerometer of the IMU sensor. The optimization algorithm used to train the neural network was the first order gradient descent method "Adam" [2].

RESULTS AND DISCUSSION

The generated foot pattern has an average RMSE for level-ground walking and stairs ascending and stairs descending of 3.65˚. Figure 1 demonstrates the foot patterns during stairs ascending, stairs descending, and level ground walking.
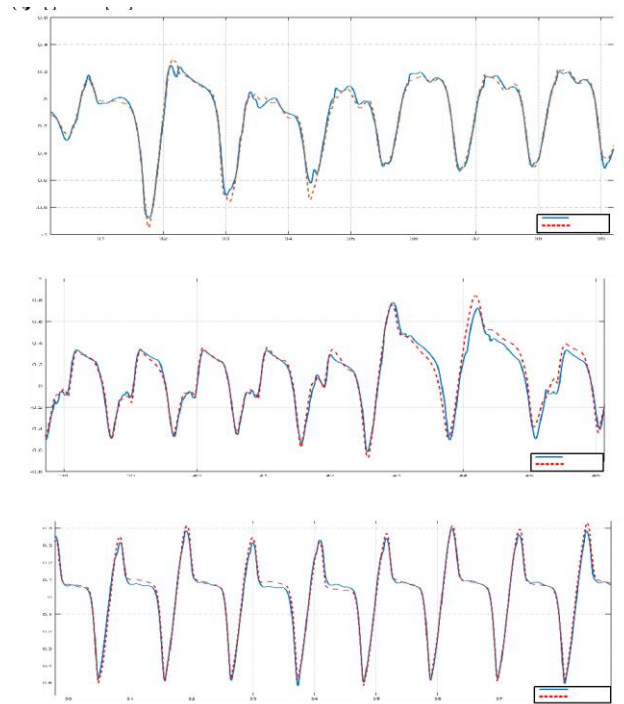
Figure 1 A graph demonstrates the estimated and real waling patterns on different terrains (a) stairs ascend, (b) stairs descend, and (c) ground-level.

CONCLUSION

The proposed method generates a continuous control signal for a prosthetic ankle-foot over variant terrains using minimal feedback signals. This method reduces the computation load and the high cost associated with the conventional method.

ACKNOWLEDGEMENT

REFERENCES

[1] Al Kouzbary, H., et al. *IEEE Transactions on Neural Networks and Learning Systems,* 2021.

[2] Kingma D. P., & Ba J., *arXiv preprint arXiv:***1412**.6980, 2014.

NANOPLASTICS FOR IMMUNOLOGICAL ASSESSMENTS

Yoshitaka Nakanishi[1], Yukio Fujiwara[2] and Yuta Nakashima [1]
[1] Faculty of Advanced Science and Technology, Kumamoto University, Kumamoto, Japan.
[2] Faculty of Life Sciences, Kumamoto University, Kumamoto, Japan.
Email: y-naka@mech.kumamoto-u.ac.jp

INTRODUCTION

Nanoplastics (NPs), small particles of plastic pollution, are known to be one of the most important environmental threats to ecosystems. Despite their ubiquity in all spheres of life and ecology, little is known about how exposure to NPs influences living organisms. Furthermore, NPs research lacks standardised protocols and methods for the investigation of living organisms under laboratory conditions. Therefore, this study proposed both a method to generate NPs for various biological tests and a microchamber device capable of both quantitative and time-dependent assessments of inflammatory cytokine secretion from human monocyte-derived macrophages (HMDMs)[1-3].

METHODS

NPs were generated using a pin-on-disc machine, where a pin made of PE, PP, PVC, or PET was pressed onto a quartz glass disc (Fig.1). The pin and disc were soaked in a saline solution at room temperature. A UV lamp was used to irradiate the frictional surfaces through the quartz glass disc to deteriorate the plastic materials. The
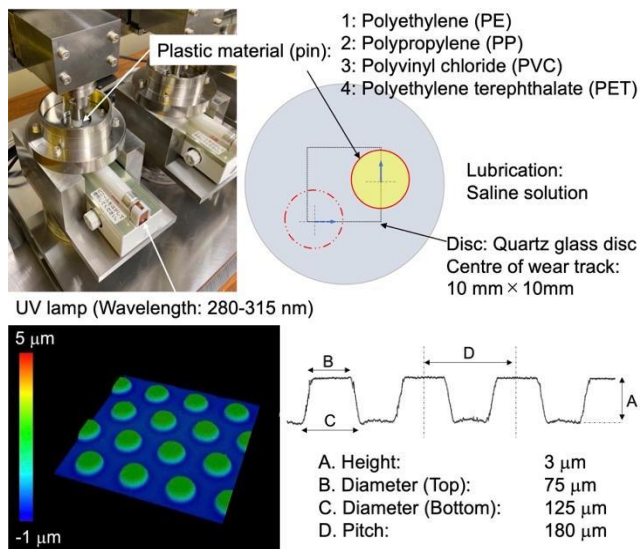
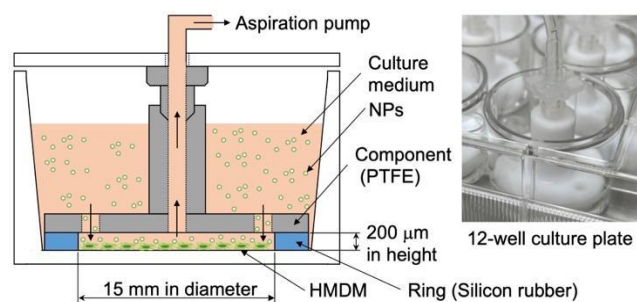glass surface was processed by the combined application of conventional photoresist masking and micro-slurry-jet for inducing fatigue failure of plastic materials [4].

Fig.2 shows the assay procedure for inflammation using a micro-chamber device. The configuration enabled the NPs to pass near the HMDMs, which is important for the phagocytosis of NPs and contributes to quantitative assessment.

RESULTS AND DISCUSSION

Almost all the NPs generated were fragment shaped. Through visual inspection, aspect ratios, and complexity, it was concluded that fragment-shaped NPs/MPs were similar to those of the particles found in the different natural environments.

Although approximately the same morphological aspects of NPs/MPs were administered, the secretion of TNF-α differed depending on the plastic material. It was not obvious whether these differences were derived from the molecular architectures, side chain structures, or addition agents, such as plasticising materials.

Figure 1 Generation method of NPs.

A. Height: 3 μm
B. Diameter (Top): 75 μm
C. Diameter (Bottom): 125 μm
D. Pitch: 180 μm

Figure 2 Fabrication of micro-chamber devices in a CO_2 incubator.

Control
PE (D: 2.40 ± 3.3 μm, R: 1.54 ± 0.44, C: 1.16 ± 0.13, N: 609)
PP (D: 2.61 ± 2.8 μm, R: 1.58 ± 0.44, C: 1.25 ± 0.24, N: 586)
PVC (D: 2.50 ± 2.7 μm, R: 1.54 ± 0.36, C: 1.19 ± 0.13, N: 340)
PET (D: 2.73 ± 2.3 μm, R: 1.57 ± 0.42, C: 1.20 ± 0.17, N: 232)
LPS (10 ng/ml)
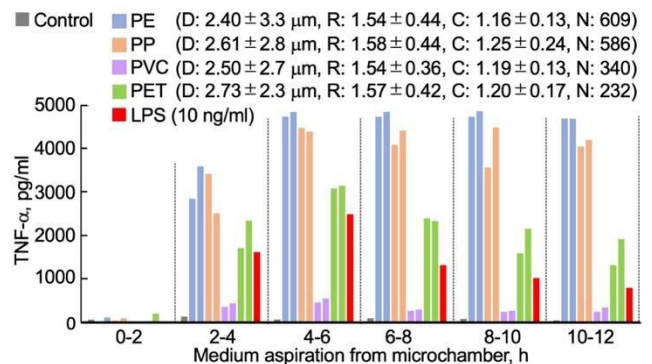
Figure 3 Secretion of TNF-α by HMDMs in micro-chamber device. LPS: Lipopolysaccharide. D: equivalent circle diameter of NPs. R: aspect ratio of NPs. C: Complexity. N: Number of NPs evaluated.

CONCLUSION

We concluded that the generation method for NPs was acceptable given that the UV degradation, fatigue failure, and hydrolytic degradation of plastic materials, whose fragmentation mechanisms are thought to occur in the environment, were combined.

The configurations of micro-chamber device enabled quantitative and time-dependent assessments.

REFERENCES

[1] Nakanishi Y et al. *Wear* **523**: 204749, 2023.
[2] Nakanishi Y et al. *Biotribology* **33-34**: 100235, 2023.
[3] Nakanishi Y et al. *Wear* **477**: 203816, 2021.
[4] Nakanishi Y et al. *Precision Eng* **67**: 172-177, 2021.

QUANTIFICATION OF LOAD AND LOADING DIRECTION OF PATELLAR COMPONENT IN TOTAL KNEE ARTHROPLASTY USING A SURGICAL ASSISTANCE SYSTEM

Kanako Ichimura[1], Takeshi Shimoto[1], Shinya Kawahara[2] and Yasuharu Nakashima[2]

[1] Fukuoka Institute of Technology, Fukuoka, Japan.

[2] Kyushu University, Fukuoka, Japan.

Email: mhm22102@bene.fit.ac.jp

INTRODUCTION

The patellofemoral joint enhances quadriceps function and promotes knee extension [1]. However, imbalances in the patellofemoral joint after total knee arthroplasty (TKA) can lead to postoperative complications, such as anterior knee pain due to compressive forces on the patella. Additionally, the thickness of the polyethylene inserts changes the relative position of the patellar and femoral components. The effect of this is that the tissues leading to the patella are stretched or contracted. However, it is not known how tissue stretching after TKA affects the knee joint. Therefore, *in vivo* quantification of the load and loading direction on the patella can contribute new knowledge to the field of orthopaedics. The purpose of this study is to quantify the load and the loading direction applied to the patella component using the surgical support system we developed.

METHODS

The target was the right knee joint and the artificial knee joint was the posterior-stabilised (PS) type. Tri-axial force sensor was used to measure the load and the loading direction applied to the patella component. It was incorporated into the patella component. The system was developed for use during trials in which knee stability adjustments are made during surgery. The load and the loading direction applied to the patella component can be measured in real time when the surgeon checks the stability of the knee. The surgeon can check the measured quantitative values numerically and visually on a personal computer. In addition, this system is also possible to take video images. Data can be accumulated by saving images and measurements at any time. Therefore, it can be applied not only to intra-operative evaluation but also to post-operative feedback by accumulating data. A simple experiment were conducted to verify the usefulness of the developed system. The maximum extension and maximum flexion were 0 deg and 90 deg, respectively, and the motion from the extended position to flexion and back to the extended position was measured.

RESULTS AND DISCUSSION

The results of the experiment were shown in Figure 1. The load in the medial/lateral direction was always applied in the lateral direction. The patellar groove of the medial condyle of the femoral component has a larger curvature than that of the lateral condyle. Therefore, it was considered that the patellar component moved to the medial side of the patellar groove. In the inferior/superior direction, the loading direction was applied upward in flexion movements and downward in extension movements. It was confirmed that the load was applied in the direction of motion. In the anterior/posterior direction, the maximum load value was shown at the position of maximum extension. The quadriceps muscle and patellar tendon tense as the knee flexion, causing the patellar component to push against the femoral component to stay in the knee joint. It was considered that this move influenced the load of anterior/posterior direction.
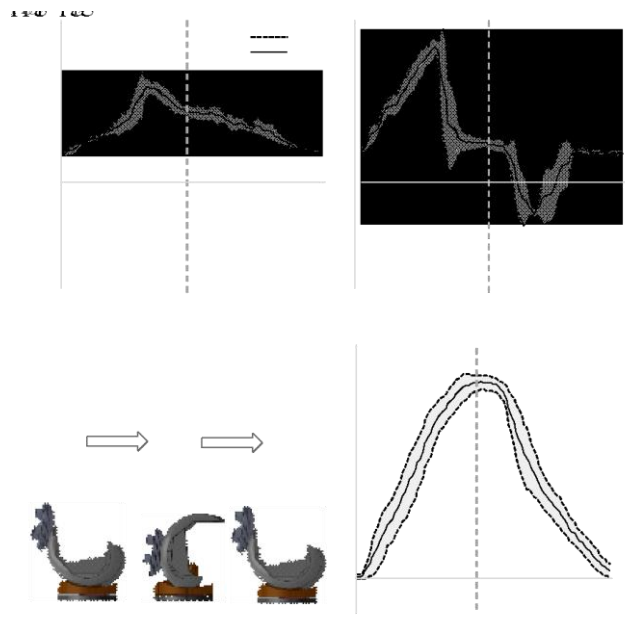
Figure 1 Results of the experiment.

CONCLUSION

In this study, a system was developed to quantify the load and the loading direction applied to the patella component. Measurement experiment on flexion/extension motion allowed the load and the loading direction of patella component due to the geometry and motion of the artificial knee joint. The results obtained with the developed system could provide new insights into the field of orthopaedics.

REFERENCES

[1] Matz J et al. *Canadian Journal of Surgery* **62**: 57-65, 2019.

STABILIZING LOW-COST THIN PRESSURE SENSORS USING NEURAL NETWORKS FOR PRESSURE MONITORING IN IOT-INTEGRATED SCOLIOSIS BRACES

Abd Alghani Khamis[1], Mouaz Kouzbary[1], Noor Azuan Abu Osman [1,2], and Hamam Mokayed[3]
[1]Centre for Applied Biomechanics, Department of Biomedical Engineering, Faculty of Engineering, University of Malaya, Kuala Lumpur, Malaysia.
[2]The Chancellery, Universiti Tenaga Nasional, Kajang, 43000, Malaysia
[3]Department of Computer Science, Electrical and Space Engineering, Luleå University of Technology, Luleå, Sweden.
Email: azuan@um.edu.my

INTRODUCTION

Compliance monitoring, and pressure sensing, may enhance scoliosis braces treatment outcomes [1]. Internet of things integration with healthcare may enable remote monitoring and tracking of relative data [2]. The study investigates the impact of Nonlinear Autoregressive with eXogenous inputs neural network (NARX) implementation on low-cost pressure sensor's readings stability, considering both no load and loaded states. Additionally, the outlook for further improvements using expanded database is discussed.

METHODS

This study employed a methodology to investigate the impact of implementing the NARX on enhancing the stability of low-cost pressure sensor readings intended for integration into scoliosis braces. Experimental data was collected from the sensor in both the no load and loaded states for loads ranging between 0 and 1.17kg. To address the challenges of drift and noise, the hardware implementation incorporated Watson's bridge, instrumental amplifier, and low pass filter. Median filtering was also applied to eliminate spikes in the data. However, the persistent issue of dynamic drift prompted the utilization of the NARX algorithm, which has demonstrated effectiveness in handling non-stationary signals and has been successfully applied in gyroscope calibration and drift cancellation [3]. By leveraging these techniques, the study aimed to optimize the stability of the pressure sensor readings, thus facilitating their future integration into affordable Internet of Things (IoT) enabled scoliosis braces.

RESULTS AND DISCUSSION

The collected experimental data for both the no load and loaded states were compared against the actual theoretical values, and the performance metrics were calculated to evaluate the effectiveness of the NARX algorithm in predicting the actual values. Table 1 presents the performance metrics, including the correlation coefficient (R), integral of the squared error (ISE), root mean square error (RMSE), and mean absolute error (MAE), for both the denormalized original data and the data after applying the NARX algorithm. The NARX model was shown to enhance the performance of the sensor in estimating the actual values and reducing the errors. Although accuracy has improved, the dynamic error can still be seen when load is left on the sensor as shown in figure 1.
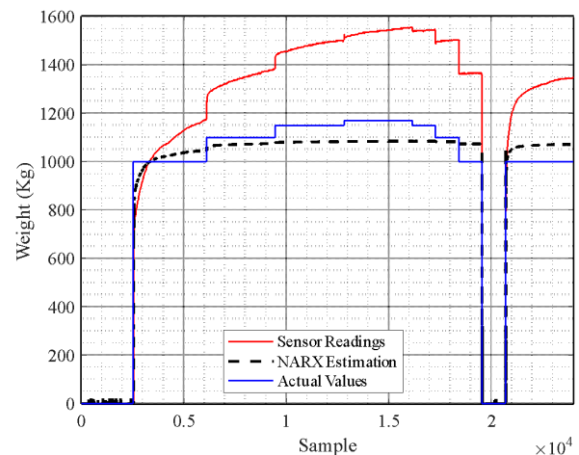
Figure 1 Sensor's readings at several load steps.

CONCLUSION

The implementation of the NARX algorithm demonstrated improved performance, enhancing the stability and accuracy of low-cost pressure sensor readings for scoliosis braces. However, dynamic error persisted when the load was applied to the sensor. Further research is needed to address this issue and optimize the integration of IoT-enabled scoliosis braces.

ACKNOWLEDGEMENT

REFERENCES

[1] Lori A., et al. " *JBJS* **98**.1: 9-14, 2016.
[2] Abd Alghani, K., et al. " *IJERPH* **20**.2: 1319, 2023.
[3] Michael J., et al. *J Biomech* **105**: 115-125, 2023.
[4] Tham, L.K., et al. *IEEE Access* **9**: 36559-36570, 2021.

Table 1: Performance metrics of the original data and the data after applying the NARX algorithm in predicting the actual values.

	R	ISE	RMSE	MAE
Sensor Readings	0.9746	3.82e+8	997.24	915.8
NARX Estimation	0.987	1.65e+6	65.69	48.4

DEVELOPMENT AND USE OF MICROTUBULAR SENSORS FOR NON-INVASIVE BLOOD PRESSURE MONITORING

Subramaniam Shangari[1], Vishnu Sujeesh[2], Anshul Sarin[3], Yu Longteng[2], Lim Yinghao[4], Lim Chwee Teck[3], Leo Hwa Liang[2]

[1] Department of Medicine, National University of Singapore, Singapore
[2] Department of Biomedical Engineering, National University of Singapore, Singapore
[3] Department of Mechanical Engineering, National University of Singapore, Singapore
[4] Department of Cardiology, National University Heart Centre, Singapore

Email: shang_02@nus.edu.sg

INTRODUCTION

Continuous and real time intravascular pressure measurement plays an essential role in critical care monitoring. It allows clinicians to observe vital haemodynamic parameters of a patient which aids in early detection of abnormalities and intervention during or after medical procedures [1]. Traditionally, a catheter is inserted into the artery of a patient to obtain direct and continuous intra-arterial blood pressures. However, catheters generally pose a great risk of infections which may indirectly correlate to an increased mortality rate [2]. In efforts to reduce the chances of infections, non -invasive blood pressure monitoring tools and devices are explored and becoming available in the market. Although these devices provide accurate readings, they are incapable of operating for long hours without perpetual support and supervision of skilled medical professionals.

METHODS

To address the current limitations of the non - invasive monitoring devices, we adapted a promising technology of microtubular sensors to detect minute pulsations on the surface of human skin [3]. Manufacturing procedures, design of sensors were carefully fine-tuned to improve sensitivity and promote efficient mass production. Along with that, fabrication of microtubular sensors and strategic filling of eGaln were introduced to ensure minimal defects and high quality in production. After quality checks and assurance of repeatability, the sensors were put to test to measure and document radial artery pulsations with various mounting methods. Tape (Tegaderm™ film), crepe bandages, tourniquets were used to mount the sensor over the radial artery to retrieve heart rate waveform data.

RESULTS AND DISCUSSION

Given the intention to be deployed in a clinical setting, the measuring device which includes the sensor and mounting setup needs to be reliably attached to the patients for accurate measurements. Figure 1 evidently displays that the sensor with tourniquet had the most stable and consistent graph. Despite possible introduction of artifacts caused by movement, pulsatile waveforms were comparatively sturdy and clear.
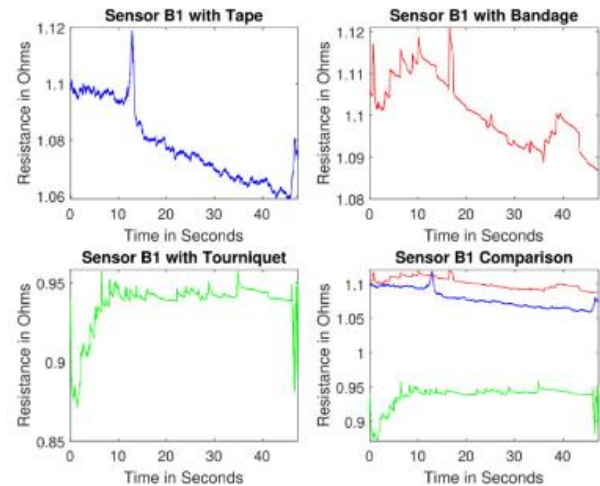
Figure 1 Data collected from different mounting methods

CONCLUSION

In a nutshell, eGaIn filled microtubular sensors were explored as a pain-free and non-invasive approach to monitor physiological blood pressure. This method has shown promising pulse waveform data with a tourniquet which could later be transduced into blood pressure. It was also observed that sensor drift influences the development of a reliable and robust sensor. Hence, standardising the fabrication process with highly precise technologies could improve the reproducibility of the sensor without compromising its standards.

ACKNOWLEDGEMENT

REFERENCES

[1] Saugel, B et al., *Best Practice & Research Clinical Anaesthesiology,* **28**(4): 309-322. 2014.
[2] Lakhal, K et al., *Chest,***153**(4): 1023-1039, 2018.
[3] Xi, W. et al., *Proceedings of the National Academy of Sciences*, **114**(40): 10590-10595, 2017.

DEVELOPMENT OF A GAME-BASED VIRTUAL REALITY PINCH FORCE CONTROL TRAINING SYSTEM FOR BRAIN ACTIVATION

Luigi Gan[1], Chien-Ju Lin[2], Hsiao-Feng Chieh[2] and Fong-Chin Su [1,2]

[1]Department of Biomedical Engineering, [2]Medical Device Innovation Center, National Cheng Kung University, Tainan, Taiwan.

Email: fcsu@ncku.edu.tw

INTRODUCTION

Aging can cause impairments in hand function due to the loss of muscle strength, reduced finger mobility, degenerative changes in the motor cortex etc. And this can lead to the loss of ability to produce and control submaximal forces during thumb and finger opposition, which in turn could reduce one's ability to perform activities of daily living (ADLs). Plenty of gamebased virtual reality (VR) rehabilitation systems have been developed, but most of them are only concerned in providing range of motion exercises, and do not include a force control component. One way of determining if a developed rehabilitation or training system is effective is to compare the induced brain activation of the newer system to traditional methods, as higher brain activations can promote neural plasticity, which is the brain's ability to reorganize itself [1]. With that, the current study developed a game-based VR force control training system, where the user needs to feed a baby using a fork. And the fork in this can only be grabbed by maintaining a certain amount of pinch force calculated from the user's maximum voluntary contraction. Furthermore, this study compared the effects of adding force control to a VR hand tracking system on brain activation and determined if it can be more effective in promoting neural plasticity as compared to regular a VR hand tracking system.

METHODS

This study, approved by the NCKU Institutional Review Board recruited 5 healthy right-handed adults (4 males and 1 female) with an average age of 23±2.12 yrs. The intrasubject experiment utilized a 30 channel fNIRS (NIRx) or functional near infrared spectroscopy, to measure the brain activation while playing the VR game under the two conditions: with force control (wFC) and without force control (woFC). The regions of interest for this experiment include the contralateral/ipsilateral prefronal cortices (cPFC, iPFC), the contralateral/ ipsilateral premotor cortices (cPMC, iPMC), the contralateral/ipsilateral supplementary motor areas (cSMA, iSMA), and the contralateral/ipsilateral primary motor cortices (cM1, iM1). Each condition was repeated for 5 trials, and the raw data were processed and converted to oxygenated hemoglobin concentrations (HbO) using Homer3 a MATLAB (MathWorks) based GUI for processing and analysing fNIRS data. Wilcoxon signed-rank test was used for statistical analysis.

Figure 1 An in-game screenshot including the 3D baby/food/fork models, and a force bar indicating the pinch force production.

RESULTS AND DISCUSSION

The wFC condition, when compared to the woFC condition had significantly higher brain activations in the following regions: cPFC, cM1, iPFC, and iPMC. The higher activations in the cPFC and iPFC under the wFC condition can be attributed to the increased task complexity and higher level of sustained attention required, in order to maintain the pinch force production under the visual guidance of the force bar [2]. Additionally, the higher activations in the cM1 and iPMC is due to the involvement of both brain regions in force control tasks [3].

CONCLUSION

Adding a force control component to a VR hand tracking system led to higher activations in some brain regions, thus making it better than the regular VR hand tracking system in promoting neural plasticity. In the future, more subjects including elderlies and subjects with hand impairments can be recruited to further validate the developed system.

ACKNOWLEDGEMENTS

REFERENCES
[1] Hui-Hui Chiang. *Unpublished master's thesis.* National Cheng Kung University, Taiwan. 2019.
[2] Derosière et al. *NeuroImage* **85:** 471-477, 2014.
[3] Kuhtz-Buschbeck et al. *Journal of Neuroscience* **14(2)**: 382-390, 2007.

EVALUATION OF TEMPERATURE VISUALIZATION INSIDE THE AGAR PHANTOM SIMULATING A LIVING BODY IN MAGNETIC HYPERTHERMIA

Ryuhei Kubota[1], Keiko Ishii[2], Koji Fumoto[1]

[1] Mechanical Engineering, Aoyama Gakuin University / Advanced Thermal and Fluid Control Lab, Sagamihara-Shi, Japan.
[2] Precision Mechanics, Chuo University / Thermal Fluid Engineering Lab, Bunkyo-Ku, Japan.
Email: c5622159@aoyama.jp

INTRODUCTION

Cancer is the leading cause of death among Japanese, and improvement of cancer treatment technology is required. The current major treatment, chemotherapy, surgery, and radiation therapy are highly invasive to the body. Hyperthermia is a minimally invasive treatment that applies the heat-sensitive characteristics of cancer cells by heating the tumor to kill it. Among them, magnetic hyperthermia is a therapy that heats the tumor by inserting magnetic nanoparticles(MNPs) as heating elements into the tumor [1]. This treatment is expected to become a new treatment method due to its minimally invasive feature and its ability to heat cancer cells deep within the human body. However, the heat generation characteristics of MNPs and the method of measuring the temperature inside the body have not yet been clarified, so practical use has not yet been realized [2]. In this report, the Laser-Induced Fluorescence (LIF) method was used to evaluate how the heat generated by MNPs is transferred to the agar phantoms that simulating a living body during the heating experiment [3].

METHODS

In this experiment, Magnetic nanoparticles $(Fe_3O_4,$ 45mg/ml), a heating element was dispersed in pure water and inserted them into the center of the agar phantom. The experimental principle used was the LIF method. This method uses a temperature-sensitive dye whose fluorescence intensity changes with temperature. The temperature distribution was visualized by recording the changes in fluorescence intensity in the phantom during the heating experiment. The experimental procedure was as follows:

A. Using an originally created thermostatic environment creation system, heated samples were maintained at a constant 37°C.
B. A laser was irradiated onto the sample.
C. The high-frequency power supply was turned on and recording were started.
D. The frequency was 200kHz, and the experimental duration was 4500 seconds.
E. The recorded images were processed using the image analysis software "ImageJ" to obtain visualized temperature images based on the relationship between temperature and fluorescence intensity.

RESULTS AND DISCUSSION

Figure 1 shows temperature visualization images of the phantom section every 1500s. The figure shows that heat generated in the MNPs area is transferred to the agar phantom area. This confirms that when MNPs are heated inside the body, It's the potential for heat transfer to normal cells, leading to cell damage. Temperature rise in the phantom area suggests the importance of temperature monitoring during the heating of the affected cancer area.

Conventional research has only evaluated temperature distributions at points, lines, or on surfaces. However, the present experimental results provide a non-contact visualization of time-series changes in the internal temperature distribution. This result will contribute to the practical use of magnetic hyperthermia.
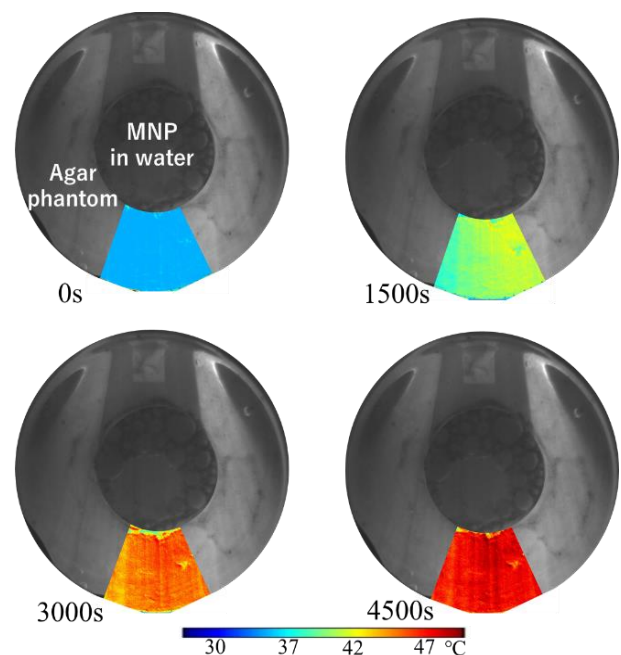
Figure 1 Temperature visualization by the LIF method

CONCLUSION

The temperature rises in the phantom section simulating normal cells was confirmed from the evaluation of internal temperature visualization by the LIF method. On the day of the presentation, the results of experiments using magnetic agar with magnetic nanoparticles dispersed in the phantom simulating cancer cells will be reported in order to bring the results closer to the clinical environment.

REFERENCES

[1] Sharma S.K., et al. *Nano Today* **29**: 795, 2019.
[2] Kandala S.K.et al. *International Journal of Hyperthermia* **38**: 611-622, 2021.
[3] Abdelghany, A. et al. *Experimental in Fluids* **63**:52, 2022.

EVALUATION OF HEAT GENERATION CHARACTERISTICS OF MAGNETIC NANOPARTICLES CONSIDERING POLYDISPERSITY IN MAGNETIC HYPERTHERMIA

Hiroki Nakajima[1], Koji Fumoto[1]

[1] Mechanical Engineering, Aoyama Gakuin University / Advanced Thermal and Fluid Control Laboratory, Sagamihara-shi, Japan.
Email: c5623191@aoyama.jp

INTRODUCTION

Conventional cancer treatment methods are highly invasive, and magnetic hyperthermia is attracting attention as a new cancer treatment method. This therapy focuses on the characteristic that cancer cells shrink and die when heated to 42°C or higher. Conventional hyperthermia has difficulty in heating cancer cells that exist deep in the body. In magnetic hyperthermia, on the other hand, magnetic nanoparticles accumulate in the affected cancer site, and a high frequency alternating magnetic field is applied from outside the body to generate heat in the magnetic nanoparticles, thereby heating only the cancer site locally. This enables minimally invasive and deep-seated cancer cell death. The volumetric power dissipation of magnetic nanoparticles under a high-frequency AC magnetic field can be calculated using the Equation (1) [1]. However, the heat generation characteristics of magnetic nanoparticles by magnetic hyperthermia are still unknown and have not yet been put to practical use.

Therefore, the purpose of this study is to create a simulated model of magnetic hyperthermia and to examine the optimization of heating efficiency by magnetic nanoparticles using electromagnetic field analysis. Therefore, a model of a coil was created, and the magnetic field obtained from it was used to evaluate the efficiency of heat generation when polydisperse magnetic nanoparticles, which are more similar to clinical practice, are used.

$$P = \pi \mu_0 \chi_0 H_0{}^2 f \frac{2\pi f \tau}{1 + (2\pi f \tau)^2} \qquad (1)$$

P: volumetric power dissipation, μ_0: permeability of free space, χ_0: equilibrium susceptibility, H_0: maximum magnetic field,
f: frequency, τ: effective relaxation time

METHODS

The analytical model used in this study consists of a coil and the air surrounding it. The coil specifications are shown below (Table 1). The coil was designed to simulate the matching device (T020-5322B, Thamway Co., Ltd.) used in our laboratory. The simulation software STAR-CCM+ (SIEMENS) was used for the calculations and generation of the computational grid. Since the actual particle size is non-uniform, this study attempted to calculate the rate of temperature rise for polydispersion by introducing a Gaussian function $g(x)$ into Equation (1), as shown in Equation (2).

$$\bar{P} = \int_0^\infty P g(R) dR \qquad (2)$$

Table 1: Coil specification

AC current frequency (kHz)	200
Maximum current value (A)	45.3
Coil inner diameter (mm)	83
Coil length (mm)	86
Number of coil turns (T)	16
Wire rod	Copper pipe (outer diameter4.0 mm，inner diameter3.0 mm)

RESULTS AND DISCUSSION

The change in the rate of temperature rise of the magnetic fluid when the standard deviation σ is varied is shown below (Figure 1). Here, the mean particle size is kept constant. The rate of temperature rise decreases as the standard deviation increases. In particular, a comparison of the rate of temperature rise between a polydisperse and monodisperse states, where the standard deviation is as close to zero as possible, shows that polydisperse plays a significant role in the rate of temperature rise. Therefore, the actual heat generation is expected to be smaller than that calculated from Equation (1).
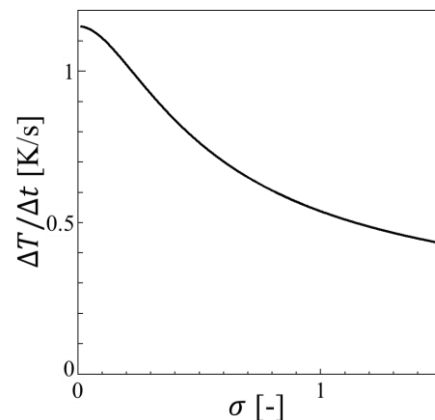

Figure 1: Polydispersity

CONCLUSION

By using the combination of the electromagnetic field analysis model and the model that introduces the distribution function into the formula for calculating the heating value of magnetic nanoparticles, it was confirmed that the polydispersity of magnetic nanoparticles decreases the rate of temperature rise in biological tissues. On the day of the presentation, the heating efficiency of biological tissue obtained by an analytical model that is closer to clinical practice will also be discussed.

REFERENCES

[1] Rosensweig R.E. *Journal of Magnetism and Magnetic Materials* **252**: 370-374, 2002.

RESEARCH ON THE CONTROL OF HEAT GENERATED
BY MAGNETIC NANOPARTICLES IN MAGNETIC HYPERTHERMIA

Shuichi Ideno[1], Koji Fumoto[1]

[1] Mechanical Engineering, Aoyama Gakuin University / Advanced Thermal and Fluid Control Laboratory,

Sagamihara-shi, Japan

Email: c5623155@aoyama.jp

INTRODUCTION

Conventional cancer treatment methods impose a heavy physical and psychological burden on patients due to side effects and high invasiveness. Therefore, the development of minimally invasive cancer treatment methods is desired. Hyperthermia is a minimally invasive therapy that selectively heats tumors by utilizing the characteristic of cancer cells to die at 42°C or higher. Among these, magnetic hyperthermia is expected to be put to practical use [1]. In this method, magnetic nanoparticles (MNPs) are inserted into the tumor as heating elements, which can warm tumors located deep inside the body. However, it has not yet achieved practical application due to the difficulty of controlling the heat generation of the MNPs and their temperature inside the body [2]. Therefore, the objective of this research is to control the temperature distribution in the affected area during magnetic hyperthermia treatment. In this report, we present the results of evaluating the concentration-dependent heating efficiency of the MNPs.

METHODS

In this experiment, a heating sample was prepared by dispersing magnetic nanoparticles (Fe_3O_4) at a concentration of 10 mg/mL to 60 mg/mL in agar, which simulates a living body. The sample was heated by applying an AC magnetic field, and the temperature rise at the center of the sample was measured using an optical fiber thermometer (FL-2000, Anritsu Meter Co., Ltd.). In addition, the Specific Absorption Rate (SAR) was calculated by Equation (1). SAR is usually expressed in watts per gram [W/g] [3].

$$SAR = \frac{mC_{mag} + (1-m)C_{agar}}{m}\left(\frac{dT}{dt}\right)_{max} \qquad (1)$$

where m is the mass fraction of MNPs, C_{mag} and C_{agar} are the specific heat of magnetite and agar, respectively, and $\left(\frac{dT}{dt}\right)_{max}$ is the maximum temperature gradient of the measured temperature rise curve.

The experimental procedure was as follows,

    A. The sample was fixed at the center of the coil.

    B. The sample was confirmed to be in a steady state at room temperature.

    C. AC magnetic field was generated in the coil and heating of the sample was started. The frequency was set at 200 kHz.

    D. The temperature rise was measured for 3600 seconds from the start of heating.

    E. The SAR was calculated based on the measured temperature rise curve.

RESULTS AND DISCUSSION

Figure 1 shows the calculated SAR for each MNPs concentration. These results show that the SAR increases with increasing MNPs concentration. In particular, the SAR increases significantly at high concentration above 40 mg/mL. This may be attributed to the stronger inter-particle interaction, which interferes with the spin of magnetic moments inside MNPs and promotes Néel relaxation loss. The temperature increase value at the center of the sample for 3600 seconds also increases with increasing MNPs concentration. Therefore, it is considered that the higher the MNPs concentration, the higher heating efficiency and temperature increase. This suggests that insertion of high concentration of MNPs into tumors is effective for efficient cancer cell destruction.
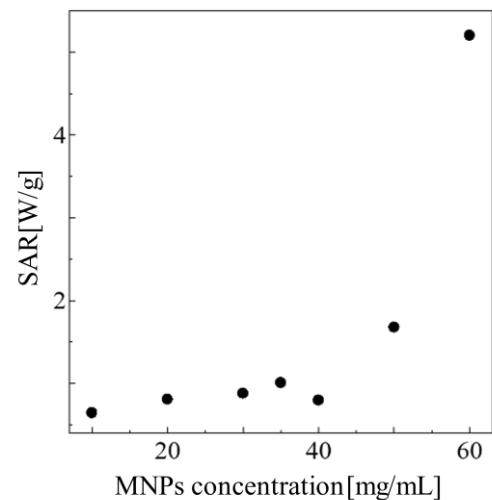

Figure 1 Calculated SAR at each MNPs concentration.

CONCLUSION

MNPs were dispersed in agar, which simulates a living body, and the concentration-dependent heating efficiency was evaluated. As a result, high heating efficiency and temperature increase were confirmed at high MNPs concentration. On the day of the presentation, the results of an experiment using a heated sample inserted inside a phantom that simulates normal tissue will be presented, considering heat dissipation to normal tissue and blood flow around the tumor.

REFERENCES

[1] Dutz S., et al. *Int J Hyperthermia* **29**: 790-800, 2013.

[2] Rajan A., et al. *J Nanoparticle Res* **22**: 1-27, 2020.

[3] Hirosawa F., et al. *Appl Nanosci* **7**: 209-214, 2017.

FEASIBILITY OF VIRTUAL REALITY-BASED EXERGAME TO ENHANCE CARDIOPULMONARY FITNESS IN CHILDREN WITH DEVELOPMENTAL COORDINATION DISORDER

Ya-Ju Ju [1], Yi-Chun Du [2], Po-Sen Hu Kao3, Rong-Ju Cherng [1,3*]

[1] Institute of Allied Health Sciences, College of Medicine, National Cheng Kung University, Tainan, Taiwan
[2] Institute of Biomedical Engineering, College of Engineering, National Cheng Kung University, Tainan, Taiwan
[3] Department of Physical Therapy, College of Medicine, National Cheng Kung University, Tainan, Taiwan
Email: rjc47@mail.ncku.edu.tw

INTRODUCTION

Developmental coordination disorder (DCD) is a neurodevelopmental disorder which is characterized with medical inexplainable motor skill deficits. Such motor skill deficits often limit children's participation in physical activities, further impact their overall health, including reduced cardiopulmonary fitness [1]. With the aid of multimedia technology, virtual reality (VR) has been and is still being widely used to provide variety training scenarios for sports and therapeutic program for patients with rehabilitation needs. Therefore, we have developed a VR-based exergaming program to enhance the cardiopulmonary fitness in children with DCD. The purposes of the study were to examine the feasibility and effect of such VR-based program.

METHODS

Two-phases study design was adopted. Thirteen children with DCD and 10 young adults were recruited in phase I to examined the test-retest and concurrent validity of our system (including a self- developed heart rate monitor) with a laboratory class heart rate device. In phase II, additional 13 children with DCD joined the study to test the feasibility of the system with the outcome measures of the enjoyment rating scale, intrinsic motivation inventory scale (IMI scale) and 20 m-shuttle run test (20mSRT).

RESULTS AND DISCUSSION

In phase I, the results showed good to excellent test-retest reliability in static task of the games and moderate to good in dynamic task. The concurrent validities were excellent both in static and dynamic tasks of the game (Table 1). In phase II, the results showed more than half of the children (18 out of 26) gave the highest score of the enjoyment rating scale and high average scores of IMI. Furthermore, 26 children with DCD after 8-week training of the program showed significant improvement of the total running distance of 20mSRT from 129.23 to 176.92 m ($p < 0.001$).

CONCLUSION

It suggested that the VR-based exergaming program has a potential to be used as an alternative intervention program to enhance the cardiopulmonary fitness in children with DCD.

ACKNOWLEDGEMENT

REFERENCES

[1] Cairney J., et al. BMC *Public Health*: **15**: 266, 2015.

Table 1 Summary of the reliability and concurrent validity results.

		Test-retest reliability				Concurrent validity	
		Adult (N = 10)		DCD Children (N = 13)		Adult (N = 20)	DCD Children (N = 26)
		Test 1	Test 2	Test 1	Test 2		
Static task	Self-heart rate device	83.1 ± 10.1	83.7 ± 11.7**	92.3 ± 12.3	90.1 ± 9.9**	81.5 ± 10.7**	96.6 ± 11**
	Laboratory class-heart rate device	82.3 ± 11.8	82.5 ± 12.2	92.4 ± 10.4	92.9 ± 9	81 ± 11.7	97.4 ± 9.6
Dynamic task	Self-heart rate device	116 ± 17.8	119.2 ± 19*	106.7 ± 11.9	112.4 ± 14.7**	117.6 ± 17.9**	105.8 ± 13.6**
	Laboratory class-heart rate device	119.1 ± 19.1	121.5 ± 18.9	107.1 ± 12.5	111.7 ± 11.7**	118.7 ± 18.5	104.4 ± 12.2

** Correlation is significant at the 0.01 level.
* Correlation is significant at the 0.05 level.

DEVELOPMENT OF A BIOMECHANICAL FEEDBACK TEACHING DEVICE –EDEMA MASSAGE TECHNIQUES APPLICATION FOR FOREARM

Yu-Chen Lin [1], Chieh-Hsiang Hsu [2], and Li-Chieh Kuo [2] and Yu-Sheng Lin*[3]

[1] Department of Occupational Therapy, Da-Yeh University, Changhua, Taiwan.
[2] Department of Occupational Therapy, National Cheng Kung University, Tainan, Taiwan.
[3] Department of Mechanical Engineering, Southern Taiwan University of Science and Technology, Tainan, Taiwan.
*Email: yushenglin@stust.edu.tw

INTRODUCTION

Edema, characterized by excessive fluid accumulation in body tissues, can cause discomfort, stiffness, and impaired function, significantly impacting quality of life. While traditional interventions exist, cases requiring Manual Edema Mobilization (MEM) necessitate specific attention and utilization [1, 2]. For MEM techniques, it is crucial to apply light massage pressure, with a recommended pressure of less than 30mmHg, to prevent lymphatic pathway collapse [3]. However, the lack of suitable tools for training and educating clinical practitioners in applying appropriate pressure poses a challenge. This study aims to address this gap by developing a biomechanical feedback teaching system for forearm edema massage techniques. The system will be utilized to analyze the performance of professional therapists during manual lymphatic massage, enhancing the efficacy and precision of treatment delivery.

METHODS

A. Development

The biomechanical feedback teaching system is designed with two main components: an upper arm prosthesis and a load measurement system for data analysis. Figure 1 illustrates the development process. To create the prosthesis, a digital model of the forearm is generated using a 3D scanner (Einscan H). The model is modified to accommodate a 6-axis force sensor (nano 25, ATI industrial automation). The prosthesis is then 3D printed using a FDM printer and a soft, tissue-like material called TPU. Data measurement is facilitated by National Instrument, and a user interface is programmed using LabVIEW.

| A. 3D Scan | B. Reconstruction | C. 3D Printing Prosthesis | D. Measurement and force visualization |

Figure 1 The process of developing the teaching system

B. Measurement and Experimental Tests

The biomechanical feedback teaching system enables the recording of normal, lateral force, and moments applied to the prosthesis during the experiments. In this study, seven experienced therapists with diverse backgrounds in physical therapy and occupational therapy participated. They performed simulated manual lymphatic massage treatments using the system. Prior to participating in the study, the participants were provided with information about the study's objectives. However, they were not allowed to discuss the details with each other.

RESULTS AND DISCUSSION

Table 1 displays the statistical measurements of performance during the manual lymphatic massage for each participant. The recorded values include the forward force (F_x), lateral force (F_y), and normal force (F_z) exerted during the massage. The results indicate that the force performance of the participants can be categorized into two groups: a gentle group and a strong group. The gentle group applies a slightly gentler force during the massage, while the strong group applies a stronger force. Additionally, it is observed that the strong group tends to have higher associated lateral force, suggesting that they may apply a slight twisting technique during the treatment.

Table 1 A statistic record of all the performance

	Forward (F_x)	Lateral (F_y)	Normal (F_z)
A	4.16 N	3.96 N	17.68 N
B	11.06 N	2.17 N	19.29 N
C	15.48 N	4.60 N	21.90 N
D	4.59 N	1.86 N	14.81 N
E	14.33 N	7.15 N	47.05 N
F	7.75 N	2.37 N	19.67 N
G	12.51 N	7.94 N	20.13 N

CONCLUSION

This study demonstrates the process of developing a biomechanical feedback teaching system. The preliminary results show that two groups of force performance. The future work will continue on studying the technique in different professional backgrounds.

ACKNOWLEDGEMENT

REFERENCES

[1] Miller, L. K. et al., *J Hand Ther*, **30**(4), 432-446, 2017.
[2] Priganc, V. W. et al., *J Hand Ther*, **21**(4), 2008.
[3] Howard, S. B. et al., *J Hand Ther*, **14**(4), 291-301, 2001.

INNOVATIVE DESIGN OF MINIMAL INVASIVE BIODEGRADABLE POLY(GLYCEROL-DODECANOATE) NUCLEUS PULPOSUS SCAFFOLD WITH FUNCTION REGENERATION

Kaixiang Jin[1], Lizhen Wang[1*] and Yubo Fan[1*]

[1] Key Laboratory of Biomechanics and Mechanobiology (Beihang University), Ministry of Education, Beijing Advanced
Innovation Center for Biomedical Engineering, School of Biological Science and Medical Engineering, School of
Engineering Medicine, Beihang University, Beijing, China.
Email: yubofan@buaa.edu.cn lizhenwang@buaa.edu.cn

INTRODUCTION

Degeneration of nucleus pulposus (NP) is irreversible in most of spine diseases, and traditional spinal fusion or discectomy usually injure adjacent segments[1]. Here, an innovative minimally invasive biodegradable NP scaffold with function regeneration inspired by cucumber tendril is developed using shape memory polymer poly(glycerol-dodecanoate) (PGD), whose mechanical property is controlled to the similar with human NP by adjusting synthetic parameters. The chemokine stromal cell-derived factor-1α (SDF-1α) is immobilized to the scaffold recruiting autologous stem cells from peripheral tissue.

METHODS

The characteristics of PGD polymer, including shape transform temperature (27.8 °C-36.6 °C), crosslink densities (1.51E02-4.28E02), and degradation duration (8 weeks-16 weeks), are adjusted and optimized to match the requirements of NP applications[2] by its synthetic parameters. A PGD rod with small diameters (~1.2 mm) at room temperature is delivered through the hollow needle into the nucleus cavity of New Zealand white rabbits. It will curl and deform to a vortex-plate shape with a bigger cross-section (~4 mm^2) triggered by body temperature after implanted.
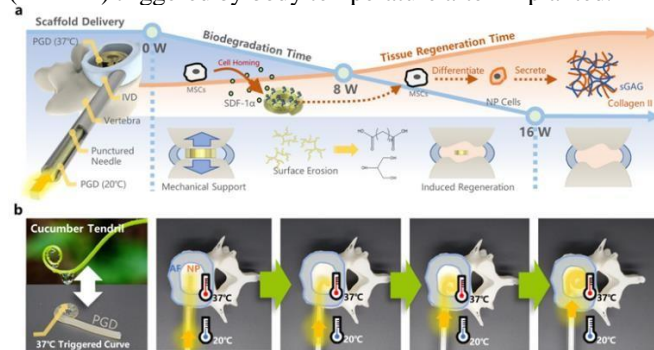

Figure 1 Design of biodegradable minimally invasive PGD NP scaffold with regeneration. **a**, Schematic of the PGD NP scaffold's design. **b**, Shape deformation of minimally invasive design inspired by cucumber tendril triggered by temperature.

RESULTS AND DISCUSSION

The disc height of the PGD+SDF-1α group was maintained and provided enough mechanical support after 1~8 weeks of implantation, avoiding the extrusion of chemokines SDF-1α then affected the disc regeneration. The NP was regenerated for the recruited MSCs induced by the chemokines. Effective instantaneous and equilibrium modulus of the disc in the PGD+SDF-1α group were significantly higher than in the four other groups, and there was no difference with the native intact disc. The reason was that the PGD NP scaffold with chemokine SDF-1α inhibited

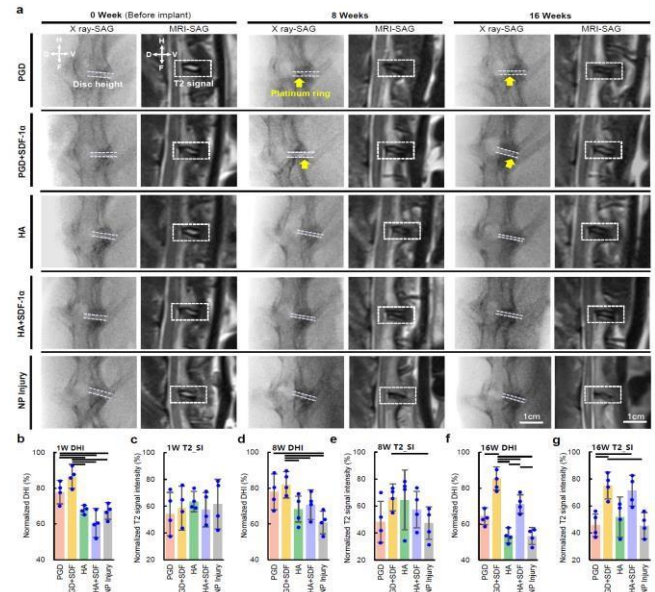the degeneration process of the disc and restored native function of NP.

Figure 1 Disc height and T2 MRI signal intensity of discs implanted with PGD, PGD+ SDF-1α, HA, HA+ SDF-1α scaffolds. **a**, X-ray and MRI T2 images L5-L6 discs for native intact disc and four experimental group before and after 8,16 weeks implantation. **b, d, f,** Normalized DHI of L5-L6 disc in five experimental groups. **c, e, g,** Normalized T2 signal intensity of L5-L6 disc in nucleus cavity.

CONCLUSION

PGD NP scaffold can maintain the disc height, also recruit autologous stem cells, and regenerate degenerated NP through its released SDF-1α within 16 weeks. The design of a minimally invasive NP scaffold with regeneration inspired by a tendril of cucumber vine will be an innovative idea for treatment of disc degeneration, which also has potential application in clinic.

ACKNOWLEDGEMENT

REFERENCES

[1] Front Bioeng Biotechnol 9, 592118, 2021. [2] Spine, 30(24): E724-E729, 2005